Freeform mirror designs for aerospatial multi spectral band imaging systems

Louis Duveau

N°d'ordre NNT : : 2022LYSES017

THESE de DOCTORAT DE L'UNIVERSITE DE LYON
opérée au sein de
Office National d'Etudes et de Recherches Aérospatiales
ONERA

Ecole Doctorale N° 488
ÉCOLE DOCTORALE SCIENCES INGÉNIERIE SANTÉ
Spécialité / discipline de doctorat :
Optique, Photonique, Hyperfréquences

Soutenue publiquement le 04/07/2022, par :
Louis Duveau

Freeform mirror designs for aerospatial multi spectral band imaging systems

---

Devant le jury composé de :

Ferrari, Marc, Astronome, LAM	Président
Sortais, Yvan, Pr. Université Paris Saclay / IOGS	Rapporteur
Nourrit, Vincent, Maître de conférence IMT Bretagne	Rapporteur
Paolacci-Riera, Sylive, responsable Innovation AID	Examinatrice
Lépine, Thierry MC Univ Paris-Saclay/IOGS/LaHC	Directeur de thèse
Druart, Guillaume, Directeur de recherches ONERA	Co-directeur de thèse

Acknowledgements

Mes premiers remerciements vont vers Guillaume Druart du Département d'Optique Théorique et Appliquée de l'ONERA et Thierry Lépine du Laboratoire Hubert Curien pour m'avoir fait confiance et m'avoir confié ce travail de thèse. A Guillaume, merci pour le temps passé, les discussions enrichissantes et tous les conseils avisés. A Thierry, merci pour tes avis toujours pertinents et éclairés. Plus généralement, je tiens à remercier l'ensemble de l'équipe ERIO pour leur accueil chaleureux et leur aide tout au long de ces trois années. Je tiens également a remercier toutes les enseignants qui ont, pendant toute ma scolarité, donné le goût d'apprendre et de comprendre le monde qui m'entoure. Je pense notamment à Mr Souchal, Mme Piquemal, Mr Hello, et à tous les enseignants de l'institut d'optique de Saint Etienne. Merci à tous mes amis, qu'ils soient scientifiques ou non, pour les longues soirées au coin du feu et les nombreux fous rires qui m'ont aidé à continuer mon travail malgré le contexte difficile de ces trois années. Je me dois également de remercier ma famille. Merci à Jeanne, Clément et mes parents pour leur soutien non seulement pendant cette thèse mais également pendant toutes mes études, sans vous l'épreuve aurait été bien plus difficile. Clémentine, merci de m'avoir supporté pendant ces longs mois de rédaction. Si ce fut difficile pour moi, je salue tous les efforts que tu as consentis pour me rendre la vie plus douce. Enfin, je tiens à remercier tout particulièrement mon grand-père qui, de par son intérêt constant pour mes travaux, à été sans le savoir ma principale source de motivation depuis des années déjà. Il est un modèle pour moi, de par sa curiosité sans cesse renouvelée, sa bienveillance et sa positivité.

Contents

List of Figures

List of Tables

Chapter 1

Introduction

In this introduction, we will detail the scope of this research and why the present work focuses on catoptric applications instead of using dioptric surfaces. Then, we will explain what is a freeform surface and the reasons for using it over classical surfaces. Finally, the challenges of freeform optical design are detailed.

1.1 Scope of the manuscript

This manuscript focuses on compact aerospatial optical systems due to the nature of the research at ONERA. In particular it means that the present document will mostly detail systems designed for nanosatellite applications or optronic pods, but comparable designs could be used for a large number of applications.

1.1.1 Context

The present work, due to the nature of research at ONERA and the cofunding of this PhD by the french innovation defense lab (AID), focuses on improving the imaging systems for compact aircraft or spacecrafts. Compact spacecrafts are called nanosatellites. A recent tendency is to launch small satellites of only a few kilograms in low earth orbit (around 600km altitude). Such satellites are particularly useful as a complement of classical satellites thanks to a reduced cost, allowing for constellations of multiple satellites, or short missions at a reduced price. However, theses satellites must also be very compact, which has deep impact on the optical systems carried. Finding ways to minimize the volume taken by the optical payload is critical in the development of imaging nanosatellites.

On military aircraft, drones or planes, the use of optronic pods has become common. These pods are also used by civil defense, such as rescue helicopters, or for industrial purposes. These pods are most of the time gyrostabilized spheres that carry multiple optical instruments. The result is a multiplication of independant optical systems that only share the platform. The miniaturization of these systems allows to increase the number of functions in the same pod or to reduce the size of the pod for it to be carried by a smaller craft. In this work, we will study the possibility to design multi

spectral band systems that has the maximal number of surfaces in common for all the cameras, effectively reducing the overall number of surfaces and possibly the volume of the whole instrument.

1.1.2 Multispectral imaging design

Multispectral imaging is defined as the fact of taking the image of a scene over several wavelengths. If instead of selecting a few specific wavelengths the payload takes a spectrum of the source, the optical system is an hyperspectral imager. Most of the time the selected wavelengths are relatively close to each other, in the visible and near infrared spectrum as an example. An interesting parameter in multispectral instrument is the width of the spectral band over which the incident flux is collected by the sensor. This can range from a few nanometers wide spectrum to a full spectral band. In our work, we study the feasability of multi spectral band designs, which are designed to image very different spectral bands, namely the visible and infrared spectral bands, including thermal infrared imagers, from 0.4 μm wavelength to about 14 μm.

Indeed, the tendency in optical design is to increase the number of spectral bands of imaging systems to gather more information about the imaged scene. This tendency is visible in large satellites. To improve the compactness of such designs, we will study the feasibility of finding a way for the different spectral bands to share most of the optical surfaces. Sharing the optical surfaces between several spectral bands would allow to ease the coregistration of the images made by the different detectors. It could also potentially result in more compact and cheaper designs. However it requires to generate truly panchromatic optical systems from visible to thermal infrared.

1.1.3 Panchromatic imaging systems

Dioptric, catoptric and catadioptric designs

A dioptric design is a design using glass materials such as the lens shown in figure 1.1[1]. In the figure, the complexity of the design is clearly visible. The number of lenses and mechanical pieces is due to the fact that the system is a zoom and is designed with moving parts modifying the focal length and to the fact that the system must be corrected for chromatic aberrations and for a large range of temperatures. A catoptric design is a design using only mirrors. An example of a catoptric design is the Ritchey Chrétien Telescope, like the one shown in figure 1.2. A catadioptric system is a design that uses both lenses and mirrors. Note that on axis catoptric and catadioptric systems present obscuration, which is the loss of rays around the optical axis due to

[1]Canon EF 200-400mm cut, by Gode Nehler on march 15 2015, Wikimedia Commons $https://commons.wikimedia.org/wiki/File:Canon_EF_200-400mm_cut.jpg$, licence CC BY-SA 4.0 - $https://creativecommons.org/licenses/by-sa/4.0/$

the presence of the secondary mirror. This leads to transmission loss, and modification of the pupil shape and therefore impacts the optical quality of the design.

FIGURE 1.1: Cut of a Canon EF 200-400mm lens.

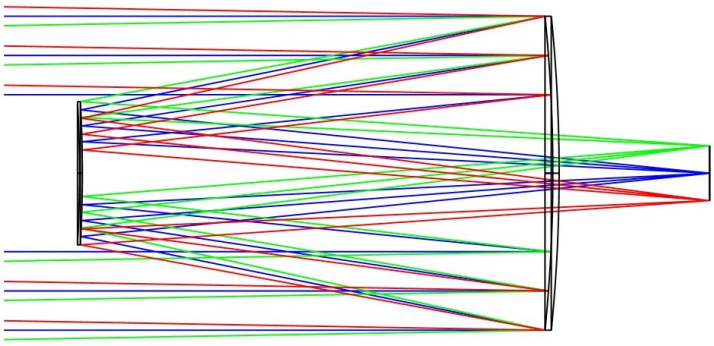

FIGURE 1.2: Ritchey Chrétien Telescope with a 2 degrees full field of view, a focal length of 100mm and an f-number f/5. The central obscuration is clearly visible in this picture.

Dioptric panchromatic systems

Lenses are known to make compact designs. As the beam is transmitted, lenses can be placed fairly close to each other and make for systems that can be shorter than their focal length [2] . Moreover, and particularly for thermal infrared applications, the index of the materials used to manufacture

[2]This is however not always the case. In infrared imaging, the retrofocus [1], [2] or the Petzval lens [3] are frequently used, and are longer than their focal length as an example

the lenses can be high. This effect allows to reduce the angle of incidence of incoming rays onto each optical surface and, as the aberrations are dependant on this angle of incidence [4], effectively reduces the aberrations of the system. However, using lenses is not always the main choice of the designer, as this solution is not devoid from drawbacks too.

The main drawback of using lenses is chromatism. The index of refractive materials varies with the wavelength. This causes an uneven refraction of the light and thus chromatic aberrations. Usually, it is possible to correct the system for chromatic aberration, when the useful spectrum is not too wide. However, correcting the chromatic aberration from visible to thermal infrared is usually not feasible and at least very difficult. Indeed, there are actually only a few optical materials that transmit both visible light and thermal infrared, which complicates the achromatization of the design, as the chromatism is corrected using the differences between the properties of the optical materials. Moreover, many of those materials are not commonly used due to their limited use or other properties. As an example, some of those materials are water soluble (KBr, KCl, NaCl, CsBr, CsI, etc...). All of these issues occur while the achromatisation calls for the use of many different materials at the same time in the design.

Moreover, each lens will reflect or absorb part of the incoming light. The first contributor is the Fresnel reflection, which increases with the index of the material. Using a material with a high index will reduce the aberrations caused by the lens, but also reduce the transmission. This reflection can also lead to the appearance of straylight and narcisse effects. The materials themselves will also absorb part of the light (and potentially re emit signal in the LWIR spectrum). The reflection can be mitigated using antireflect coating on the lens, but such coating is usually optimized for a specific set of wavelengths and having an efficient coating from visible to thermal infrared is also a very difficult challenge. The combined effect of reflections and absorption and their side effects will finally reduce the signal to noise ratio in the final image.

Finally, the lenses must be cased into a mount that is not in the same material. In case of large temperature variation, the difference between the expansion of the glass versus the expansion of the mount can lead to mechanical stress onto the materials and modification of the optical properties of the design. A design corrected at a certain temperature could present large aberrations if the temperature varies. For the design to be usable in large temperature ranges, the number of lenses and mounting materials must be further increased, adding to the issue.

The complexity to solve the chromatism and thermal issues is illustrated by the work of Herman et al. [5] and Sparrold et al. [6]. In those two communications they detail the optomechanical design of an achromatic and athermic lens over the SWIR-LWIR domains. For an even broader spectrum, VIS - LWIR as an example, the list of optical materials available is even shorter and the chromatic aberrations larger, leading to an even more complex solution.

The use of gradient-index lenses, which are lenses with a spatial variation of the material index, is also in study to find potential compact and panchromatic designs using gradient-index [7].

Diffractive optics for achromatization

To compensate the chromatic aberrations, the use of diffractive optics can be evaluated [8], [9]. However standard diffractive lenses cannot be used for panchromatic imaging systems. Indeed, the correction is calculated to correct the chromatism in a spectral band using a specific order of diffraction and is not fully efficient in the full waveband. Recently, the use of multi-order diffractive lenses proved useful for broadband correction of the chromatism [10]–[12], but the examples given are limited in their ability to correct the geometric and chromatic aberrations over the whole field of view (FOV).

Catoptric designs

Mirrors usually can be seen as having the opposite drawbacks and advantages compared to lenses. As an example they cannot be placed close to each other as the second mirror would prevent almost all light to reach the primary due to obscuration, leading to less compact designs and modification in the pupil shape of the design that impacts the optical quality. Moreover, there is no more possibility to increase the material index to reduce geometrical aberrations.

On the other hand, mirrors do not introduce chromatism as the angle of exitance of a reflected ray depends only on the angle of incidence of the incoming ray on the mirror and not on the wavelength of such ray. Moreover, the reflectance of such materials after polishing is high for large spectra, from visible to infrared as shown in figure 1.3[3]. This implies that designing catoptric systems can be made with low to no consideration over the spectral band of the system, each catoptric system being in itself panchromatic by design. In practice, there is caution to be taken for short wavelengths depending on the manufacturing process, as short wavelengths might be more affected by the roughness of the surface and suffer diffraction or diffusion on a surface, while this effect would remain negligible for larger wavelength such as long wave infrared.

Moreover, metals are good thermal conductors and can be used to manufacture the mount of the mirrors. This allows for an easier athermalization of the systems. Indeed, if the entire system is thermalized (i.e. the temperature is uniform) such system is homothetically transformed which does not affect optical quality.

The reasons for using catoptric designs instead of dioptric designs are numerous, but the main are the weight difference and the fact that mirror systems are achromatic and highly transmittive. However, for smaller

[3] by DrBob on march 1 2007, Wikimedia Commons *https://commons.wikimedia.org/wiki/File:Image-Metal-reflectance.png*, licence CC BY-SA 3.0 - *https://creativecommons.org/licenses/by-sa/3.0*

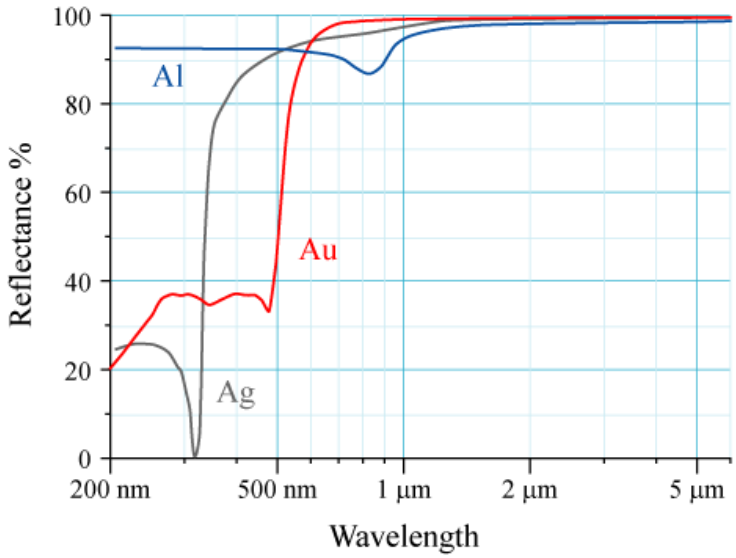

FIGURE 1.3: Reflectance vs. wavelength curves for aluminium (Al), silver (Ag), and gold (Au) metal mirrors at normal incidence.

systems, and even more for large field of view and aperture, the trade off is more balanced, and is detailed in a proceeding from Druart et al. [13]. The compactness of dioptric designs is a good argument to use lenses in nanosatellites, and in compact designs overall.

However, the difference in compactness is only relevant if the system is used for a narrow or single spectral band. For larger spectral band or even for multi spectral band designs, the advantages of mirrors remain. The present work intends to increase the compactness of mirror designs to pave the way for future multi spectral band designs that could be integrated in compact systems such as nanosatellites and optronic pods.

1.2 Catoptric imaging systems

1.2.1 Off axis geometries and impacts on the optical quality

In optical design of catoptric telescopes, the use of off axis configurations have been proposed to suppress central obscuration. An off axis design is a system where some or all optical surfaces are tilted or decentered such that there is no more rotational invariance in the design around an optical axis. As an example, for a design with only spherical surfaces, it means that there is no straight line passing by all the centers of curvature of the surfaces. Such off axis designs can reach diffraction limited perfomances and can be corrected from straylight, though with different main problematic. Using off axis geometries however adds a new family of aberrations called nodal aberrations.

Nodal Aberration Theory

The general theory of optical aberrations has been developed and explained by many authors [14]–[19]. A recent summary to begin with is the one from Sasian [20]. In his article for sixth-order wave aberration in axially symmetric systems [21], [22] Sasian concludes that real ray tracing is inavoidable for the calculation of aberration coefficients. This implies that the theory is only useful up to a certain limit but ray tracing algorithms and optimization are needed for fine calculation of the wavefront error.

However, the Nodal Aberration theory, introduced by Shack and Thompson [23], further developed mainly by Kevin P Thompson and his peers [24]–[29] describes the modified field dependencies of the usual aberrations in off axis designs.

First, Thomson showed that in slightly tilted and decentered rotationally symmetric designs new kinds of aberrations seem to appear. In fact it is the field dependance of third order aberrations that are modified to show constant coma or binodal astigmatism. Then, Thompson et al. extended this aberration theory to off axis designs, leading to a better understanding of the optical quality of such systems. This allows to generate starting points as mentioned in chapter 2. Such theory is very relevant for off axis designs [30], [31], but does not allow to find the best designs for any set of specifications.

This manuscript does not make use of the mathematical tools of Nodal aberration theory, but uses the conclusions of it, notably by looking at the aberrations calculated by real ray tracing and comparing it to the typical aberrations predicted by the nodal aberration theory.

Usually, specifications can be reached using only rotationally symmetric surfaces if the tilts are small [32]. Indeed the nodal aberrations in these cases stay limited and thus do not impact significantly the optical quality. However, for uncooled infrared imaging or large field of views, the tilts become important and the use of freeform surfaces (see subsection 1.2.2) becomes mandatory.

Geometry classification

In this manuscript, emphasis is made on design geometries. This is a topic that is frequently discussed as an example by bauer et al. [33] or Papa et al. [34]. We will use the geometry notations from Volatier et al. article [35], which are more complete than geometry from [36]. In this article, three main geometries using two mirrors are described. The three geometries are the U, Z and α geometries. They are described below:

1. The U geometry is given with same sign tilts of both mirrors. This geometry also implies that there is no crossing of the incoming beam with the output beam. This geometry is shown in figure 1.4.

2. The α geometry is also defined by same sign tilts for both mirrors. However, this geometry involves a crossing between the incoming beam and the output beam. This geometry is visible in figure 1.5.

3. The Z geometry is defined by opposite signs tilts for both mirrors. The geometry is shown in figure 1.6.

Each configuration can be easily identified by looking at the parabasal ray path (see definition in subsection 1.2.2). This classification has the advantage to be easily expanded to a larger number of mirrors. Most configurations can be defined by finding the classification of successive pairs of mirrors.

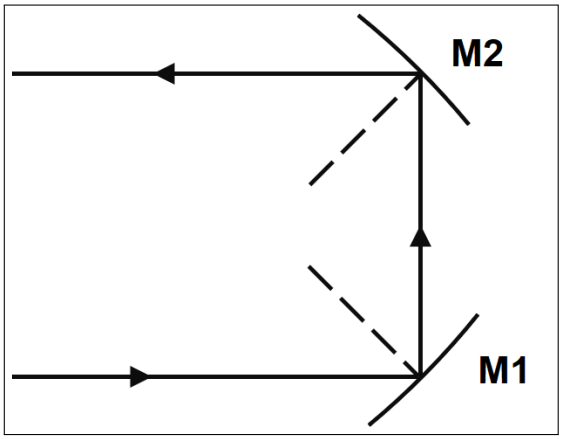

FIGURE 1.4: U geometry with two mirrors

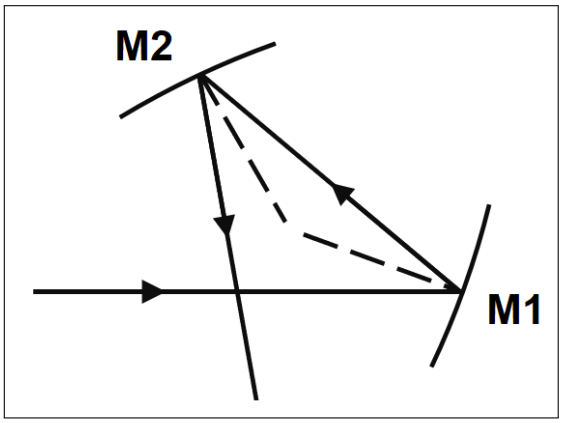

FIGURE 1.5: α geometry with two mirrors

As an example, the most common configuration is the three mirror anastigmat (TMA). In this manuscript, to help the reader by using commonly employed terms, we will call TMA the geometry associated with the first off axis designs labeled as such [37]. However, the name does not certify the geometry, as any three mirror telescope that is corrected for astigmatism is technically a three mirror anastigmat.

Using the expanded classification, we can see in figure 1.7 that the fist two mirrors of the TMA are in a Z-shape configuration, and that the secondary and third mirror are also in a Z-shape configuration. The configuration can thus be labeled as a ZZ configuration.

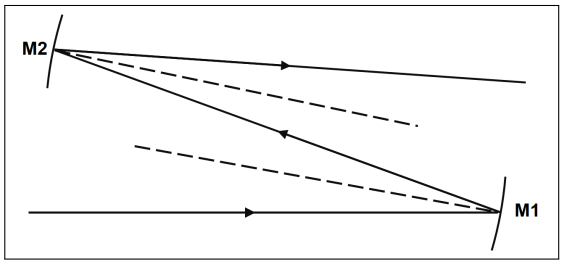

FIGURE 1.6: Z geometry with two mirrors

The Pamplemousse configuration, detailed in chapter 4, can be labeled as an $\alpha\alpha$ configuration and so on. The αZ configuration, described in chapter 4 is named from this extended classification.

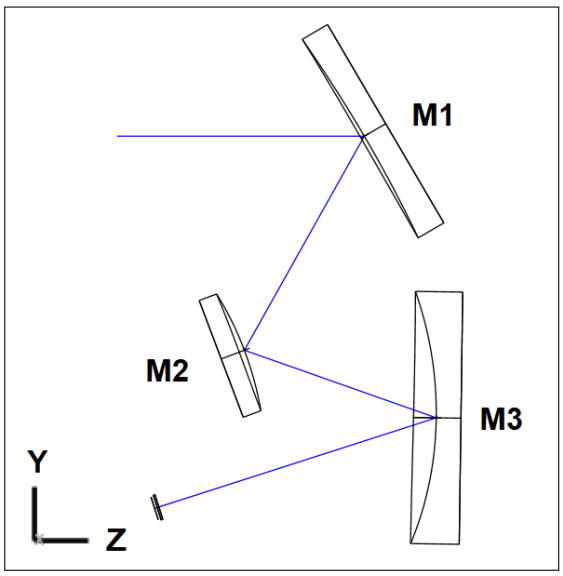

FIGURE 1.7: Parabasal ray path of a TMA (or ZZ) configuration

1.2.2 Definitions

Freeform surfaces

A freeform surface is a surface that is neither a rotationnally symmetric surface nor a decentered portion of a rotationnally symmetric surface [38].

Sometimes, a freeform surface is defined as a surface that must be made using a machine that has three independent axes [39]. This definitions that relies on manufacturing process might not describe accurately all freeform surfaces. As an example, it does not cover molded optics and additions to the definition should be made. Moreover, it leaves room for interpretation as whether an highly decentered rotationnally symmetric surface is a freeform or not. An example of such surface is the first parabolic mirror of the

Extremely Large Telescope. This mirror is a segmented mirror with an overall parabolic shape, so that any segment of the mirror is an off axis portion of a parabola, which is rotationally symmetric [40]. However, with a diameter of 39 meters, the optical axis is too far from most segments and thus each one has to be manufactured as a freeform surface. Note that this definition also include rather old designs, some of which that had a practical use in commercial designs such as the Quintic mirror from Polaroid [41]. Another similar definition is given by Geyl et al. [42] as a surface that has uncorrelated third order coma and astigmatism, which is not the case in rotationnally symmetric surfaces.

As said above, a highly decentered rotationnally symmetric surface must in practice be manufactured as a freeform surface. However for designers such surface has not been designed as a freeform and thus should not be labeled as one at the design stage. Additionally, in most cases there is no reason to design an off centered rotationnally symmetric surface if the manufacturing used allows for more complex shapes that could improve the design.

In this manuscript, we will label rotationally symmetric surfaces as classical surfaces, as the use of aspheres is now generalized. The term aspheres describes a rotationally symmetric surface that is not spherical. This definition of an aspheric surface includes the conicoids.

The use of freeform surfaces in off axis designs can lead, compared to classical rotationally symmetric surfaces, to several improvements in the systems. These improvements are:

1. Improved aberration correction, particularly the nodal aberrations, leading to a lower root mean square (RMS) wavefront error and thus a smaller point spread function for non diffraction limited designs

2. Allowing for large tilts and decenters while keeping the RMS wavefront error, allowing for large field of view and large aperture unobscured designs.

3. Reduction of the number of optical surfaces in off axis designs

4. Increase in the compactness of optical systems.

Most of the time, all of these improvement are brought at the same time by the introduction of freeform surfaces. These improvements can be seen in the designs presented in article from Reimers et al. [43]. In this article the introduction of freeform surfaces in the Offner–Chrisp geometry [44] allowed for an improvement in compactness and reduction of the RMS wavefront error generated by the telescope. The same conclusions are given by Geyl et al. [45] where the freeform allow to reduce the wavefront error and the volume occupied by the system and shows the existence of a trade-off between those two improvements. The work of Schiesser et al. [46] also demonstrates that the use of freeform surfaces in planar symmetric systems allows the designer to find more compact designs with lower wavefront errors.

In practice, freeform surfaces are already in use, and the development of this technology is fast [47].

Chief ray and parabasal ray

For any given field, i.e. any given angle in the object space, there is one ray called the chief ray that reaches the center of the entrance pupil. In classical designs, all surfaces share an axis of symmetry called the optical axis. In centered designs, the optical axis is the reference around which the design lies. In absence of obscuration, the chief ray for the central field follows the optical axis, in a straight line from the object to the image, as it hits every surface at a 90 degrees angle and is therefore not refracted.

In this manuscript, the work is solely focused on off axis optical design. An off-axis design is a design where mirrors are tilted and/or decentered so that there is no longer an optical axis. In such design, we use the parabasal ray as an extension of the optical axis. We define the parabasal ray as the chief ray for the central field. The parabasal ray becomes the reference ray for the design, and particularly when using the method of parabasal ray tracking described in Chapter 2.

1.3 Challenges of freefom optical conception

As shown above, freeform surfaces have great potential for imaging design, and even more for multi spectral band systems. The fact that it is not already commonly used is the best proof that there are still many difficulties in freeform optical systems design and manufacturing. There are difficulties in all four aspects of systems construction: Optimization, Manufacturing, Metrology and Alignment. Claytor et al [48] made a good introduction to the numerous challenges of freeform optics production, even though the state of the art evolved since 2004.

1.3.1 Optimization

The optimization of freeform systems is a huge part of this work. Article from Van Grol et al. [49] shows the complexity of the optimization of a standard lens. In this article, the local minima for three lenses are given. As freeform surfaces have many more variables than classical surfaces, the optimization is made on a function with high dimensions, leading to more local minima and saddle points. A saddle point is a point where the gradient of the function is zero, but is not a local minima. This poses several problems in the optimization that prevents from easily obtaining a satisfying result. More details on this are given in chapter 2.

1.3.2 Manufacturing

Manufacturing of freeform surfaces is also made very complex by the difficulty to polish them while keeping the surface shape as close as possible from the calculated one. Many machining methods exist and are detailed in article from Fang et al. [50]. In their article J. Rolland et al. [38] describe rapidly the main manufacturing methods. The categories given by them are ultraprecision machining, loose abrasive or bound abrasive finishing, molding/replication, and novel processes.

Ultraprecision machining include all methods allowing to make freeform optics using single point diamond turning, where the surface is manufactured by a diamond manufacturing head. Usually the piece is placed on a lathe, thus the name of diamond turning. Figure 1.8 shows several machining methods. Slow tool servo (STS) or Fast tool servo (FTS) use a linear movement of the machining head to generate non rotationnaly symmetric surfaces. The difference between both is the ability of fast tool servo to move the tool faster, using piezoelectric actuators as an example, at the cost of a increased difficulty to have the correct shape with the adequate roughness. A study of the roughness of freeform mirrors generated by ultraprecision machining is available in article from Zhang et al. [51].

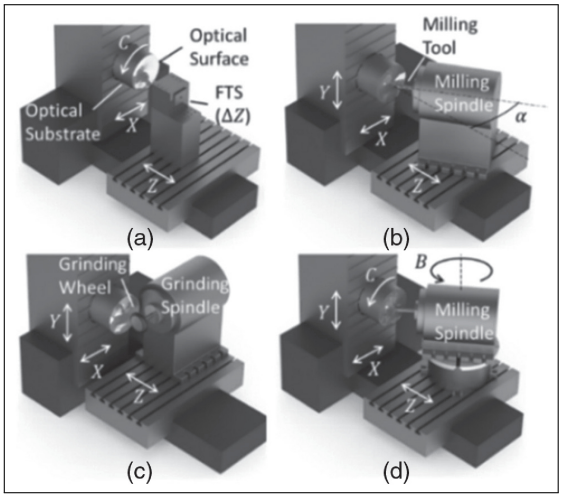

FIGURE 1.8: Geometric characteristics of ultra-precision machining processes: (a) coordinated-axis diamond turning (X-Z-C), (b) three axis milling (X-Y-Z), (c) three axis grinding (X-Y-Z) and (d) five-axis milling (X-Y-Z-B-C). From [38]

Abrasive finishing consist in polishing subapertures of the surface until the piece has the correct shape [52]. It is mostly used for fine finishing of a surface previously pre-shaped using a milling technique. Most known methods are sub-aperture mechanical polishing [53], magnetorheological finishing [54] or ion beam figuring [55]. Molding of freeform optics is a key technology, as it could lead to low cost high volume production of freeform

optics. Molding freeform mirrors could lead to achromatic systems not using any costly material.

However, there are still many challenges to resolve [56].In this manuscript, all manufactured surfaces have been made using the Slow tool servo method, which is the slowest but most precise method for low cost manufacturing of small parts [57]–[59].

The manufacturing of freeform surfaces is a challenge in itself. In the present work, the surface sag, freeform departure and orthoradial slopes have been given for most mirrors. This allows the experienced reader to evaluate the manufacturability of the surfaces. Indeed, my experience in the manufacturing of freeform surfaces does not allow me to draw conclusion on the manufacturability of a freeform surface, and even more in an quickly evolving domain. Although not used for the optimization of the designs presented in this work, the surface RMS departure from the base sphere or the RMS slope can be easily and quickly computed provided that the adequate surface definition is used. The knowledge of these parameters can be used to ease the manufacturability of surfaces if the manufacturing process requires constraints over the surface sag. The benefits for manufacturing of sag orthogonal polynomials is explained in the article from Takaki et al. [60]. There exist also slope orthogonal polynomials that have been defined for similar purposes [61]. The design method presented in the present work could thus be used with a more "manufacturing-aware" merit function. In their article Garrard et al. [62] detail a method that takes into account manufacturing during design process.

1.3.3 Metrology

Manufacturing of freeform optics is also limited by the capacity to measure the optical surface. Indeed, to ensure that a surface has been correctly manufactured it is mandatory to measure it.

Measurement of optical surfaces is mainly performed using interferometry, but this method requires a null surface that serves as a reference. The null must be as close to the manufactured surface as possible as the interferometry is very precise but is limited in the sag of the measured wavefront. The null must then be also manufactured and precisely measured, which is costly. Moreover such null can be hard to align. A common type of null to generate an adequate wavefront is the computer generated hologram (CGH) [63]. The CGH can also include fiducials to ease the alignment during the metrology of the freeform surface [64]. Other methods exist, such as the Shack-Hartmann method or the use of the Quadri-Wave Lateral Shearing Interferometry [65], but are limited in resolution.

As the present work do not focuses on metrology, we invite the reader to consult the literature on this subject, and in particular the articles of Savio et al. [66] which is very complete on metrology techniques for freeform surfaces (including non optical parts) and the article from Trumper et al.

[67]. Other interesting articles are articles from Supranowitz et al. [68] on stitching interferometry for the metrology of freeform surfaces, from Hausel et al. [69] on the interest of deflectometry compared to interferometry for freeform metrology. More details on deflectometry are available in the work of Pérard ad Beyerer [70]. An example of freeform tested by deflectometry is given in the communication from Houllier et al. [71].

1.3.4 Alignment

The final issue of freeform catoptric designs is the alignment of those systems. In off axis system, there is no optical axis to serve as a reference for the integration of the system. In this scope, each surface must be aligned in a three dimensional fashion, with many more degrees of freedom in the alignment of each surface. Such alignment is tedious, and one can easily understand that the alignment process would be very complex. This is even more complex for non planar symmetric designs. Several methods exist. The main method is using mechanical fiducials. Examples of fiducials usable for freeform optics alignment are given in article from Brunelle et al. [72]. The article talks about alignment of freeform surfaces for testing, but similar methods can be used for alignment of the surfaces. A very good example is the three mirror design by Zhu et al. [73]. In this article, the first and third mirror are manufactured in a single substrate and spherical surfaces are manufactured on this M1-M3 piece and on the back face of the secondary mirror. These spherical surfaces are used to align the system as shown in their figure 7.

In the present manuscript our goal is to minimize the number of variables to tweak during the alignment, and even to remove any active alignment if possible. This is traduced by a minimization of the number of compensators in the tolerancing process.

1.3.5 Previous related works

For nanosatellites, a standard called CubeSat exists [74]. This standard gives specific volume and interfaces specifications for nanosatellites. The volume is measured in "units", labeled U, which are 10cm side cubes. Usually, cubesats range from 1U to 12U. This standard has been brought to us by the California Polytechnic State University and Stanford University in 1999 in order to reduce the costs to perform research in space. Communication from Zuccaro Marchi et al. [75] shows the interest of these nanosatellites for research, and freeform designs among them. The reading of the communication from Esposito and Zuccaro Marchi [76] on Hyperscout is also advised to show an example of a 1U optical cubesat. A more precise and detailed description of the interest of cubesat missions is the excellent article from Poghosyan and Golkar [77], and notably the section 4.1 that details the optical payloads of CubeSats.

Our work intends to design multispectral band optical payloads using mirrors for nanosatellites - and therefore for cubesats. However, the fixed volume reverse the way systems must be designed. With CubeSats we need to fit the optical system in the allocated volume instead of building the satellite around the payload.

Example of designs that were calculated for earth observation using freeform surfaces are numerous. We are particularly interested in infrared nanosatellites as the specifications for such designs require the use of freeform optics to fit a catoptric system in a cubesat. Beier et al. developed a freeform anamorphic telescope for space telescopes [78]. Jahn et al. used the principle of the slicer [79]–[82] used to divide a rectangular field of view into a linear one for spectroscopy. Jahn et al. reversed this principle using freeform mirrors to image a linear field of view on a rectangular detector [83]. Houllier et al. conceived a two unit TMA and manufactured the third mirror [71]. Although not for space applications, the two mirror system designed and manufactured by Xie et al. [84] could be used in spaceborne application due to similar focal length and field of view.

For optronic pods, the folded geometries are interesting. The pamplemousse shape is particularly interesting as the mirrors naturally lies in a sphere. The geometry is visible in literature [85]–[87] and is detailed in chapter 4.

Chapter 2

Tools and methods for freeform optical design

This chapter details the optical design method used in next chapters. This method relies on the use of polynomial basis for the description of surface shapes. The first section gives an overview of surface shapes commonly used for optical design. The second section details several point repartition in the pupil plane, still focusing on the repartitions used in the present work, some of which follow quadrature rules. The third section presents a systematic exploration of the optimization of three freeform catoptric designs using each of the aforementioned bases and four different quadrature schemes. The results of this study is presented in the last section.

These parameters affect the merit function and therefore the design optimization. Usually in optical design, a merit function is generated in order to optimize the system. This merit function takes as input the parameters of the system and user defined parameters and returns a single value. In Zemax OpticStudio, the merit function is a square sum of operands, which are diverse functions that can be used to evaluate the optical quality using ray tracing and to constrain the system parameters that can not be fixed beforehand, such as the focal length as an example. The parameters of the system are then optimized in order to minimize the value returned by the merit function. As the merit function is a square sum of elemental functions that are not necessarily differentiable, the merit function is usually not differentiable either and the optimization relies on black box descent algorithms. The most renowned for non linear least square problems is the Levenberg-Marquardt algorithm, also known as the Damped Least Square method, which is the default algorithm in Zemax OpticStudio.

2.1 Freeform surfaces representations

There are several ways to describe the shape of freeform optics. This sections presents a review of most known ways of describing a freeform surface that has been actually been studied for optical design. This review is however only a summary focusing on the representations useful for the present manuscript as previous work already performed a detailed review of all available descriptions [88]–[91]. The common way in optical design is

to define a surface by using a polynomial basis. However, some approaches are based on interpolations around a grid of samples, much like in computer assisted design for mechanical parts. Finally, the surface can also be generated by a sum of local functions. The main example for this generation is the development of surfaces defined using radial basis functions [92]–[96].

2.1.1 Polynomial representations

The main interest of using a polynomial basis is that the number of parameters can be kept relatively low and progressively increased if necessary. It allows to reduce the computational power needed to optimize the design on a standard computer in at most a few hours of optimization time. Moreover, for any degree n all subsets of polynomials basis with degrees of n or less describe the exact same space of surfaces, making a conversion from one representation to the other relatively easy. The surface sag can be described using the following equation:

$$z(x,y) = z_{base}(x,y) + \sum_{i}^{N} a_i P_i(x,y) \tag{2.1}$$

With z_{base} the sag of a base surface, commonly a sphere, a conic or a biconic surface, and P_i a set of polynoms, here taken up to the N^{th} polynom. The entire set of surfaces that have an unique sag for any x, y coordinate forms a vector set that can be fully described by any basis of 2D polynomials. This ensures that any surface can be described using any polynomial basis. Using this property, the use of a base surface description seems to be theoretically useless and redundant. However, the use of a base sphere serves two purposes. First, it allows to design a surface where most of the sag is described by the base surface, and only a departure from this sphere is computed. The visualization of this departure allows to clearly emphasize the non rotationally symmetric part of the surface. The second and best reason for this surface definition is the fact that the spherical or conical surfaces are the usual surfaces descriptions, so that a standard spherical surface can be easily transformed into a freeform surface and vice versa while keeping the overall shape and specifications of the system.

In the present work, three polynomial bases have been selected:

1. XY polynomials
2. Zernike polynomials
3. Freeform Qbfs polynomials

As Zernike polynomials and Qbfs polynomials have been designed to be orthonormal over the unit disk, it is convenient to define the surface with radial coordinates and a normalization around the surface edge. The surface

sag becomes, as detailed in [97]:

$$z(u,\varphi) = z_{base}(r,\varphi) + \frac{B(u,\varphi)}{P(r,\varphi)} \sum_{i}^{N} a_i P_i(u,\varphi) \tag{2.2}$$

with r being the radial coordinate $r = \sqrt{x^2+y^2}$, u being the normalized radial coordinate $u = r/r_{norm}$, B is a boundary function, setting boundary values to the data. An example is the boundary function $(u^2-1)u^2$ in the rotationally symmetric Qbfs polynomials. It sets the aspheric sag to be equal to zero at the center of the surface and over the normalization radius. P is a projection factor to define the added sag normally to the base surface instead of along the Z axis. If this projection factor is not identical for all surface definitions the sag is not given along the Z axis and thus the exact conversion from one basis subset to the other is not possible.

XY polynomials

XY polynomials, are simply the Taylor expansion in X and Y. They can be written using the form:

$$z(x,y) = z_{base}(x,y) + \sum_{m,n}^{M,N} a_{m,n} \bar{x}^m \bar{y}^n \tag{2.3}$$

With $\bar{x} = \frac{x}{r_{norm}}$ and $\bar{y} = \frac{y}{r_{norm}}$ the normalized coordinates, and $a_{m,n}$ the coefficient for each monomial. The main advantage of this basis is that it is particularly straightforward, making the shape of each monomial relatively easy to comprehend for the designer. The derivative of each monomial can be also quickly written if needed. However, this basis is not orthogonal, so the coefficients of this basis are not linked to any physical quantity. In the present work, z_{base} is a conic given by the equation:

$$z(r) = \frac{cr^2}{1+\sqrt{1-(1+k)c^2r^2}} \tag{2.4}$$

Where c is the curvature of the surface, k is the conic constant and r is the radial coordinate $r = \sqrt{x^2+y^2}$.

Zernike polynomials

Zernike Polynomials are the most known in the optical community as they are used by all designers to decompose the wavefront into aberrations. They are mostly used for their property of being orthonormal over the unit circle -The basis can be reconstructed for different pupil shapes as shown in articles from Mahajan and Dai [98]–[101]- with the first terms performing a decomposition of the wavefront that closely follows the Seidel aberrations of the system. Here we are using a normalized version of the polynoms so the basis becomes orthonormal over the unit circle. For more details

about Zernike polynomials and their orthonormalization please refer to the literature mentioned above [88]–[91] as each of these contains all necessary information on this basis or the work of Born & Wolf [18] or Noll [102]. Zernike polynomials are defined by the following equation with (m+n) even:

$$z(r,\varphi) = \frac{cr^2}{1+\sqrt{1-(1+k)c^2r^2}} + \sum_{n=0}^{N}\sum_{m=-n}^{n} a_{n,m}Z_n^m(\rho,\varphi) \tag{2.5}$$

Where c is the curvature of the surface, k is the conic constant, Z_i is the ith Zernike polynomial, (r,φ) are the polar coordinates of the point in the surface, $\rho = r/r_{max}$ is the normalized radial coordinate, and N is the maximal radial term chosen. n is the radial term of the polynomial. Most of the time the radius of the surface is variable, and thus r_{max} might not be fixed. To avoid instability in the optimization the normalization radius can often be fixed. Several types of Zernike polynomials exist, with differences in the ordering scheme. In the present work, the ordering used is the one used for Zernike Standard coefficients in Zemax, which uses the ordering from Born and Wolf [18] and are normalized over the RMS contribution. Several other ordering exist but are not detailed here but can easily be found in the literature.

Each polynomial Z_n^m is defined by:

$$Z_n^m(\rho,\varphi) = N_{n,m}R_{n,m}(\rho)A_{n,m}(\theta) \tag{2.6}$$

Where $N_{n,m}$ is a normalization factor, $R_{n,m}(\rho)$ is the radial component and $A_{n,m}$ is the azimutal component.

$$N_{n,m} = \sqrt{\frac{2(n+1)}{1+\delta_{m,0}}} \tag{2.7}$$

δ is the Kronecker delta, which is equal to 1 if $m = 0$ and 0 if $m \neq 0$.

$$R_{n,m}(\rho) = \sum_{k=0}^{\frac{n-|m|}{2}} (-1)^k \frac{(n-k)!}{k!(\frac{n-m}{2}-k)(\frac{n+m}{2}-k)}\rho^{n-2k} \tag{2.8}$$

$$A_{n,m}(\theta) = \begin{cases} cos(m\varphi) & m \geq 0 \\ sin(m\varphi) & m < 0 \end{cases} \tag{2.9}$$

This basis is the most used in the optical community due to its link with the aberrations. As the Zernike polynomials are orthonormal the root mean square of the sag departure (here noted Δz) is easily calculated:

$$\sigma_{\Delta z}^2 = \sum_{(n,m)\neq(0,0)} a_{n,m}^2 \tag{2.10}$$

It results that for optical design, the orthogonality allows the designer to easily compute the RMS sag of the freeform departure, which can be used

for tolerancing.

Q type polynomials

Q polynomials have been developed by Forbes [61]. Just like the sum of the squared coefficients from the Zernike polynomials gives the RMS freeform sag of the surface, the Q polynomials have been designed to be orthogonal in gradient. Due to this property, the sum of squared coefficients of the Q polynomials is the RMS gradient of the departure from the base shape.

The surface sag is described by the following equation:

$$z(r,\varphi) = \frac{cr^2}{1+\sqrt{1-(1+k)c^2r^2}} + \frac{\bar{r}^2(1-\bar{r}^2)}{\sqrt{1-c^2r^2}} \sum_{n=0} a_n^0 Q_n^0(\bar{r}^2) + \frac{1}{\sqrt{1-c^2r^2}} \sum_{m=1} \bar{r}^m \sum_{n=0} (a_n^m cos(m\varphi) + b_n^m sin(m\varphi)) Q_n^m(\bar{r}^2) \tag{2.11}$$

The upper limits of the indices of summations are the following: for a given maximal order N, the sum for the first sum (m=0), all terms with $2n+4 \leq N$ are summed. For the second sum, the terms considered are those for which $2n+m < N$.

There is no simple definition for the radial terms Q_n^m, however the method to compute the Q polynomials is given in the initial article [61]. The Q_n^0, which are the rotationally symmetric terms, are the Q_{bfs} created by Forbes for aspheric lens design in previous articles [103], [104]. Due to the presence of a projection factor, the departure is not given along the z axis, and due to this fact, any conversion from Zernike or XY to Q polynomials needs an approximation. For this reason, the work described in the present manuscript mainly used the Zernike and XY polynomials in order to be able to convert the design from one basis to the other.

Other polynomial bases

Many other bases can be used for optical design. The 2D Chebyshev polynoms are orthogonal over the unit square with the weighting function $\frac{1}{1-x^2}$ or the weighting function $\sqrt{1-x^2}$. The Legendre polynomials are another basis orthogonal over the unit square but using a uniform weighting function. The Berstein polynomials also have been used for optical surface description. All of these surfaces are valid surfaces for the optimization of freeform designs. However we chose XY, Zernike and Q polynomials as the first two are the most common bases in the community, and the Q polynomials slope orthogonality might be very convenient in many applications to control the freeform slopes of the surfaces during the optimization process [105], [106]

2.1.2 Non polynomial representations

There are several surfaces descriptions that do not rely on polynomial expansion. Some examples are the Non-Uniformal Rational B-Splines (NURBS) that interpolate the surface from a point cloud. This allows to define the surface using a set of points and a given interpolation between those points. Polygonal interpolation can be used, such as Nagata patches. Finally, radial basis functions (RBF) have been studied to improve the optimization of optical designs. The radial basis function method is based on the addition of a function that locally adds a rotationally symmetric sag around a specific point of the surface. By adding numerous RBF in the surface, the shape of the surface can be generated. All these descriptions can lead to surface shapes that are not constrained by a maximal radial order. However, to design a surface with imaging capabilities such descriptions need a large set of points to be useful. This implies that there are many variables to optimize. To compute precisely a large set of variables, a large number of rays must also be traced to generate a viable merit function.

In order to minimize this number, the ray distribution inside the pupil must be carefully chosen. The next section details possible pupil samplings for ray tracing.

2.2 Pupil sampling for optimization and analysis of optical systems

For any given field angle, the wavefront or spot diagram can be calculated by using ray tracing. However, only a finite number of rays can be traced, leading to errors in optical quality assessment. To try and reduce this error, the number of rays can be increased, but it is also necessary to select an adequate distribution of the rays in the pupil to minimize the error for any given number of rays. The goal of this distribution choice is actually to trace as few rays as possible, leading to a faster computation of the merit function and thus to a faster convergence of the system. In freeform optical design, this is more important than ever as the large number of variables slows the descent method, sometimes to the point where the algorithm cannot converge in less than a few days of optimization. In this section we will focus mainly on a few distributions, some of which are quadratures. An overview of more samplings not discussed in the present work is given in Houllier's manuscript [91].

2.2.1 Miscellaneous samplings

This section details miscellaneous distributions in the pupil that can be used. In this case, we are mostly looking at distributions that can reliably generate a spot diagram that we can use for RMS spot radius measurement. For this purpose, we aim to trace rays that are uniformly distributed in the pupil to simulate a flat incoming wavefront with a constant amplitude.

Random radial sampling

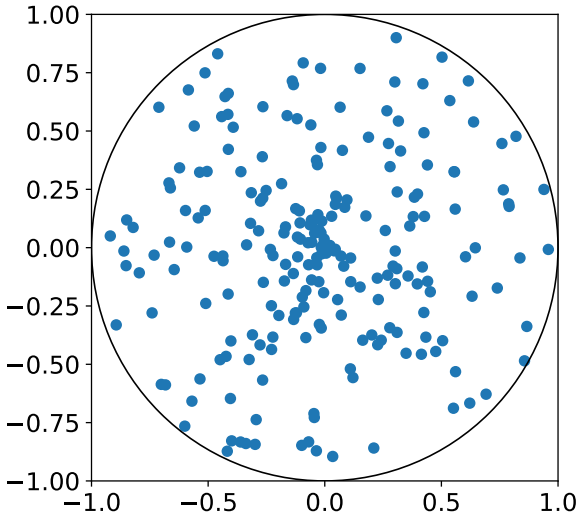

FIGURE 2.1: Random radial distribution with 225 points. Uniform weighting.

As optical systems are often designed with a circular entrance pupil, the first and naive distribution is a random radial sampling, with each point being defined in polar coordinates with a radius r randomly chosen between 0 and 1 and a random azimuth in $[0, 2\pi)$ (the parenthesis showing that the value 2π is outside of the range). This allows to generate easily the required number of rays. Such distribution is shown in figure 2.1. However, this distribution generates a cluster of points around the center of the pupil. If the merit function or the RMS spot radius is computed using such ray distribution the center of the pupil would be over represented and the aberrations would be underestimated.

Random cartesian sampling

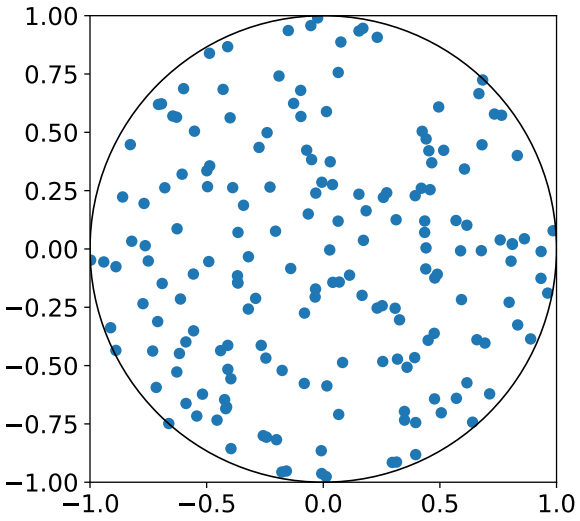

FIGURE 2.2: Random cartesian distribution with 225 point, some of which have been removed due to being out of the unit disk. Uniform weighting.

To cope for such clustering, a random cartesian sampling can be generated, with x and y positions being randomly selected in $[-1, 1]$. Then, any point outside of the unit disk is removed to only keep points passing through the pupil. Such distribution is shown in figure 2.2. Yet, the clustering issue is not solved, and there are still clusters of points. Because of these clusters, the area represented by each ray is not uniform, and therefore it does not simulate accurately a collimated beam from a point source at infinity.

Cartesian uniform sampling

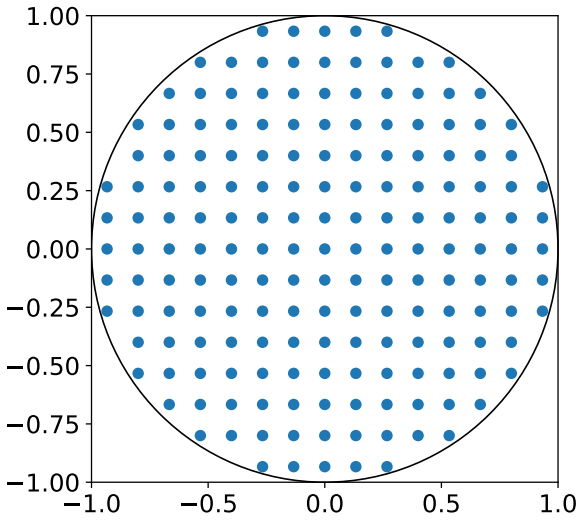

FIGURE 2.3: Uniform cartesian distribution with 225 points, some of which have been removed due to being out of the unit disk. Uniform weighting.

To avoid the clustering issue from the previous distribution, a uniform cartesian sampling can be used. A uniform grid is generated and any point outside of the unit disk is ignored. This leads to the distribution shown in figure 2.3.

Poisson-disk sampling

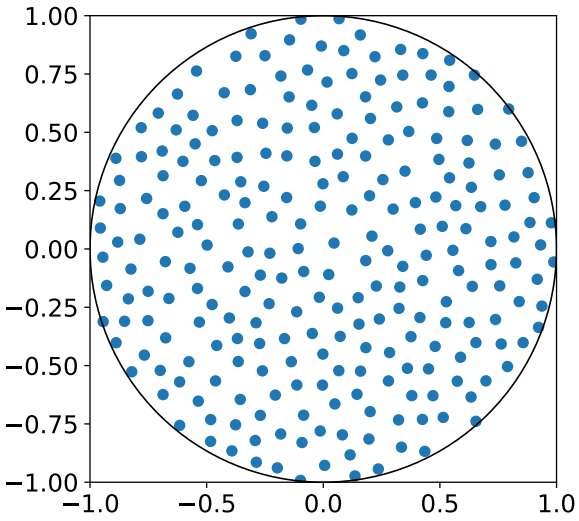

FIGURE 2.4: Poisson Disk distribution with 225 points. Uniform weighting.

Sometimes, the local minimum for the merit function does not result in a design with the properties that were anticipated. As an example, the RMS spot radius of the final design can still be very high even with a merit function value particularly low. This is mostly true for merit functions that estimate the design with only a limited number of rays. This happens when the rays used in the merit function are placed so that some wavefront errors are not possible to measure. As an example, the following system shown in figure 2.5 has been optimized using nine rays in the pupil and a cartesian uniform sampling, this system is included in the designs for the systematic study of section 2.4.

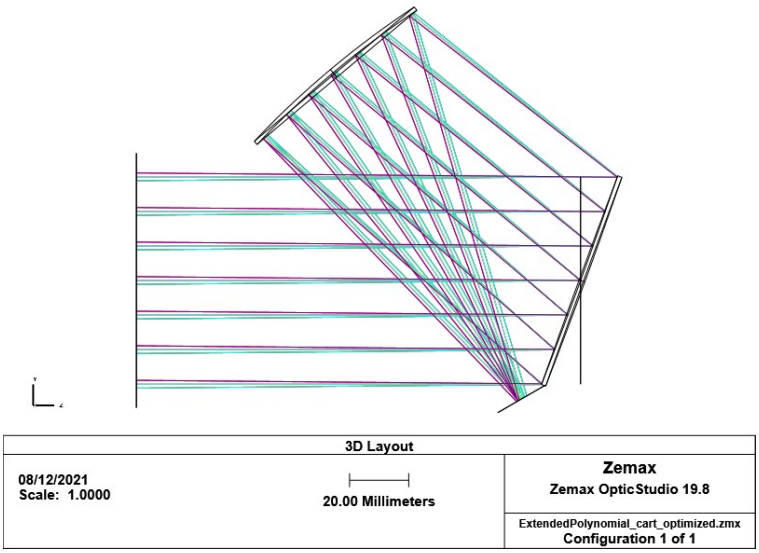

FIGURE 2.5: Two mirror design optimized with 9 rays in a cartesian uniform sampling and surfaces defined as extended polynomials

The resulting system has a cross RMS spot diagram shown in figure 2.6 where we can see that the design is optimized to minimize the spot radius for the rays in the merit function traced in orange, and not for the real spot radius in blue. All rays used for optimization end close to the centroid, hence the low value of the merit function, but this does not depict the reality of the optical quality. To cope for this situation, a random sampling to trace the RMS spot diagram, itself used for optical quality assessment, is useful to avoid having the same distribution for the analysis and for the optimization. However, we still must avoid any clustering of the rays in the pupil. The solution is to generate a Poisson disk distribution, such as the one pictured in figure 2.4.

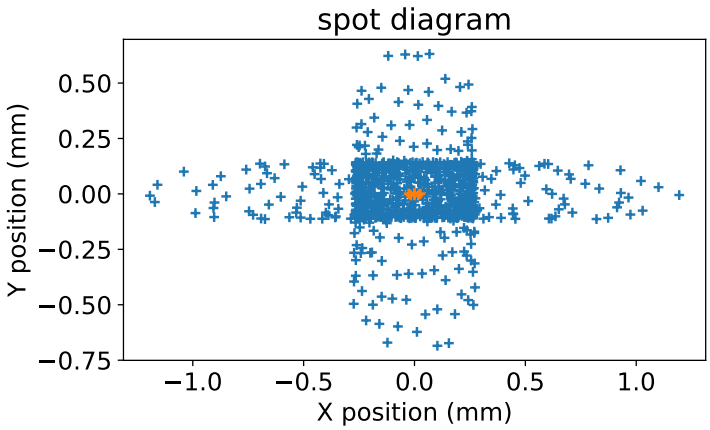

FIGURE 2.6: Spot diagrams for the Poisson disk distribution with 900 rays (blue) and cartesian uniform sampling with 9 rays (red).

The Poisson Disk distribution generates a blue noise distribution. Every point in this distribution is generated so that no point is closer than a fixed radius r, and every point has at least a neighbor that is closer than 2r. The method used here is the Robert Bridson method [107] that is an O(n) algorithm, brought to python by Pavel Zun [108]. This procedural method generates the distribution from two parameters r and k. Without giving technical details explained in the article from Bridson, the method relies on a few simple steps. First a point is randomly taken among an active list of points. This list is initially empty and the first point of the list is placed randomly in the pupil. Then, the algorithm tries to randomly place a point around the selected point at a distance between r and 2r. If this point has no neighbor closer than r this point is kept and added to the active list. If not, another random sample is generated up to 30 samples. If no sample is found, the central point is removed from the active list and the process is repeated until no point is left in the active list. This process generates a distribution in the plane with points that are regularly spaced without clustering, ensuring that each ray has the same importance for the spot radius generation.

2.2.2 Quadratures

Another way to define optical quality is to measure the RMS wavefront error for each sample field. It must be emphasized that the wavefront is mathematically a surface, that can be described with the same polynomial bases than the mirror surfaces. However, the wavefront error induced by the optical system can be of higher order than the surfaces shapes. To compute the wavefront error, there are better theoretical solutions than a random sampling or a regular cartesian grid. Quadratures are weighted distributions

that are mathematically defined to be able to average a polynomial surface up to a certain order without errors. Some quadratures have been defined and studied by Forbes for optical design. Quadratures separate the radial averaging and the azimuthal one. In the present manuscript, several quadratures are defined and studied, however it must be noted that a further reduction in the number of rays is possible using two dimensional quadrature, that are designed specially to calculate uniformly weighted averages over the unit disk and called cubatures in this article from Forbes [109].

Gaussian quadrature

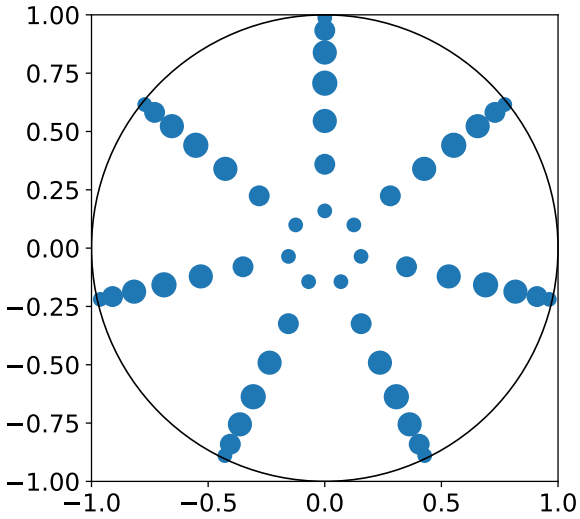

FIGURE 2.7: Gaussian quadrature distribution with 7 rings and 7 arms (49 points). Point area is proportional to its weight.

The most used quadrature is the Gaussian Quadrature, defined in article from Forbes [110] for the optimization of rotationally symmetric design. This method is designed to maximize the accuracy of the averaging over a surface. This is performed by the use of a Gaussian Quadrature in the choice of radial positions and their weight so that a rotationally symmetric wavefront error can be exactly computed up to the order $2N_r - 1$ with N_r the number of rings used in the design. The averaging over the azimutal (or angular) coordinates is made with no error using a uniform sampling up to the order $m - 1$, m being the number of arms of the quadrature. However the maximal order of the wavefront for any given field of view is unknown and its shape can not be described by any finite number of terms most of the time, so the result still is an approximation of the RMS wavefront error. A Gaussian quadrature with 7 arms and 7 rings is shown in figure 2.7. As given in the article from Forbes [110], the integration of a surface defined by the function $s = f(r, \theta)$

can be approximated by:

$$I \approx R^2 \sum_{j=1}^{N_r} w_j \left(2\frac{\pi}{N_\theta} \sum_{k=1}^{N_\theta} f(R\rho_j^{1/2}, \theta) \right) \tag{2.12}$$

With R the radius of the pupil, N_r the number of rings, N_θ the number of arms, and $\rho = r^2/R^2$. ρ_j and w_j positions are given by the roots of Legendre Polynomials and their derivatives. For N_r rings, be x_j the roots of P_{N_r} the Legendre polynomial of degree N_r. As Legendre polynomials are defined in [-1,1], the radial position to evaluate are $\rho_j = (x_j + 1)/2$, so the normalized radial coordinates $\rho_j^{1/2} = r/R$ are:

$$\rho_j^{1/2} = \sqrt{\frac{x_j + 1}{2}} \tag{2.13}$$

The

and the weights are given by:

$$w_j = \frac{1 - x_j}{4(N_r P_{N_r - 1}(x_j))^2} \tag{2.14}$$

Gauss-Radau quadrature

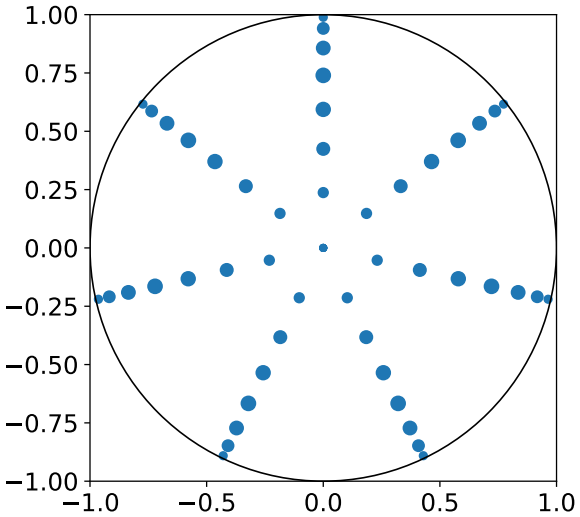

FIGURE 2.8: Gauss Radau distribution with 7 rings and 7 arms, plus the central point (total 50 points). Point area is proportional to its weight.

It is possible to recompute the integration with a fixed boundary, here the radial coordinate $r = 0$. This has theoretically no mathematical advantage with respect to the gaussian quadrature in terms of integration as the radial Radau quadrature only exactly computes a polynom of order $2N_r - 2$. The

expected performances are thus similar to those of the gaussian quadrature. However, using a Gauss-Radau quadrature only adds the chief rays in the merit function, which sould not be computationally heavy and ensure that the center of the pupil is not left without any ray traced. A Gauss-Radau quadrature with 7 arms and 7 rings is shown in figure 2.8. This time the radial coordinates and weights are still given by equations 2.13 and 2.14 but with the roots x_j of the polynom $P_{N_r} + PN_{r-1}$.

Gauss-Lobatto quadrature

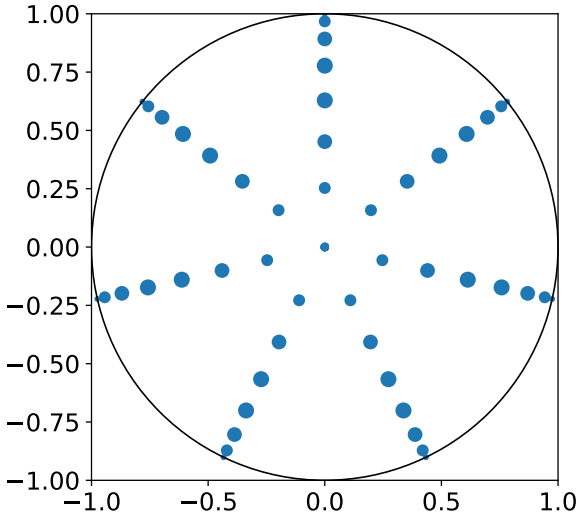

FIGURE 2.9: Gauss-Lobatto distribution with 7 rings and 7 arms, the last ring being the unit circle, plus the central point (total 50 points). Point area is proportional to its weight.

Some off-axis designs could be optimized with the Gaussian and Radau quadrature but tracing a large bundle of rays in the pupil (for spot diagram evaluations as an example) could lead to errors in the tracing of some marginal rays, even with the help of ray aiming. To solve this issue, the use of a Gauss-Lobatto quadrature has been studied. This quadrature now also adds a boundary constraint for $r = 1$. It adds a whole ring, while still theoretically being able to calculate a radial polynom only up to the order $2N_r - 3$. It proved useful for limiting the errors of ray tracing during the optimization, however the latest version of the Zemax OpticStudio at the time of the redaction of this manuscript (21.3.1) added a Beta version of an enhanced ray aiming that was also efficient in avoiding marginal rays tracing errors. A Gauss-Lobatto quadrature with 7 arms and 7 rings is shown in figure 2.8. For the Gauss-Lobatto quadrature, the radial coordinates are given by the roots x_j of P'_{N_r-1}, P' being the first derivative of P, with the added values $x_0 = -1$ and $x_{N_r} = 1$ in the equation 2.13. The weights are now given

by:

$$w_j = \frac{1}{2N_r(N_r-1)P_{N_r-1}(x_j)^2} \tag{2.15}$$

This distribution looks very similar to the Gauss-Radau, but rays with small weight are added on the very edge of the pupil, ensuring that some marginal rays are traced.

2.3 Design method for freeform catoptric optical systems

With the tools defined above, it is mandatory to find a rigorous method to design freeform catoptric optical systems. Several methods have already been given to generate such systems. This method is fairly close to the method from Zhu et al. [73] and is also inspired by Bauer et al. [33].

Each step is followed by various analyses of the design and or modifications of the merit function to ensure a convergence towards a satisfying local minimum. The first three steps describe the starting point generation. Before describing this generation, the aforementioned parabasal ray tracking method must be explained, together with the merit function generation.

The solution chosen is to generate first an off axis system with spherical surfaces using the optimizer of the system. This system will be used as a starting point for the freeform design optimization. The overall method lies on the following steps:

1. Generation of an on axis design with only spherical surfaces, reduced aperture and field of view
2. Addition of tilts following the rules of the parabasal ray tracking
3. Addition of the geometrical constraints to avoid vignetting. This is the starting point of freeform optimization mentioned in the next subsection.
4. Addition of the freeform variables up to the third order and first freeform optimization
5. Increase of the aperture and field of view until the specifications are met. Progressive increase of the number of freeform variables if needed.

2.3.1 Starting point generation

As an example, Fuersbach et al. proposed a method starting with an on-axis fully obstructed design and progressively increasing the tilt of the surfaces to maintain the optical quality [87]. However, there is no guarantee that this method leads to a better solution than starting with an already decentered

surface using only spherical surfaces. Zhong and Gross proposed to design a best solution using nodal aberration theory and gaussian brackets [111], but in the same manner, this does not ensure that this best design using spherical surfaces is the best starting point for the optimization of the freeform system. This mathematical approach is not yet sufficient to generate systems that have a proven mathematical edge over already designed systems. In article from Volatier et al. we showed that a differentiation of the Fermat path's principle can lead to a stigmatic system in the center field [35], [112], [113].

Other solutions are unsupervised generation of systems, i.e. using an optimization to generate the starting point. A first example, which we will be using in this work, is an optimization of a system with spherical surfaces, using the tilts of the surfaces as variables. Another method that can be used. The Simultaneous Multiple Surface method, or SMS method [114]–[117], can also be used for starting point generation of imaging systems [118]. This method has a different approach than conventional optical design. Instead of defining surfaces and tracing rays through this system to optimize the parameters of the surfaces, the SMS method uses the fact that all rays should have the same total optical path length (OPL). In any medium, the optical path length of a ray is the length of the ray multiplied by the index of the medium, and the total OPL is the sum of the OPLs of the ray from the entrance pupil to the image. This equality of the OPL to generate a perfect image for any given object field allows the designer to set a bundle of equations by choosing some fields to image perfectly, the number of fields that can be chosen being directly linked to the number of surfaces generated. This bundle of equations can be solved to find the adequate surfaces with only a small number of hypotheses (usually the center point of each surface). The resulting starting point are then perfectly designed for the specified field points but the whole system needs to be reoptimized to balance the optical quality which can be poor in the rest of the field of view. The SMS method has been successfully used for the design of freeform optics [119], [120].

Finally, a promising solution is a solution using neural networks for starting point generation of freeform systems [121]. Neural networks try to mimic the brain. Several layers of neurons, each neuron being a weighted function with several inputs and outputs. Each layer of neurons take the outputs of the neurons from the previous layer. At the end, the whole system forms a complex function. This neural network is then optimized by learning: a set of example outputs is given to the neural network for several inputs, which are here the specifications of the design. This learning data is used to optimize the weights and parameters of the neural network. Basically, the neural network learns using examples how to transform specifications into an optical design just like a human would learn how to write a merit function. Finally, this neural network can be used to generate data. In optical design it could be used to generate starting points from nothing by having learnt from the large set of already existing systems. However, this is still ongoing research as the amount of data available to educate the network is quite low in optical design compared to other

applications of the method.

Many methods already use the nodal aberration theory to correct the wavefront of the optical system. However, a method such as the one from Zhong and Gross [111] still uses optimization to find a solution, and therefore not removing the main issue in optical design which is the use of black box optimization, even for starting point generation. Such black box optimization such as gradient descent methods only gives a result that is at best a local minimum relatively close from the starting point, hence the many methods for the starting point generation. However, the freeform designs typically adds from three to several dozens of variables to a surface. The topology of the merit function then changes drastically. For catoptric uncooled thermal imagers, the tilts of the surfaces regarding the incident beam is particularly high, typically 10 to 30 degrees. In such conditions, the aberrations of a design with spherical or conic surfaces only are very high, making the use of freeform surfaces mandatory, but also allowing the designer to doubt that the best spherical system is necessarily the best starting point possible. Actually, no proof exists in this direction, and the odds of finding a method that does not rely on black box optimization in a few years from now are very thin. The problematic here is very close to the problems faced in machine learning and neural network optimization. Several black box optimization algorithms exist in this domain (see section 2.1 of Van Turnhout manuscript [122]) and could probably be implemented with success in optical design, but would still not take into account the specificities of the optical design problem, like the knowledge of the Fermat path. For these reasons, the present method intends to be user friendly so that the designer can still guide the optimization thanks to his experience. The method must then be simple and intuitive despite the high number of variables.

This method is applicable to any off axis optical system, but needs modifications for designs with double pass surfaces. Such double pass surfaces can be seen in the work of Nie et al. [123] or in augmented reality prisms [124], from the initial description by Morishima et al. and derived works [124]–[129]. If the parabasal ray is transmitted or reflected several times on the surface a modification of this method must be used for the double pass surfaces, as the parabasal ray hits the surface on several different positions. A different method, such as the one developed by Reshidko and Sasian [130], [131] could be used by the developer in such situation.

2.3.2 Parabasal ray tracking and degeneracy

However, the method that will be given in the next section relies on the control of the parabasal ray to allow the designer to better control the position of each surface. To control the path of this parabasal ray, the simplest method in sequential optical design of off axis catoptric designs is to make the parabasal ray hit every mirror in its center and to define the mirror to be normal to its local reference frame so that the whole path of the parabasal ray does not rely anymore on the mirrors definition. This allows to decouple the

surfaces definitions and their positions in sequential design. To ensure that every mirror is hit in its center, the local slope of the surface in any direction must be zero in the local reference frame. Then, the path of the parabasal ray is defined using only the tilt of the mirrors. Moreover, this reduces the risk of aberration correction degeneracy in the design.

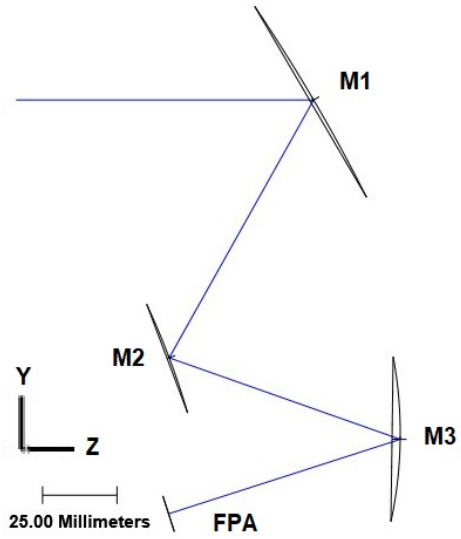

FIGURE 2.10: Parabasal path for a three mirror anastigmat design. The two layouts show that the parabasal ray path is not dependent on the surface shape as long as the local slope is zero at the surface center.

In freeform optical design, caution must be used to avoid aberration correction degeneracy. This degeneracy is the phenomenom where two variables or linear combination of variables have a similar effect on the wavefront or surface shape and balance each other, potentially leading the optimizer to make the said variables diverge. A thorough study of degeneracy in optical design has been made by Tataki et al. [132].

If the variables are on different surfaces, this might lead to large freeform departures of each surface with minimal optical quality improvement, hence the attempt of the optical community to use nodal aberration theory to reduce the number of variables in the optimization to the strict minimum, as explained in Bauer's article [33]. If all affected variables are on the same surface, there are also several issues. First, the designer loses control over the surfaces as any modification of the variables affect deeply the surface shape. Moreover, using large numbers for variables also increases the difference between two successive floats leading to numerical instability of the merit function and risk of having errors in the ray tracing algorithm. An example of degeneracy is the tilt of the surface and the equivalent coefficients in the surface shape description. Another example is the focus term in Zernike polynomials that generates a sphere like departure in the first order of the

Taylor expansion of the sag of a sphere. Then, optimizing over the focus term usually ends up with very small radius of curvature that is compensated by a very large focus term for a non significant correction given that the rotationally symmetric terms are also corrected up to a certain order. The risks of errors due to numerical round-off are detailed in section 2.4.

This parabasal ray tracking ensures a user friendly optimization result, that is easily readable by the designer. If the designer decides to increase or lower the tilt of a surface, the wavefront correction would be lost, however the surfaces following the affected surfaces will be moved accordingly. However, in orthogonal bases, the monomial for any given radial term generates a local slope at the surface center. To keep the parabasal ray tracking, the tip and tilt variables must be computed after each modification of the other variables, potentially slowing the optimization process. This effect tends to favor the XY polynomials that are not affected. In the next section, a comparative study of Zernike Polynomials, Q-type polynomials and XY is performed for various ray tracing distributions and sampling density in an attempt to find a potential best situation for our design method.

2.3.3 Merit function generation

The merit function is a function which is then minimized using an optimization process, presently the Levenberg-Marquardt algorithm or Damped Least Square method. This method is used for optimization in non linear problems. The merit function is composed by many elemental functions called operands. Each operands take several inputs, including one weight parameter and a target, and returns a single double value. The value returned by the merit function is the squared sum of all operands.

$$MF = \sqrt{\frac{\sum_i W_i (V_i - T_i)^2}{\sum_i W_i}} \tag{2.16}$$

with W_i, V_i and T_i being respectively the weight, value and target of the i^th operand.

The merit function is mainly divided in two parts. The first part is usually not modified by the designer, but generated by the optical design software. This part uses the ray tracing algorithm to trace a bunch of rays to the focal plane for each field. This allows to calculate the spot radius or wavefront error and evaluate the overall optical quality. The second part, usually generated by the optical designer, deals with specificities of the design, such as focal length, geometrical requirements or F number. The designer can then include the system requirements into the merit function. As the merit function is a weighted sum of all operands, the weighting is only important in comparison to the weight of all other operands. Increasing the weight on an operand is equivalent to reducing the weight of all other operands.

Focal length and distortion

The focal length is defined as the distance between the rear principal plane and the focal plane. However, this definition only holds for centered rotationally symmetric systems in paraxial conditions. In systems with large apertures and field of view, and even more when those systems are off axis, the paraxial assumptions are not valid and thus this focal length definition does not hold. However, the focal length is only a way to define the magnification of the optical system, alongside the distortion which is a modification of the magnification with the field angle. In non paraxial centered designs, an effective focal length is computed using the best focus, but this definition is not satisfactory in our case as the distortion in off axis systems is not rotationally symmetric anymore. A way to avoid using the focal length is to define directly the position of the image for a given field. In the merit function, for several chosen fields, such as the corners of the field of view, the position of the centroid is measured in the merit function and then constrained to ensure a system with a magnification equivalent to a perfect lens with the desired focal length. A perfect lens can be defined as a lens that does not create aberrations, and for any object located at infinity with a field θ, the position of the image is:

$$y' = f * tan(\theta) \tag{2.17}$$

with f being the focal length of the equivalent perfect lens.

This way of contraining the image position ensures a given focal length and control over the distortion of the system. This is particularly useful for off axis systems that do not have rotationally symmetric distortion, and therefore for which control of the magnification over the whole field of view is complex. Using this method, the magnification can be made very precise by increasing the weight on the centroid positions or adding more fields where the magnification is computed. However, increasing the weight on the magnification decreases the overall importance of optical quality in the merit function. The optical designer must then carefully tune the weighting of the merit function to ensure a satisfying result.

After constraining the image position, the equivalent focal length must be evaluated. For this evaluation a dense grid of object sources is used, and for each object a ray trace is performed to evaluate the centroid of the corresponding spot in the image plane. This method results in a distorted grid of centroids (red dots in Figure 2.11). This grid is then compared to the reference grid that would be generated by a perfect lens (blue dots in Figure 2.11). This blue reference grid can be scaled using the focal length parameter. The effective focal length of the design is taken as the focal length that minimizes the difference between the reference grid and the distorted grid. This difference is calculated by a minimization of the least square summation of the distance between each centroid from the distorted grid and its corresponding position in the reference grid. An example of such difference in position is the distance B shown in the Figure 2.11. This

minimization is made using the Broyden–Fletcher–Goldfarb–Shanno (BFGS) algorithm, which is one of the most used quasi Newton algorithms for unconstrained non linear optimization problems, to find the effective focal length.

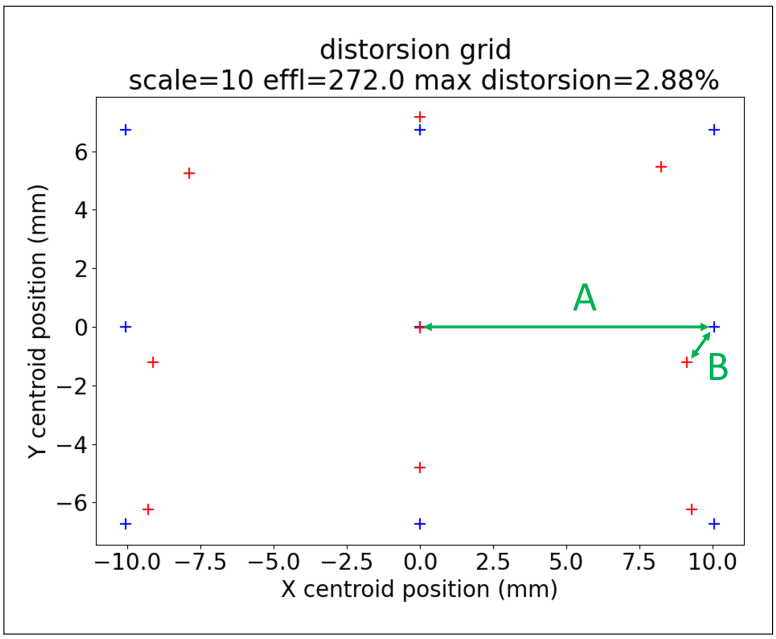

FIGURE 2.11: Example of a distortion grid for the calculation of the effective focal length and maximal distortion.

Coincidentally, each field is also given a distortion number, which is the ratio between on one side the distance separating any centroid and its ideal position (distance B in the Figure 2.11) and on the other side the distance of such ideal point from the position of the centroid for the center field (distance A in the figure 2.11). The max distortion given in figure 2.11 is the maximum distortion number for the entire grid. This definition of an equivalent focal length can also be used to measure the focal length and distortion of the manufactured system, as shown in chapter 4.

Geometrical constraints

As detailed above, the starting design has adequate constraints on the system to ensure an unobstructed design that complies with the overall volume. These constraints are based on key points positions on the design, given in the figure 2.12 for a TMA system in a one unit cubesat. Note that this way of generating the design can be expanded to any off axis system. Constraints about the overall volume are equations 2.18 and 2.19. Equation 2.18 ensures that the Y extent of the systems stays lower than 100mm, which is the size of a cubesat. Equation 2.19 serves the same purpose for the Z extent. There is generally no constraint on X extent for planar symmetric designs as the system is then only limited by the diameter of the largest mirror. However, it

is obviously possible to add the key points over the X dimension to constrain this system.

$$Y_A - min(Y_I, Y_H) < 99mm \tag{2.18}$$

$$max(Z_A, Z_D, Z_F, Z_I) - min(Z_B, Z_C, Z_G, Z_H) < 99mm \tag{2.19}$$

Equations 2.20, 2.21 and 2.22 are necessary to keep the design unobscured and prevent vignetting, by ensuring a minimal distance between the mirrors and the optical beam.

$$Y_B - Y_C > 3mm \tag{2.20}$$

$$Y_D - Y_F > 3mm \tag{2.21}$$

$$Y_E - Y_G > 3mm \tag{2.22}$$

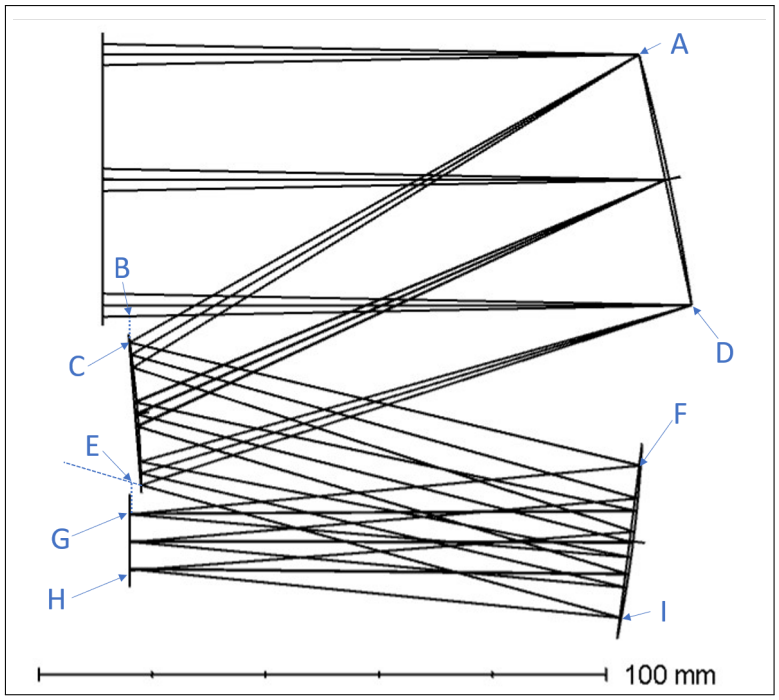

FIGURE 2.12: All spherical design used as a starting point for optimization of TMA designs.

As the optimization algorithm uses a classical gradient descent method, the merit function must remain differentiable and smooth. To achieve such a smooth merit function, the constraints are weighted constraints and any violation of those constraints lead to a penalty on the merit function, calculated according to the chosen weight. Any constraint that would need an infinite weight, meaning that the constraint must absolutely be respected, must be avoided as it would cause the gradient to become infinite and create instability in the gradient descent. To avoid this situation, margins were taken when defining the constraints to ensure that specifications are

met. Depending on the weight over those constraints and the design specifications, these margins can be modified.

Aperture

The aperture is defined by the diameter of the system stop. To reach the desired aperture a constraint on the working F number is added. In OpticStudio the working F number is computed using ray tracing of marginal rays of the system. This ensures that the result is not due to a paraxial calculation and is usable in our design process. To ensure that the diffraction limited point spread function is rotationally symmetric we must ensure that the entrance and exit pupils are circular. To ensure that the exit pupil is circular, we can constrain the sagittal and tangential magnifications are equal. Then, if the magnification is symmetrical, the image of the exit pupil by the system is also circular and thus the entrance pupil is also circular. The diameter of the stop is then a variable of the optimizer and the weight of the operand corresponding to the working F number is adjustable to ensure the optimal trade-off between the aperture and all the other constraints.

2.4 Systematic study of basis and sampling impact on optimization of freeform catoptric designs

This work intends to reproduce and extent the scope of the work of Dr. Anika Brömel [97] or Dr. Muslimov [133] on the impact of freeform description for optical design. It is also inspired by the work of Kaya et al. [134], [135] on the selection of the sampling scheme for the fitting of freeform surfaces in addition to the thoughts about which surface description to choose, which is a core problem for the numerical evaluation of the merit function. Brömel's work focused on the comparison of several bases for freeform design and concluded that the choice of representation is of importance in optimization, with an edge for Zernike and Q-type polynomials. Muslimov's article also tends to demonstrate that orthogonal bases give better results compared to XY polynomials in their example. Furthermore, the erratum of the article from Reshidko and Sasian [130], [131] shows that the surface representation has no significant result on the optical quality for their systems.

However, as mentioned in the previous section, the parabasal ray tracking method forces the mirrors slopes to be zero at the mirror center. This implies that the mirror tip, tilt and piston must be calculated on the fly, depending on the other polynomial coefficients to take into account this specification. This calculation adds another step inside the optimization loop for systems designed using Zernike polynomials or Q-type polynomials, while the XY polynomials are unaffected. In this section, the performances for the three polynomial bases selected have been studied, but with the addition of a study on the sampling impact of the pupil, to study the coupled impact of pupil sampling and surface description.

2.4.1 Systematical study introduction

For this systematic study, three systems have been used: first, a two-mirror (2M) design has been analyzed. This design has been shown as a good candidate for pushbroom applications and was used in Volatier et al. [35]. This design has fixed tilts of the surfaces. The second design is a three mirror design (TMA) in the fashion of those described in Chapter 3. Finally, a pamplemousse configuration has been studied. The pamplemousse (PPM) configuration is detailed in Chapter 4. These designs have been selected as these are the main configurations studied in the scope of this manuscript that have equivalents in literature, so that this study can be reperformed over a large scope of designs that are already in use by the community. All those systems have been modified from an optimized point up to a design with only spherical surfaces. The specifications of each design are given in table 2.1 and the systems descriptions are given in tables B.1, B.2 and B.3 in appendix B. The stop diameters are 70mm, 39mm and 10.4mm for respectively the 2M, the TMA and the PPM. The pupil position for the 2M configuration is not exactly the M1, but a dummy surface placed at the same position and normal to the parabasal ray in the object space. This is purely a simulated and artificial placement that is not manufacturable (half the stop being virtual). This pupil position comes from the two mirror design in Volatier et al. [35]. All three initial designs are shown in figure 2.13.

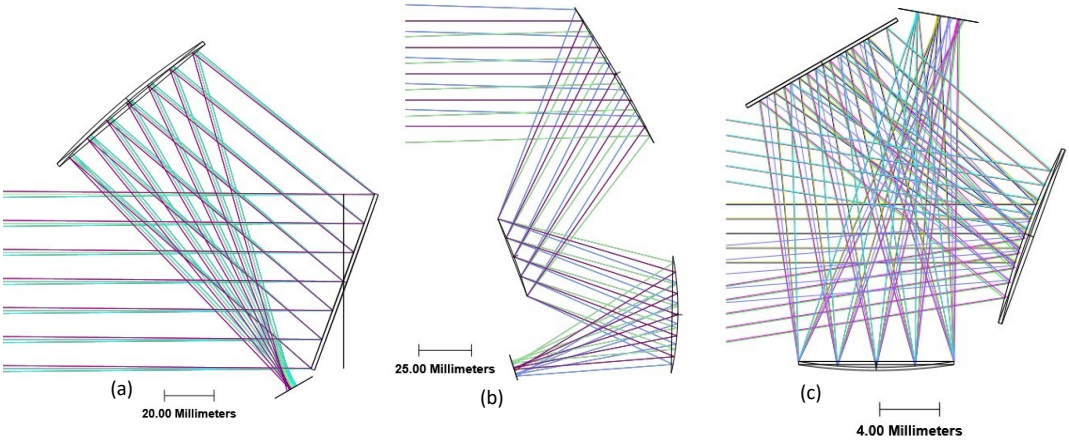

FIGURE 2.13: Initial layout for the three designs using only spherical mirrors. From left to right: (a) the 2M design, (b) the TMA design, (c) the PPPM

TABLE 2.1: Specifications of the 2M, TMA and PPM designs.

Specification	**2M**	**TMA**	**PPM**
focal length (mm)	150	100	9
half X FOV (degrees)	3	2.2	12
half Y FOV (degrees)	0.5	1.65	9
F#	<2.3	1.5	2
pupil position	M1(Artificial)	M2	M3

For every system, a merit function is generated using the method previously detailed. Then, variants of each system are automatically generated using Python. Python is used to generate the merit function and parameters of each system through the ZOS-API. A variant is created for several combinations of distributions, sampling density and surface description. The surfaces descriptions are:

1. The XY polynomials (or Extended Polynomials in Zemax OpticStudio)
2. The Zernike polynomials
3. The Q-type polynomials

The evaluated distributions are:

1. Cartesian grid
2. Gaussian quadrature
3. Gauss-Radau quadrature
4. Gauss-Lobatto quadrature

and the sampling density is given in number of rays: 9, 25, 100, 225, 400, 625, 900. For the cartesian grid, the rays are equally distributed in the unit square and rays outside of the unit circle are ignored. For the quadratures, the number of rings and arms are equal. I developed an algorithm to generate the files with the adequate surface definitions and variables. The algorithm also generates the merit function by adding to the initial merit function of the system a merit function to evaluate the RMS spot radius of the system over the field of view. The initial merit function here is the merit function common to any variation of each system, i.e. the part of the merit function that is usually written by the optical designer. The added part is the part usually generated by the software. Each RMS spot radius is generated by evaluating the end position of several rays that are placed in the pupil according to the distribution descriptions. The weighting of each ray is given by the quadrature calculations. For the cartesian grid, a uniform weighting is applied.

For all three designs, the mirror shapes are made variable, with the curvature radius and freeform departure up to the fifth radial order (for XY polynomials, the order is the sum of the order in X and Y). As the system is planar symmetric only coefficient associated to even orders in X are optimized. Using extended polynomials and to avoid degeneracy, the coefficient associated with the monomial X^2 is not used. Indeed, the polynom $X^2 + Y^2$ is equivalent to the first approximation of a sphere which is already defined by the curvature radius. Inversely, the polynom $X^2 - Y^2$ is associated with first order astigmatism (more specifically at zero degree), which is a polynomial we need to define the final surface shape. So only one of those two coefficients (X^2 or Y^2) must be optimized alongside the radius of curvature. Here we choose to only optimize the Y^2 polynomial and not the polynomial X^2. The same method applies for the focus term for system optimized using Zernike Polynomials. For Q-type polynomials the first rotationally symmetric is by design the first spherical aberration, so that no degeneracy with the curvature radius can happen. Overall, each surface has 10 variables, 1 for the curvature radius and 9 for the freeform shape.

All three designs also have as variables the distances between surfaces, i.e. the distances between the mirrors centers and the distance between the last mirror center and the center of the focal plane. For the pamplemousse and the TMA, the tilts of the surfaces are also variable around the X axis so that the designs remain planar symmetric.

The optimized systems layouts are comparable to those presented in figure 2.14.

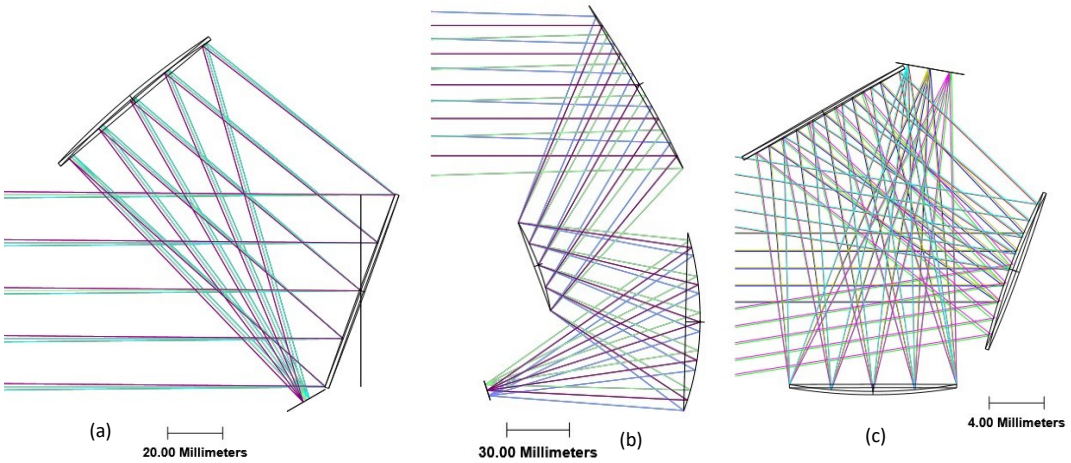

FIGURE 2.14: Layout of the designs optimized with a gaussian quadrature with 30 rings and 30 arms, using surfaces defined with extended polynomials. From left to right: (a) the 2M design, (b) the TMA design, (c) the PPM

This brings a total of 3 systems, 4 distributions, 3 polynomial bases and 7 densities, leading to 252 designs to optimize. Each design has been then optimized using the built-in damped least square method for 200 cycles. The duration of each cycle, the total time required for the 200 cycles and the merit

function after each cycle has been stored. The data are presented in the next subsection. The designs have been optimized only for 200 cycles, which is short, due to the time needed for one optimization cycle. The duration of one cycle with the tilts as variable is rather long, from 5 seconds to a few minutes. For any system, if the cycle optimization does not decrease the merit function by at least one bit for 5 cycles the optimization is stopped and the number of cycles is stored. One bit being the smallest variation possible in the numerical evaluation of the function.

2.4.2 Results and statistical analysis

Each optimized design has been saved. To compare the results of each optimization, the mean RMS spot radius is computed. This mean is calculated via ray tracing of the spot diagram over a uniformly distributed grid of objects separated by 0.5 degrees each. The spot diagram is generated by a ray tracing using a Poisson-disk distribution in the pupil with 120 rays. The results are visible in figures 2.15, 2.16 and 2.17. In each of these figures, the mean RMS spot radius is plotted against the number of rays traced in the pupil to calculate the merit function. Each color represents the pupil sampling type. Red for the cartesian distribution, blue for the gaussian quadrature, green for the Gauss-Radau quadrature and black for the Gauss-Lobatto one. Each line type represents the surface type, with a continuous line for XY polynomials (also called Extended Polynomials), a dashed line for Zernike Polynomials and and dashed-dot line for Q-type freeform polynomials. I would like to thank Clement Freslier for his work in generating the following figures from the data I generated.

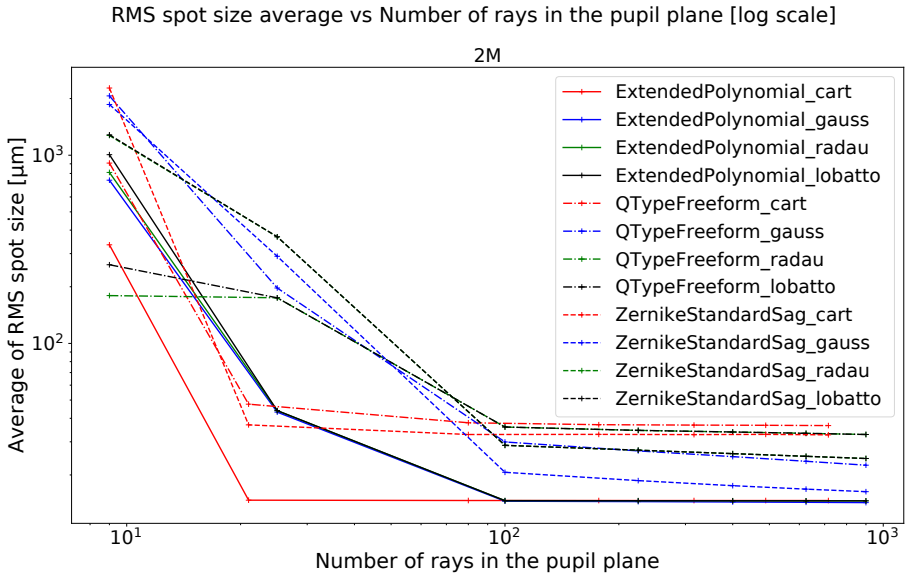

FIGURE 2.15: RMS spot size over the full field of view depending on the number of samples in the pupil plane, the number of traced rays being the number of samples multiplied by the number of evaluated fields. Results for the 2M system.

It was expected that tracing more rays for the merit function generation would end up in better optical quality of the design. In figure 2.15 it is visible that for any quadrature, the mean RMS spot size over the full field of view is smaller when the design has been optimized using XY polynomials. This result is completed by a tendency for the Gaussian quadrature to give better results than other pupil distributions for any fixed surface type. However a result on only one design is not sufficient to draw conclusions. This analysis can be performed also on TMA and PPM designs.

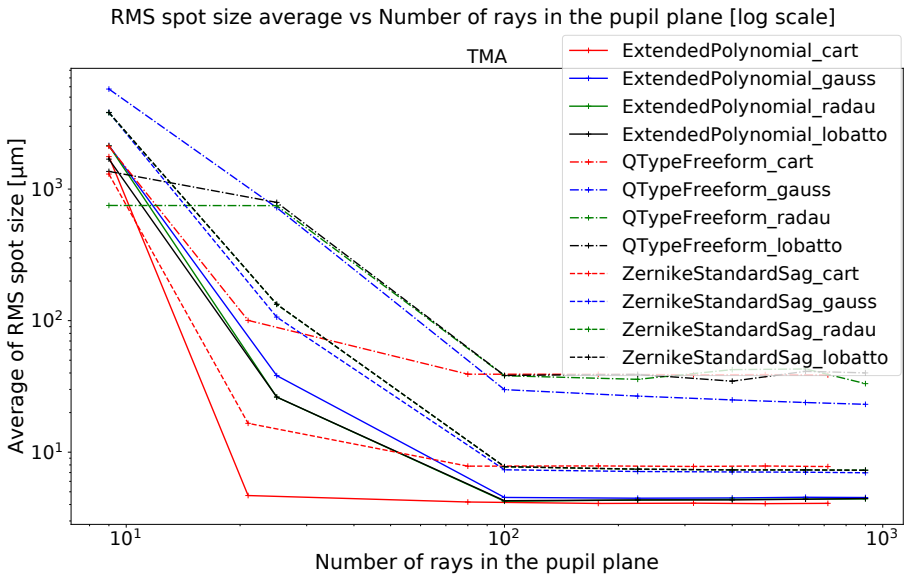

FIGURE 2.16: RMS spot size over the full field of view depending on the number of samples in the pupil plane, the number of traced rays being the number of samples multiplied by the number of evaluated fields. Results for the TMA system.

The tendency is confirmed by figures 2.16 and 2.17. Please note that the initial value of the graph is not plotted because of the large gap from the first optimization cycle. However the initial value, which is the same for all plots in a figure, is written in the top of the figure. From these three figures, the XY (or Extended Polynomials) are consistently giving better results than Zernike Polynomials, which in turn results in better solutions than Q-type freeform polynomials. We would expect the sampling to be the most important parameter and the surface descriptions to give all equivalent results. Indeed, the Zernike and XY describe exactly the same space of solutions and the Q-type freeform, while having a slightly different solution space should not result in systems with an order of magnitude larger spot size. This result is both unexpected and particularly interesting. First, the choice of the ray distribution in the pupil seems to be of little interest for a dense sampling. For sparse sampling, the cartesian distribution, which is the simplest of all, gave better results. It gives better results than all quadratures with 25 rays (26 for the Gauss-Radau and Gauss-Lobatto quadratures, as the central ray is also traced, 21 for the cartesian sampling as 4 samples out of the 5x5 grid do not fall inside the unit circle). As the reasons for these results have not been

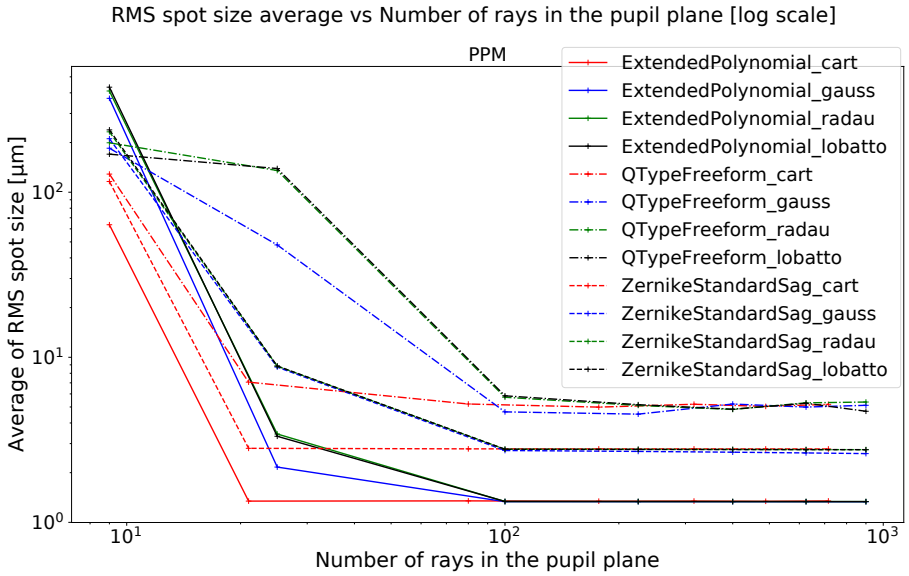

FIGURE 2.17: RMS spot size over the full field of view depending on the number of samples in the pupil plane, the number of traced rays being the number of samples multiplied by the number of evaluated fields. Results for the PPM system.

identified yet, these results have to be taken with caution. Please see the next subsection that outlines the limitations and perspectives of this study.

The merit function depends on the surface shape, but not on the way this shape is defined. This means that the merit function result definition does not change if the basis used to define the surfaces is modified. The merit function however explicitly depends on the number and position of the rays traced. These two results imply that for a specific sampling (type of the sampling and density) and a specific system (2M, TMA or PPM), the merit function definition for all three surface types is identical. The evolution of the merit function over time can thus be compared. We studied 3 systems, 4 sampling schemes and 7 pupil densities leading to 84 graphs comparing the evolution of the merit function. The figures 2.18 and 2.19 show the evolution of the merit function respectively for the cartesian distribution with 21 rays in the pupil and for the gaussian quadrature with 900 rays (30 arms and 30 rings) and for all three systems (these numbers have to be multiplied by the number of fields used for the optimization, here 7 for the two mirror and 6 for the TMA and Pamplemousse). Some other figures are displayed in the Appendix B or are available on demand and show similar trends. If the optimization was stopped due to the merit function being constant for at least 5 cycles, the last cycle number is displayed next to the corresponding point in the figure. The initial value of the merit function is identical for all three plots (red green and blue) as the initial system is composed of spherical surfaces (i.e. each variable is equal to zero initially for all surface definitions). As the first optimization step drastically reduces the merit function, the initial value of the merit function is given above the figure instead of being plotted to reduce the plotted dynamic and help distinguish smaller differences between

plots. Please note that the merit function is not sufficient to evaluate the optical quality of the design on its own, as some operands also constraint the geometry, aperture and other specifications of the design. A system can have a lower merit function with a worse optical quality if it better fits the other requirements. The designer can change the weight of operands to adjust the trade off if required.

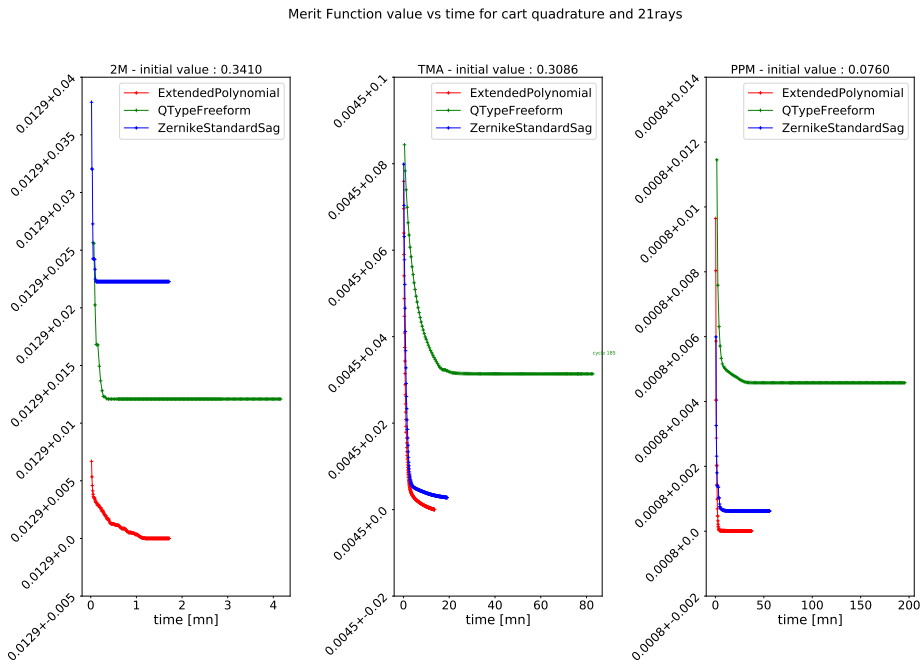

FIGURE 2.18: Evolution of the merit function over time for a cartesian quadrature and 21 samples in the pupil (i.e. 21 rays per field)

It appears from figures 2.18 and 2.19 that the XY polynomial does not only result in better optical quality, but also in a faster convergence with cycles notably faster for the XY polynomials and Zernike polynomials than for the Q-type freeforms.

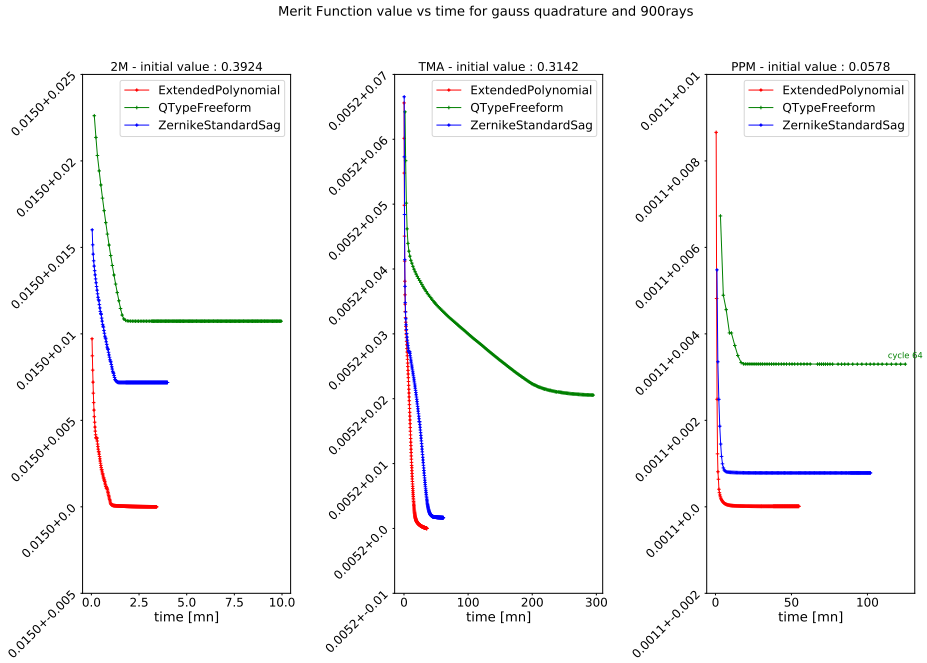

FIGURE 2.19: Evolution of the merit function over the number of optimization cycles for a gaussian quadrature and 900 samples in the pupil (i.e. 900 rays per field)

2.4.3 Remarks on those results

This study gives interesting insight on the importance of the ray distribution in the pupil and of the choice of surface representation. First, it is interesting to remark that the most efficient basis, whether for the end result of the optimization and for the duration of each optimization cycle, is the only non orthogonal basis. However, this study cannot be used to give a definitive answer to the question of the choice of polynomial surface representation because of the complexity of the subject that leads to several limitations in the study.

Limitations of this study

The first and most visible limitation is the small number of configurations tested. Only three catoptric configurations have been tested, fairly limiting the scope of these results. The same argument holds for the number of pupil distributions tested and the limited number of polynomial surface representations included in the study. Moreover, the optimizer is the Zemax OpticStudio Damped Least Square, which exact properties are not known. It is most probable that since the damping is not controllable the optimizer algorithm automatically adjusts the damping parameter. The best candidate for such algorithm is a Levenberg Marquardt algorithm. In the same fashion every single operand of the merit function is ultimately a black box that could lead to approximations and calculation errors. For fairly simple designs

that were optimized outside of this software, I found that the results with a Levenberg-Marquardt algorithm and the Zemax optimized were identical, though it does not imply that the optimizer is the same algorithm. Several other algorithms could be tested to see if such tendency remains visible. A previous study on optimization algorithm has been made by Houllier and Lépine [136].

Comparison with the work of Dr. Brömel and Dr. Muslimov

The results of this study differs from the work of Brömel [97] and Muslimov [133]. In their article, Muslimov et al. use a methodology that is very similar, by implementing a merit function in Zemax OpticStudio and optimize the design using several surfaces definitions. The conclusion of their article is in contradiction with the result of our study. This surprising result cannot be explained easily by any data given in the article or by the data gathered and generated for our study. It is probable that the better results given using one surface definition is strongly dependent on the merit function definition, which itself is strongly linked to the style of the designer.

If we compare our results to the work of Dr Brömel, the results of our study are comparable. In our work we studied the impact of ray distribution in the pupil for the merit function generation and concluded in no significant difference for a large number of rays, typically above 100 rays for each field (to be multiplied by the number of wavelengths for non catoptric designs), which was not included in her work. In her manuscript, she however analyzed the impact of polynomial order and non catoptric systems, and it seems that the conclusions differs depending on those parameters. As an example, the XY polynomials seem to give worst results for HMD designs. Her conclusion outlines that orthogonal descriptions give better overall results, but she concludes that the surface shape is ultimately of little importance and the results seem more dependent on the choice of quality criteria and parameters.

Overall, the vast diversity of designs of interest ends in a difficulty to define one or a handful of designs that could be seen as a common benchmark for such considerations. With our work being contradictory to the work of Muslimov et al. and only in partial accordance to the work of Brömel, no final conclusion can be drawn. Due to the lack of common benchmark with a common design, variables and merit function, made with algorithms from software that have been since updated and are not open source, all of our studies are probably not fully reproducible. As the conclusion of Brömel suggests, this consideration is not significant compared to how the designer generated the merit function and overall what we could call the style of the designer. In this situation, it seems fair to admit that no polynomial representation can actually be considered as definitively better than the other, and that while design methods are not common, this choice should be more determined by practical considerations such as tolerancing or designer habits.

Notes on numerical accuracy and floating point error

As optical design is made using computers, the whole process is submitted to numerical errors, and more precisely floating point errors. In numerical calculation, the data must be stored in the computer and thus be represented with a number in base 2. To represent a real number, the most used representation is the floating point number. This name comes from the fact that it allows to represent reals with a decimal point anywhere between two significant figures. This representation is made using a fixed number of bits in the computer memory. This implies that not any real can be represented as a floating point. However this is sadly a necessary sacrifice of precision to gain in computation speed for optimization algorithms that need very heavy computations. More information on numerical computation can be found in Higham's book [137]. This subject is very complex and is a whole branch of science in itself but a basic knowledge of the source of errors is necessary for designers that are involved in the optimization of complex systems.

There are three main sources of numerical errors:

- Initial errors: These errors are due to an error in the initial data of the problem. An example is data from measurements.
- Rounding error: This error arises from the fact that the data is stored with a finite precision, like a finite number of bits or a finite number of significant numbers.
- Truncation errors: These are errors due to a calculation of a finite number of terms in a series. As an example, the evaluation of an integral by a sum.

One can avoid rounding and truncation errors by using symbolic arithmetic, however the computation in symbolic arithmetic is much slower than using a floating point representation and this still does not avoid initial errors. There are many problems that arise when performing numerical computations. First, small errors will occur due to the round off of the result of a calculation. This error is often very small. Most computers and softwares use natively the double precision floating point number defined in the IEE754 standard. Without giving too many details on the structure of such number, the double precision number is stored with 64 bits. This is structured with 11 exponent bits, 1 sign bit and 52 bits for the significand. This number has approximately 16 significant digits ($53log_{10}(2) = 15.955$), so the error is still negligible.

However this error can be increased due to error propagation, where small errors in the input of a function lead to an error in the result. Sometimes, using the same repeated operation is not detrimental as the error can take positive and negative signs and cancel out. However in some cases, a small relative error can be increased by the operation, and finally leads to an increase in the relative error in the result. Sometimes, when using many times such kind of operations this leads to a catastrophic divergence of the

error, ending with an error several orders of magnitude larger than the exact results.

Finally another way of having large errors is the catastrophic cancellation. The idea is simple. The difference between two large values that are very close to each other, most significant digits (or bits) cancel out and the small relative inaccuracy in both numbers due to rounding error becomes a very large relative error in the result. As an example, the number $1 - \sqrt{1 - 1e^{-16}}$ computed with double precision representation results in a value of $\approx 1.11e^{-16}$, which is plain wrong, while the alternate computation $\frac{1e^{-16}}{1+\sqrt{1-1e^{-16}}}$ gives the approximate result $5e^{-17}$ that is closer to the real solution and avoids such catastrophic cancellation. In optical design, the catastrophic cancellation can happen fairly easily, even more when conceiving freeform systems. Indeed, the degeneracy that we talked about earlier in this chapter leads to differences of two larges values, resulting in a lack of significance of the result. The sag and slopes calculated can then be wrong, and lead to a wrong ray tracing in the system. This can result in having a design that does not have the required performances while manufactured with extreme precision due to this numerical error affecting the ray tracing. Generally speaking, cancellation has high risks of occurring when large order polynomials are involved. This is one of the main reasons for which our study only defined surfaces up to the fifth order, as we could not know how the polynomials were evaluated and thus catastrophic errors could arise and distort the results. However, one of the main arguments for the use of orthogonal basis is the existence of a three term recurrence relation given in equations A.5 and A.6 with a_n, b_n and c_n real number and $a_n c_{n+1} > 0$. This relation can be used to evaluate a polynomial value which gives a fast and more accurate evaluation of the polynom than the naive and straighforward calculation, provided that the values a_n, b_n and c_n can be calculated. This has been developed for Zernike Polynomials by Forbes [104] and also used to develop a recurrence relation for his Q-type polynoms [61], [138]. The proof of existence of such recurrence is given in the appendix A.

As said before, this recurrence relation is of most interest for the optical design as it has been proven that such recurrence relations are very useful for the evaluation of the polynomials. Several recurrence relations have been implemented for Zernike polynomials, such as the improved version by Andersen [139]. This is an important argument as the orthogonal polynomials then appear to be less sensitive to numerical errors than others such as XY polynomials. However, a clever method can be used to compute with low numerical errors any polynomial using Horner or Clenshaw methods [140], [141]. Article from Mesztenyi and Witzgall [142] is also an interesting source to try and reduce the loss of significance due to lack of precision in fixed precision arithmetic.

In the same fashion, the rounding errors in the interpolation can also be computed [143]. However this error is negligible compared to the truncature error that occurs due to the finite number of sampling rays in the pupil used to calculate the merit function.

Conclusion and perspectives on this study

This study finds results that are not in line with previous work. With an analysis of the flaws of our own study, such as the low number of systems used for the benchmark, the lack of knowledge of the exact algorithms in use in the software (please see article from Houllier and Lépine [136] for a comparison of algorithms) and the many parameters that could influence the result whether directly or not, the only conclusion of our study is that the XY polynomials perform better in the designs that are included in the scope of the study, using the design method we generated and that for a large number of rays traced the ray distribution in the pupil is not a relevant parameter for our systems. A more general conclusion is impossible, and the results of the previous studies should be taken carefully in the light of these new findings. It results that one polynomial representation can be more efficient that others, but that result is most probably influenced by many variables that are specific to each designer and its design method, such as the merit function generation, the structure of the lens data (as an example, the parabasal ray tracking could influence our results in ways we don't fully understand yet), and variables specific to the systems. It appears that in absence of clear common benchmark systems, with explicit merit functions and surface shapes, this question could remain unanswerable. However, the differences shown by any study are low enough to be able to design systems up to the diffraction limit using any type of surface.
For these reasons, we recommend to any designer not to choose the polynomial basis for a design on the basis of hypothetical numerical superiority, but instead to use the polynomial best adapted to the design (such as Zernike for tolerancing over the RMS freeform departure and Q-type for the RMS freefom slopes) and to his design method, like using the XY polynomials to perform parabasal ray tracking. In the rest of this manuscript, the method detailed in this chapter will be used to generate and optimize several optical systems for various applications, in the purpose to show that freeform surfaces can lead to efficient catoptric systems that could be ultimately used for compact multi spectral band imaging.

Chapter 3

Nanosatellite applications

3.1 Introduction

As mentioned in the introduction, one of the main interests of the freeform technology is to manufacture imaging nanosatellites using catoptric designs for several reasons such as achromatism, resistance to radiations, high transmission, etc... In the infrared spectrum these arguments are very interesting as usual materials are costly, absorbing and induce chromatism due to large constringence.

In this chapter, we will discuss the conception of several systems for infrared imaging in the scope of the study of urban heat islands, taken as examples of possible nanosatellite applications of uncooled thermal infrared imaging using catoptric designs.

The Urban Heat Island (UHI) is a rather commonly known phenomenon. In urban areas, this effect is inscreased due to the intense human activity and energy consumed in a small area and the use of materials with a low albedo and high volumetric heat capacity. To cool down buildings, more energy is used and add up to the issue [144]. To measure those effects, both on-site and remote data collection of temperature can be used. As an example articles such as the one from De Ridder et al. [145] on the Paris UHI during the 2003 heat wave could benefit from dense and frequent land temperature measurements. The use of remote temperature measurements seems to be the solution [146]. It is possible to use data collected by satellites such as the Landsat satellites [147]. These satellites are placed in sun-synchronous orbits. A sun-synchronous orbit is an orbit around the earth in which the satellite always passes over any given point of the surface of the planet at the same local mean solar time. However such orbits generates long revisit periods (16 days for Landsat mission satellites). Moreover the images are always made at the same solar time and does not give a sufficient amount of data to analyze properly the UHI. To increase the revisit frequency up to a few measurements per day, which is necessary to sample the circadian cycle, the number of satellites must be increased dramatically [148]. However, such satellites embark high performance but expensive payloads and a constellation of this type of satellites is not financially reasonable. To keep a good spatial sampling combined with a high revisit frequency, the use of multiple satellites in a constellation is mandatory but at a low cost and at a low mass. Therefore cubesats, which are small satellites of only a few cubic

decimeters, are getting more and more popular for such scientific missions [77]. Such satellites can be mass-produced for a reasonable price. However, it implies the manufacturing of ultra compact optical payloads, which is made possible using freeform surfaces.

The principal requirements for the optical payload are:

1. The payload must provide images in the thermal infrared spectrum. The measurements must be done in several spectral bands to correct for atmospheric and emissivity effects in order to retrieve the Land Surface Temperature.

2. The spatial resolution must be between 50 to 100m and the swath between 50 to 100km.

3. The whole satellite must be a 12U cubesat in low earth orbit altitude.

In order to keep a low cost, compact and easy to manufacture solution, we will study a design with an uncooled microbolometer and an off-axis unobscured telescope [13]. The use of a fully reflective design allows to consider for multispectral imaging by using filters before the detector to divide the microbolometer into several regions sensible to different spectra. This is possible thanks to the broad sensitivity of microbolometers in long wave infrared. Moreover, using only mirrors results in fully achromatic designs that could be used for multi spectral band imaging using a spectral separation after the last mirror , allowing to use several detectors with the same optical system. Fully reflective systems are also very interesting for creating an athermic solution if the whole instrument is made in the same material. Moreover mirrors can be made to be lighter than lenses. To produce an image of the scene with such a satellite, using a pushbroom technique is very useful to have a simple and compact instrument.The pushbroom method uses the motion of the satellite to generate images. The movement of the satellite above the scene allows to produce a two dimensional image with a mono-dimensional field of view of the optical system orthogonal to the movement by appending consecutive images.

The intent of this work is to design the simplest imaging system possible using only freeform mirrors. A good starting point is a two mirrors design. One mirror is not enough to correct the imaging quality over a given non null field of view as shown in Volatier et al. [35].

3.2 Two mirror design

Using the method given in chapter 2, we can define a two mirror design using freeform mirrors. This design, closely related to the one used for the systematic study, allows to correct a linear field of view [35]. In figure 7 and table 2 from Volatier et al., the alpha configuration seems particularly interesting for the good optical quality and low distortion, while still being compact. The specifications of the design are given in table 3.1. The F number

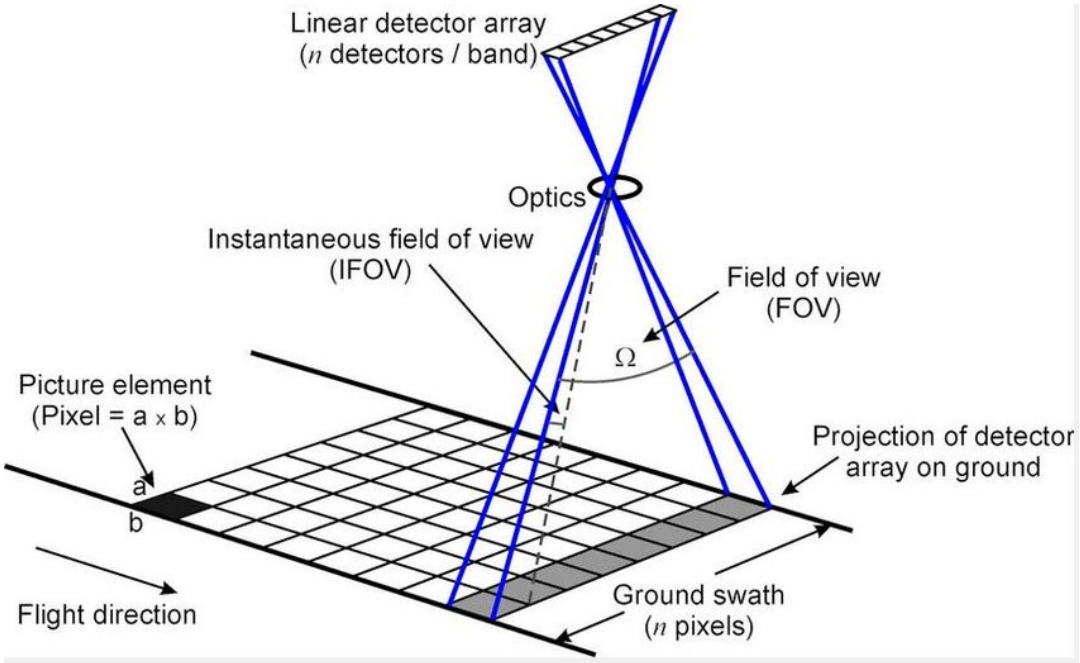

FIGURE 3.1: Visual explanation of the pushbroom method. [149]

TABLE 3.1: Specifications of the two-mirrors design.

Specification	**2M**
focal length (mm)	150
half X FOV (degrees)	3
half Y FOV (degrees)	0.5
F#	<2.3
pupil position	M1(Artificial)

is 2.3, which is too high for uncooled infrared imaging. The pupil position is not exactly the M1, but is a dummy surface placed at the same position and normal to the parabasal ray in the object space. This is purely a simulated and artificial placement that is not manufacturable (half the stop being virtual). This placement is often used by designers as it eases the ray tracing and thus accelerates the optimization phase. An added step to really place the pupil on the M1 would be necessary and would only results to small changes on the design.

As shown in figure 3.3, the optical quality is diffraction limited at $\lambda = 10\mu m$, which corresponds to a $28\mu m$ RMS spot radius at F/2.3, over most of the linear field of view of six times one degrees. However in this project, we need to have several spectral bands in the infrared (IR) spectrum. The easiest solution being to increase the FOV along the Y field to place filters before the detector. We also need to increase the time during which a ground pixel is seen by the optical system, in order to increase the signal to noise ratio (SNR) by using post-processing Time Delay and Integration (TDI). The

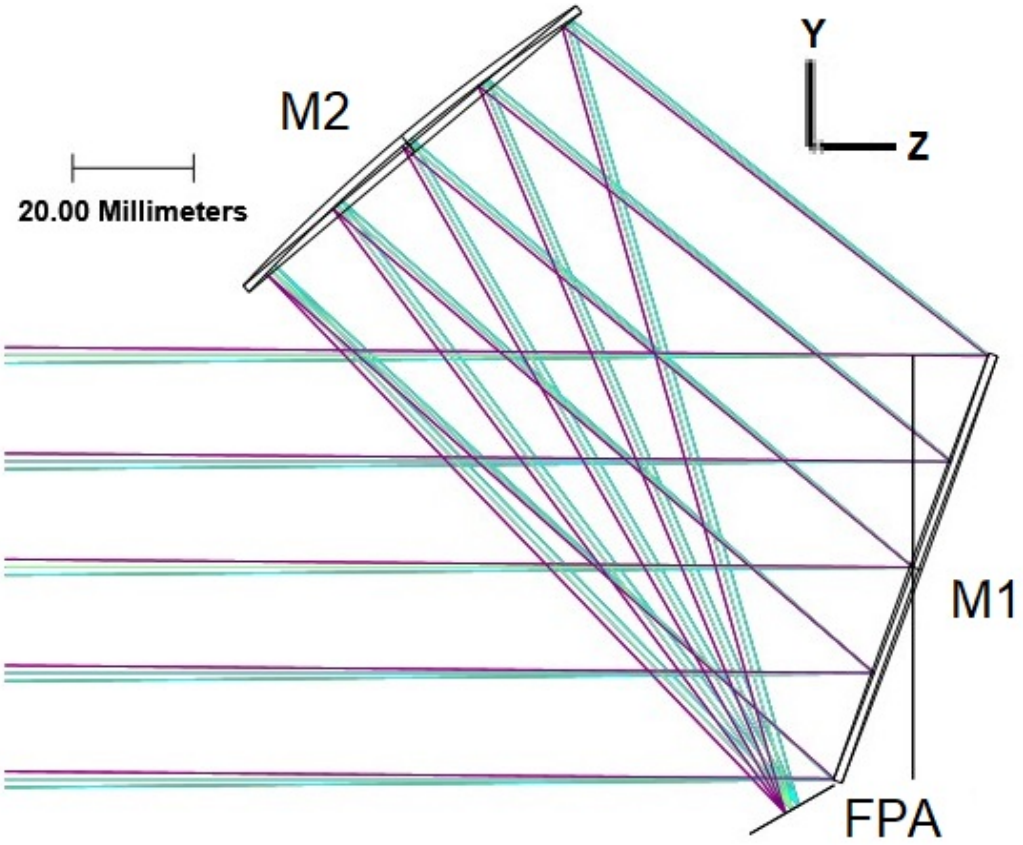

FIGURE 3.2: Layout of a two mirror solution for the specifications given in the table 3.1

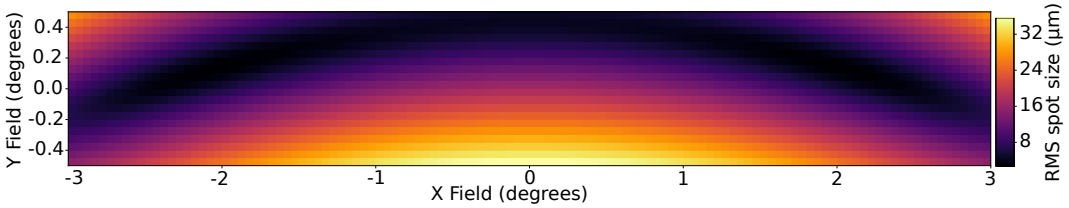

FIGURE 3.3: RMS spot radius in the focal plane of the two mirror design over a 6x1 degrees field of view

TDI uses a larger field of view in order to image the same portion of the land several times during a flyby by different lines of pixels and thus the noise can be reduced after a thorough registration of the images. To this end, we will increase the field of view of the system and use a full XGA matrix (1024 x 768 pixels) of 12 μm pitch microbolometers. Using the whole detector will allow for the use of several filters and thus have a multispectral instrument in the LWIR spectrum. Each spectral band corresponding to a portion of the field of view as shown in figure 3.5.

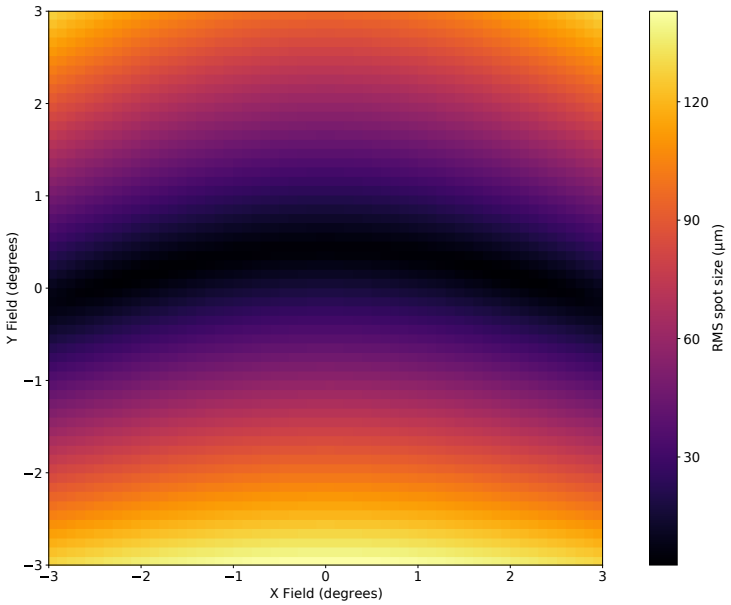

FIGURE 3.4: RMS spot radius in the focal plane of the two mirror design over a 6x6 degrees field of view

However, if we expand the field of view of the two mirror system, the rms spot radius rapidly increases, as shown in figure 3.4. Even a reoptimization using a large number of freeform parameters is not enough to correct the aberrations over a rectangular field of view. An additional mirror is required to better correct the aberrations.

3.3 Three mirror anastigmat

The solution selected here is using an off axis three mirror anastigmat (TMA) telescope. With an uncooled infrared detector, the system must have a low F number, under 1.5, to keep an acceptable noise equivalent temperature difference (NETD). Such a design has already been studied [71], [73]. Still, designing a low F number catoptric design is not particularly common. Most of this section has already been disclosed in OPTRO 2020 [150] and ICSO 2021 [151] conferences.

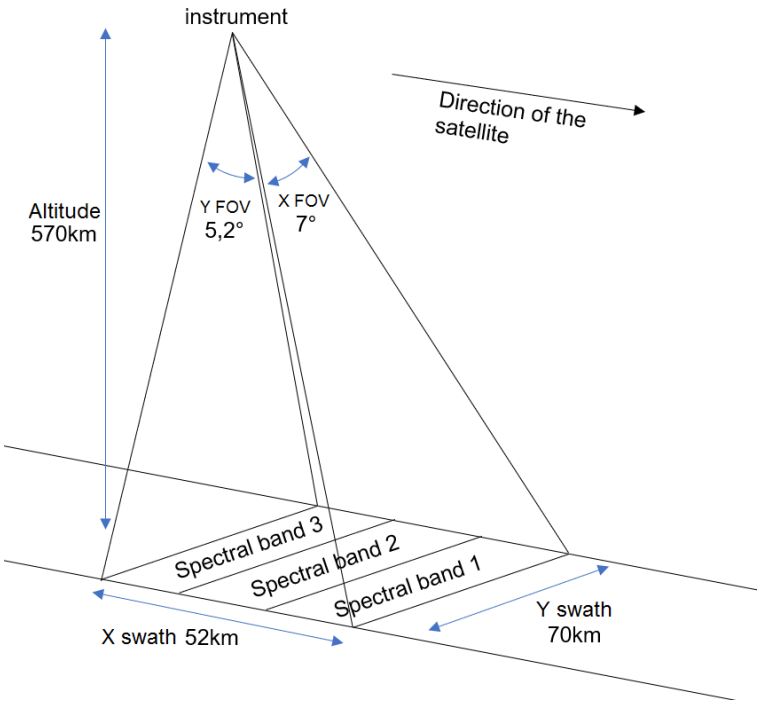

FIGURE 3.5: Summary of specifications and illustration of the field division for the multispectral imaging

3.3.1 Specifications

The spatial resolution is limited by the pixel size, which is associated with an instantaneous field of view (IFOV) depending on the focal length of the instrument. Knowing the altitude, this IFOV can be expressed as dimensions of visible ground area, or ground sampling distance (GSD). The optical system modulation transfer function is also an important indicator to ensure that the Nyquist frequency of the detector is actually resolved. For this design we chose a 70m GSD, compliant with the requirements. The orbits have been calculated by students from ISAE to be around 570km with a small eccentricity. The focal length can be deduced as shown in equation 3.1:

$$f = \frac{mean\ altitude * pixel\ size}{GSD} \approx 100mm \tag{3.1}$$

But the image also suffers from motion blur due to the satellite movement above the ground. The mean orbital speed of this satellite would be as given by equation 3.2:

$$v_0 = \sqrt{\frac{\mu}{a}} \approx 7,6km/s \tag{3.2}$$

with μ the standard gravitational parameter and a the semimajor axis of the orbit.

This motion blur causes a loss in high frequency content and thus in resolution. To minimize the motion blur, the motion of the satellite in respect to the ground must be less than the GSD during the acquisition of an image.

TABLE 3.2: Summary of specifications

specification	value
effective focal length	100mm
half FOV X	3,5°
half FOV Y	2,6°
F#	1.5
pixel size	12μm
number of pixels	1024 X * 768 Y
max X dimension	130mm
max Y dimension	250mm
max Z dimension	200mm

For a GSD of 70m and a displacement of 7600m/s, the ideal framerate would be 110Hz. Such framerate does not yet exists in off the shelf microbolometers. The end user would need to accomodate the motion blur, wait for faster microbolometers to be conceived, or the focal length could be reduced to increase the GSD and thus reduce the needed framerate.

The half field of view (half FOV) along each direction is given by equation 3.3:

$$\begin{aligned} half\,FOV &= tan^{-1}(\frac{half\,image\,size}{f}) \\ half\,FOV\,X &\approx 3,5^\circ \\ half\,FOV\,Y &\approx 2,6^\circ \end{aligned} \tag{3.3}$$

Finally, The whole 12U must be shared between the optical system, electronics and the platform subsystems, and we therefore decide to allocate only 8U to the telescope. A 12U has usually an overall volume of 200x200x300mm^3 and a standard 8U is a 200x200x200mm^3 cube which shape is not optimal for a TMA. Using a different subidivision of the satellite, we will choose an allocated volume of 130 x 250 x 200mm^3 (X,Y,Z) which is included in the 200 x 200 x 300mm^3 dimension of the satellite. Table 3.2 and figure 3.5 summarize the specifications of the optical payload.

3.3.2 Design of the TMA

The optical system is designed with three freeform mirrors defined with XY polynomials. A standard optical design software has been used, while avoiding using any functions that use paraxial data. As an example, the design must ensure a symmetric resolution, thus keeping circular entrance and exit apertures. The focal length, being a paraxial value, is not relevant anymore. The focal length and distortion are kept by ensuring the same magnification as a 100mm classical design and this magnification is kept

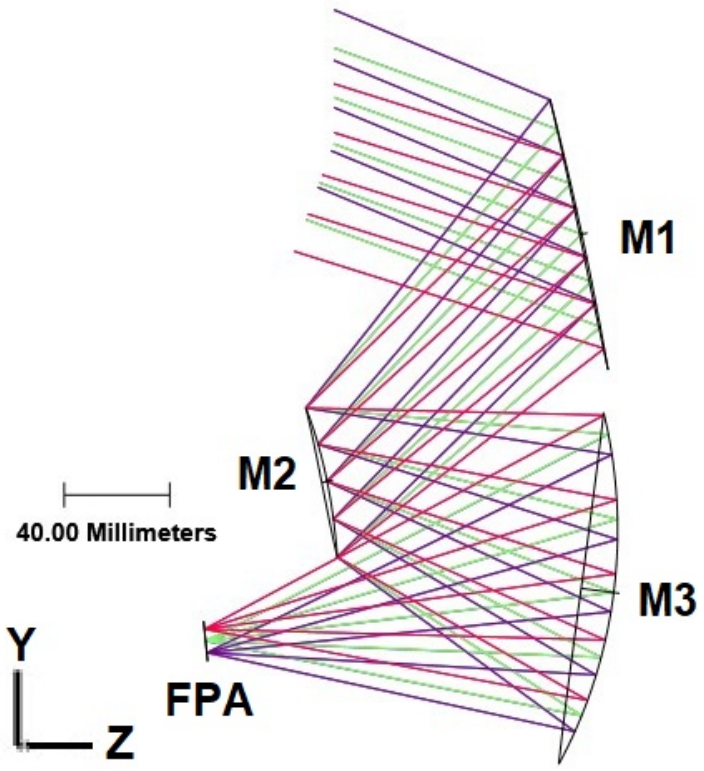

FIGURE 3.6: Layout of the optical system

over the field by fixing the real image position and shape. The pupil is the secondary mirror, which is the solution that empirically allowed to have the most compact system. The result is the TMA described in tables B.4 and B.5 and visible in the figure 3.6.

The performances are visible in the figures 3.7 and 3.8. The optical system is diffraction limited for a $10\mu m$ wavelength and the total dimensions of the optical design are included in a 120*240*150mm (X,Y,Z) cube, leaving enough margin for mirror supports and detector integration.

The accuracy of the temperature measurement is limited by the noise-equivalent temperature difference (NETD). This NETD is the temperature difference that generates a signal to noise ratio of one. As uncooled microbolometers used at a fast frequency (a few dozens of Hz) have a low sensitivity and a high thermal noise, the signal needed is high and therefore the F number must be kept as low as possible. This is also useful to increase the diffraction limit of the system and therefore the MTF at higher spatial frequencies.

The residual fixed pattern noise (RFPN) is also problematic. Microbolometers suffer from high fixed pattern noise, which must be kept under the NETD. To correct this effect, infrared systems are carefully calibrated before launch. See Chapter 4 where a calibration of such a detector is performed. However, if any parameter is forgotten in the calibration, a drift might appear. As an example, the signal of uncooled systems can be modified by the temperature of the detector, but also the temperature of the

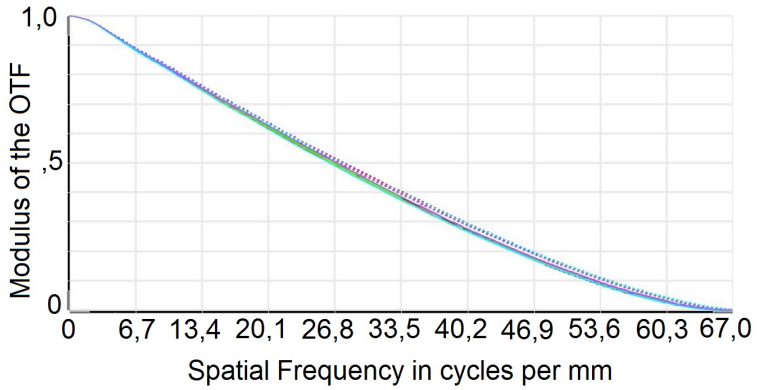

FIGURE 3.7: Modulation transfer function at $\lambda = 10\mu m$

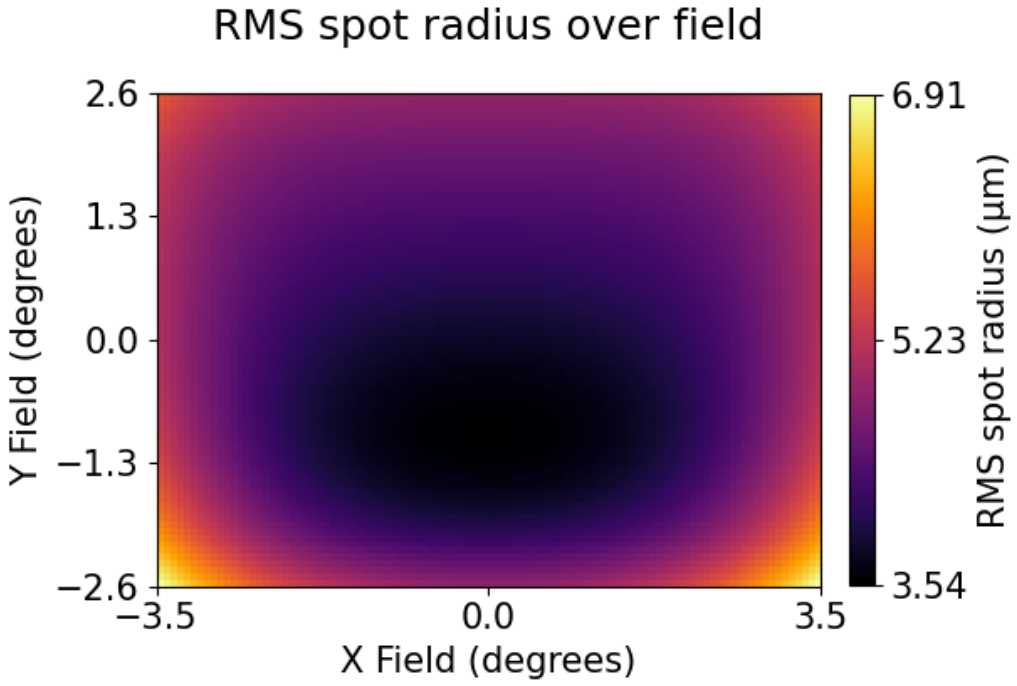

FIGURE 3.8: RMS spot radius over the field. Min RMS spot radius=3,5μm. Max RMS spot radius=6,9μm. Mean RMS spot radius=4,4μm.

platform or some mechanical parts. As the focal plane array is uncooled, so is the rest of the satellite. Every part located in front of the detector directly or via a reflection on a mirror will emit infrared straylight and perturb the measurement. This straylight is not critical as long as it stays stable (or predictable) over time, but space applications imply a large temperature variation depending on the solar illumination on the satellite. A frequent recalibration thus seems mandatory. As nanosatellites are intended to be as lightweight and small as possible, the integration of a blackbody is usually impossible. To recalibrate the system, cross calibration with data collected by reference satellites could be performed [152]–[155].

The problem is identical with straylight from out of field reaching the detector. The straylight added by the system itself depends on its temperature, so this aspect must be undestood and controlled to maintain both optical and radiometric performances and can be corrected via calibration. The out of field straylight is however more problematic. If such parasite light reaches the detector, it means that the unknown out of field temperature modifies the temperature measurement inside the FOV of the instrument. This implies that out of field straylight must be as limited as possible by design.

For this design, a specific set of constraints have been implemented to nullify the specular out of field straylight. Specular straylight is the straylight of an idealized system where mirrors have a reflection factor of one, and all the other parts absorb all light, without taking into account diffusion or emission by the surfaces. It may not be sufficient to include only specular straylight, and would be better to also minimize first order scattered light, as discussed in the article from Clermont and Aballea [156]. However, at this stage the system does not yet include any mechanical interface and this study remains a useful step in the design process. The constraints used are the following:

1. no ray must reach the detector without being reflected on the third mirror. This is reached by ensuring that the detector can only see the M3 or baffles.

2. no ray can reach the third mirror without being first reflected on the first and second mirrors or without having a high angle of incidence ensuring that it gets reflected far from the detector.

Provided that the constraints are fulfilled, any ray reaching the detector must be reflected by all three mirrors and therefore is a ray from inside the FOV of the instrument.

The first constraint is achieved using the secondary mirror as baffling, preventing rays from the first mirror to reach the detector, with an added baffle larger than the secondary to ensure this effect. In practice this baffle could be fixed on the secondary mirror support and have an additional surface texturation to reduce scattering as detailed in the article from Clermont and Aballea [156]. As the detector is placed behind the secondary,

no light can reach the detector from this mirror either. Finally, a horizontal baffle prevents any ray going straight from the object space to the detector. The result is that the only optical element seen from the detector is the third mirror. The second constraint is achieved using the horizontal baffle in figure 3.9: only rays that are far out of field can reach the third mirror. These rays with a high angle of incidence on the third mirror are reflected far from the detector, in the bottom of the satellite (they are represented in yellow in the figure 3.9). A baffling on the entrance aperture of the satellite could prevent these rays to reach the third mirror, limiting the amount of diffused light reaching the detector. A vertical baffle, in green in figure 3.9, is added to represent the side of the allocated volume where a baffle would be placed. The straylight analysis is summarized on the figure 3.9. The figure displays a non sequential ray tracing on the system, with the three added baffles. Four sources have been placed:

1. a collimated source at +2.6°Y for the red rays.
2. a collimated source at -2.6°Y for the green rays.
3. an isotropic source on the detector for the purple rays.
4. an isotropic source out of field for the yellow rays.

The green and red rays outlines the useful entrance beam, the yellow rays show the rays hitting directly the third mirror from the object space, and the purple rays are used to analyse potential straylight paths. If those rays are, after back propagation in the system, included in the red and green outlined beam in the object space it means that only useful rays from this beam can reach the detector.

Only the rays reaching the third mirror are drawn, as any ray that is not diffused or emitted inside the instrument is unable to reach the detector without first hitting this mirror thanks to the baffles. The green and red rays outline the entrance beam and as pictured in the figure there are no rays emitted by the source on the detector that goes out of the field of view. By back propagation, this means that there are no out of field rays that can be reflected on the detector.

The oblique purple rays that are reflected on the bottom of the third mirror and reach the green baffle of figure 3.9 would be cut out in the final design, as visible in the sequential ray tracing in figure 3.6. Indeed in this figure the bottom of the third mirror is not useful, and thus can be cut out or masked.

The first key parameter for evaluating the surface shapes of a freeform design is the sag departure from the best fit sphere. It allows to have a first evaluation of the manufacturability in a glance, freeform sag departure being one of the main criteria for manufacturing capabilities, as discussed by Tataki et al. [60]. However, the sag departure is not the only relevant parameter, and the slopes of the surfaces are also an important parameter. For any fixed point M in polar coordinates in the plane of definition of the surface, the

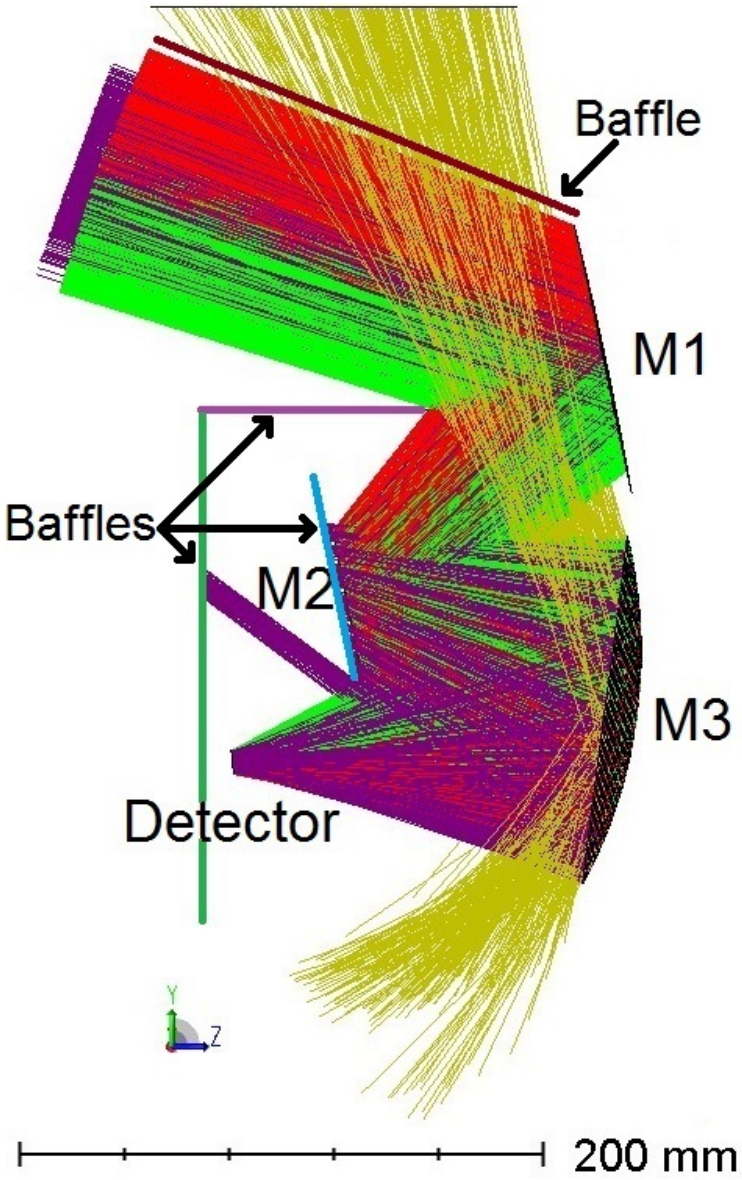

FIGURE 3.9: Straylight analysis summary of the optical system

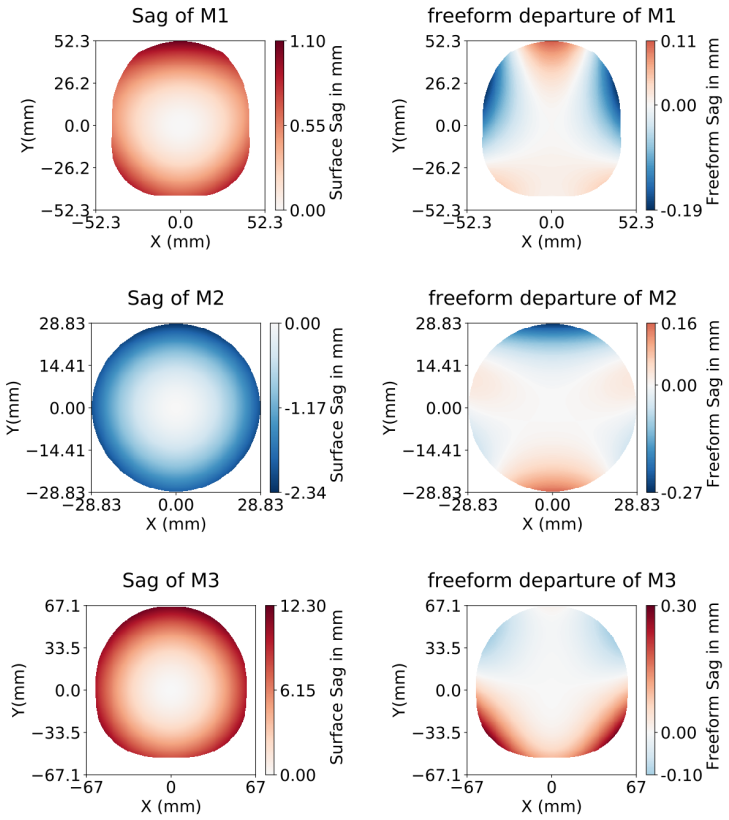

FIGURE 3.10: Sag of the mirrors and departure from the best fit sphere for each mirror.

pole O being the center of the surface, the orthoradial slope at this point is the slope along the vector orthogonal to the vector $\overrightarrow{OM}$ such that those two vectors form an orthogonal basis of the plane. These orthoradial slopes are then the slopes along concentric circles around the center of the surface. In diamond turning manufacturing techniques, the surface is rotating around its normal vector at the surface center and the freeform sag is created by translation of the manufacturing head along this axis of rotation. Orthoradial slopes are then directly linked to the translation speed of the head and the rotation speed of the lathe. Small slopes implies that the surface is easier to manufacture with better surface quality and in less time [59]. Figure 3.11 shows the orthoradial slopes of the mirrors.

The freeform sags are only of a few hundreds of micrometers and the freeform slopes of only a few degrees, which is well within the capabilities of slow tool servo [58]. It is however important to note that it is important to try to minimize those slopes and departures for manufacturing and cost aspects [157].

Finally, the length between the last mirror and the detector has been kept long enough to ensure that a dichroic filter can be placed to allow the use of a second detector, in the visible spectrum as an example. The principle is depicted in the following figure 3.12, where detector 1 is an uncooled

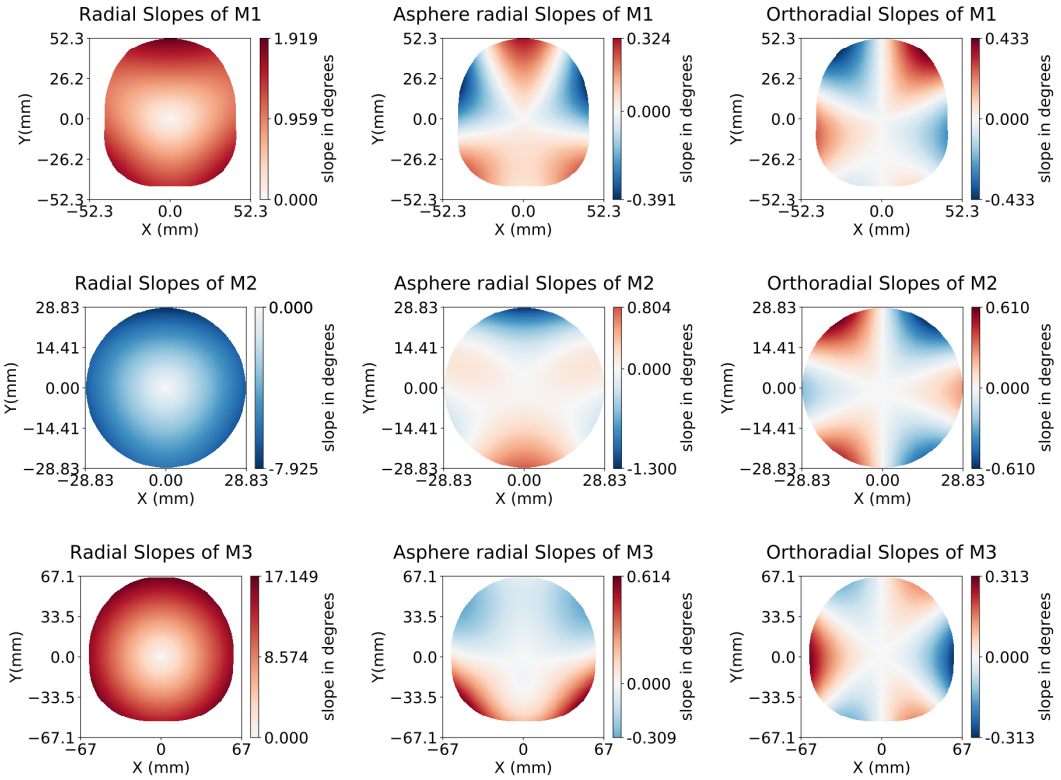

FIGURE 3.11: local slopes of the three mirrors

microbolometer and the detector 2 is a detector sensitive to another spectral band.

The mirrors are unchanged, so the performances for the reflected wavefronts should also be identical. The figure 3.13 shows the nominal expected performances at $\lambda = 1\mu m$. The performances for the transmitted wavefront are lowered due to aberrations added by the filter. The new RMS spot radius over the whole FOV is given in figure 3.14

The design occupies a volume of 121(X)x240(Y)x151(Z)mm^3, for an allocated volume of 130x250x200mm^3. Following the fact that this design did not occupy all the allocated volume and that microbolometers are still not fast enough to ensure a 100Hz imaging system did not appear in the meantime, a study with a lower focal length and larger field of view, using a GSD of 100m, has been performed to reduce the motion blur using a new SXGA (1280 x 1024 pixels) microbolometer with 12μm pixel pitch disclosed by Lynred. The design is visible in appendix C.

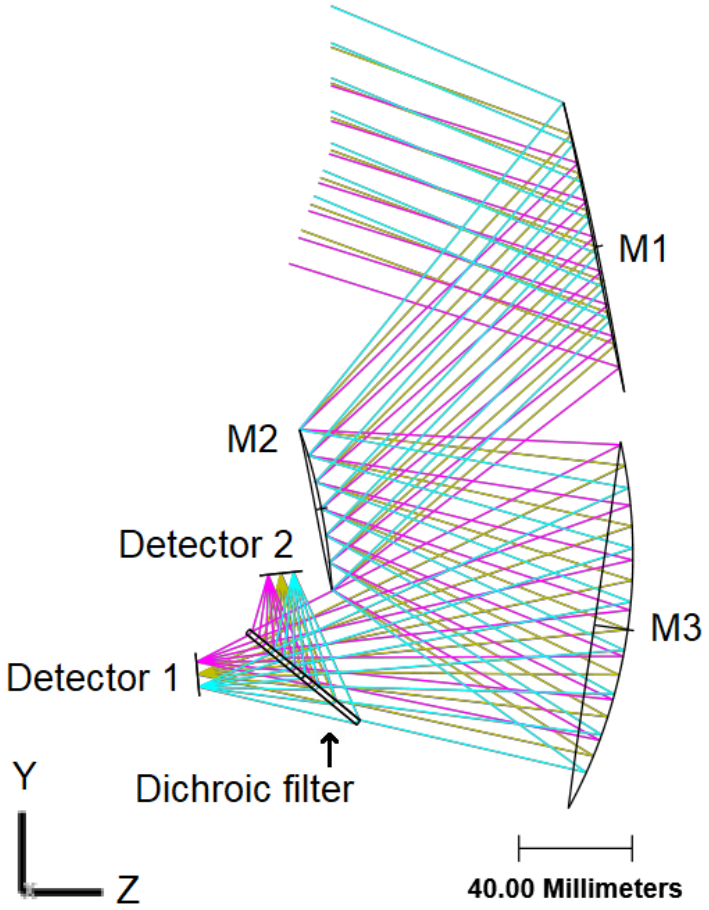

FIGURE 3.12: Layout of a multi spectral bands solution with a 2mm germanium freeform dichroic filter

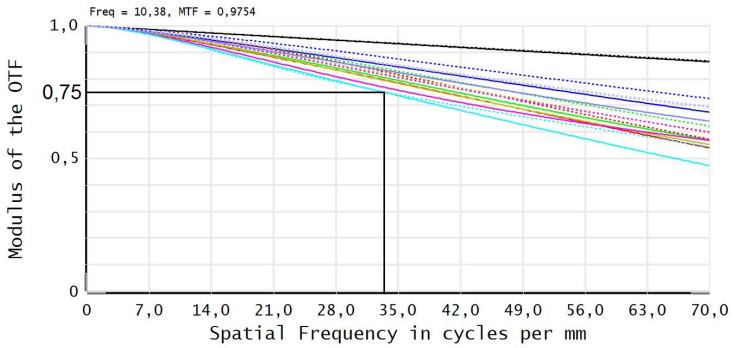

FIGURE 3.13: MTF for the SWIR (wavelength: 1μm). At Nyquist Frequency (33,3cy/mm) the MTF is above 70%.

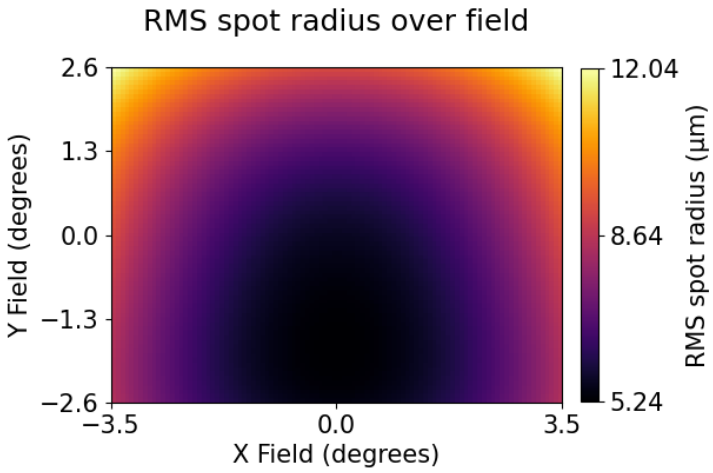

FIGURE 3.14: RMS spot radius over the FOV after transmission in a 2mm tilted germanium window for a 10μm wavelength. Min RMS spot radius=5,2μm. Max RMS spot radius=12,0μm. Mean RMS spot radius=7,3μm.

3.3.3 Prototype design and manufacturing

The system has been proposed for another project at ONERA called FLYLAB. The FLYLAB project is intended to promote optical nanosatellites and demonstrate the feasibility of optical cubesats. This project, more mature than the UHI monitoring project, has similar optical specifications. However, the volume specifications are smaller. The optical payload must be able to perform visible and infrared imaging, in a 2.5U cubesat with the shape given in figure 3.15. In the present subsection, a design is proposed for a potential multi spectral band design. In this subsection, only the thermal infrared solution is developed, as the spectral separation requires a specific study to design dichroic filters to separate thermal infrared from visible or near infrared signal.

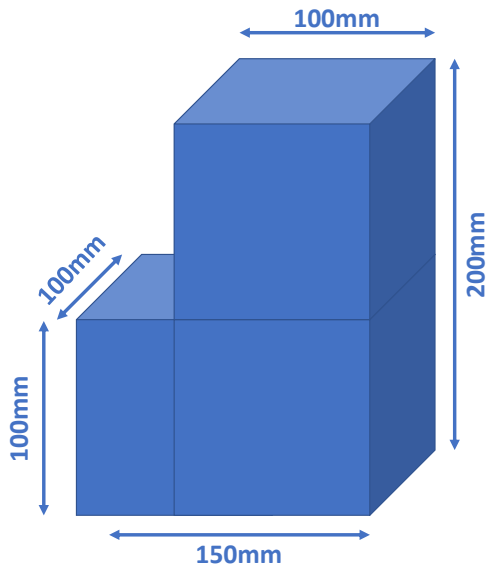

FIGURE 3.15: Allocated volume for the FLYLAB project.

Design

To reduce the volume of the design without reducing the aperture, which would be detrimental to the signal to noise ratio, there are two options. The first is to reduce the focal length. For the UHI project, a reduction of the focal length to 70mm can lead to a design fitting in a 2U volume, and lead to a GSD of about 100m, which would be still compliant. The second option is to reduce the field of view of the design. An ATTO640 microbolometer (640 x 480 pixels with a 12μm pixel pitch) has been selected for the study.

The new parameters are given in table 3.3 and the design specifications are given in tables B.6 and B.7. The layout is shown in figure 3.16, with the outline of the allocated volume in blue. This outline shows that a 100mm focal length design can be fitted inside the allocated volume, and that there is room left for the spectral separation and the second focal plane array. Finally, the nominal RMS spot radius over the field of view is given in figure 3.17

The departures from the best spheres for each mirror are pictured on figure 3.18 and the surface slopes are given in figure 3.19.

TABLE 3.3: Summary of specifications of the TMA prototype

specification	value
effective focal length	100mm
half FOV X	2.2°
half FOV Y	1.65°
F#	1.5
pixel size	12μm
number of pixels	640 X * 480 Y
max X dimension	100mm
max Y dimension	200mm
max Z dimension	120mm

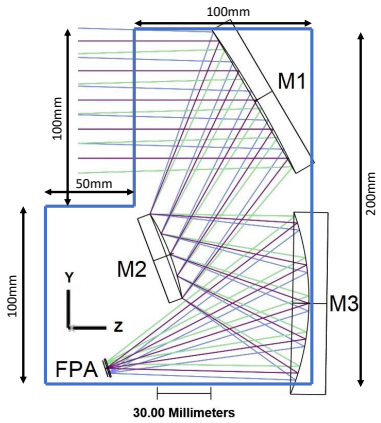

FIGURE 3.16: Layout of the TMA design resulting of the optimization, and the outline of the allocated volume is shown in blue

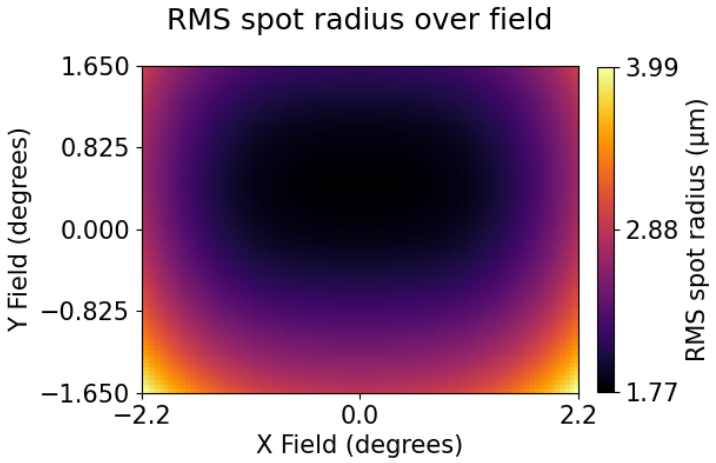

FIGURE 3.17: RMS spot radius in the focal plane of the TMA mirror design over a 4.4x3.3 degrees field of view. Min RMS spot radius=1,8μm. Max RMS spot radius=4,0μm. Mean RMS spot radius=2,3μm.

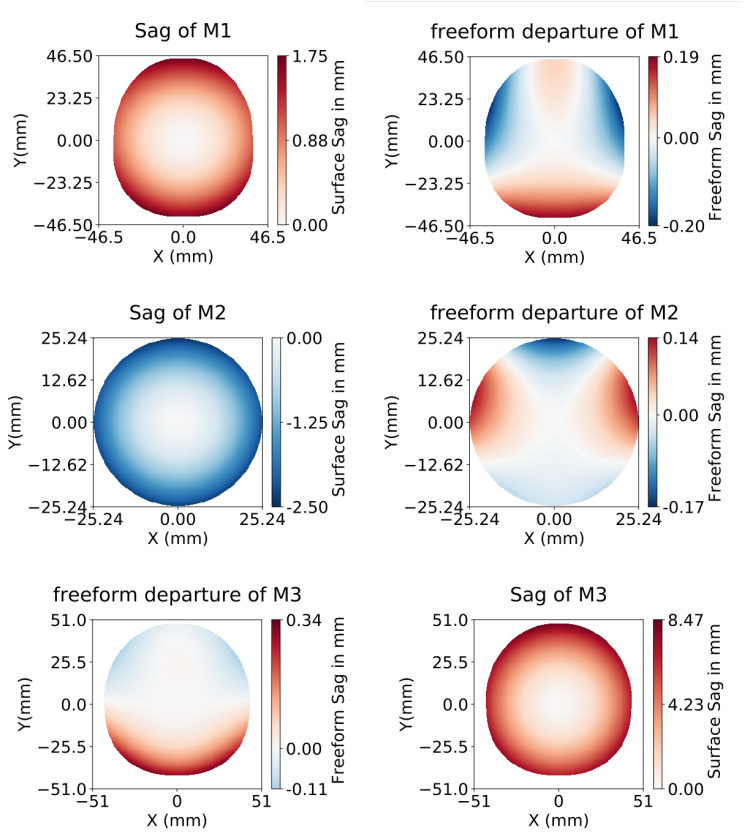

FIGURE 3.18: Sag of the mirrors and departure from the best fit sphere for each mirror.

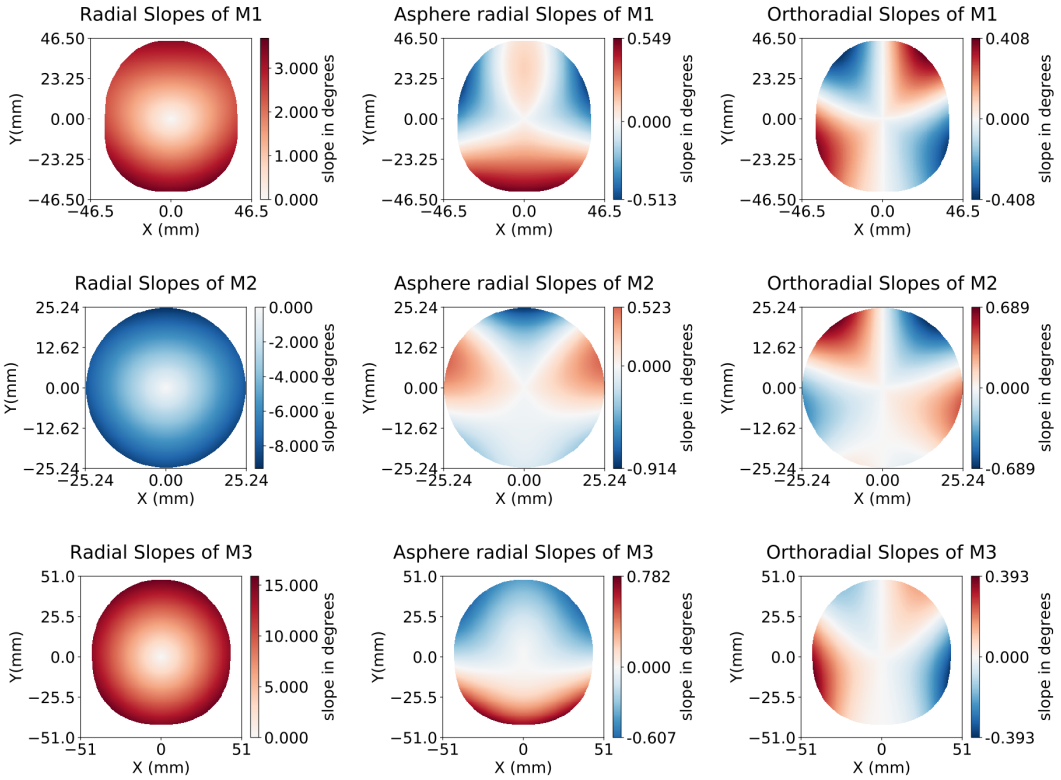

FIGURE 3.19: local slopes of the three mirrors

Tolerancing

To ensure manufacturability, the tolerance to alignment have been calculated using a Monte Carlo approach with one thousand systems, each tolerance parameter being generated using a normal distribution. The tolerancing specifications are given in table 3.4 and the results are given in table 3.5. These tolerances are about two times larger than in Fuerschbach article [158] for comparison. Such tolerances have been verified with Optics and Microsystems which are our mechanical manufacturer for the projects of this thesis and are easily attained. Compensators are the focus (Z position of the detector) and the tip/tilt of the third mirror.

TABLE 3.4: Summary of tolerances

parameter	value
Position of the mirrors	100 μm (X,Y)
Position of the mirrors	50 μm (Z)
Tilt of the mirrors	0.03 degrees (Rx, Ry)
Clocking of the mirrors	0.1 degree (Rz)
Tilt of the focal plane	0.1 degree

TABLE 3.5: Tolerancing results

Nominal RMS spot radius (field averaged)	2,98 μm
Mean RMS spot radius	3,95 μm
standard deviation	0,51 μm
M3 tilt about X standard deviation	0,016 degrees
M3 tilt about Y standard deviation	0,017 degrees
focus standard deviation	16 μm

Manufacturing

The mirrors have been manufactured in France by SAVIMEX, and are shown in figure 3.20. The blue layer is a protective cover that will be removed during the integration process, the mirrors themselves are in aluminium and are uncoated.

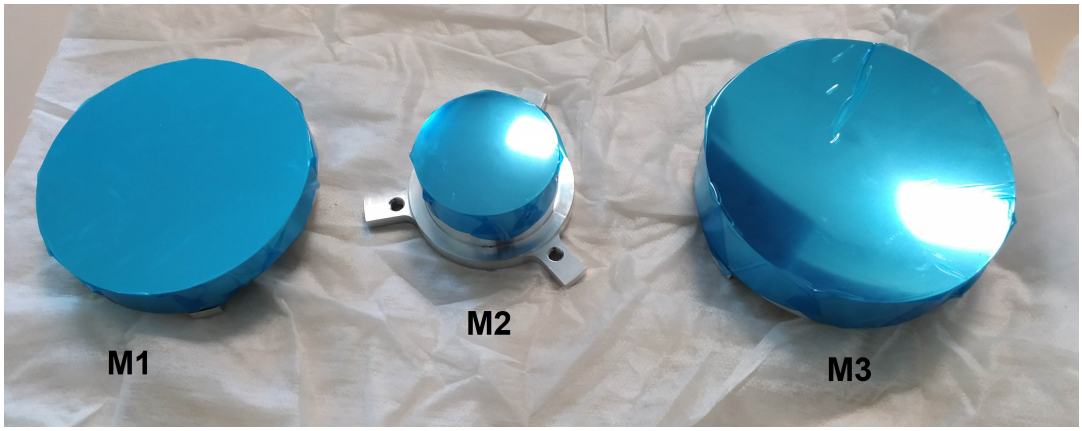

FIGURE 3.20: Mirrors of the TMA manufactured by SAVIMEX.

The mirrors shapes are given in figures 3.21,3.22 and 3.23. The shapes of the surfaces have been measured using a Luphoscan. The shape of each mirror has been included into the design to update the simulation and take into account the mirrors surface error to update the desired alignment, which had not been taken into account during tolerancing.

The mechanical structure is not manufactured yet and is expected to be received in early 2022. A first mechanical design by Optics and Microsystems is shown in figure 3.24.

The preliminary results of this study demonstrate the possibility to create a very compact TMA for nanosatellite imagery in France at a low cost. Future work will characterize the system and develop multi spectral band capabilities to really exploit the benefits of freeform mirrors.

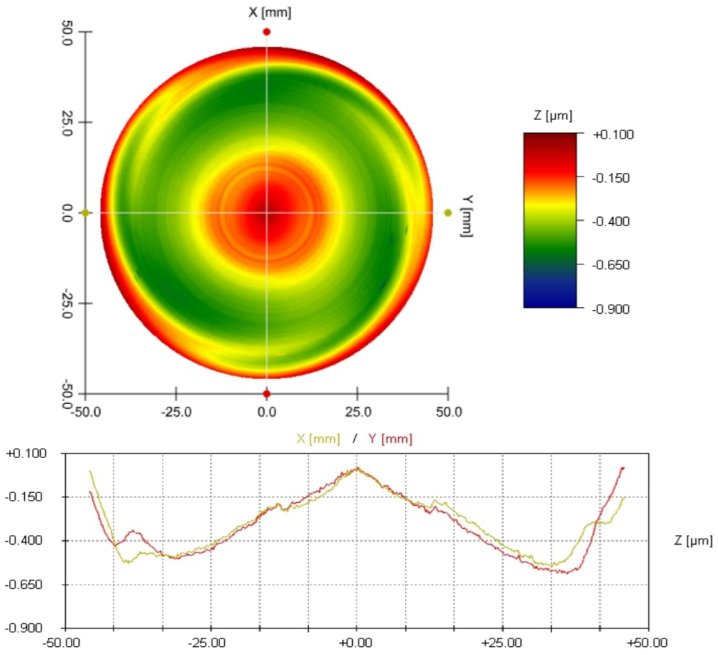

FIGURE 3.21: Shape error of the M1 as measured by SAVIMEX

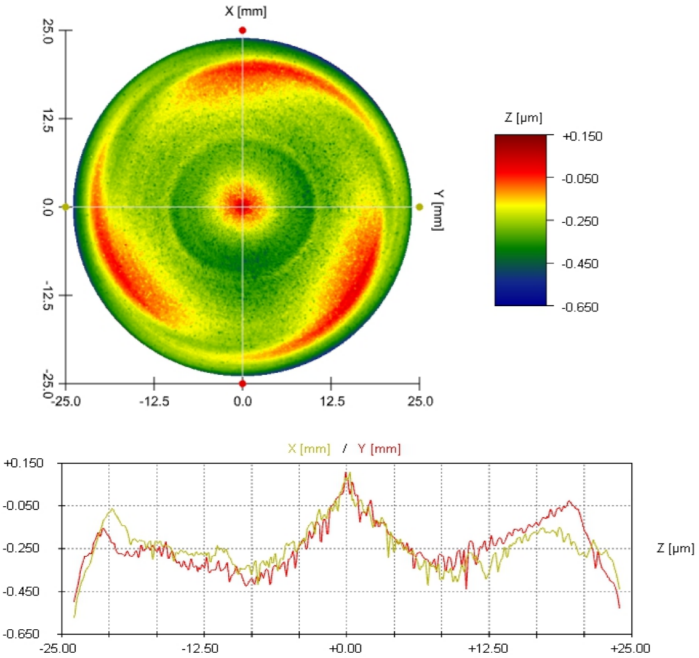

FIGURE 3.22: Shape error of the M2 as measured by SAVIMEX

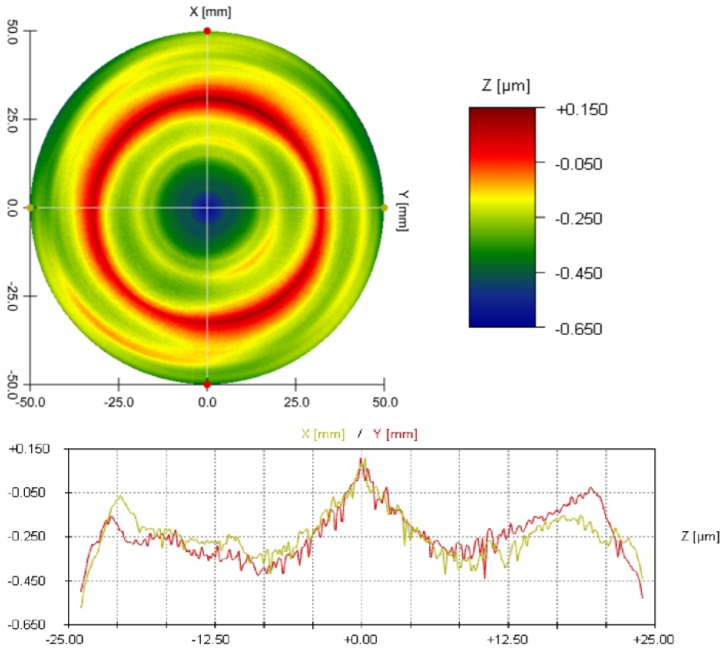

FIGURE 3.23: Shape error of the M3 as measured by SAVIMEX

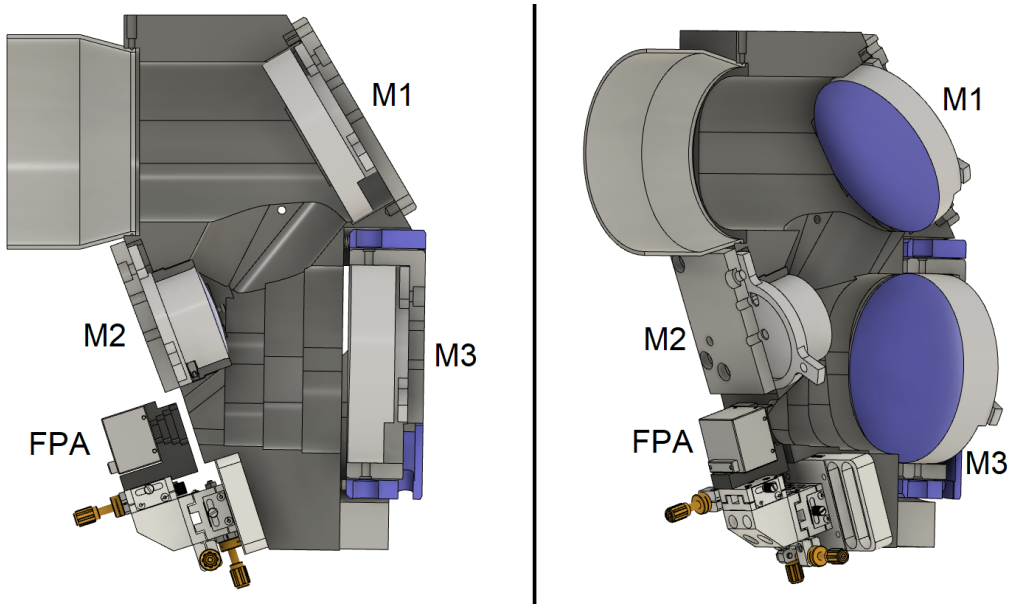

FIGURE 3.24: Cut view of the first mechanical design of the TMA. The FPA is the camera, which is an ATTO640 detector, packaged by Device-Alab.

3.4 Non planar symmetric design

3.4.1 Introduction

For an increased compactness, the exploration of freeform systems can go beyond the planar symmetric designs. For the FLYLAB study, we also searched to investigate if there was a way to perform VIS-SWIR imaging using only a 1U volume of the 2.5U, leaving a 1.5U volume for another optical system. For such compact systems, it is not possible to attain a F/1.5 design, therefore an uncooled thermal infrared system could not be adapted is such a small volume for a focal length of 100mm or more. We chose to choose a F number of 5 and try to fit the longest focal length in a 1U volume, and explore non planar symmetric systems.

The non planar symmetric TMA of this section is derived from the classical TMA geometry, but with some modifications in order to place the focal plane array next to the secondary mirror along the X axis instead of the Y axis. The goal is to evaluate whether such a geometry has potential to further increase the compactness of freeform designs. Moreover, this study also serves the purpose of testing the design method on more complex designs with more degrees of freedom. For this study, we choose to design a reference TMA and optimize it to have the best performing system fulfilling the specifications given in table 3.6. As we intend to use such systems for nanosatellite applications, we added the constraint of having the parabasal ray normal to the XY plane, which correspond to the platform side. This means that the ray is normal to one of the cubesat faces, which is sometimes needed to include the design in a larger satellite and have several systems coregistrated.

TABLE 3.6: **Specifications of the designs for the study**

Parameter	value
field of view	2,84°(Y) x 4,24°(X)
F#	5
maximal volume	1U ($100x100x100mm^3$)

3.4.2 Optimization of a planar symmetric design

The optimization has been performed using the method from Chapter 2. This time, the optimization has been made using Zernike Polynomials, but as shown in the systematic study, the choice of the basis between XY polynomials and Zernike polynomials is not critical for our method of optical design. The constraints on the design are based on the key points positions shown in the figure 3.25. As the reader might have noticed, the constraints of this design and layout have been used to illustrate the method in Chapter 2. Constraints about the overall volume are equations 3.4 and 3.5. Equation 3.4 ensures that the Y extent of the systems stays lower than 100mm. Equation

3.5 serves the same purpose for the Z extent. There is no constraint on X extent as it was not necessary in this study, every design having after optimization an X extent lower than 100mm.

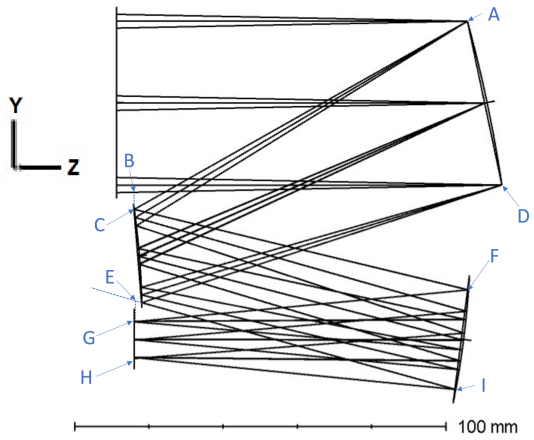

FIGURE 3.25: All spherical design used as a starting point for optimization , with the position of the key points

$$Y_A - min(Y_I, Y_H) < 99mm \tag{3.4}$$

$$max(Z_A, Z_D, Z_F, Z_I) - min(Z_B, Z_C, Z_G, Z_H) < 99mm \tag{3.5}$$

Equations 3.6, 3.7 and 3.8 are necessary to keep the design unobscured and prevent vignetting, by ensuring a minimal distance between the mirrors and the optical beam.

$$Y_B - Y_C > 3mm \tag{3.6}$$

$$Y_D - Y_F > 3mm \tag{3.7}$$

$$Y_E - Y_G > 3mm \tag{3.8}$$

We also added a constraint (equation 3.9) on the relative distance along Z axis between the bottom edge of the first mirror and the top of the third mirror to allow to manufacture both the first and third mirror in a single substrate which is a way to improve manufacturability and eases the assembly of such systems [73], [159]. The constraint given by Equation 3.9 has a small weighting to allow for a different solution if it significantly improves the result.

$$Z_D - Z_F = 0 \tag{3.9}$$

The variables are the radii of curvature, the diameter of the M1, which is the pupil, the thicknesses between consecutive surfaces and the tilt of the surfaces. Diameter of each surface is not fixed. The pupil has been placed on the first mirror to minimize its size. As this mirror is the largest of the three, increasing the size of the M1 allows to increase the entrance aperture and thus the focal length for a fixed F number. Any displacement of the pupil

would increase linearly the size of the M1 with the distance mirror-pupil and the field angle. This is also the pupil placement that gave the best results after optimization. Other solutions such as reimaging systems and systems with a stop not placed on a mirror have been studied. Those systems are however less compact and therefore are limited to specific applications that will not be disclosed in this manuscript.

After optimization with only spherical surfaces, the design has a poor image quality, shown in Figure 3.26. Indeed, the minimal RMS spot radius is over $68\mu m$, which is 18.6 times the Airy spot radius ($3.66\mu m$ at $0.6\mu m$). First, we can see a defocus that varies along the Y axis, which is the direction of the decenters. In reference [27], Thompson et al. showed using the nodal aberration theory that any misaligned TMA that is otherwise corrected presents a constant coma over the field of view and a linear asymmetric astigmatism. These aberrations are visible in figure 3.27, which proves that our design using spherical surfaces cannot correct such off axis aberrations, but can be used as a starting point to optimize our planar symmetric freeform design.

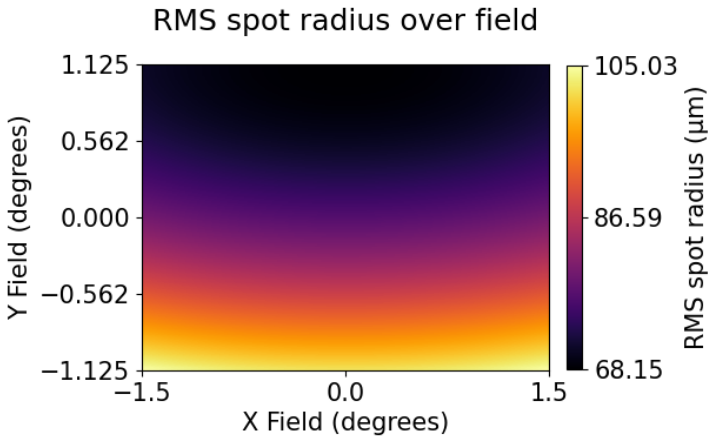

FIGURE 3.26: RMS spot radius of the image for the FOV of the full spherical starting design. Min RMS spot radius: $68.15\mu m$. Airy spot radius 3.66μm at 0.6μm.

The planar symmetric freeform system is obtained via re-optimization of this starting point. The merit function is unchanged, weighting included. The optical quality is improved by using freeform surfaces. The system has three freeform surfaces each defined as a reference sphere and a departure from this base sphere, first defined up to the fifth radial order, then up to the seventh order to obtain the final design. The end result of this optimization is the system pictured in the figure 3.28, with the optical quality shown in left image in figure 3.29.

The resulting design is somewhat suprising as there is a large gap between M1 and M3, which seems unoptimal in terms of compactness at first sight. However, this placement is indeed optimal within a cubic volume and with the constraint of having the parabasal ray normal to the XY plane, as

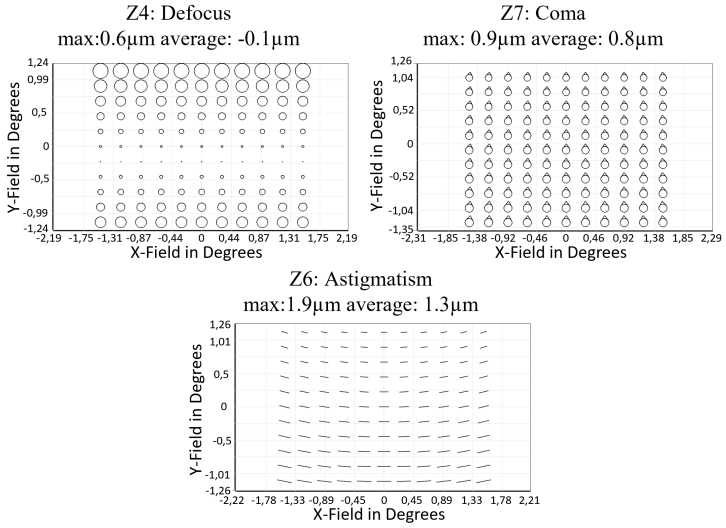

FIGURE 3.27: Defocus, third order coma and third order astigmatism of the starting design.

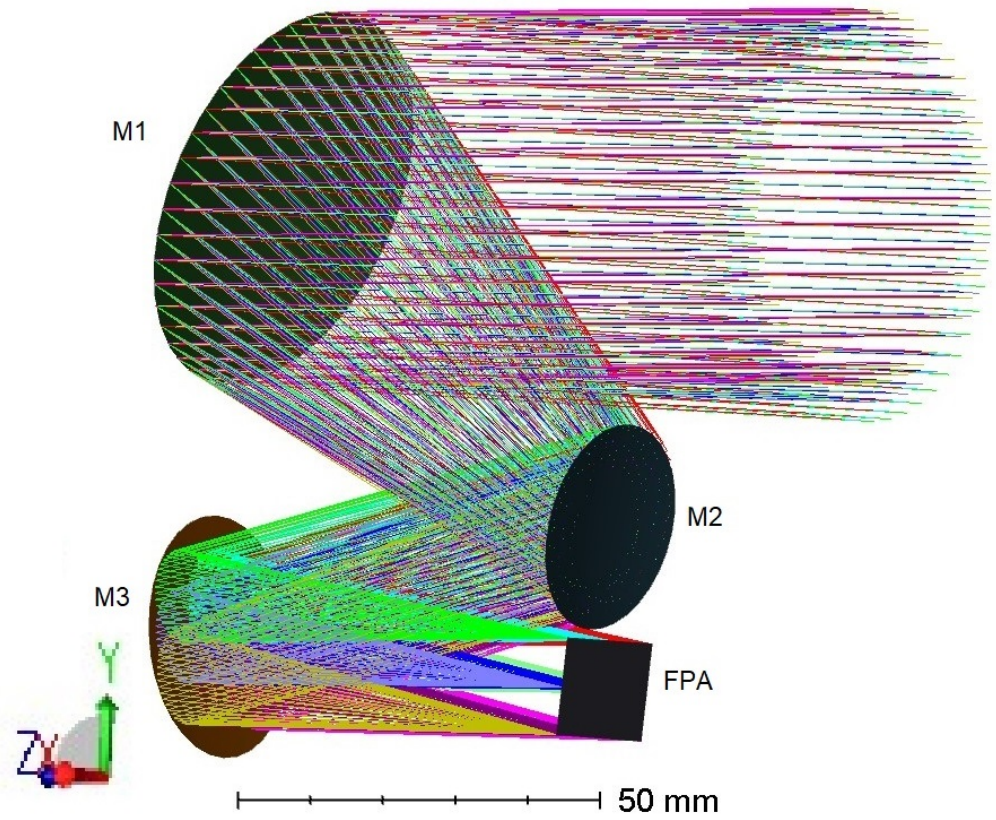

FIGURE 3.28: Layout of the planar symmetric design

the Y extent is limited by the entrance aperture, the M2 diameter and the size of the FPA. This means that the position of the M3 does not modify the merit function as long as its bottom edge remains above the bottom edge of the FPA. This position is the result of the optimization process, with the bottom of the third mirror and the bottom of the FPA aligned on a horizontal line, as in the work of Schiesser et al. [46]. A similar design has been conceived with an added constraint to reduce the gap between the M1 and the M3, and the details are given in appendix D.

The planar symmetric system is diffraction limited at $0.6\mu m$ as visible in figure 3.29. In terms of compactness, the primary mirror (M1 in the figures 3.28 and 3.30) has a bigger diameter than any other optical surface of the system, and some volume inside the allocated 1U around those smaller surfaces is lost, as shown in figure 3.30. A first approximation of the occupation ratio of the design in the 1U volume is the volume taken by the smallest enclosing rectangular parallelepiped. In this case, the occupation ratio is 38%. Some of this lost space could be used for electronic parts, but our goal is to explore the space of potential solutions to find if a larger focal length can be put in the same cubic volumes and with the same specifications (object field of view, image numerical aperture, inside a 1U cubesat).

Usually, an increase of focal length is associated with a decrease in field of view, with a fixed detector size. However, two designs with different focal length and field of view are hard to compare as the decrease of the field of view could be an explanation to any improvement in the optical quality. This is the reason we chose to keep a constant field of view in this study.

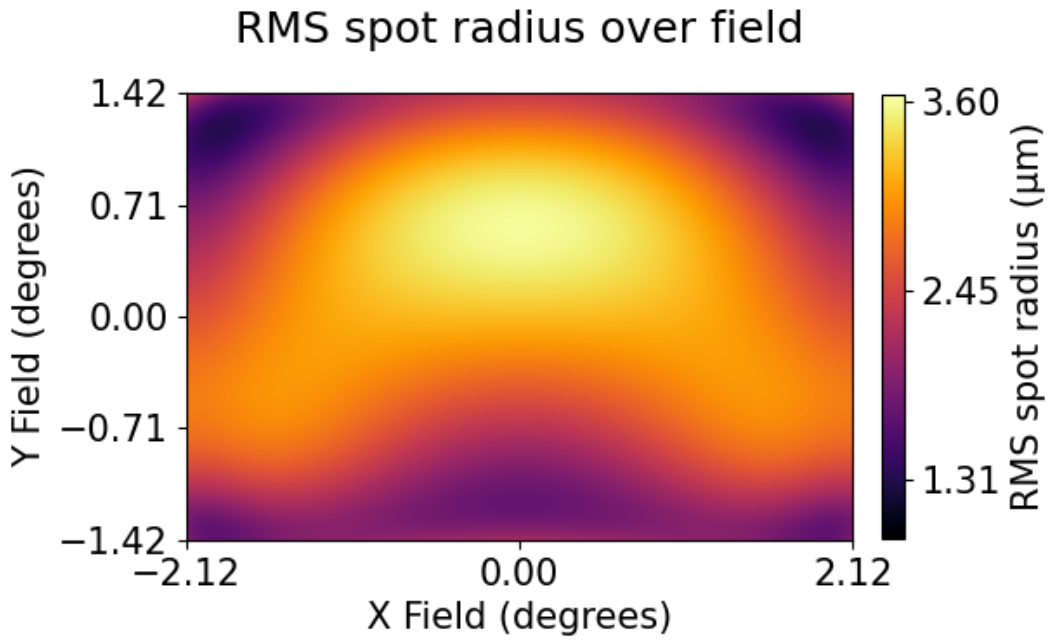

FIGURE 3.29: RMS spot radius at the rectangular image plane over the whole FOV of the planar symmetric design. Max RMS spot radius: 3.60μm. Mean RMS spot radius: 2.61μm. Airy spot radius 3.66μm at 0.6μm.

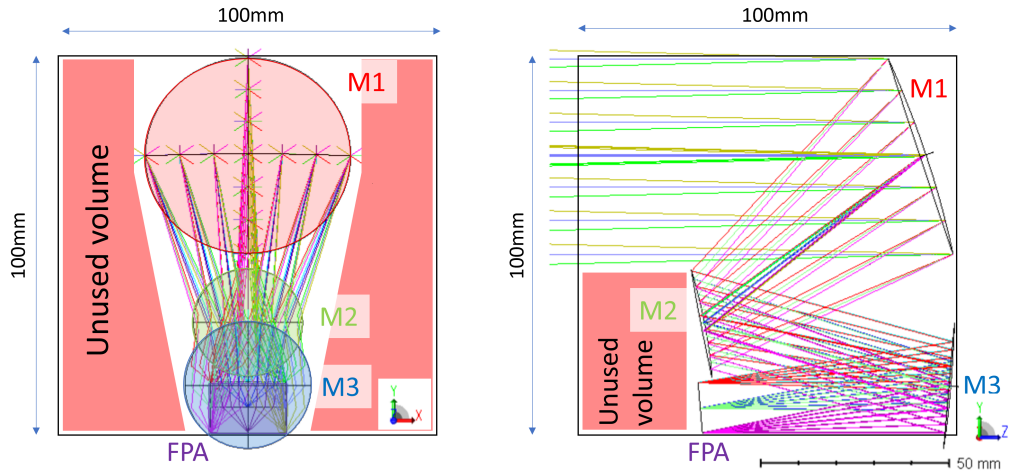

FIGURE 3.30: Layout of the planar symmetric design projected on the XY plane on the left and the YZ plane on the right. The pink colored areas in the figure are the areas unused for the optical design. Occupation ratio 38%.

The lens data for the planar symmetric designs is given in tables B.8 and B.9 from appendix B.

3.4.3 Construct of a non planar symmetric design

The use of the allocated volume by the planar symmetric TMA along the X axis is sub optimal. An optimal occupation of the volume over the X axis is proposed by removing the planar symmetry of the design. The solution proposed is to place the M2 and the FPA next to each other along the X axis instead of the Y axis, as shown in the projected layouts in figure 3.32. In the present case, the X extent of the system is given by the diameter of the primary mirror as this diameter is bigger than the sum of the diameter of the secondary mirror and the X extent of the focal plane. As the pupil is placed on this mirror, its diameter cannot be reduced without also reducing the image numerical aperture, and thus the X extent is actually the lowest possible.

With this position, the constraints along the Y axis are reduced. The Y extent was limited by the size of the incoming beam, the diameter of the M2 and the Y extent of the FPA. With this modification, it is now possible to reduce the Y extent while keeping the focal length constant or, as we did in this section, to increase the focal length with a constant numerical aperture, and thus the M1, M2 and FPA dimensions, while keeping the same Y extent. The constraints and degrees of freedom of the system are then modified to force this specific configuration. In practice, it means that each mirror can now be oriented around its local Y axis. In a first approach the local rotation around the X axis of the third mirror is now fixed at zero to keep the detector center and the center of the secondary mirror at the same position along the Y axis, leading to simplifications in the constraints needed to ensure that the system is unobscured. The constraint given by equation 3.8 is deleted and replaced by a similar constraint over the X axis. As this new system is not symmetrical, the freeform parameters that are not symmetrical about the Y axis are also used to optimize the system. Overall, each surface is now defined by the 35 first Zernike polynomials. The focus is still kept at zero, and now both tip and tilt parameters are controlled to ensure the parabasal ray tracking.

Using this setup, the focal length is then gradually increased until the 1U volume is fully occupied by the optical system while keeping a diffraction limited system at $0.6\mu m$.

After optimization the resulting optical system is the asymmetric design shown in figure 3.31 and the resulting RMS spot diagram is given in figure 3.33.

The lens data for the non planar symmetric designs is given in tables B.10 and B.11 from appendix B.

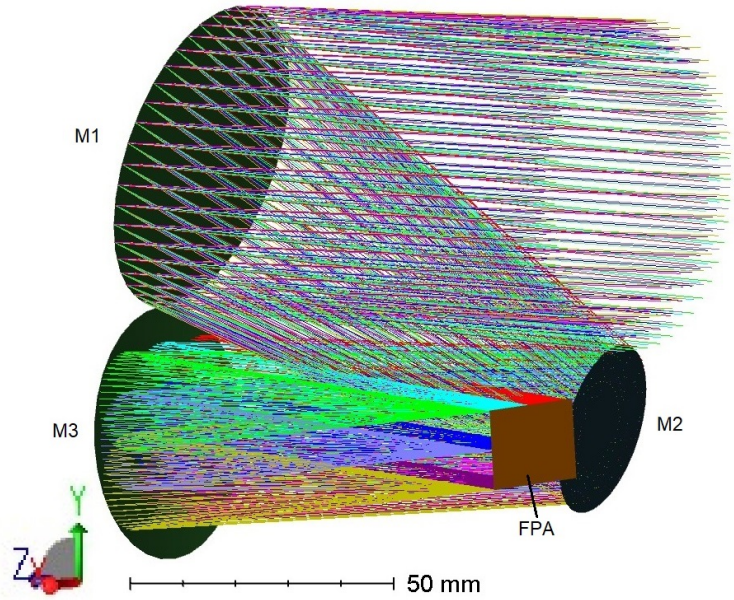

FIGURE 3.31: Layout of the non planar symmetric design

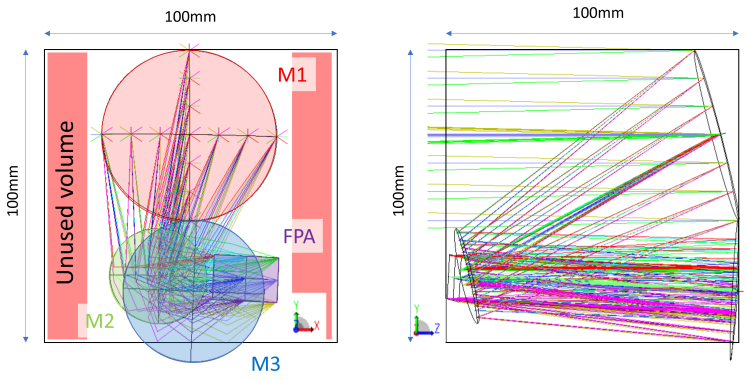

FIGURE 3.32: Layout of the non planar symmetric design projected on the XY plane on the left and the YZ plane on the right. Occupation ratio 59%.

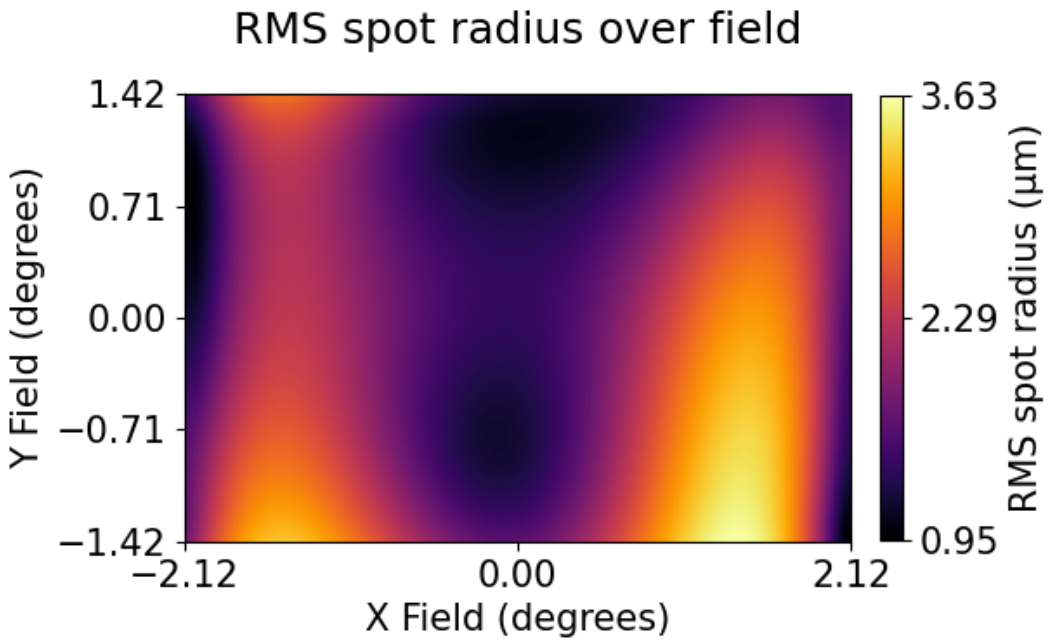

FIGURE 3.33: RMS spot radius at the rectangular image plane over the whole FOV of the asymmetric design. Max RMS spot radius: 3.63μm. Mean RMS spot radius: 2.01μm. Airy spot radius 3.66μm at 0.6μm.

3.4.4 Key parameters difference

A comparison of the main parameters for the planar symmetric and non planar symmetric designs is given in table 3.7.

TABLE 3.7: **Systems comparison**

Parameter	planar symmetric system	non planar symmetric system
focal length	269.1mm	298.1mm
field of view	2.84°Y x 4.24°X	2.84°Y x 4.24°X
F#	5,04	5,05
max. distortion	1.83%	2.10%
Extent X*Y*Z (mm^3)	54.6x99.9x69.6	60.0x99.2x99.1
Occupation ratio	38%	59%

The removal of the planar symmetry allowed for an increase in focal length of 11% in the volume of the 1U cubesat with a constant object field of view and image numerical aperture. This situation is unrealistic as the size of the detector is most of the time fixed, ending with a smaller field of view as the focal length is increased. With a fixed detector size and therefore a field of view that is reduced accordingly, the increase of focal length could be larger. However in this study it would not have been possible to attribute the improvements to the geometry if the field of view was reduced to increase the focal length.

As visible in the table 3.7, the non planar symmetric design occupies a larger volume overall. The removal of the planar symmetry did not improve

the compactness of the design generally speaking, as the smallest enclosing rectangular parallelepiped has also increased in the meantime. Instead, it allowed to fold the geometry in a more optimized manner in the cube and using more efficiently the shape of the allocated volume.

Optical quality

To assess optical quality, RMS spot radius has been computed for each system over the whole FOV as shown previously in figures 3.29 and 3.33. To ease a visual comparison, figure 3.34 shows both RMS field maps next to each other with a common colormap for both images and goes from $0.97\mu m$ to $3.63\mu m$. However, the reader must notice that the RMS spot radius for the planar symmetric design ranges from $1.31\mu m$ to $3.60\mu m$. Maximum spot radius is comparable for both systems, but the mean optical quality is better for the non planar symmetric design, with a mean RMS spot radius of 2.01μm versus a mean of 2.61μm RMS spot radius for the planar symmetric design. For reference, the Airy spot radius is 3.66μm for a 0.6μm wavelength. This means that both systems are diffraction limited a $0.6\mu m$. Mirrors being achromatic, this systems remains diffraction limited for any larger wavelength.

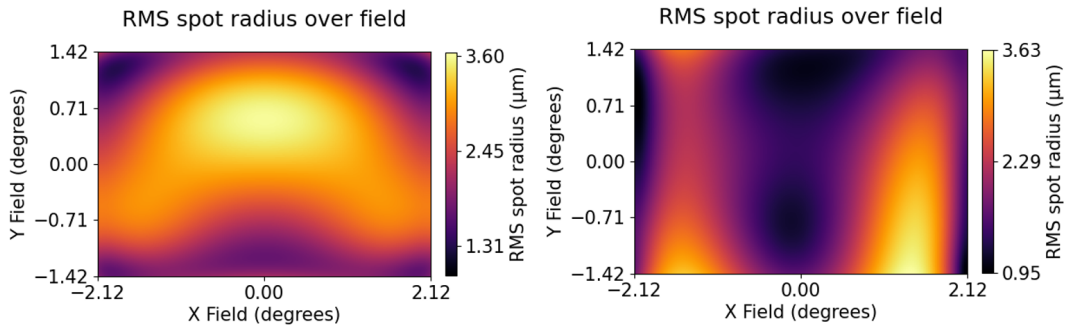

FIGURE 3.34: Left: RMS spot radius at the rectangular image plane over the whole FOV of the planar symmetric design. Max RMS spot radius: 3.60μm. Mean RMS spot radius: 2.61μm. Airy spot radius 3.66μm at 0.6μm.
Right: RMS spot radius at the rectangular image plane over the whole FOV of the asymmetric design. Max RMS spot radius: 3.63μm. Mean RMS spot radius: 2.01μm. Airy spot radius 3.66μm at 0.6μm.

Third order aberrations over the field of view are shown in figure 3.35. First, none of the designs present constant coma or linear astigmatism. Similarly, both designs show little defocus over the whole FOV. As we can see the coma values are comparable for both designs, even though the aberration does not impact the same fields. However, Defocus and Astigmatism for the non planar symmetric design are halved compared to the planar symmetric design. Both designs present typical binodal astigmatism predicted by the nodal aberration theory.

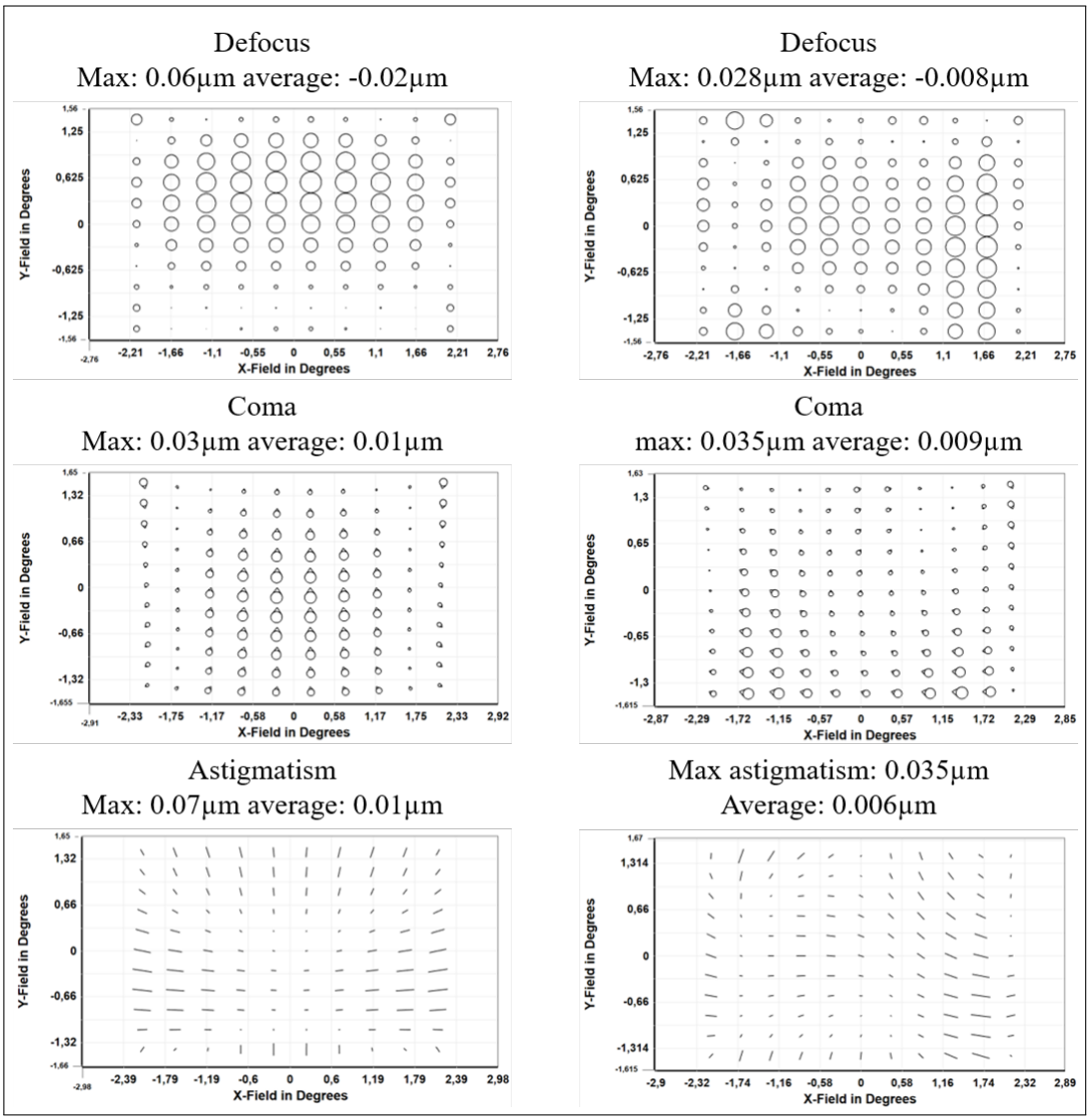

FIGURE 3.35: Left: Aberrations of the planar symmetric design. Right: Aberrations of the asymmetric design.

Distortion

Figure 3.36 presents the distortion of each system, showing low distortion for both systems (1.83% for the planar symmetric design and 2.10% for the non planar symmetric system). Because the distortion is low, the figure shows an upscaled distortion by a factor of five to allow for visual understanding of the distortion shape.

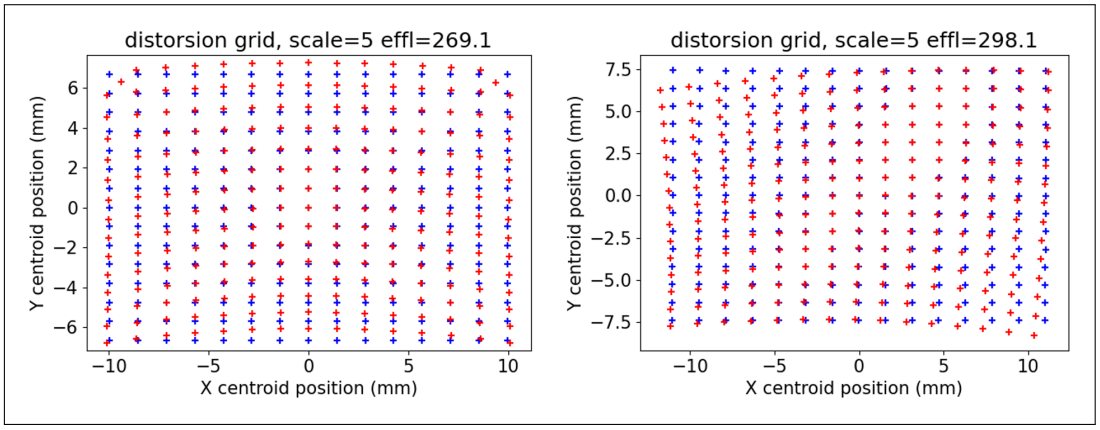

FIGURE 3.36: Upscaled (by a factor of five) grid distortion of both systems. Left: Planar symmetric design. Right: Asymmetric design

Surfaces shapes

In figure 3.37, it is noticeable that freeform departure from the base sphere is smaller for every surface in the asymmetric design.

For any testing or manufacturing method that is limited by the freeform departure, the asymmetric design have simpler surfaces to manufacture. As shown in table 3.8 the RMS sag departure from the base sphere is smaller for the non planar symmetric design, which is one of the main criteria for manufacturing capabilities, as discussed by Tataki et al. [60].

TABLE 3.8: **RMS freeform departure of the mirrors**

Mirror	Planar symmetric design	non planar symmetric design
M1 RMS freeform sag	44.6μm	29.7μm
M2 RMS freeform sag	57.3μm	36.2μm
M3 RMS freeform sag	15.7μm	11.2μm

Figure 3.38 shows the orthoradial slopes of the mirrors for both systems. As for the freeform departure, the maximum and RMS slopes of the asymmetric design are smaller as shown in table 3.9.

Overall, for all manufacturing techniques that don't take advantage of the planar symmetry of the system the asymmetric surfaces seem easier to manufacture and test. As in all optical design, the end result is always a tradeoff between optical quality and other requirements. In this case,

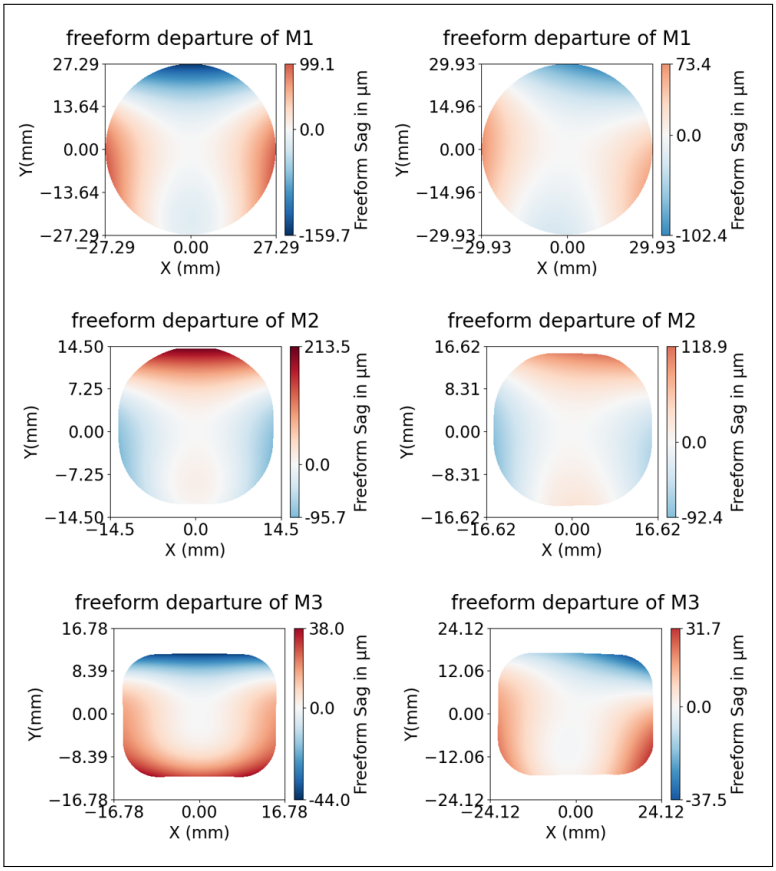

FIGURE 3.37: Sag of the freeform departure of the mirrors (base sphere removed). Left: Planar symmetric design. Right: Asymmetric design.

TABLE 3.9: **RMS orthoradial slope of the mirrors**

Mirror	Planar symmetric design	non planar symmetric design
M1 RMS orthoradial slope	0.262°	0.154°
M2 RMS orthoradial slope	0.684°	0.385°
M3 RMS orthoradial slope	0.315°	0.111°

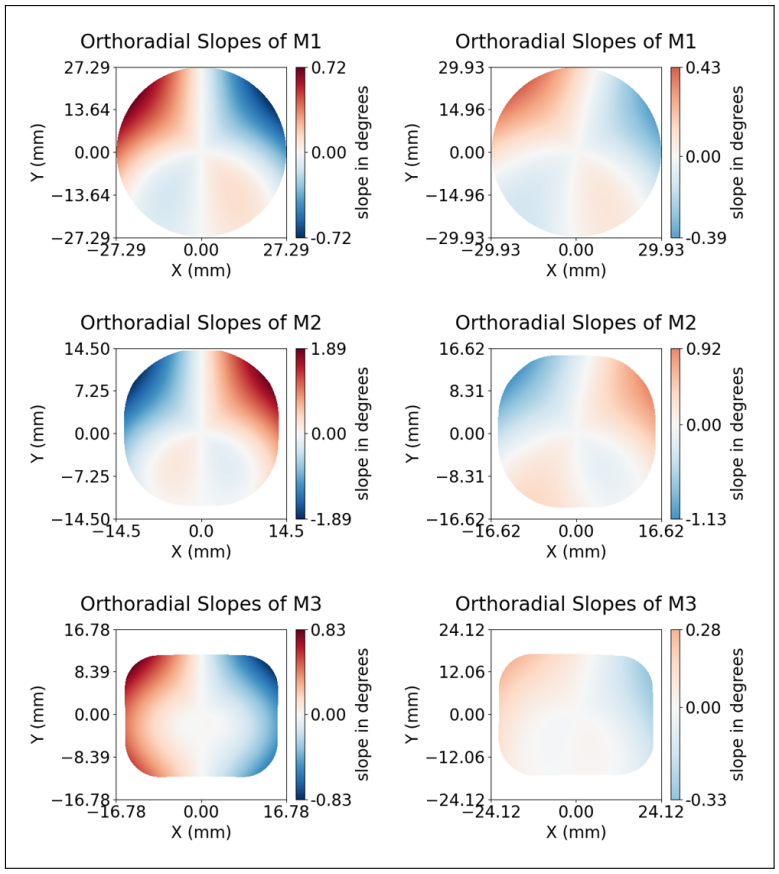

FIGURE 3.38: Orthoradial slopes of the mirrors. Left: Planar symmetric design. Right: Asymmetric design.

a planar symmetric design with similar optical quality or with a similar freeform departure and slopes could probably be conceived, but not within the allocated volume nor with the same focal length.

Tolerancing

Finally, the tolerancing of the design to misalignments is critical. If the system uses surfaces that are simpler to manufacture but requires a more complex alignment, choosing the non planar symmetric design would still end up being limited in its use. We studied the system sensitivity over small misalignments of the mirrors, with only a focus compensation. The tolerances are listed in table 3.10 and are in the usual range for freeform surfaces manufacturing [158]. The number of Monte Carlo Trials was limited by computational power.

Finally,

TABLE 3.10: **Tolerancing data**

Tolerance type	Value
Mirrors tilt (X,Y,Z)	$1mrad$
Mirrors position (local X, local Y)	$50\mu m$
Distance between mirrors (local Z)	$100\mu m$
Number of Monte Carlo trials	1000

Results are shown in table 3.11. The RMS spot radius computed is the mean of the RMS spot radius taken on nine points: the central field, and the edge of the field for each of the eight cardinal and intercardinal directions.

TABLE 3.11: **Tolerancing results**

RMS spot radius	Planar symmetric design	Asymmetric design
Nominal value	$2.38\mu m$	$1.46\mu m$
Mean value	$10.4\mu m$	$7.02\mu m$
Std. deviation	$4.59\mu m$	$3.01\mu m$

Results show that the asymmetric system is less sensitive to alignment errors. Even though the alignment of such non planar configuration might be more complex, the asymmetric system is less sensible to alignment errors. This is particularly interesting for systems that do not require manual alignment process. An example of such design is the αZ design manufactured in Chapter 4. An exploration of a non planar symmetric design derived from such folded systems is in progress at ONERA.

In summary, we have designed a system without planar symmetry derived from a planar symmetric design that serves as a reference. Both systems have received a similar treatment, with the same merit function for optimization and using freeform technologies to reach diffraction limited performances. The only difference is the geometrical constraint on the positioning of the focal plane array relatively to the third mirror.

The end result is a 11% larger focal length for the asymmetric system, within the same cubic volume of 1U and with the same field of view. A deeper analysis shows that this system has an improved nominal optical quality while surfaces are easier to manufacture due to reduced freeform departure and orthoradial slopes. A tolerance analysis shows as well that this system is less sensitive to alignment errors. Asymmetric designs should be considered for optical payloads whose volumes are fixed and not compatible with the shape of planar symmetric systems.

It has been brought to our attention that a planar symmetric design could be designed with comparable properties as the planar symmetric one, but lacking the constraint of having the parabasal ray normal to the XY plane. Such configuration has been reproduced and is shown in appendix D. Exploration of non planar symmetric variants of this configuration is in progress to evaluate if an improvement using non planar symmetric systems can be shown.

3.5 Conclusion

The TMA design proved to be useful for field of views of several degrees at most. Indeed, to increase the Y field of view, the decenter of the mirrors must be increased, up to a point where the comparison with the systems of the study of Bauer et al.[33] or Papa et al. [34] do not hold, and therefore the conclusions of their studies. If we intend to increase the field of view, the tilts of the mirrrors must be increased, leading to very strong nodal aberrations that are hard to correct, leading to either a degradation of the RMS spot radius or very large departure from the best fit sphere. This is mostly true for the Y FOV, as ultrawide X FOV systems have been designed [160]. A solution is to reduce the aperture, which is not possible in our case for photometric reasons. Another solution is to change the configuration, possibly to choose a configuration that was initially not a good choice. For pamplemousse configurations as an example, increasing the field of view does not affect the decenters and tilts as severely. The next chapter intends to search for off axis unobscured designs with large field of view and aperture.

Chapter 4

Alpha-Z: Design, manufacturing and characterization of a new configuration

4.1 The pamplemousse configuration

For designs with spherical allocated volumes, the pamplemousse configuration [85]–[87] (or $\alpha - \alpha$ configuration using the notations from the chapter 1) is promising as the overall shape of the design is such that the mirrors naturally fit in a sphere as shown in figure 4.1. This configuration has already been manufactured and tested by Fuerschbach et al. [158].

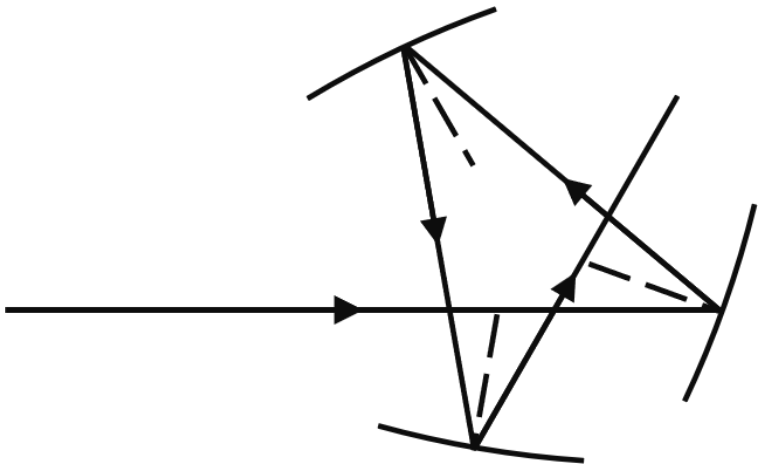

FIGURE 4.1: Pamplemousse configuration

Figure 4.2 shows a redesign of the pamplemousse from the literature [158] using the design method previously detailed in chapter 2. The specifications of the design are given in the initial article or deduced from it without any hypothesis and given in table 4.1. The resulting redesign has the characteristics given in tables B.12 and B.13 in appendix B.

TABLE 4.1: Specifications of the initial pamplemousse

Specification	Value
focal length	57.2mm
half X FOV	4 degrees
half Y FOV	3 degrees
F#	1.9
pupil position	M2

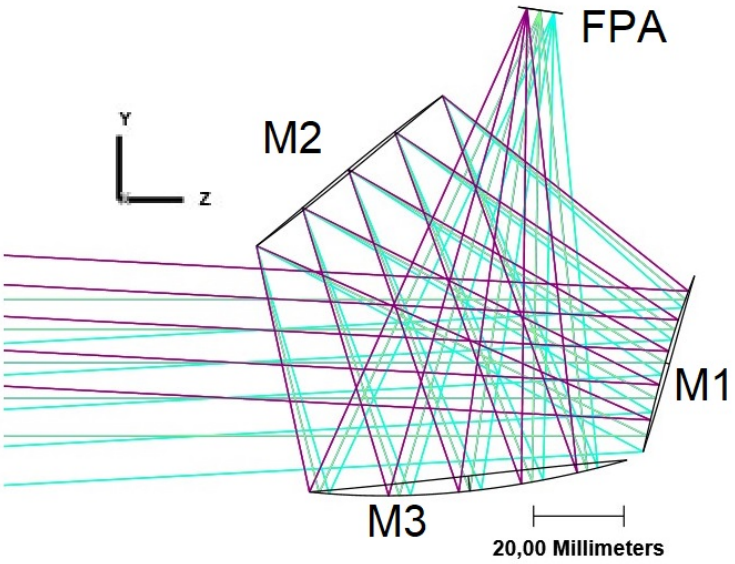

FIGURE 4.2: Pamplemousse design with same specifications as the one described in literature [87], FOV: 8x6 degrees, F#1.9

Some modifications from the initial design have been made. The pupil placement has been modified to be exactly the surface of the secondary mirror to ensure that the pupil is a physical surface, which was not the case in the initial design. The design has also been optimized with compactness in mind, effectively reducing the overall volume of the system. To evaluate this reduction, the positions of the impact of the plotted rays on the mirrors have been measured on the layout of the pamplemousse in the aforementioned article. Then, a calculation of the smallest enclosing circle has been made to find the circumcircle of the design. For the original pamplemousse from Fuerschbach et al., the radius of this circle is 59.8mm. This is not the overall volume needed to manufacture the system as the mirrors thicknesses and the camera volume are not taken into account, but it can be used as a comparison point with our redesign of the system. In the redesigned system, the impact positions have been plotted with accuracy by using a ray tracing algorithm and storing for each ray the projection on the YZ plane of the impact position of the ray on a mirror. The result of this calculation gives a circumcircle that

has a radius of 50.5mm, which is 15.6% smaller than for the initial design. The calculation of this circumcircle is a more complex problem than it seems and has been computed using the python code from the Naguyi project [161].

In article [33] the configuration is described as a worst case scenario for the optimization of imaging optics. This fact has however only been shown for small fields of view where classical TMA configurations are known to be most efficient as detailed in chapter 3. As the pamplemousse configuration involves large decenters and tilts of optical surfaces for any field angle and aperture, the off axis aberrations are natively greater than for configurations with less tilted mirrors. However, this does not mean that the configuration can not be used. Indeed, if the aberrations can be lowered by the use of freeform surfaces, the configuration could actually be used for imaging purposes. The RMS spot size has been computed over the whole FOV for the design of figure 4.2 and is plotted in figure 4.3.

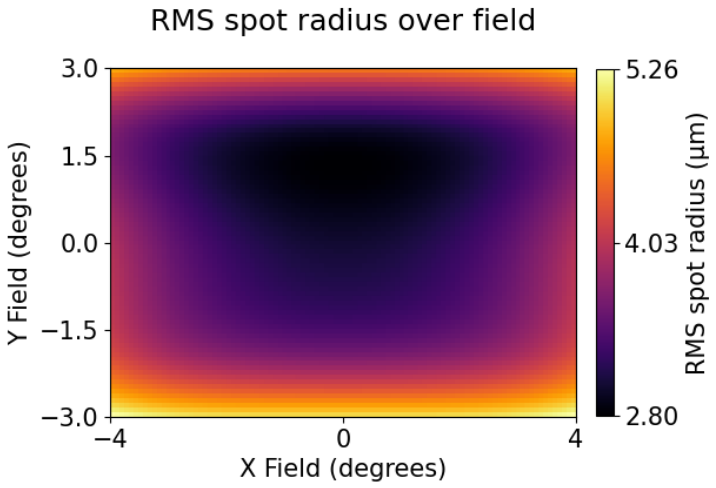

FIGURE 4.3: RMS spot size over the whole FOV of the redesigned pamplemousse. Min RMS spot radius=2,8μm. Max RMS spot radius=5,3μm. Mean RMS spot radius=3,6μm.

Intuitively, the drawbacks of using this configuration should decrease as the field increases due to the fact that the tilts and decenters do not vary much as the field of view of the pamplemousse configuration increases while it has been shown in chapter 3 that the decenters in the TMA configuration are closely related to the FOV and F number, actually limiting the Y FOV. To test this assumption, several pamplemousse with increasing FOV and decreasing F number have been designed. The final design obtained was a system with a FOV of 24 by 18 degrees and a F number of 1.5. This allows to study the feasability of such designs for large Y FOV and compatible with uncooled LWIR imagery. The specifications of the design are given in table 4.2. The focal length has been reduced to 18mm to be compatible with the microbolometer focal plane array that has been used for the caracterization

TABLE 4.2: Specifications of the large FOV pamplemousse

Specification	Value
focal length	18 mm
half X FOV	12 degrees
half Y FOV	9 degrees
F#	1.5
pupil position	M3

of the system. The pupil position has been switched from the second mirror to the third for several reasons. First, this ensures a quasi circular exit pupil. The exit pupil is not strictly circular due to the tilt of the third mirror with respect to the parabasal ray, but this tilt remains low and ensures a quasi circular diffraction pattern. If the magnification is symmetric, which is the case here, the entrance pupil is then also quasi circular too. Finally, without this pupil placement, the diameter of the third mirror is very large due to the large FOV. This placement is also useful to minimize the overall volume of the design.

The large FOV pamplemousse geometry and surface shapes are given in tables B.14 and B.15 in the appendix B.

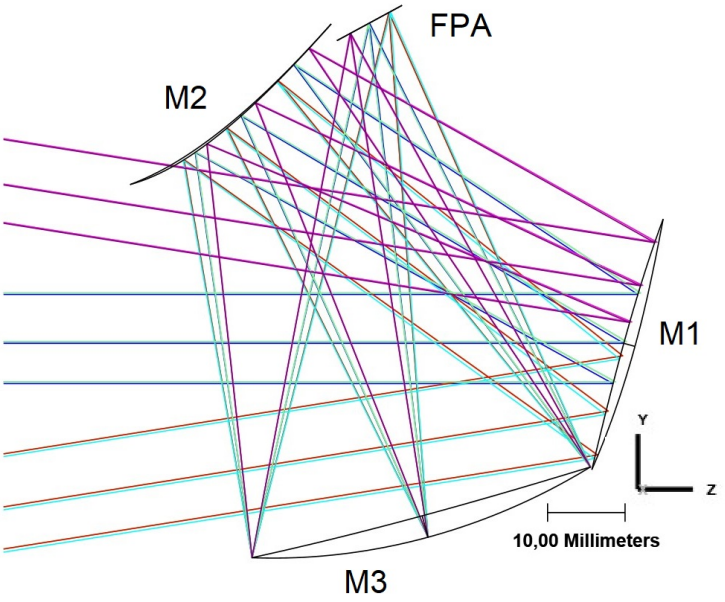

FIGURE 4.4: pamplemousse with a 24x18 FOV, F#1.5

As shown in figure 4.4, a pamplemousse configuration with a Y FOV of 18 degrees can be designed using the method described in chapter 2. The associated RMS spot scan over the FOV is shown in figure 4.5. This result proves that the pamplemousse configuration is still of interest if the designer is seeking for compact and achromatic designs with large FOV. In this work,

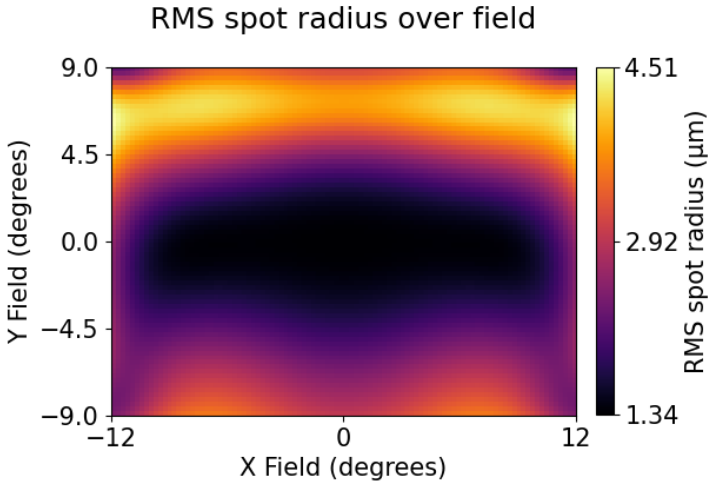

FIGURE 4.5: RMS field map of the pamplemousse from figure 4.4. Min RMS spot radius=1,3μm. Max RMS spot radius=4,5μm. Mean RMS spot radius=2,5μm.

the pamplemousse has been studied for a potential use in optronic pods, where the geometry natively put the mirrors in an ideal disposition to be mounted into a circumscribed sphere, and for large FOV that can not be reached with a more conventional configuration such as the one studied in chapter 3.

Increasing the F number and FOV however reduces the back focal length of the design, as the focal plane array gets close to the rays coming from the entrance aperture. This effect and the overall geometry of the pamplemousse are major drawbacks for the straylight management. In this configuration, the detector is naturally placed in front of the entrance aperture and this position hinders the straylight management. To emphasize the straylight path, figures 4.6, 4.7 and 4.8 each present a different straylight path. In those figures, a source that generates rays in an isotropic manner has been placed on the detector and rays leaving the system from a straylight path are drawn. Each ray segment is color coded depending on the number of reflections onto a mirror. The first figure, figure 4.6 shows the direct straylight from the object space. To prevent this direct straylight, a large baffle would be needed to avoid this straylight but this goes against the objective of compactness of this system.

There are also straylight paths with specular reflections on the mirrors. To look for these paths, a non sequential ray tracing has been performed on this design. The figures 4.7 and 4.8 present the found straylight paths. There is straylight reaching the detector reflected from the whole FOV, including rays within the useful FOV but passing out of the virtual entrance aperture. These straylight paths can be reduced by cutting the mirrors to the shape of the useful beam or placing an adequately shaped baffle in front of each mirror but this would not remove all specular straylight.

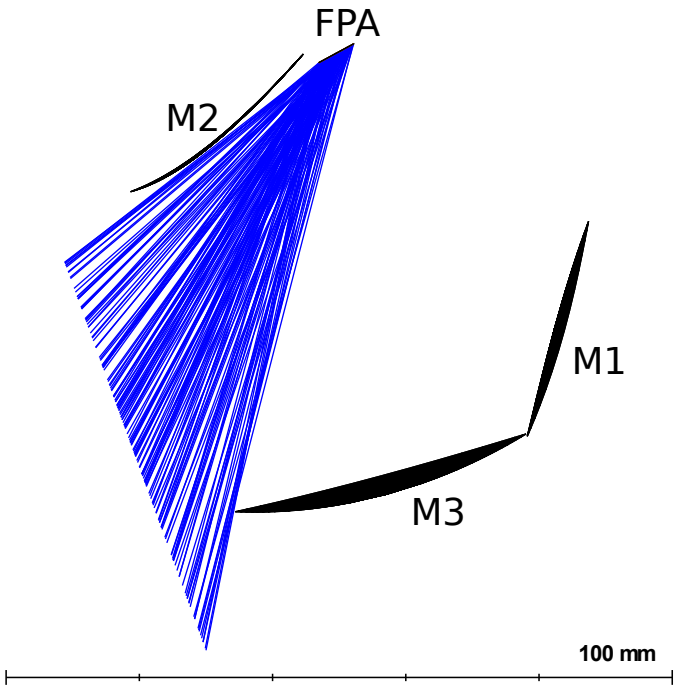

FIGURE 4.6: Direct strayligh path for the large FOV pamplemousse.

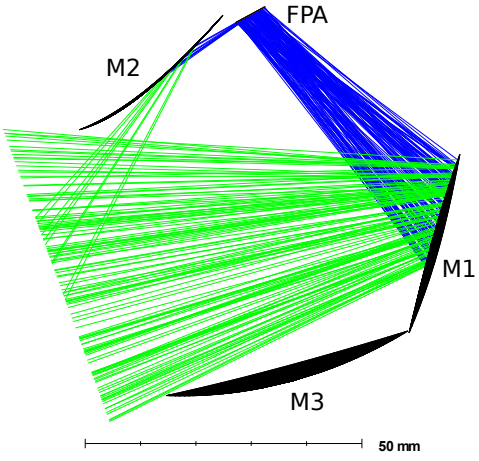

FIGURE 4.7: Strayligh path with only one reflection on any mirror for the large FOV pamplemousse. Blue rays are ray segments from the FPA, and green rays are the segments of the same rays after a single reflection on an optical surface.

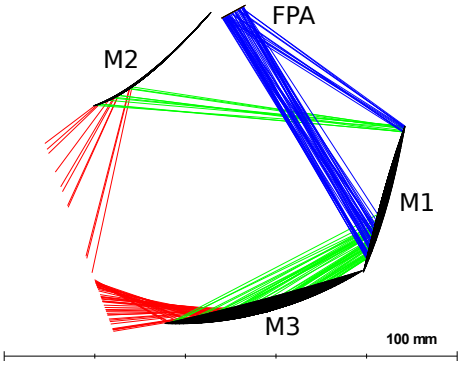

FIGURE 4.8: Strayligh path with two reflections on mirrors for the large FOV pamplemousse. Blue, green and red segments are ray segments of the same rays after respectively 0, 1 and 2 reflections on optical surfaces.

With direct and specular straylight the interest of the pamplemousse for infrared or multispectral imaging is greatly reduced. The geometry in itself complicates the placement of baffles inside the spheres due to the folding of the beam onto itself.

To avoid specular and direct straylight, the detector position must be changed in a way that places the focal plane in a position that can not be seen from the entrance aperture.

4.2 Design of the alpha-Z configuration

4.2.1 Optical design

Design

The configuration studied is the αZ configuration. This is also the configuration b in the previously mentioned article [33]. The αZ configuration differs from the pamplemousse by the positioning of the detector regarding the secondary mirror as shown in figure 4.9.

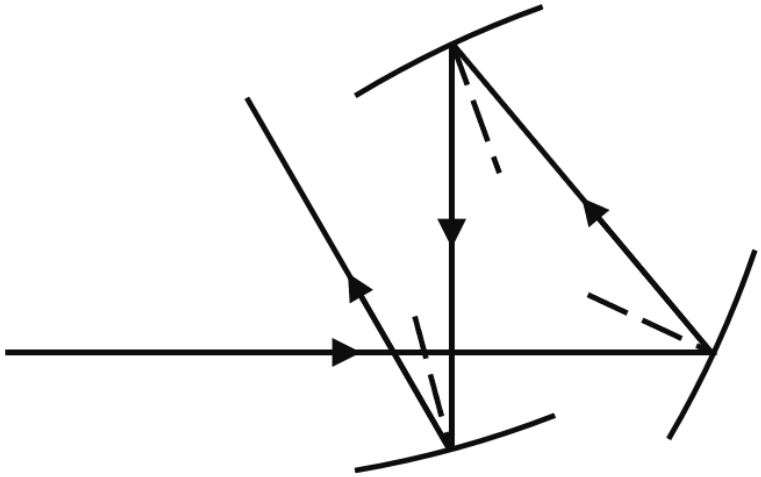

FIGURE 4.9: αZ configuration

Figure 4.10 shows an αZ with the same specifications as the large FOV pamplemousse from section 4.1. Tables B.16 and B.17 in the appendix B give the mirrors definition and positioning.

The figure 4.11 shows the principles of this configuration. First, to avoid direct illumination of the detector, this configuration places the detector close to the entrance aperture and with an angle such that straylight cannot reach the sensitive area from the entrance aperture. This effectively reduces the angle from which straylight can directly reach the detector. In figure 4.11, this angle is pictured by the two red rays, limited as much as possible by a baffle on the top of the figure. This angle can be compared to the same angle for the pamplemousse, pictured in figure 4.12.

Moreover, the placement of the detector allows the designer to use the secondary mirror and its mount as a natural baffle, preventing any ray

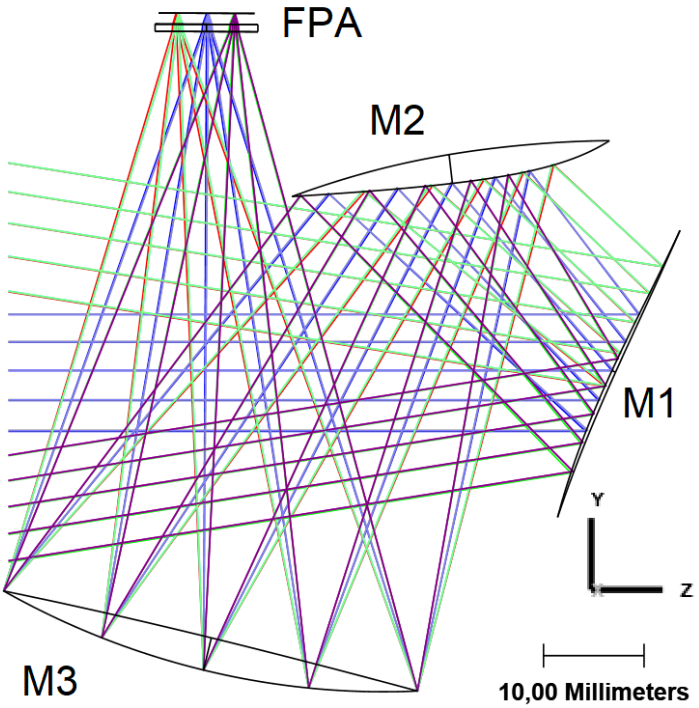

FIGURE 4.10: αZ design with a 24x18 FOV, F#1.5

coming from the first mirror to reach the focal plane array, as shown with the green line in the figure 4.11. As the focal plane is behind the secondary mirror, the rays reflected onto this mirror can neither reach the sensitive area. A non sequential ray tracing has been performed on this design too to verify if there is a straylight path involving the third mirror. It results that the angle of the M3 ensures that there is no straylight path from a single reflection onto the third mirror. The non sequential ray tracing also allowed to ensure that, in fine, there is no specular straylight in this system. Four billions rays have been traced from the detector in the direction of the third mirror with a cosine distribution large enough to cover the whole exit pupil from any point of the detector and not a single one reached the object space without being a ray from the useful FOV taking the nominal path (M3-M2-M1). Finally, another advantage of this design is that in the first optimization steps, the optimal tilt of the detector was found to be close to zero, so we could lock the design with no camera tilt, which simplifies the alignment process.

The RMS spot radius over the field of view is shown in figure 4.13. The design is diffraction limited over the whole FOV at $\lambda = 10\mu m$.

The surface shapes and local slopes are respectively given in figure 4.14 and figure 4.15. These departures, although fairly high compared to the dimensions of the mirrors, are in the manufacturable range for single point diamond turning method.

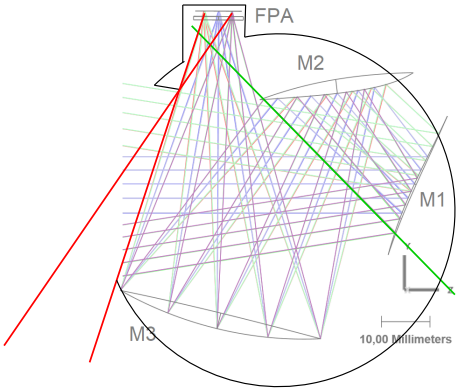

FIGURE 4.11: Direct strayligh path for the αZ configuration

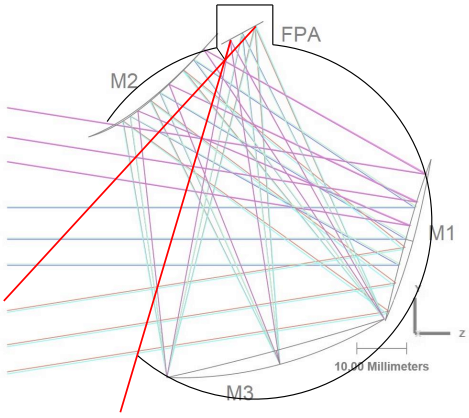

FIGURE 4.12: Direct strayligh path for the pamplemousse configuration

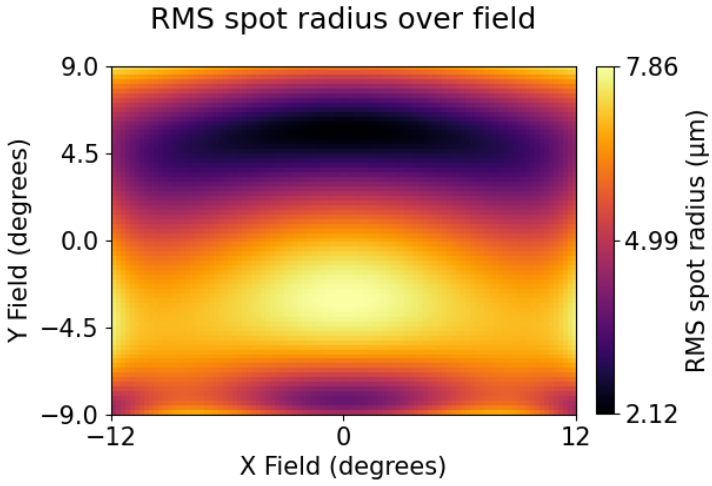

FIGURE 4.13: RMS spot radius over the field of the αZ from figure 4.10. Min RMS spot radius=2,1μm. Max RMS spot radius=7,9μm. Mean RMS spot radius=5,4μm.

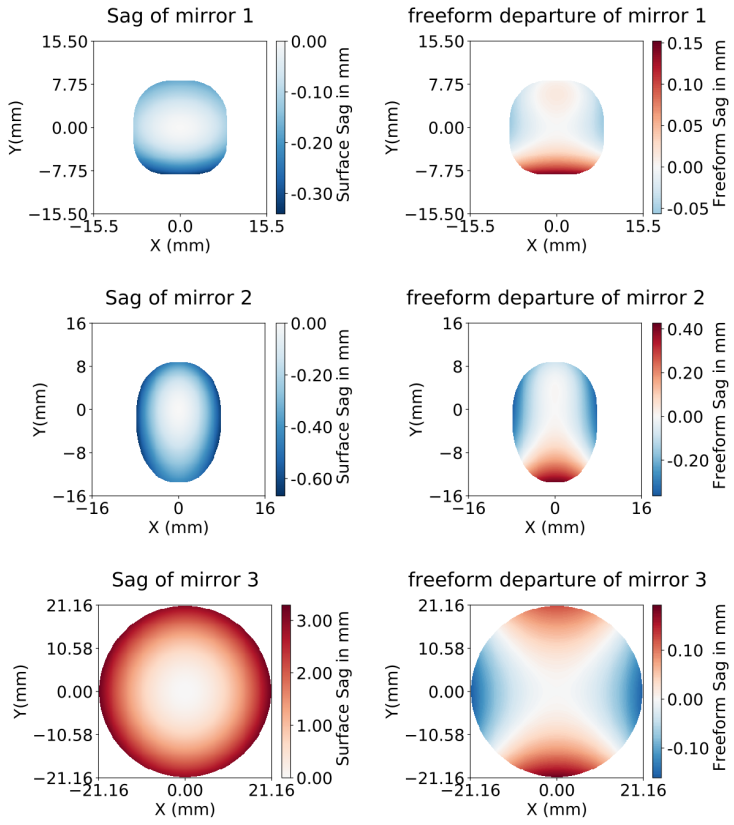

FIGURE 4.14: Surface sags and departures for the αZ design.

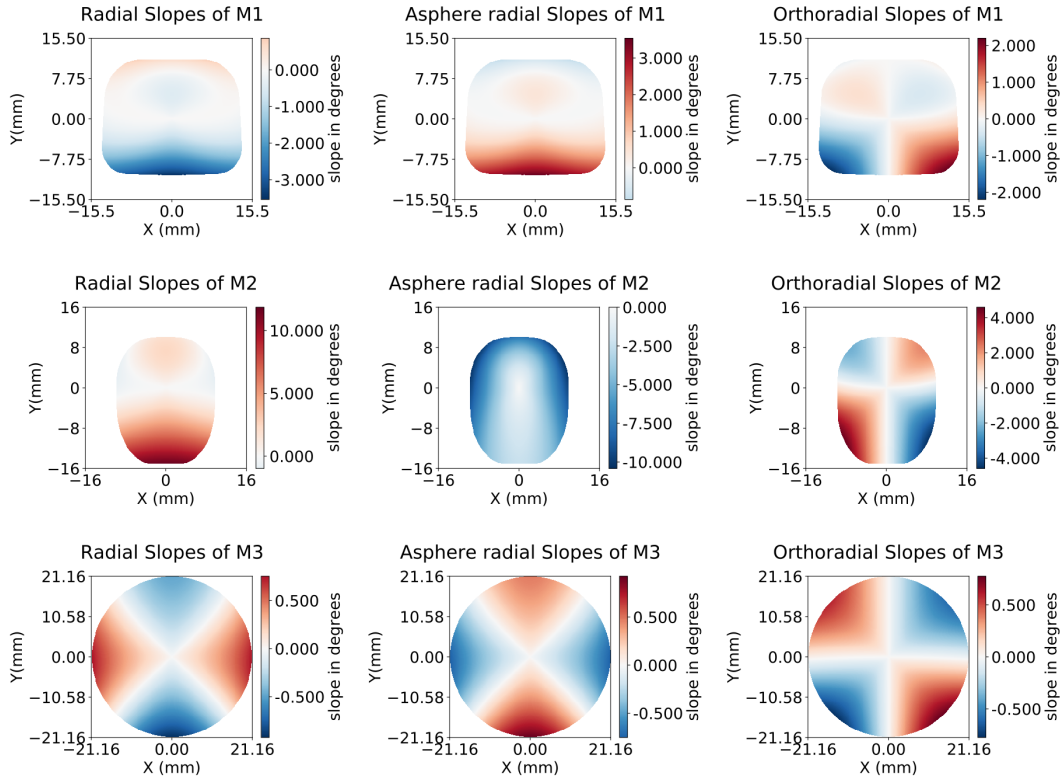

FIGURE 4.15: Surface slopes for the αZ design.

4.2.2 Distortion and focal length

We studied the effective focal length and distortion of the design by using the method described in chapter 2. The effective focal length is 18.2mm and the maximal distortion is 5.7% as shown in figure 4.16. These values are compliant with the specifications.

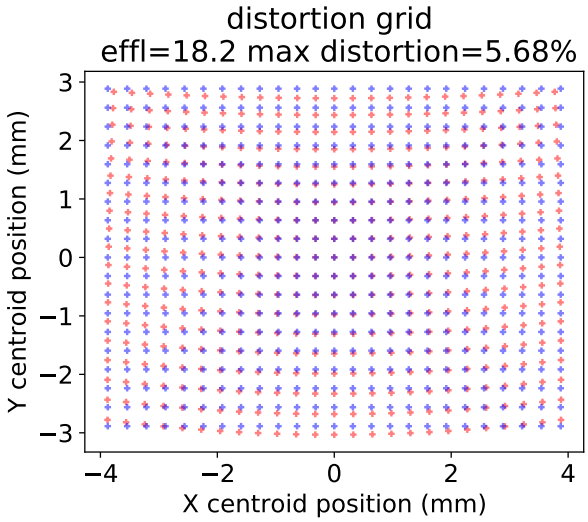

FIGURE 4.16: distortion and focal length of the αZ design.

4.2.3 Tolerancing

In classical optical design using rotationally symmetric surfaces, the design lies around an optical axis. Using this property the alignment can be done using a tube that allows a common reference for the optical axis. In off axis optical design, the alignment is purely three dimensional, which creates added alignment complexity. In such configurations, the angular alignment of any mirror can become critical. To align correctly the system all mirrors must be placed in the right configuration, which can be a tedious and long process before the specifications are met in terms of optical quality. In this design, a tolerancing of the system misalignments has been performed with standard mechanical tolerances. The goal was to determine if the system could be manufactured without alignment capabilities. To ensure that this was feasible, a thorough tolerancing was performed, with the tolerances given in table 4.3 The compensators selected are only the X,Y, and Z positions of the detector. As shown in the results in table 4.4, the system should remain diffraction limited in the infrared spectrum with only the alignment of the focal plane array.

TABLE 4.3: Alignment tolerances (if not specified, the tolerance applies to all three mirrors)

Specification	**Value**
positioning (X,Y)	100 μm
positioning Z	50 μm
tip / tilt	0.1 degrees
tip/tilt of detector	0.9 degrees
distance window/detector	400 μm
window thickness	30 μm

TABLE 4.4: Tolerancing results

Nominal RMS spot radius (field averaged)	6.15 μm
Mean RMS spot radius	13.5 μm
standard deviation	9.06 μm
X FPA decenter standard deviation	152 μm
Y FPA decenter standard deviation	60.4 μm
focus standard deviation	191 μm

4.2.4 Multi spectral band

As for the three mirror anastigmat, the final goal of this study is to generate multi spectral band imaging designs by adding a dichroic beamsplitter close to the focal plane. The difficulties of adding a dichroic beamsplitter in such situations are explained in Chapter 3. In this design, an example of how a dichroic filter could be added is shown in figure 4.17.

The tilt of the dichroic filter can be chosen accordingly to the requirements of the design. As an example, in the situation described in figure 4.17, there might be straylight issues with light from the object space reaching directly the detector, and collision problems between the FPA and the M2. If the sign of the tilt is changed, the same straylight issues might occur with a reflection on the dichroic filter. A rotation over the X axis might be a better suited option. Finally, the filter can be shaped differently to increase the back focus for the transmitted wavelength, leaving more space for the second camera. The effect of the beamsplitter on the transmitted wavefront must still be taken into account and corrected. This added piece could help reduce the RMS wavefront error for the transmitted wavefront, which could be useful if this wavelength is the lower one, having a smaller diffraction limited spot radius.

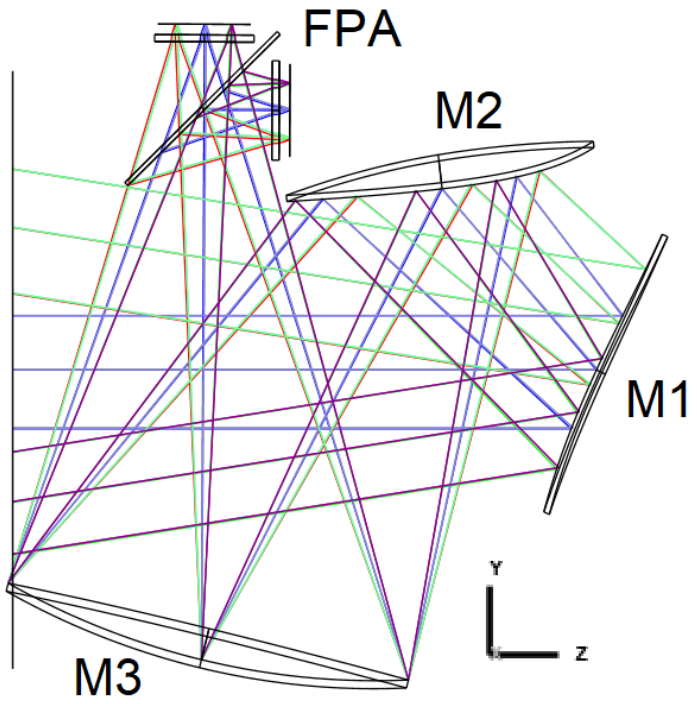

FIGURE 4.17: Illustration of a multi spectral band design.

4.3 Prototype manufacturing

The prototype has been manufactured by Optique et Microsystèmes (Opμs) for the mechanical structure and Gaggione for the mirrors. As the system has been designed without alignment capabilities, the manufacturing tolerances had to be reduced as much as possible. The solution chosen was to manufacture the structure using 5 axes machining as shown in figure 4.18. The term 5-axis refers to the ability of a CNC machine to move a part or a tool on five different CNC axes at the same time. 3-axis machines move a part in two directions (X and Y), and the tool moves up and down (Z). A 5-Axis CNC machine can rotate on two additional rotary axes (A and B) which help the cutting tool approach the part from all directions, allowing to make a precise monobloc mechanical piece.

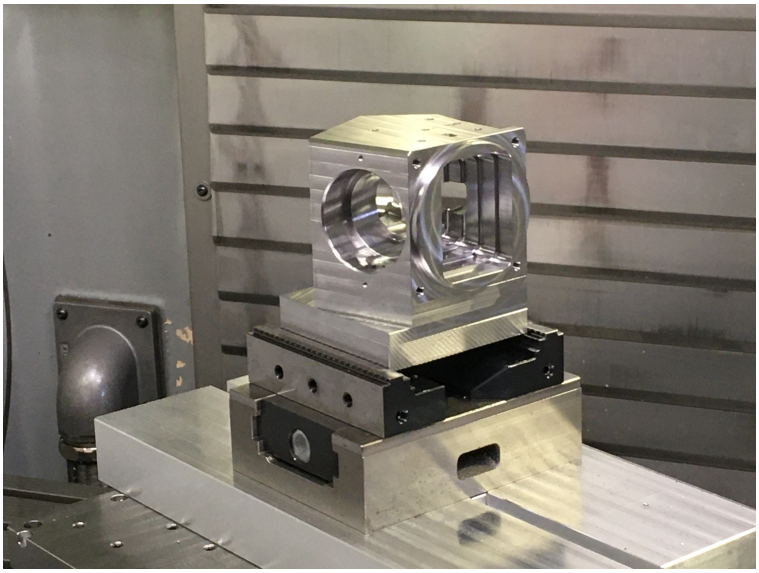

FIGURE 4.18: Manufacturing of the mechanical structure of the Alpha-Z prototype using 5 axis machining

The mirrors have been manufactured using slow tool servo diamond turning [50]. For more details on the manufacturing methods, please refer to chapter 1. The draft of the mirrors is visible in figure 4.19 and the manufacturing of the third mirror is shown in figure 4.20.

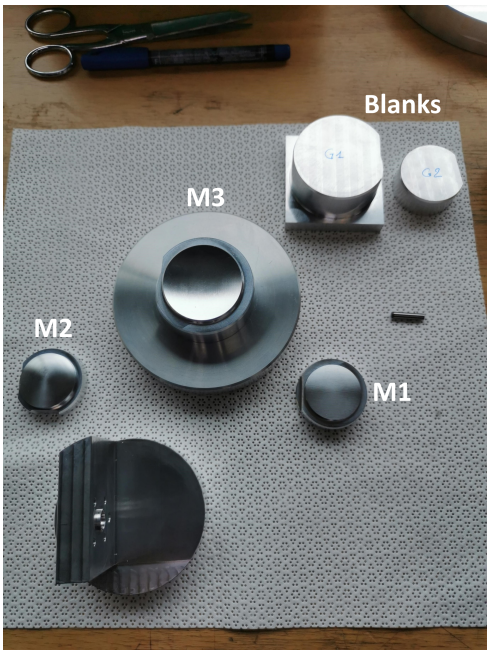

FIGURE 4.19: Draft of the three freeform mirrors of the Alpha-Z prototype. The three manufactured surfaces are drafts of the mirrors, and the two block marked G1 and G2 are blanks for the final mirrors (respectively M3 and M1 or M2)

FIGURE 4.20: Diamond turning of the third mirror of the Alpha-Z prototype

In figure 4.21, a cross section of the mechanical part of the instrument has been manufactured using 3D printing to show the inside of the design, and particularly the position of the mirrors and the baffle shape designed to limit the straylight.

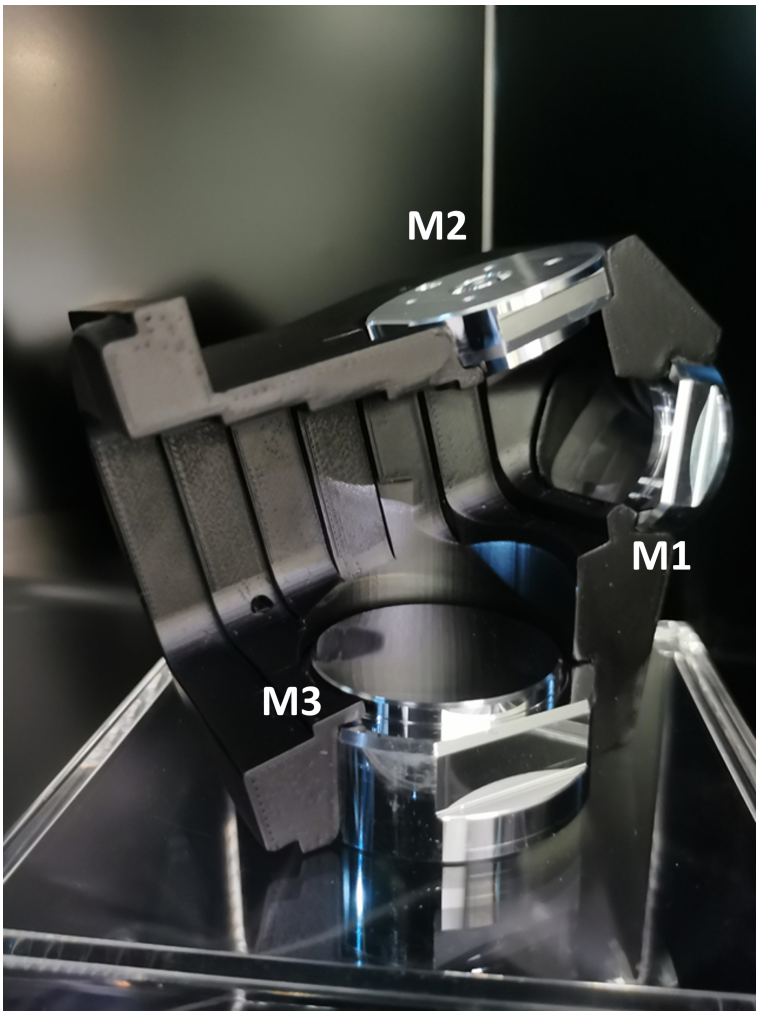

FIGURE 4.21: cross-section of the design

The mechanical part and the mirrors have been assembled by the manufacturers. The end result is shown in figures 4.22 and 4.23. Grooves from the 5 axes machining is visible in figure 4.23, and some diffused light is expected.

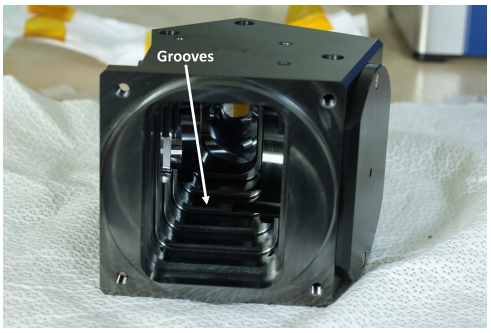

FIGURE 4.22: Entrance aperture of the finished design

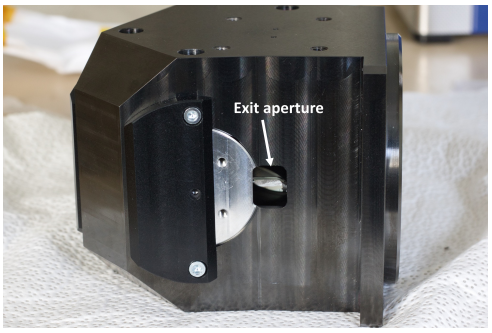

FIGURE 4.23: Exit aperture of the finished design

4.4 Prototype characterization

4.4.1 Experimental setup

Bench setup

The principal bench setup used for the characterization of the design is shown in figure 4.24. A cavity blackbody is used for the thermal infrared source. The point source is a pinhole of d=500 μm diameter in the focal plane of a collimator. The prototype is placed on a mechanical cradle that is used to perform analyses over the whole field of view.

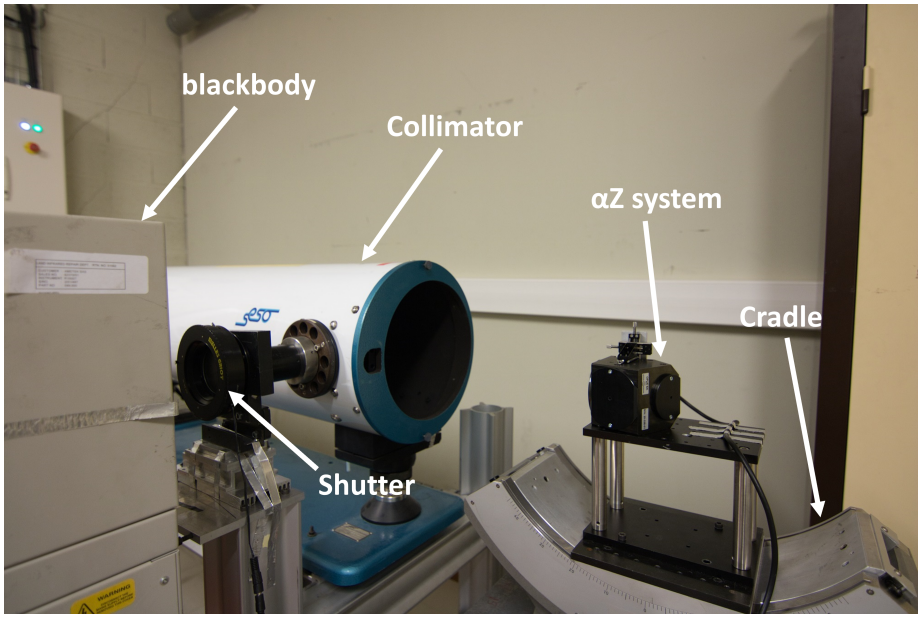

FIGURE 4.24: setup of the characterization of the alpha-Z prototype

Cavity blackbody

FIGURE 4.25: Cavity blackbody used for the characterization of the prototypes

The blackbody used for the characterization is a LANDCAL R1500T. It has a temperature ranging from 500 to 1500°C ± 3K, with a stability of 1K over 30min. The blackbody is shown in the figure 4.25.

Collimator

A collimator, shown in Figure 4.26, is used to generate an object at infinity using the light coming from the blackbody. The Blackbody is placed in front of the focal plane of the collimator, where a pinhole of suitable diameter is

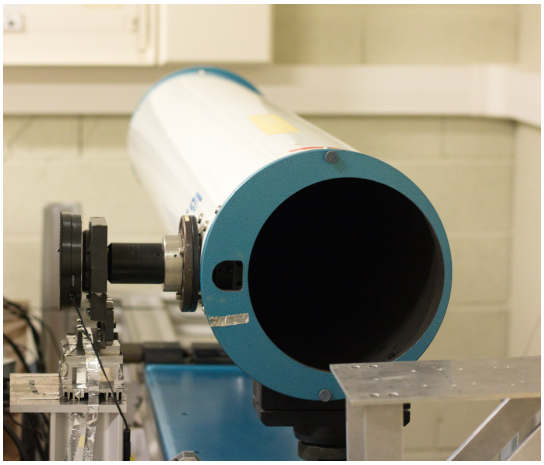

FIGURE 4.26: Collimator used for the characterization of the prototypes

placed. This diameter is chosen according to the needed angular extent of the object and the required flux on the detector. In our case, the diameter is chosen to be small enough to ensure that the image onto the detector is the PSF of the prototype. The collimator is from Thales SESO. It is an off-axis Newtonian telescope with a parabolic mirror. The focal length is 2000±20mm, and the aperture is 235mm (F# = 8.5).

Shutter

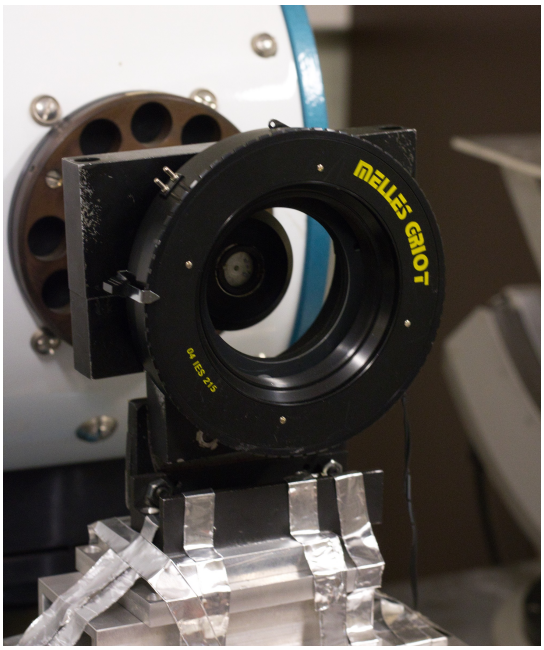

FIGURE 4.27: shutter used for the characterization of the prototypes

A motorized shutter, show in Figure 4.27, is placed between the blackbody and the focal plane of the collimator. This shutter is closed before most image acquisitions to take a dark image used to correct the non uniformity and offset of the detector. This also removes the effect of straylight, as the shutter only removes the flux coming from the collimator so that the difference between the dark and the image is only due to the light passing through the collimator.

Rotation stage and motorized cradle

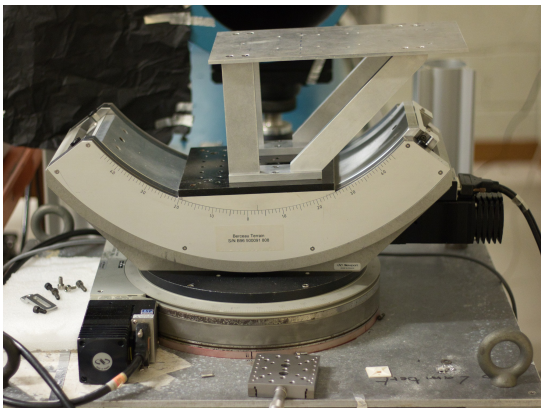

FIGURE 4.28: Rotation scale and cradle used for the characterization of the prototypes

As the collimator is fixed onto the optical bench, the study of the optical quality of the prototypes off axis can only be done by a rotation of the instrument. To achieve this, the instrument under test is placed on two mechanical scales: one rotation scale to perform rotation around the vertical axis, and one motorized cradle for the rotation around a horizontal axis. The rotation scale is a Newport RTM350PE using a stepper motor with a 0.01 degrees accuracy and a 0.002 degrees repeatability. The rotation scale and the cradle are both visible in the Figure 4.28, with the cradle being mounted on top of the rotation scale. This causes an axis composition that must be taken into account to convert any angular position of the object at infinity into rotations of each scale as shown below.

To convert the angular position into rotations of the scales, there are two phenomena that must be taken into account. First, the axis composition previously mentioned. But an alignment of the rotation axes, the collimator optical axis and the instrument optical axis must also be performed. However, in this setup there is no possibility to measure the direction of the collimator axis or the instrument optical axis. We rely on the previously made alignment of the rotation scales and the collimator and suppose the error negligible. We suppose an orthogonality of the cradle rotation axis and the rotation scale axis. Finally we also suppose that the prototype optical axis is placed precisely enough regarding the threaded holes. All those errors might

induce a small error in the alignment that is not considered, but remains inferior to one degree, as an alignment can be performed with such accuracy using the detector (details on the description of the plane blackbody).

For the axis composition, as the cradle is mounted on top of the rotation scale, the rotation of the cradle has an influence not only on the vertical angular position of the object but also on the horizontal angular position. Optical design softwares generally do not assume any composition, and thus the angular position (θ_X, θ_Y) of any source point is defined as follows:

$$\begin{aligned} tan(\theta_X) &= \frac{-l}{-n} \\ tan(\theta_Y) &= \frac{m}{-n} \\ l^2 + m^2 + n^2 &= 1 \end{aligned} \tag{4.1}$$

with l,m,n the x,y and z direction cosines in the optical design software reference frame. We define a frame of reference R_0 in the laboratory, with Y being the vertical axis pointing upwards, Z is the horizontal axis aligned with the collimator optical axis and pointing from the alpha-Z towards the collimator and X is the horizontal axis so that R_0 is an orthonormal reference frame. The negative values are due to the difference between the optical design reference frame and the reference frame of the bench, with X and Z pointing in different ways. We need to calculate the command for the scale and the cradle needed for any angular position. With the previously made assumptions, when both commands are at zero, the prototype line of sight is aligned with the optical axis of the collimator, and the PSF should appear at the center of the detector. Any command angle α_S induces a R_Y rotation around the Y axis, performed by the motorized rotation scale :

$$R_Y = \begin{pmatrix} cos(\alpha_S) & 0 & sin(\alpha_S) \\ 0 & 1 & 0 \\ -sin(\alpha_S) & 0 & cos(\alpha_S) \end{pmatrix} \tag{4.2}$$

Command angle α_C induces a R_X rotation around the local X axis, performed by the cradle.

$$R_X = \begin{pmatrix} 1 & 0 & 0 \\ 0 & cos(\alpha_C) & -sin(\alpha_C) \\ 0 & sin(\alpha_C) & cos(\alpha_C) \end{pmatrix} \tag{4.3}$$

The line of sight of the device is now given by:

$$R = R_X \cdot R_Y \cdot \begin{pmatrix} 0 \\ 0 \\ 1 \end{pmatrix} = \begin{pmatrix} sin(\alpha_S) \\ -cos(\alpha_S)sin(\alpha_C) \\ cos(\alpha_S)cos(\alpha_C) \end{pmatrix} \tag{4.4}$$

if we equalize the equations 4.1 and 4.4:

$$\begin{aligned} -tan(\theta_Y) &= \frac{m}{n} = -tan(\alpha_C) \\ tan(\theta_X) &= \frac{l}{n} = \frac{tan(\alpha_S)}{cos(\alpha_C)} \end{aligned} \tag{4.5}$$

$$\begin{aligned} \alpha_C &= \theta_Y \\ \alpha_S &= -arctan(tan(\theta_X) \times cos(\theta_Y)) \end{aligned} \tag{4.6}$$

Using these equations, we can convert angles from the optical design software into command angles for the scale and cradle. This allows to compare design specifications and analysis to the real prototype characteristics.

LWIR camera

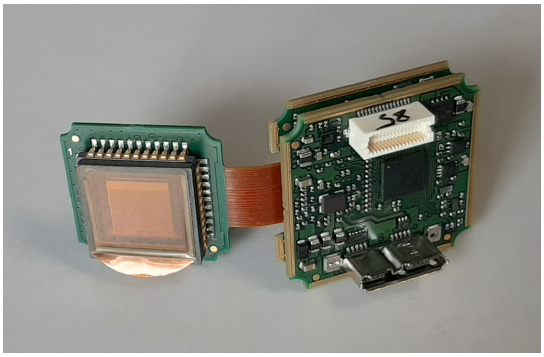

FIGURE 4.29: Camera used for the characterization of the prototypes

The LWIR camera is a camera IRLugX640 from DeviceAlab. This camera uses an atto 640 microbolometer from Lynred. This is a 12μm pitch VGA sensor with up to 60Hz framerate and a 60mK noise equivalent temperature difference (NETD) at F/1, 300K and a 30Hz framerate. Microbolometers differ from quantum detectors in the fact that they detect variations of the sensible area using the correlation between the temperature of a bolometer and its resistance. As the incident flux heats the bolometer, it can be measured. This incoming flux is directly linked to the radiance of the scene inside the solid angle (or iFOV) seen by any pixel. A thorough description of how to model a microbolometer can be seen in article [162] and such model has been used to calibrate the whole instrument, composed by this camera and the αZ imaging optical system.

Plane blackbody

A plane blackbody has been used to laterally align the detector in the focal plane of the prototype by centering the obscuration. It also has been used as a lambertian source to perform the shutterless calibration of the camera.

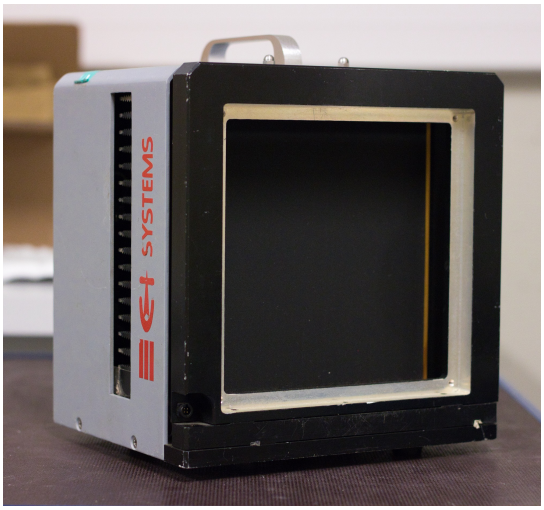

FIGURE 4.30: Plane blackbody used for the characterization of the prototypes

Visible Detector

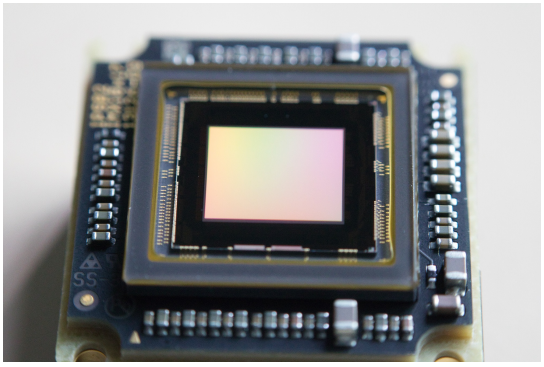

FIGURE 4.31: visible camera used for the characterization of the prototypes

The visible camera is an Allied Vision alvium 1800U-507M-BB. The camera is bare-board as the prototypes have a very low mechanical back focus. This camera uses a SONY IMX264 CMOS sensor with 3.45μm square pixels. The array has 2464 by 2056 pixels, which gives a 8.5 by 7.1mm sensible surface, which is slightly larger that the 7.7 by 5.8mm size of the LWIR detector. This camera has been used for a characterization in the visible spectrum.

4.4.2 First images

Acceptance tests

As the prototype was available before the detectors, first acceptance tests had to be made using another equipment. The goal of those test were to have a subjective evaluation of the first prototype before being able to perform the

characterization itself. As the mechanical back focal length of the Alpha-Z prototype, defined by the distance between the closest mechanical part of the system and its focal plane, is very short (about 2.5mm) no detector was available for this test. The images have been made by reimaging the focal plane onto the detector of a CANON EOS 760D with a CANON 50mm F/1.8 lens, mounted in reverse. The configuration is described in figure 4.32 and shown in figure 4.33. Mounting an objective in reverse is a common way to perform macro photography without a macro lens [163]. To reverse the lens, an inversion ring is used. It can be screwed onto the objective using the thread normally used for filters, and has the same interface as an objective on the other side. An image of the lens mounted in reverse on the camera is shown in figure 4.34.This allows to image objects closer to the lens than in the usual configuration. This has an impact on optical quality, but was enough for a quick evaluation of the lens.

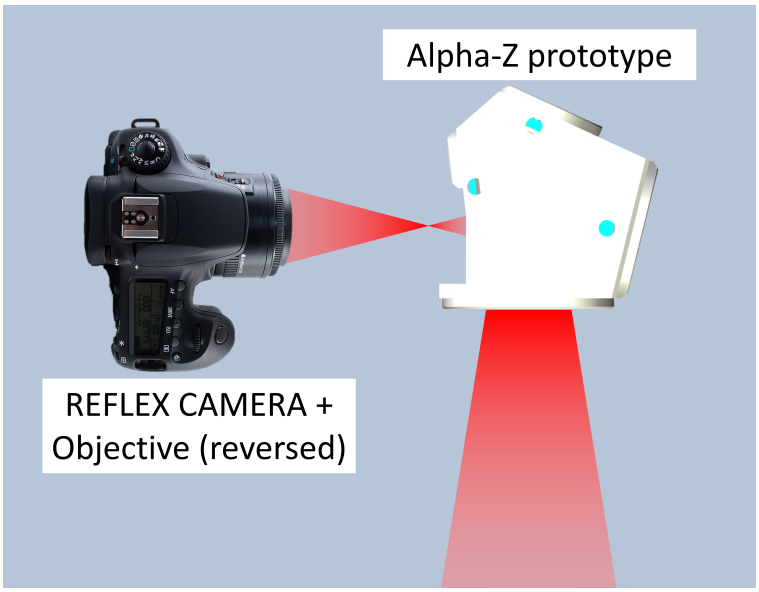

FIGURE 4.32: Configuration for the acceptance test

Figures 4.35 and 4.36 are images taken with this setup. The metallic plate visible on the right side of each picture is the back side of the second mirror of the Alpha-Z. A visual inspection of those images shows no visible diffusion of the light, which is a first good sign for multi spectral band imaging. There is a large asymmetrical distortion as expected.

Infrared images

By placing the microbolometer in the focal plane of the imaging device, we can capture images in the thermal infrared spectrum. However, raw images are very noisy. Each pixel in the array has an unique response, that is supposedly linear. Each pixel has an unique gain and offset. A first correction of the image can be done by a one point non uniformity (NUC), that corrects only the offset for each pixel. This correction is done by measuring first a

FIGURE 4.33: Picture of the described configuration

FIGURE 4.34: Close up of the reversed lens

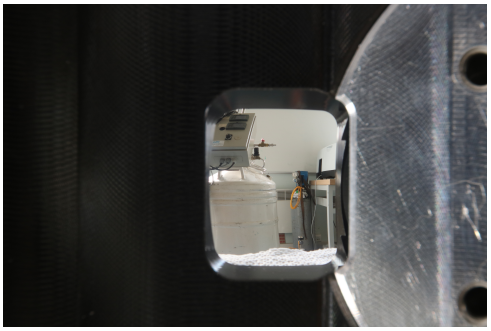

FIGURE 4.35: First image from the Alpha-Z

FIGURE 4.36: Another example image made using the Alpha-Z

uniform planar source. A planar blackbody is ideal for this correction, but for a first image, a cardboard at room temperature can be used. Figure 4.37 shows an example picture of what can be obtained with this method.

FIGURE 4.37: Image obtained using the microbolometer with a 1pt NUC. Mean of 20 images at 30 fps

4.4.3 Spot Scan

To measure the optical quality of the prototype, we chose to measure the point spread function. This allows to know the optical quality of the system, without being able to measure precisely the aberrations of the optical design. This method has benefits, as it directly measures the features of the whole device, including the camera. However, this method also has the major drawback of not measuring the detailed wavefront generated by the system. Such wavefront could be measured using interferometry, preferably in the infrared domain but could also be performed using visible wavelength, which is the case for most commercial interferometers, if we neglect the potentially diffusive effect of the optical surfaces on the system. The lack of available interferometer at ONERA at the time of our experiments and the very low F number, implying the use of a reference mirror with a large diameter respectively to its radius of curvature made us abandon this measurement, but this is a measurement that I recommend to perform in a near future. An important distinction must be made here, as the measurement of the wavefront generated by the optical system as a whole using interferometry is easier than measuring the shapes of the surfaces

with the same method. Indeed, the overall aberration generated by the design should be low per design as the expected wavefront is so close to a sphere that the resulting point spread function is diffraction limited in the LWIR spectrum. In that sense, the wavefront error should be a fraction of lambda in the LWIR domain, so at most a few wavelengths in the visible spectrum, which could be measured with phase shifting interferometry. The measure of the surfaces using classical interferometry is harder as the surfaces sometimes have departures from the best sphere up to a few hundreds of micrometers, which would lead to fringes too close to each other to be separated if the mirrors were to be measured alone.

The configuration used is the one described in subsection 4.2.2. To measure the PSF a detector is placed in the focal plane of the imaging device. As the system has been designed to be diffraction limited for the LWIR spectrum, the chosen camera is the one working in the infrared. To acquire a PSF, the shutter is closed and a first image is taken. Then an image is acquired with the shutter open. The difference between both images is then only due to the added energy coming on the detector from the point source at the focal plane of the collimator. Figure 4.38 shows the PSF for the center field.

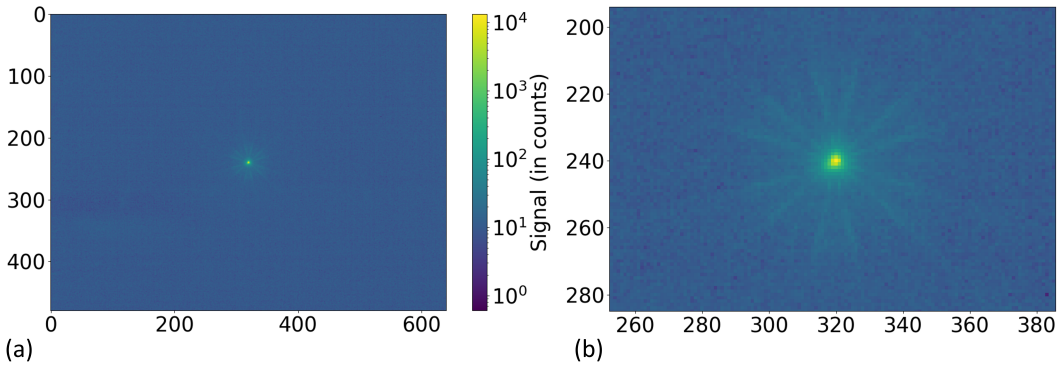

FIGURE 4.38: Example of a PSF obtained using the microbolometer, pixel pitch = 12µm. (a): full detector. (b): close-up of the PSF (same colorbar)

However, the detector can only sample spatial frequencies up to the Nyquist frequency:

$$f_N = 1/(2p) \tag{4.7}$$

with p the pixel pitch of the detector. Here $p = 12\mu m$ so $f_N = 41.7cy/mm$ However, the optical cutoff frequency of the alpha-Z is $66.7cy/mm$. A simple picture of the PSF is not enough to measure the whole MTF of the imaging system. Moreover, even with the use of a shutter, the measured PSF is sampled over several pixels that do not share the same gain. This adds noise on the acquired PSF and further decreases the accuracy of the measure.

To have a reliable PSF measurement, the PSF has been sampled using the spot scan method. This method allows a PSF sampled with a finer pitch than the pixel pitch and using only one pixel, removing the uncertainty due to the use of several pixels. First, an image of the PSF is taken and its size is measured to evaluate the size of the windows to sample (in pixels). Then a

pixel is chosen according to the field angle for which the PSF is needed. The system is then aligned so that the energy on the chosen pixel is maximal. The spot is then moved to the upper left side of the window. This places the pixel of interest on the bottom right of the PSF, giving a sample value for this part of the PSF, as show in figure 4.39. Then, the PSF is moved right by a fraction of one pixel. The pixel can now sample the PSF on a new point next to the previous one, as shown in figure 4.40. The whole PSF is then sampled in a zigzag fashion (see figure 4.41).

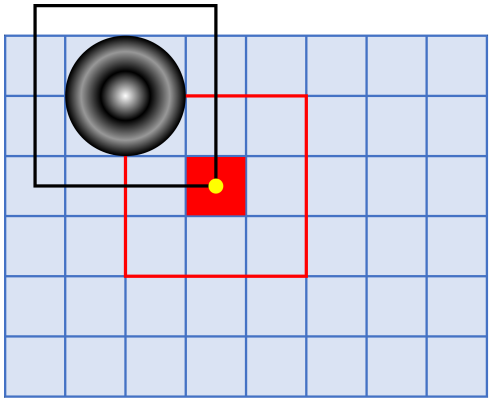

FIGURE 4.39: First sample of the PSF

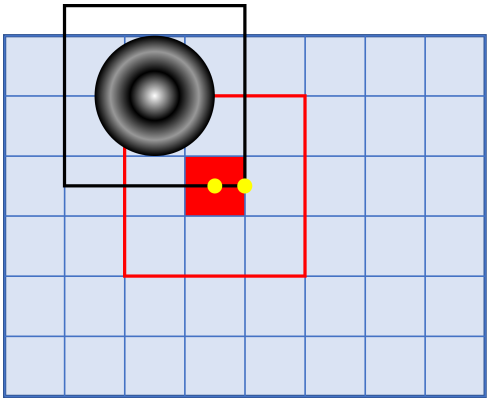

FIGURE 4.40: Second sample of the PSF (oversample factor: 2)

The end result is an image of the PSF with a sample pitch that is a fraction of the pixel pitch as shown in figure 4.42, and with all samples taken using a single pixel, removing any need to know the gain of each pixel, see Figure 4.43.

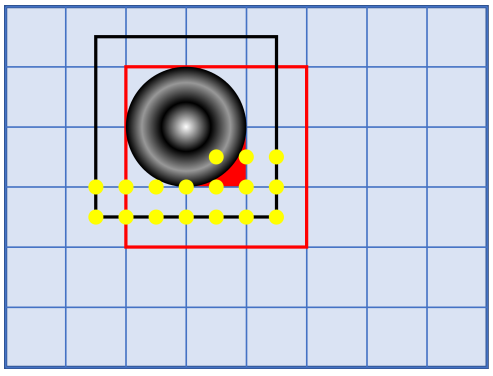

FIGURE 4.41: PSF partially sampled using the chosen pixel

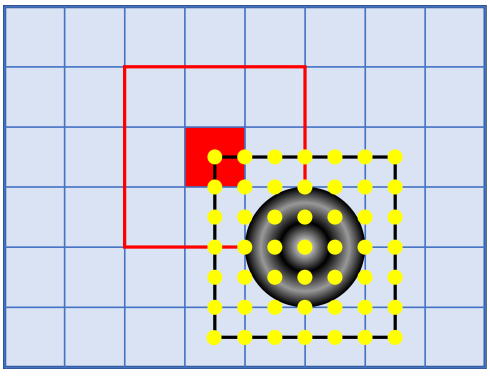

FIGURE 4.42: PSF fully sampled

For our study, an oversample by a factor of 2 is sufficient, but to ensure a sufficient number of samples per PSF, we chose a factor of 3.

As the wavefront can't be retrieved from the PSF, the aberrations cannot be measured using this technique. However, the PSF and its shape is enough

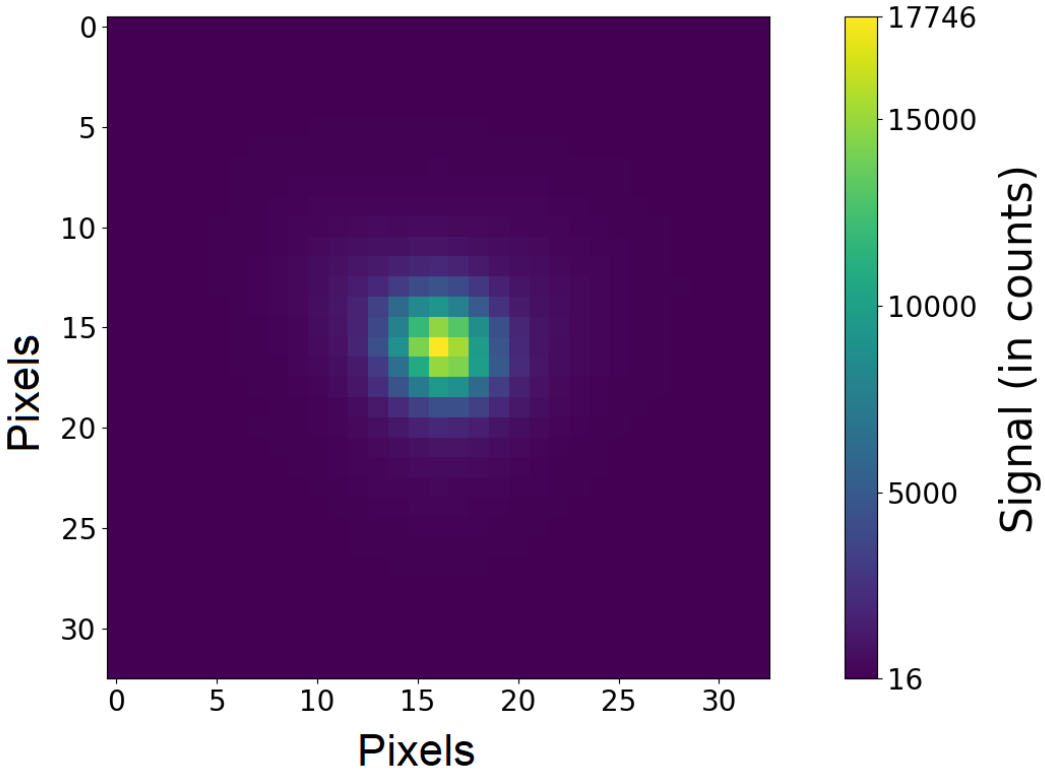

FIGURE 4.43: PSF of the prototype for the central field. The pixels displayed here are the measured samples, which are one third of a physical pixel on the detector.

to guess the dominant third order aberration if there is one, and to assess most criteria of quality of an optical system [4].

To evaluate if the system is of sufficient quality, an evaluation of the MTF has been performed. The overall MTF measured is due to the source, the optical system and the pixel, as described in equation 4.8. The effect of the source size can be translated in an effective MTF that deteriorates the measured MTF even though it is not a limitation of any of the optical devices.

$$MTF_{measured} = MTF_{source} \times MTFcollimator \times MTF_{\alpha Z} \times MTF_{pixel} \tag{4.8}$$

The effect of the source on the image spot is a convolution of the PSF with a circle of diameter $d \times f'/f_c$ with f' the focal length of the αZ prototype, f_c the focal length of the collimator and d the diameter of the source pinhole. The equivalent MTF from the source is thus the fourier transform of a disk of size $d \times f'/f_c$, given in equation 4.9.

$$MTF_{source}(\nu_\perp) == \left| 2\frac{J_1(2\pi d\nu_\perp)}{2\pi d\nu_\perp} \right| \tag{4.9}$$

with $\nu_\perp = \nu_x^2 + \nu_y^2$

The MTF of the pixel is supposed to be close to a cardinal sinus described in equation 4.10 where a is the side size of the square.

$$MTF_{pixel}\nu_x, \nu_y = sinc(a\nu_x)sinc(a\nu_y) \tag{4.10}$$

The geometrical aberrations of the collimator can lower the overall MTF. However, the collimator is diffraction limited in visible spectrum, so its geometrical aberrations can be neglected in our setup. The last contributor is the MTF of the αZ, and the upper bound for any given wavelength is the diffraction limit as given in equation 4.11.

$$MTF_{mono}(\nu_\perp, \lambda) = \frac{2}{\pi}\left(arccos(N\lambda\nu_\perp) - N_c\lambda\nu_\perp\sqrt{1-(N\lambda\nu_\perp)^2} \right) \tag{4.11}$$

To take into account that the detector's response is dependent on the energetic radiance of the object, we must take into account the polychromatic aspect of our measurement. The polychromatic MTF is calculated as given in equation 4.12:

$$MTF_{\alpha Z} < MTF_{poly}(\nu_\perp) = \frac{\int_{8\mu m}^{14\mu m} MTF_{mono}(\nu_\perp, \lambda)S_e(\lambda)d\lambda}{\int_{8\mu m}^{14\mu m} S_e(\lambda)d\lambda} \tag{4.12}$$

With $S_e(\lambda)$ the spectral sensitivity of the detector.

This upper bound for the MTF is then used as a reference for the measurement of the MTF, to evaluate if the system is diffraction limited. Figures 4.45, 4.47 and 4.49 present the PSF of the system for several object

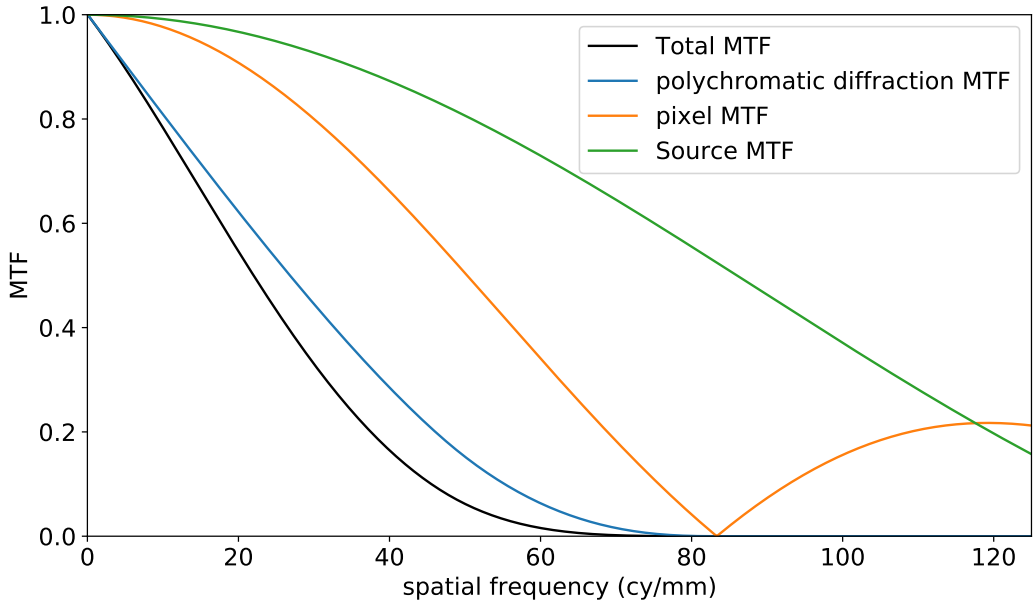

FIGURE 4.44: Calculation of the upper bound for the measured MTF

fields. Figures 4.46, 4.48 and 4.50 present the associated MTF for each one of those PSF. In some of those figures, the MTF is sometimes larger than the diffraction limit. This effect can be due to several factors, such as an uncertainty in the diameter of the source, a different response of the pixel such as a lower fill factor or a different MTF than the usual hypothesis. It can also be due to a F number slightly different to 1.5 in the edges of the field of view.

As shown in figure 4.46, the system is diffraction limited on axis.

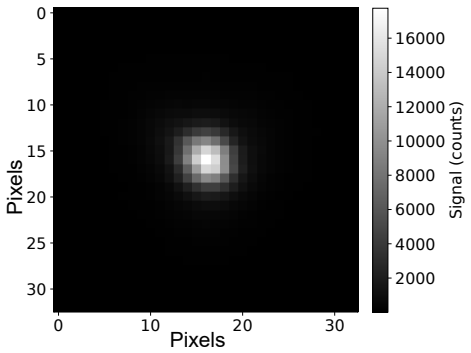

FIGURE 4.45: PSF sampled by spot scan for the center field

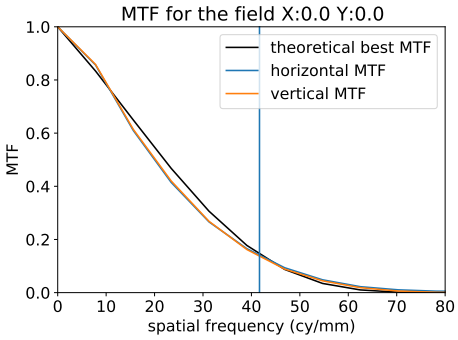

FIGURE 4.46: MTF measured from the PSF in figure 4.45

In figure 4.48, the MTF is only slightly reduced for large field of views over the X axis.

In figure 4.50, the MTF is largely reduced in one direction. By looking at the figure 4.49, we can deduce the presence of horizontal astigmatism for

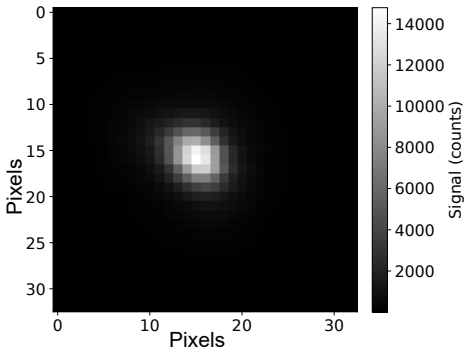

FIGURE 4.47: PSF sampled by spot scan for a field of 10.5 degrees over the X axis

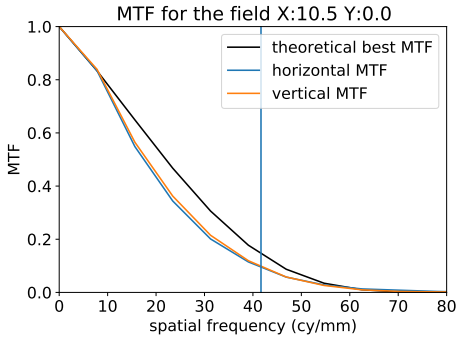

FIGURE 4.48: MTF measured from the PSF in figure 4.47

large Y fields. As in article from Fuerschbach et al. [158], we attempted to identify an alignment error that could lead to such astigmatism in the focal plane. No simple alignment error could be found to generate such aberrations. Presently, it is not possible to determine if the aberrations observed is due to alignment or mirror shape errors.

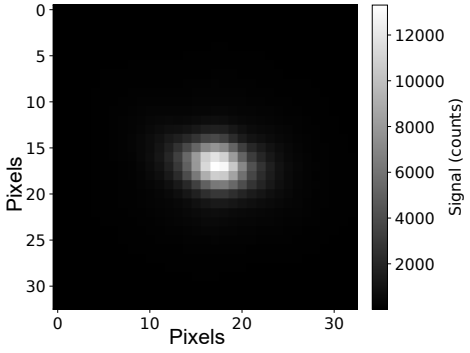

FIGURE 4.49: PSF sampled by spot scan for a field of -8 degrees over the Y axis

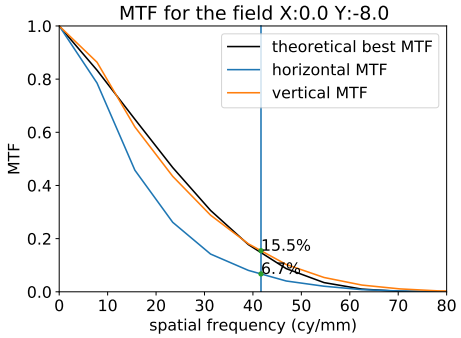

FIGURE 4.50: MTF measured from the PSF in figure 4.49

As a second system has been manufactured with different errors, several tests could be performed to determine the source of the aberrations. First, some wavefront analysis could lead to better understanding of the aberrations. This is hard to perform as the system has a very large aperture, which needs measurement instruments with also large apertures. A second experiment could be to remove and mount again the mirrors to see if the aligment is repeatable. If so, the mirrors from both designs could be switched to see if the aberrations are mostly correlated to the mirrors used in the design or to the mount used. It is also possible that it is a combination of both and then a measurement of each mirror could be mandatory to conclude.

4.4.4 Distortion

The system presents distortion, as expected from the design process. To test the distortion of the design, a grid of points has been imaged. The whole field of view is sampled into an evenly spaced grid. For each object angle, an image is taken with a one point non uniformity correction and the centroid of the PSF is computed. The centroid is only computed on a small square around the pixel giving the maximum signal in the picture, after looking for bad pixels and ignoring them to ensure that the square is adequatly placed. This methods limits the impact of the noise in the image on the results. The maximal value of each image is also stored. The overall maximum useful signal S_{max} value is found and for each image i, the maximal value of the image $S_{max,i}$ is compared to S_{max} so that any image where $S_{max,i} < S_{max}/10$ is ignored. This filters out the images where there is no visible PSF, whether it is due to an error of the shutter that did not open or due to the fact that the field angle is too large and the PSF is imaged outside of the detector. This grid is then compared to a uniformly spaced grid to measure the focal length and distortion as detailed in Chapter 2. The results are given in figure 4.51.

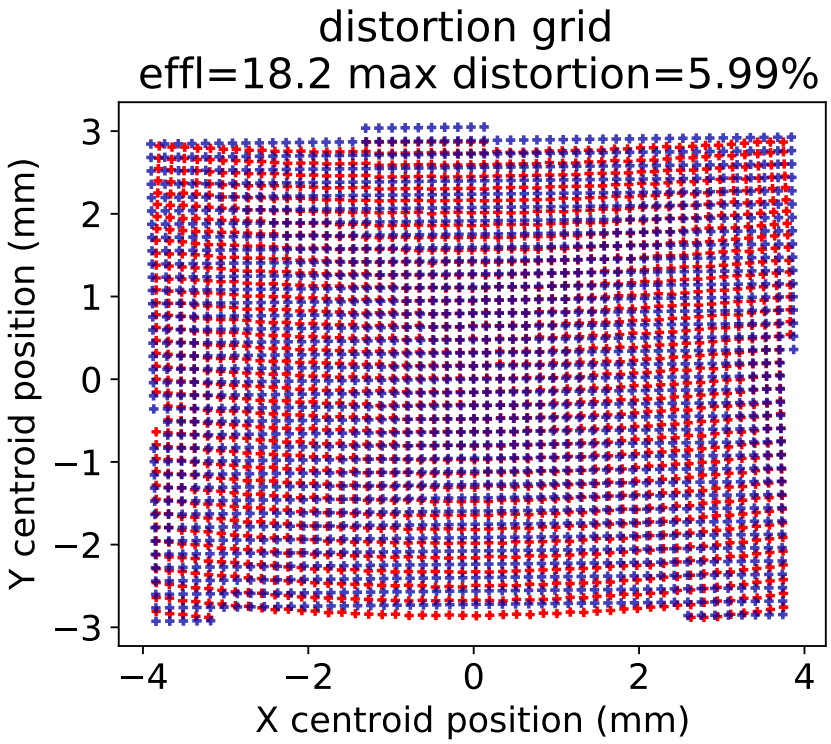

FIGURE 4.51: Measure of the distortion and focal length of the αZ prototype, by comparing the distortion grid with a reference grid with no distortion

With a focal length of 18.22mm, and a distortion of 6%, the results are consistent with the design properties. A second verification is made by comparing directly the measured grid to the theoretical grid made in subsection 4.2.2. As the system might have a clocking alignment error, i.e.

a rotation error around the optical axis, the clocking rotation between both grids is fitted using a least square sum minimization. The resulting image is shown in figure 4.52.

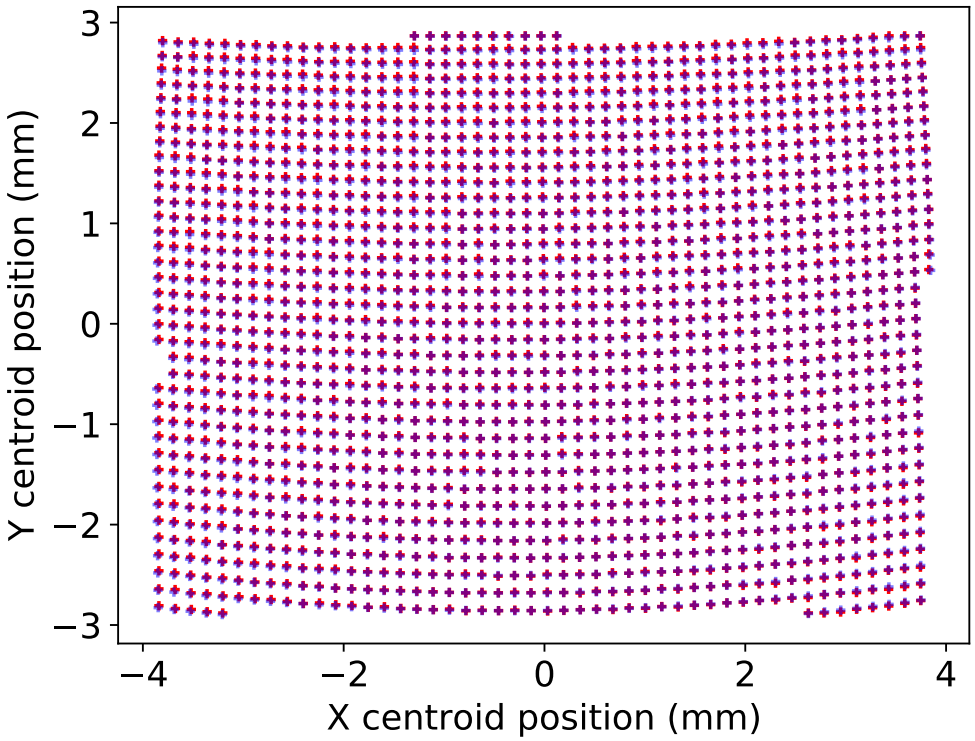

FIGURE 4.52: Comparison between the measured grid distortion and the theoretical one.

The measured distortion grid is identical to the design grid, meaning that the magnification and distortion of the prototype are exactly as designed. The distortion of the design is fairly high but can be corrected with image processing.

4.4.5 Straylight

As detailed in the section 4.2, the configuration has been developed to create a design that has a large field of view using only freeform mirrors while removing any specular straylight. Nevertheless, the prototype presents a visible straylight path that creates a straylight spot on the detector for a source located at about 25 degrees Y. The spot is visible in figure 4.53.

The figure shows a straylight spot that was not anticipated in the design process. We can deduce that this straylight is due to a diffuse or specular straylight on the mechanic of the TMA. The shape of the spot is typical of those given by a quasi specular reflection on a mechanical part. The mechanical part has been added into the non sequential design system. To account for quasi specular reflexions hitting the detector, a source has been

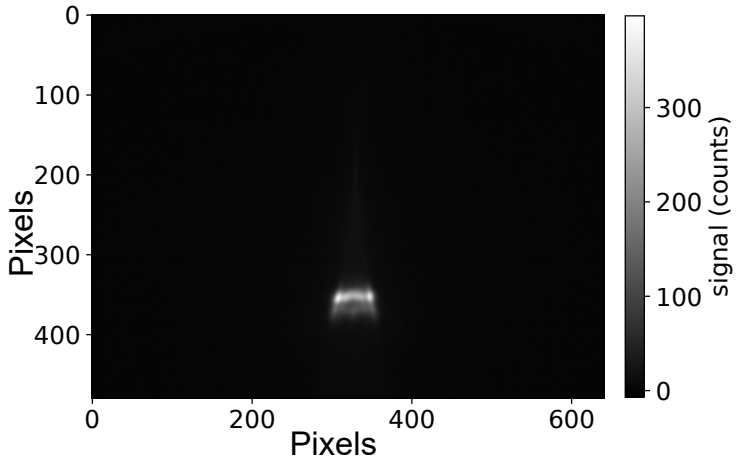

FIGURE 4.53: Straylight spot generated by a collimated source at 25 degrees. Pixels are the pixels of the infrared detector.

placed onto the detector and an ideal coating has been applied to the whole mechanical structure. This coating induces a scattering and the BRDF has been chosen to be a narrow gaussian distribution to be quasi specular while still scattering some of the incident energy. However, this definition only works if the incidence angle of the ray is close to 90 degrees, and that multiple reflections onto the mechanical structure should be negligible due to the absorption and scattering of the surface. When we trace only rays that are scattered once with an incidence angle larger than 60 degrees and leaving the system, we indeed observe a straylight path with an incidence in the object space of about 25 degrees regarding the optical axis. If we trace rays from a source located at infinity at a 25 degrees angle, we observe the straylight path shown in figure 4.54.

The straylight path identified is the path M2-M1-M2-M3 followed by a quasi specular reflection on the mechanical structure. A ray tracing simulation has been made to ensure that this is the problematic straylight route. A collimated beam with a 25 degrees angle has been simulated and the resulting image on the detector is given in figure 4.55.

The figure shows a similar pattern, even with an approximative scattering model, ensuring that the straylight path has been correctly identified. While this path was difficult to anticipate, it is also a rather simple straylight path to fix by adding a step design on the structure close to the detector to avoid such a specular reflection.

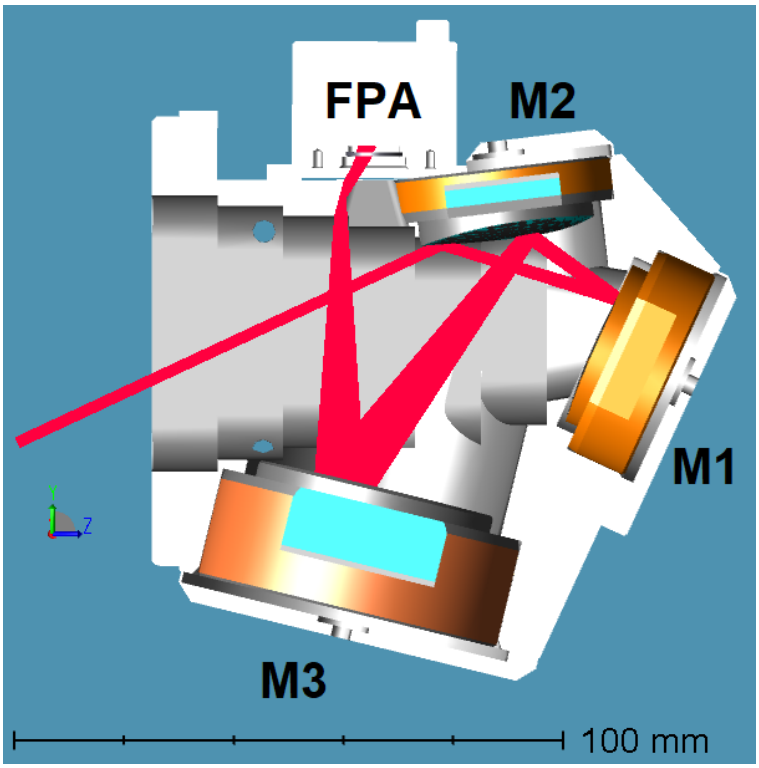

FIGURE 4.54: Straylight path of the αZ design.

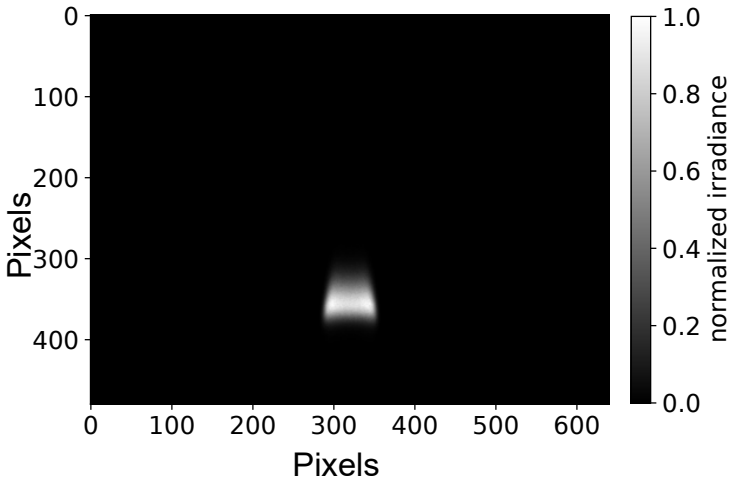

FIGURE 4.55: Simulated image of straylight from a source located at a 25 degrees angle. Image is the normalized irradiance on the detector.

4.4.6 Calibration

The purpose of this design is to create thermal infrared cameras using only mirrors, paving the way for low cost LWIR imagery. Indeed, if such designs can be molded and mounted into plastic or 3D printed casing, it would allow an industrial production of catoptric systems that are not dependant on expensive materials. The calibration of such instruments is a critical part in this process for a convincing demonstrator. First the goal is to create cameras for detection, such as security cameras or pedestrian detection for self driving vehicles as an example. For this purpose, the visual quality of the image and contrast are most important.

1 point NUC

As described in article [162] the signal of each pixel is directly linked to the temperature of the bolometer membrane and the temperature difference onto the detector is directly proportional to the radiance of the scene inside the iFOV of the pixel. For our equation, the output signal S of a pixel can be then written as:

$$S = S_0 + g\phi_e \tag{4.13}$$

with S_0 and g being respectively the offset and the gain of the pixel and ϕ_e the energetic radiance of the source. The equation uses the energetic radiance as bolometers are sensitive to the total energy received and not the number of collected electrons.

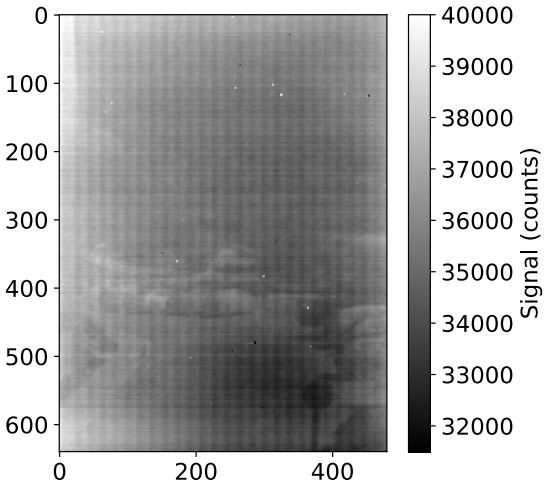

FIGURE 4.56: raw image taken with the αZ prototype

As each pixel has an unique offset S_0 and gain g, the useful signal is not clearly visible in the raw image and not usable in this form as seen in figure 4.56. The simplest correction is the one point non uniformity correction. A reference image is taken, usually using a shutter that performs as a blackbody

that emits a uniform radiance. By subtracting the reference signal S_{ref}, the offset of each pixel is removed in its output signal S_{out}.

$$S_{ref} = S_0 + g\phi_{e,ref} \tag{4.14}$$

$$S_{out} = S_i - S_{ref} = g \times (\phi_e - \phi_{e,ref}) \tag{4.15}$$

As shown in equation 4.15, the output signal is still dependent on the pixel gain, which is unique for each pixel. This still can be used to generate visually appealing images such as figure 4.57. This variation will be particularly visible for a large radiance variation of the scene. But most importantly only one measure, even made with a lambertian calibrated blackbody, is not enough to retrieve the temperature of the scene. To measure the gain of each pixel and convert the signal to a temperature measurement a two point correction is necessary.

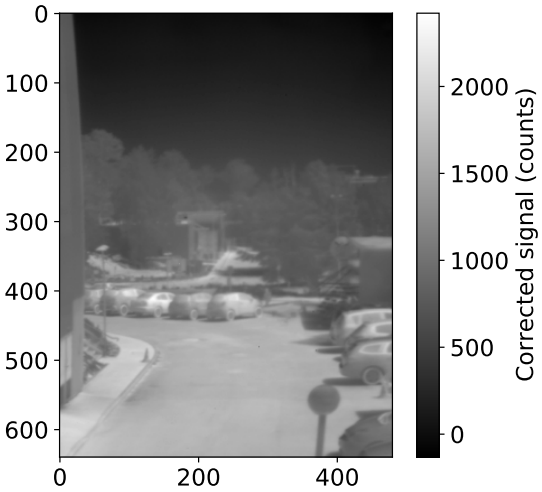

FIGURE 4.57: image taken with the αZ prototype and corrected with a 1 point non uniformity correction

2 points NUC

A 2 point NUC is made using two calibrated lambertian blackbodies at different temperatures. Two images are taken, S_{T1} and S_{T2}. Using these two equations and if the detector behavior is really linear, the gain and offset of each detector can be calculated. First, the radiance of each blackbody at any given temperature T can be calculated using an integration of Planck's law over the spectrum of the camera:

$$\phi_e(T) = \int_8^{14} \frac{2hc^2}{\lambda^5} \frac{1}{e^{hc/(\lambda k_B T)} - 1} \, \mathrm{d}\lambda \tag{4.16}$$

with h the Planck constant, k_B the Boltzmann constant, c the speed of light and λ the wavelength in micrometers. From there, the radiance of each blackbody can be calculated, allowing to measure the offset and gain for each pixel.

$$g = \frac{S_{T1} - S_{T2}}{\phi_e(T1) - \phi_e(T2)} \tag{4.17}$$

$$S_0 = (S_{T1} + S_{T2}) - g(\phi_e(T1) + \phi_e(T2)) \tag{4.18}$$

So for each pixel:

$$\phi_e = \frac{S - S_0}{g} \tag{4.19}$$

The function $\phi_e(T)$ is strictly increasing, and therefore injective. It means that for any radiance generated by the blackbody in the spectral domain of interest there is a unique temperature associated. So for any measure, we can deduce the source radiance and therefore an estimated temperature of the source by reverting the function and assuming that the source behaves like a blackbody.

Using this method, two matrices g and S_0 are generated, storing the correction values for each pixel, and the same image as before treated with a two point NUC is shown in figure 4.58.

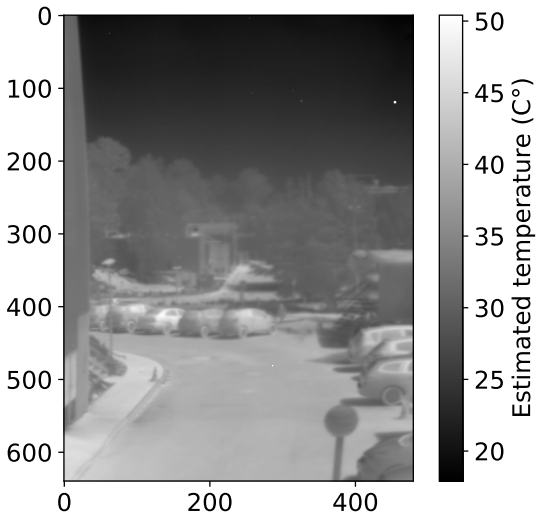

FIGURE 4.58: image taken with the αZ prototype and corrected with a 2 point non uniformity correction

This technique allows for a very good thermal measurement, however, it implies a regular calibration with two well calibrated blackbodies. In spatial applications, one of those blackbodies can be the deep space, or cross calibration with another device can be used. However, the calibration must be made frequently, as there are many additionnal sources of error with a low frequency variation. Most of these errors come from the temperature detector

itself, as it has a direct impact on the output signal, and from the varying temperature of the structure around the detector. Additional measurements can be made to correct the signal without frequent recalibrations. This calibration is called a shutterless calibration.

Shutterless calibration

A shutterless calibration can be done using the αZ prototype. To perform this calibration, the system is put in a climatic chamber and measurement are made on a blackbody while varying the parameters such as the temperature of the detector and the temperature of the mechanical part of the system that can emit in the LWIR domain. In this study, only the detector temperature can be accessed, so the measurements where performed with a stabilized detector temperature, assuming that the temperature of the mechanic would be stabilized too. To modify the detector and mechanics temperature, the air temperature inside the climatic chamber can be controlled, and measurements are made for varying blackbodies temperatures for each chamber temperature.

As the signal is supposedly proportional to the temperature of the detector [162] it can be assumed that a corrected model for our analysis is:

$$S = S_0 + \alpha\phi_e + \beta T_{det} \tag{4.20}$$

With T_{det} the temperature of the detector. If the detector uses blind pixels to correct for this effect, the coefficient β could be very low. The matrices S_0, α and β are calculated by performing a least square fitting of the models on all images taken in the climatic chamber. From this equation we can deduce the radiance of the source and compute its estimated blackbody temperature. To estimate the quality of the correction, it is applied to the images made in front of the blackbodies in the climatic chamber. The resulting images are shown in figures 4.59 and 4.60.

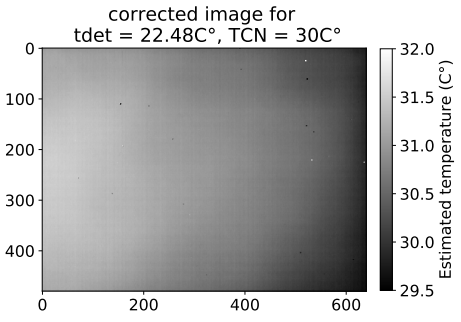

FIGURE 4.59: Calibration image at mid temperature range corrected with the shutterless protocol.

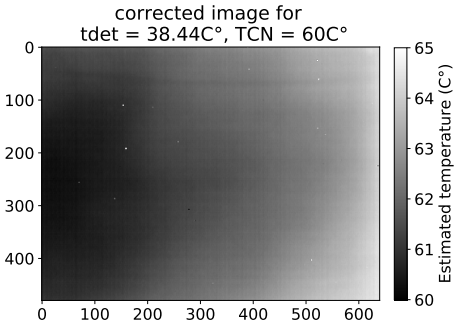

FIGURE 4.60: Calibration image at a high temperature range corrected with the shutterless protocol.

The correction is not satisfying and show significant deviation from our model, probably due to the effect of the structure temperature. To show this deviation, the difference between the signal of one pixel (dots) and the fitted model (red surface) is shown in figure 4.61. The surface show visible quadratic effects and coupled effect.

The model is updated to take into account non linear and coupled effects. The model is detailed in equation 4.21.

$$S = \sum_{i=0}^{n} \sum_{j=0}^{n-i} \alpha_{i,j} \, \phi_e^i \, T_{det}^j \tag{4.21}$$

The correction parameters is again fitted to the data, and the new model fits better with the data than the previous one as visible with the green surface in figure 4.61. It implies that the shutterless calibration will be satisfying in conditions that are close to the calibration conditions in terms. In practical, we expect inaccuracies due to the structure temperature that was not included in the calibration.

Adding a quadratic term in the model for ϕ_e implies that getting the source radiance from the signal now mathematically admits two solutions. However, only one is inside the calibration range at any moment, allowing to automatically detect the correct solution.

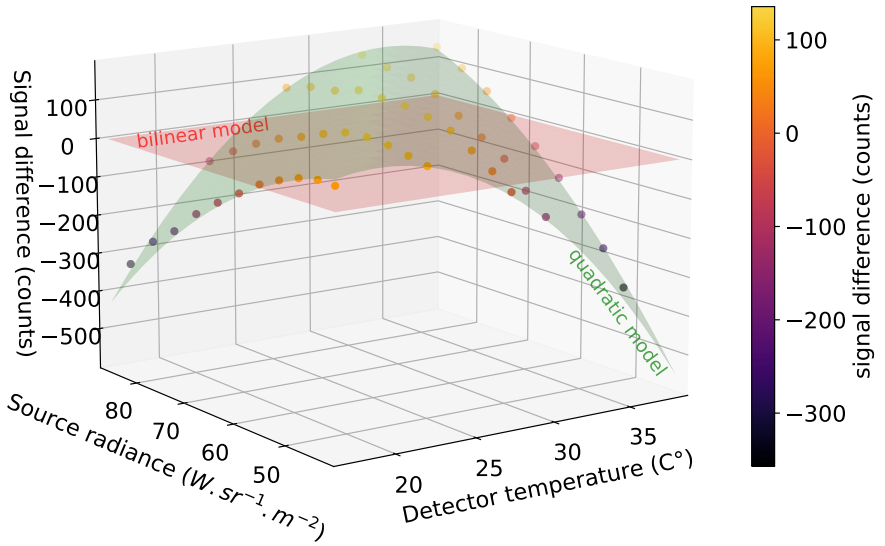

FIGURE 4.61: Signal difference of the pixel signal (dots) and the quadratic model (green) with respect to the bilinear model (red)

As shown in the figures 4.62 and 4.63 the correction is valid on the calibration data.

However, as shown in figure 4.64, the correction for this measure has a bias of about 2 to 3 degrees with respect to the two points non uniformity correction. On the temperatures used in the two point calibration, this bias is still apparent, showing that our shutterless calibration is still not precise enough for an absolute measurement, probably due to variables not

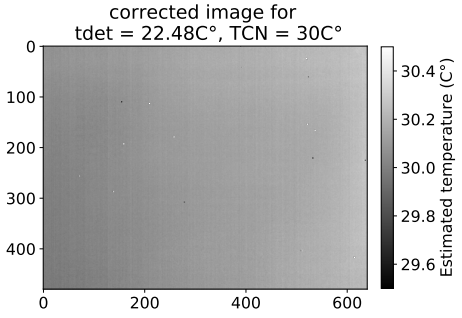

FIGURE 4.62: Calibration image at mid temperature range corrected with the updated shutterless model.

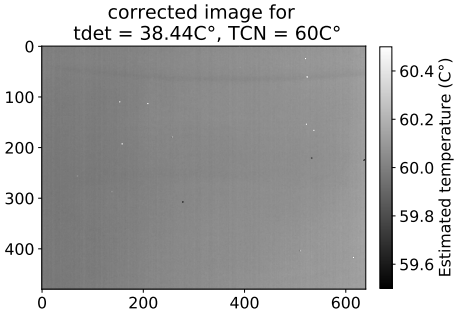

FIGURE 4.63: Calibration image at a high temperature range corrected with the updated shutterless model.

studied in the climatic chamber. This shows the complexity of the shutterless calibration where all contributors must be tested during the calibration process and measured on the field.

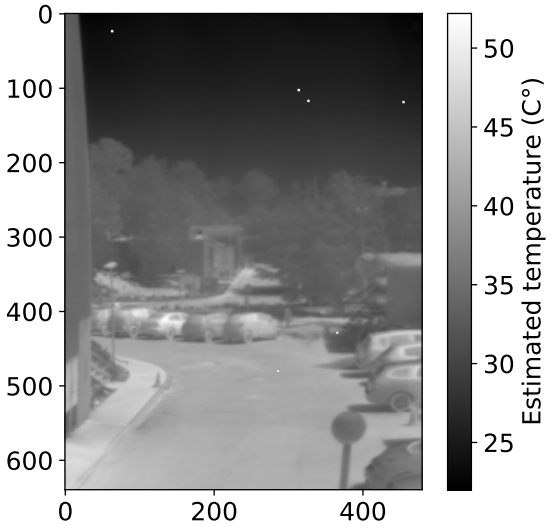

FIGURE 4.64: image taken with the αZ prototype and corrected with the shutterless calibration

4.4.7 Noise Equivalent Temperature Detection

The Noise Equivalent Temperature Detection (NETD) is defined as the smallest temperature variation that induces a signal change equal to the noise, i.e. a SNR of 1. This represent the smallest temperature that can be

detected with the instrument. The NETD of each pixel p is defined as:

$$NETD_p = \frac{\sigma_S}{\frac{\Delta_S}{\Delta_{T_{CN}}}} \tag{4.22}$$

With σ_S the temporal noise, Δ_S the variation of the mean signal due to a temperature variation of $\Delta_{T_{CN}}$. As those data are measured, the NETD depends on the choice of the temperature used to measure the noise and the temperature variation chosen. To perform this calculation, the data from the measurement inside the climatic chamber have been used. For each blackbody temperature, one hundred images have been taken. From these images we can compute the mean value of each pixel and the standard deviation around this value, allowing for a fine measurement of the NETD. Here, we chose to use the noise of the measurements at a blackbody temperature of $25C$, and calculated Δ_S with a variation of T_{CN} from 25 to $30C$.

For this instrument, the mean NETD is $105mK$ with a variance of $\sigma_{NETD} = 0.1mK$.

The detector ATTO640 was given with a NETD inferior to 60mK at 300K and with an F/1 aperture. As the NETD varies with the square of the F number, it would correspond to a 135mK NETD at a F/1.5 aperture, which is compliant with the results of our study.

4.4.8 multi spectral band

introduction

The previous characterization shows that the α_Z design is already a viable solution for infrared imaging instruments with large FOV. However, to further decrease the weight, volume and cost of optronic pods, the goal is to have multiple detectors sharing the freeform three mirror design. As said in the design section of this chapter, two major steps are remaining. One of those steps is to manufacture an optical design that is actually achromatic, i.e. that reach sufficient optical quality in the visible spectrum. A convincing threshold would be to reach subpixel spot size for the visible spectrum. This implies designing a system with less aberrations and an accurate surface manufacturing. Regarding the surface manufacturing, the surface can not easily be polished after the diamond turning process as it would result in sag errors. The risk is having a microtexturation of the surface that would be large enough to be diffractive of diffusive in the visible spectrum. However, the slow tool servo method has greatly improved in recent years, and mirrors has already been manufactured for visible sprectrum [50].

Although our design has been first developed for LWIR imagery, the acceptance tests showed no diffused light. A second test with a camera that is sensible to visible wavelengths has been performed. The goal of having a diffraction limited design for LWIR imagey has not been fully reached with the present prototype, thus the results in the visible spectrum were not

expected to be close to being diffraction limited. As any visible wavelength is largely smaller than the band III wavelengths, the diffraction limit for visible wavelength is also smaller by the ratio of the two wavelengths. However, the geometrical aberrations are not affected by the wavelength in this design thanks to the use of mirrors. This measure in the visible spectrum was also an interesting way of seeing defects in our design in an indirect way, as the point spread function should now be consistently larger than the airy pattern. However, this method has limits, as the mirrors manufacturing using diamond turning could have resulted in a surface roughness large enough to generate diffusion or diffraction of visible light without affecting significantly the LWIR wavelengths. Moreover, the mechanical part could diffuse and reflect visible light in a very different manner for visible light than for LWIR light.

The camera is based on a Sony IMX250 sensor, which is a 2464x2056 array of pixels with a 3.45μm pitch. The detector is thus a rectangle of 8.5x7.1mm^2, which is larger than the ATTO640 detector size. For recall, the ATTO640 is a 640x480 array with a 12μm pitch, which results in a size of 7.7x5.8mm^2. This fact ensures that the optical quality close to the edge of the detector was not optimized, and thus could be very poor.

I would like to thank Clement Freslier for proceeding the procedures in the visible domain and extract the figure 4.67 and figures 4.68 to 4.75.

Results

Figure 4.65 shows an example of images taken in the visible spectrum.

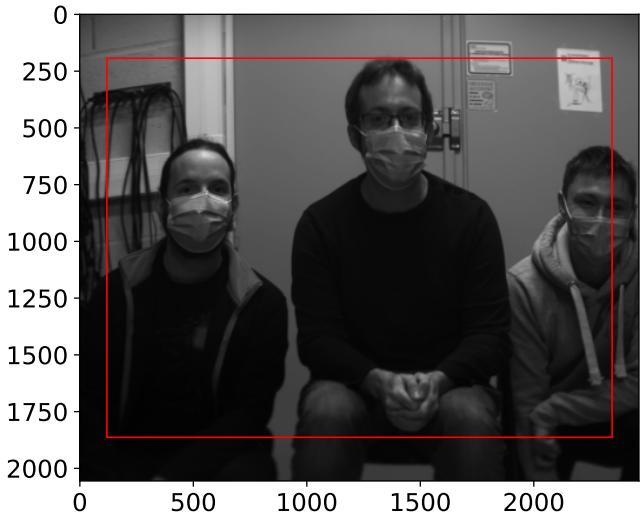

FIGURE 4.65: Example of an image taken in the visible spectrum. Red rectangle is the field for which the system has been optimized.

To analyse the optical quality, and because the visible detector has very small pixels regarding the point spread function, the point spread

function can be measured without performing spot scan. First, using spot scan with such small pixels would lead in displacements that could not be done using the cradle and rotation scale. Secondly because the aberrations are large enough to ignore the MTF after a few dozens of cycles per millimeter. Performing PSF measurements without spot scan is faster as the measurement is taken in a single image acquisition, however the gain differences between pixels should now be taken into account. In this study, we suppose that the pixels have the same gain, which is a fair assumption for recent visible detectors. A scan of PSF across all the detector have been performed, and is shown in Figure 4.66. The image actually shows normalized PSF, each one being normalized by the signal of its own brightest pixel. This allows for a visual comparison of all PSF although the most diffuse ones have lower maximum signal that the brightest ones. The distortion and focal length have not been recalculated on this grid, as this measurement has already been made in the infrared spectrum and the resuts are not dependant on the wavelength chosen. However, the visible detector being larger than the optimized area, the distorsion is increased in the sides of the image. The point spread functions visible in figure 4.66 have complex shapes and principal aberrations cannot be deduces from spot analysis. Moreover the mechanical mount is partially reflective on the visible spectrum, this effect being shown in figures 4.22 and 4.23 where diffuse reflection is clearly visible. This effect implies that possible straylight path might be existent in visible and not seen in the infrared domain, and part of the collimated light outside of the pupil might end up close to the point spread function in the focal plane. Without wavefront measurement, no evaluation of the aberrations and their source can be made.

However, by looking at the central point spread function and the associated MTF, the optical quality for the central field is comparable in the visible spectrum as the optical quality for infrared imaging. As the design has been optimized for the thermal infrared, the optical quality was not expected to be significantly greater in the visible domain, and thus these results are promising. Moreover, the simulations do not take into account straylight and surface errors, and having a relatively low MTF for the visible spectrum is then not surprising.

The next figures show the MTF and PSF for the eight cardinal points of the field of view (each corner and the center of each side, points shown are the closest points inside the red rectangle shown in figure 4.66). Figures 4.73, 4.74 and 4.75 show a rapid degradation of the optical quality in the top side of the field of view. The reason is either that the detector is off centered, and that the center point is not the on axis field for the telescope, or the optical system has straylight and/or surface errors that are rapidly deteriorating the image quality in this area. More studies are needed to better qualify the system in the visible domain.

More studies on this design should be performed, such as reducing the pupil diameter with a diaphragm before the third mirror to see if the optical quality can be improved this way. Possibly, a design that uses materials that

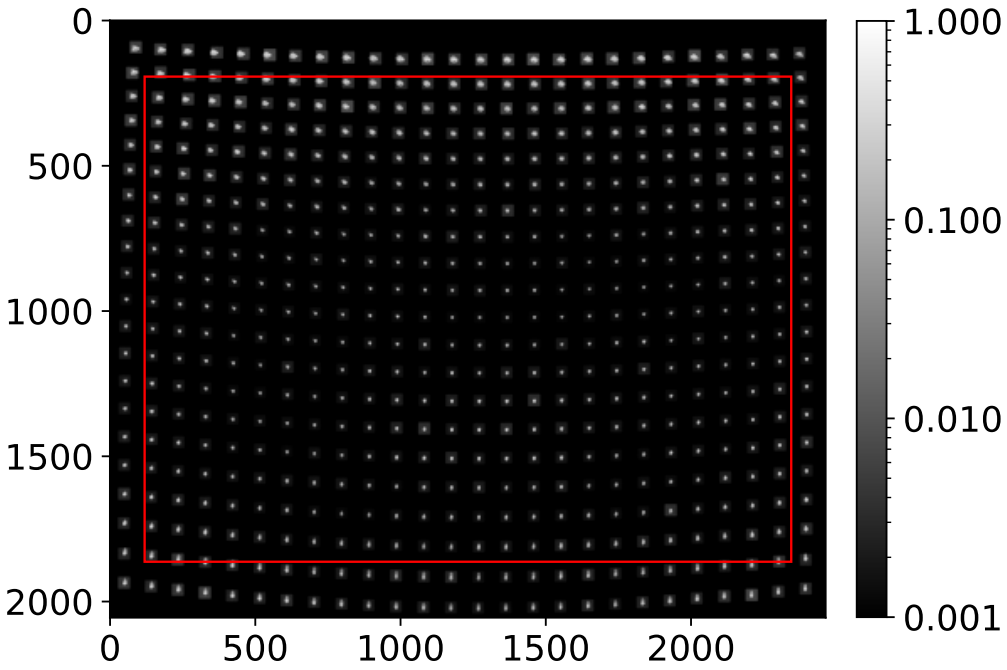

FIGURE 4.66: Scan of PSF across the detector, each normalized by its maximal signal

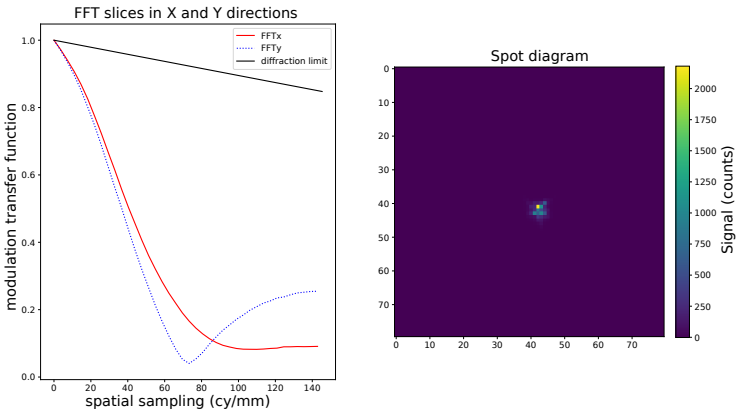

FIGURE 4.67: Modulation transfer function and point spread function in the center field in visible spectrum. The axes of the spot diagram are in detector pixels.

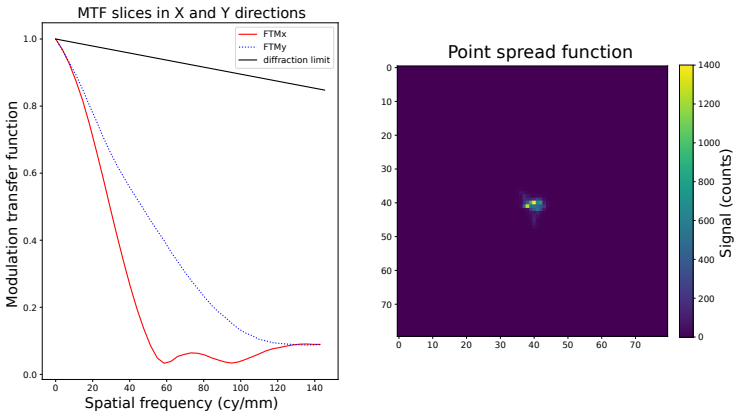

FIGURE 4.68: Modulation transfer function and point spread function in the left side of the FOV in visible spectrum. The axes of the image are in detector pixels.

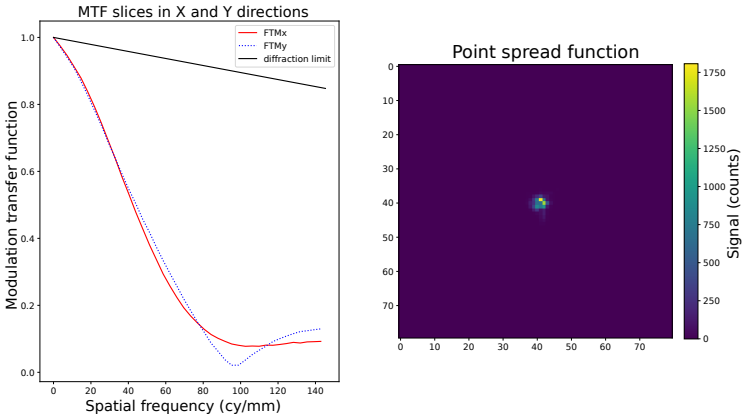

FIGURE 4.69: Modulation transfer function and point spread function in the right side of the FOV in visible spectrum. The axes of the image are in detector pixels.

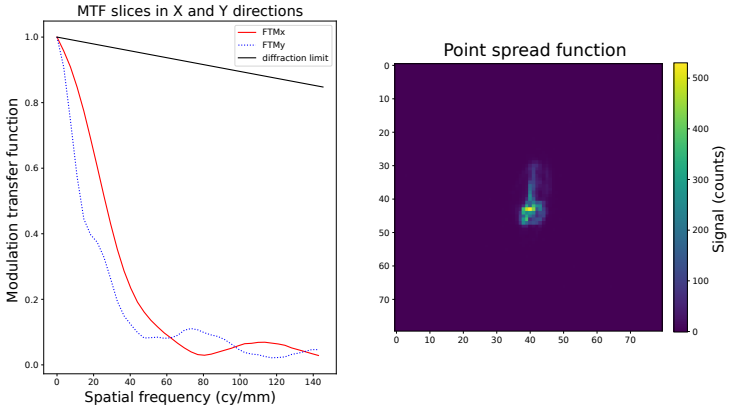

FIGURE 4.70: Modulation transfer function and point spread function in the bottom left corner of the FOV in visible spectrum. The axes of the image are in detector pixels.

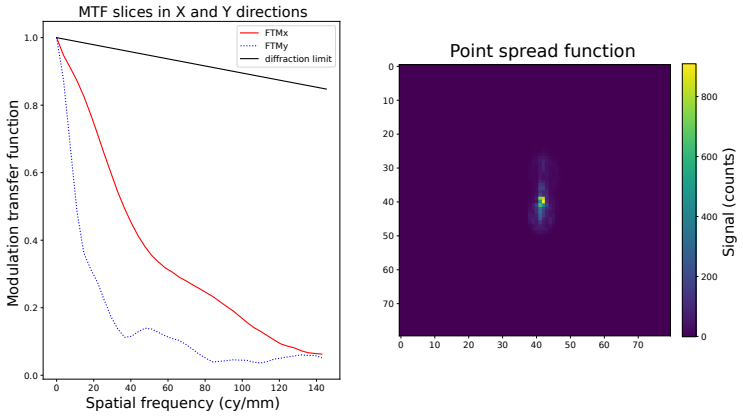

FIGURE 4.71: Modulation transfer function and point spread function in the bottom side of the FOV in visible spectrum. The axes of the image are in detector pixels.

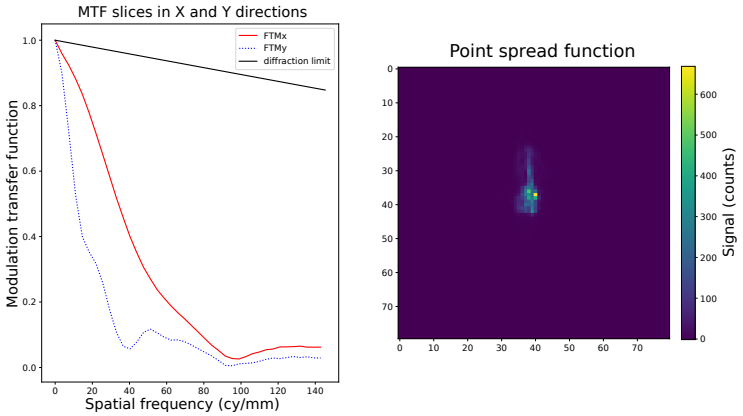

FIGURE 4.72: Modulation transfer function and point spread function in the bottom right corner of the FOV in visible spectrum. The axes of the image are in detector pixels.

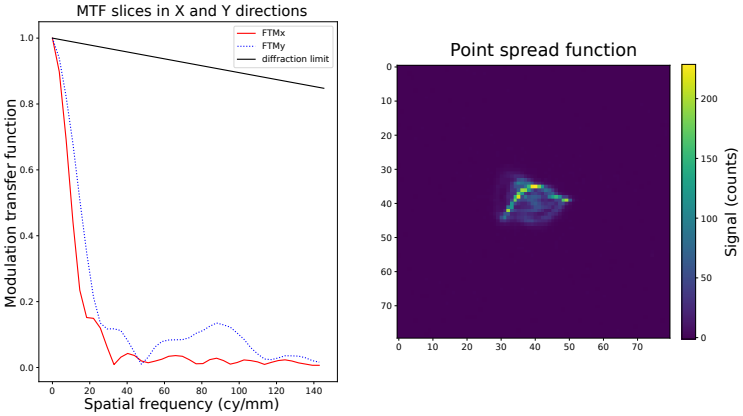

FIGURE 4.73: Modulation transfer function and point spread function in the top left corner of the FOV in visible spectrum. The axes of the image are in detector pixels.

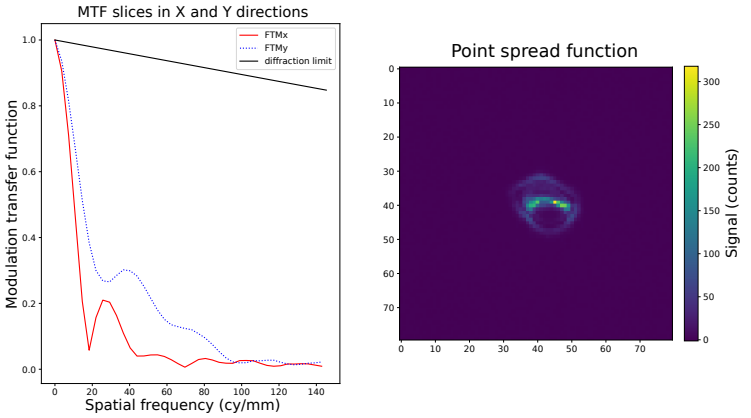

FIGURE 4.74: Modulation transfer function and point spread function in the top side of the FOV in visible spectrum. The axes of the image are in detector pixels.

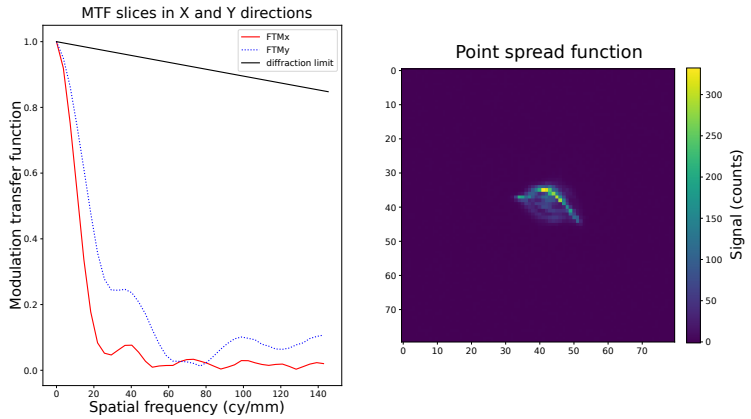

FIGURE 4.75: Modulation transfer function and point spread function in the top right corner of the FOV in visible spectrum. The axes of the image are in detector pixels.

are transparent in the infrared domain but not the visible could be used to design a variant of this system for a better multi spectral band system, with separate apertures for each spectral band. Less compact designs with real exit pupils would facilitate such implementation, would allow to use cryostats if necessary and would help reduce the straylight of the system, at the expense of an increased volume.

As a conclusion, a three mirror imager with a large field of view and a F/1.5 aperture has been designed and built around a novel geometry that has been shown to be more efficient for straylight reduction as well as aberration reduction compared to literature. This system has been fully characterized in both thermal infrared and visible light and has quasi nominal performances over the whole field of view. Such a geometry allows for a compact system that could not exist without the use of freeform surfaces due to the strong nodal aberrations that need to be corrected, demonstrating the benefits of this technology for the design of compact imaging systems.

Chapter 5

Conclusion

5.1 Summary of the manuscript

In this manuscript, the first topic addressed is the challenges of numerical optimization of catoptric freeform imaging systems. Such optimization relies heavily on the designed method and the chapter 2 details an efficient optimization method that effectively led to several optical systems that are detailed throughout the whole document. In an attempt to define the most important parameters in optical design, a systematic study has been performed, and led to the conclusion that, when surfaces are defined using a polynomial expression, the basis used for shape definition has only marginal importance if the design method do not rely on specific properties of the basis.

Then, the method has been applied to uncooled infrared TMA imaging systems in chapter 3. Such systems require a large aperture to reach a sufficient signal to noise ratio, leading to large decenters of the mirrors to avoid vignetting. Such large decenters generate strong nodal aberrations that are tough to correct without an adequate method. In this chapter, several TMA have been optimized and are compatible with classical specifications for nanosatellite payloads, and a first prototype will be finished in the course of the year. Another study also demonstrated that non planar symmetric designs are under studied, particularly regarding the fact that they could, as shown in chapter 3, help reduce even more the volume of some configurations.

Finally, we investigated the AlphaZ geometry. We showed that this geometry, in the case of large aperture designs, is particularly adapted for large field of views demonstrating that such specifications can also be met without the use of lenses. A comparison with the Pamplemousse geometry, which is visually similar, proves that the AlphaZ geometry is parlicularly efficient for straylight management without sacrificing the optical quality nor compactness of the system. These promising results have been confirmed by the realisation of a prototype that has been characterized both in the thermal infrared and the visible domains, showing the interest of freeform mirrors for multi spectral band imagers. This prototype has been designed and toleranced for a monobloc optomechanical mount to avoid any alignment of the mirrors, which is extremely tedious in decentered systems. Such solutions could lead in low cost, low mass and low consumption thermal

infrared imagers for satellite or airborne missions. As our designs are fully catoptric, they are also achromatic and, as a result, could be used for easily coregistrated multi spectral band imaging devices using a beamsplitter close to the focal plane.

5.2 Communications and publications

5.2.1 Oral presentations

During this PhD, I participated as a speaker to 3 international conferences, where I presented the optimization method applied to TMA designs. First I presented my work at the OTRO 2020 symposium, and received a best student paper award. Due to Covid-19 pandemic, I remotely presented my work at virtual event ICSO 2020 in early 2021 and at virtual event IODC 2021. Finally, I have been invited by the Zemax Team to present the optimization method specifically applied to the Zemax OpticStudio software at Zemax Envision Europe 2021.

L. Duveau, G. Druart, T. Lépine, E. Hugot, and X. Briottet, "Design strategies of three mirror telescopes with freeform surfaces," OPTRO 2020, Jan. 2020

L. Duveau, T. Lépine, E. Hugot, X. Briottet, and G. Druart, "Design strategies of an unobscured three mirror telescope with freeform surfaces for infrared nanosatellite imagery," en, in International Conference on Space Optics — ICSO 2020, Z. Sodnik, B. Cugny, and N. Karafolas, Eds., Online Only, France: SPIE, Jun. 2021, p. 11, ISBN: 978-1-5106-4548-6 978-1-5106-4549-3. DOI: 10 . 1117 / 12 . 2599153

Duveau, Louis, Jean-Baptiste Volatier, Thierry Lépine, Emmanuel Hugot, and Guillaume Druart. "Management of Rigorous Optomechanical Constraints Using Non Planar Symmetrical Systems." In OSA Optical Design and Fabrication 2021 (Flat Optics, Freeform, IODC, OFT), JTh1A.5. Washington, DC: OSA, 2021. https://doi.org/10.1364/FLATOPTICS.2021.JTh1A.5.

5.2.2 Articles

I have participated in one article as a second author. This article explores the variety of freeform two mirror systems. More specifically, my contribution to this article was the classically designed two mirror systems that were used as reference for the systems generated using the method developed by J.-B. Volatier.

J.-B. Volatier, L. Duveau, and G. Druart, "An exploration of the freeform two-mirror off-axis solution space," Journal of Physics: Photonics, Nov. 2019. DOI: 10.1088/2515-7647/ab5c0d

Articles about the systematical study and the AlphaZ design and manufacturing are in preparation and will soon be proposed for publication.

5.2.3 Patent

We submitted a patent to protect the large FOV and large aperture AlphaZ design presented in the present manuscript.

L.Duveau and G. Druart, "SYSTEME OPTIQUE IMAGEUR A TROIS MIROIRS.", Patent FR2013568, submitted on 17/12/2020. Unpublished yet.

5.3 Future developments

This work details a rather straighforward and efficient method for designing freeform optics, making the most of commercial software and therefore can be quickly used by any designer. This work should however be continued and completed with several studies. First, the systematic study showed the difficulty of comparing design methods due to the lack of common designs or specifications that could be used for representative benchmarks. We suggest using, for freeform optical design, the use of several TMA designs first, as this geometry is the most used. Several systems are needed to cover the large range of specifications. We also suggest to include less common systems such as the Alpha-Z design that covers specifications that could not be met using TMAs. Such commonplace could lead to objective comparison between design methods and would help the community evolve faster towards reliable and fast optimization of performant imaging systems. Additionally, the control over the optimization method in commercial software is only partial and is partly a black box process for the designer. For the community, this leads to uncertainties over which software is the most reliable. Development of optimization modules with the most up to date algorithms would ease the optimization process. A study of global optimization methods applied to freeform surfaces and research on how to improve such global methods would be interesting, to help fast industrial design of simple optical systems but also to help designers find a better local minimum in very complex merit functions such as those for freeform off axis designs. Finally, the large number of surface parameters in freeform design leads to heavy computational calculations. For such designs, the polynomial surface definition is not necessarily the best choice and studies of completely different methods, such as the SMS [114] method must be performed, as both methods could complement each other in finding better starting points or exploring the merit function in search of local minima.

Regarding the TMA prototype, a thorough characterization is needed. The final goal is to add a beamsplitter in the design to have a compact multi spectral band instrument. However, the addition of a beamsplitter is not an easy task provided that this beamsplitter must be efficient even though the incidence angle of incoming rays is highly variable. This is due to the fact that the beamsplitter must be tilted and close to the focal plane where the beam is convergent. The effect of this beamsplitter must be evaluated both in terms of spectral transmittance and reflectance, but also in terms of effects on the transmitted wavefront.

Regarding the Alpha-Z design, some wavefront error persist and more studies are needed to evaluate its source, such as measuring the exact output wavefront and the shapes of the mirrors. The knowledge of the surface front error for each mirror could help us correct the manufacturing process by adapting the optomechanical mount to minimize the optical aberrations. To know the surface front error, classical methods are not affordable for most research teams, so new methods such as deflectometry must be tested. The data available is not yet sufficient, however a statistical analysis of the usual errors occuring during the manufacturing process of mirrors would lead to a significant improvement in tolerancing of freeform catoptric designs.

Finally, as freeform optics allow to generate new geometries that were not possible with classical optical surfaces, non planar symmetric designs should be the next generation of full freeform optical systems. It could allow the optical design to be adapted to the allocated volume, leading to an increase in compactness in the cases where the classical design shapes are not ideal.

Appendix A

Catalog of results of the systematic study

This appendix gives additional information about the results of the systematic study. This helps the reader get confident in the method used and extract more information on the subject.

A.1 Results of the systematic study averaged over the different surfaces definitions

By averaging over the surfaces definitions, the gaussian quadrature appears to be slightly better for dense samplings.

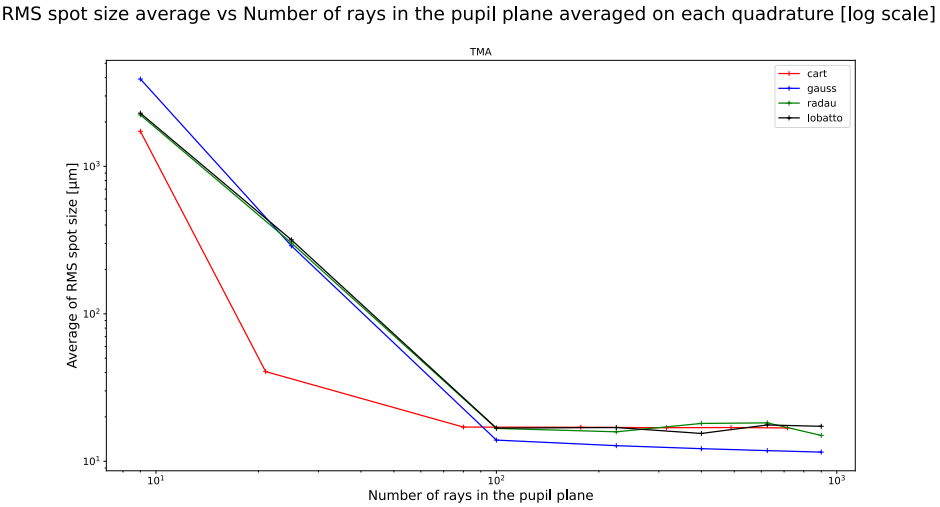

FIGURE A.1: RMS spot diagram versus the number of traced rays per field in the pupil averaged over the surface definitions in logarithmic scale for the TMA design

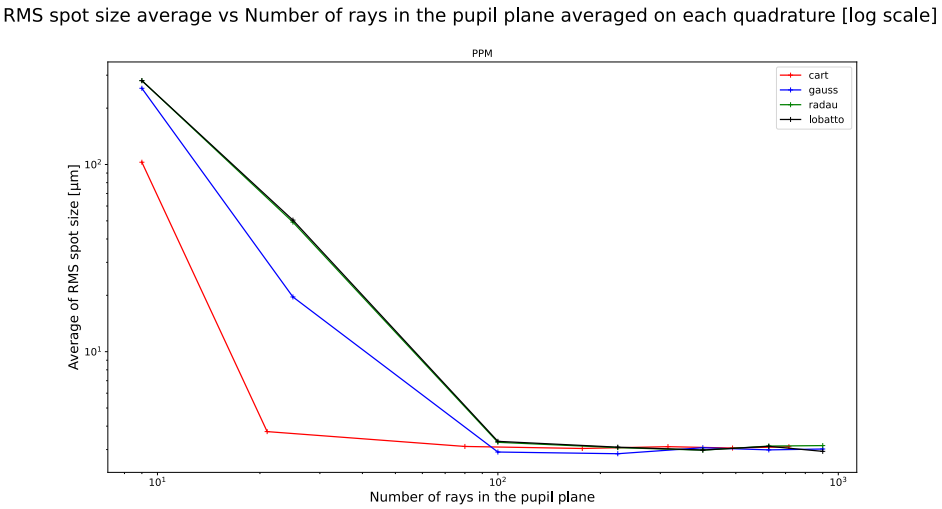

FIGURE A.2: RMS spot diagram versus the number of traced rays per field in the pupil averaged over the surface definitions in logarithmic scale for the Pamplemousse design

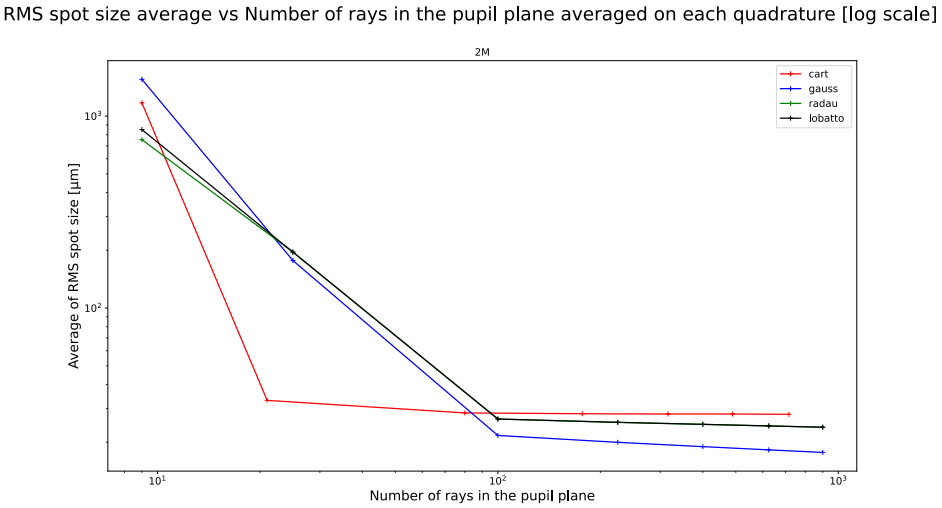

FIGURE A.3: RMS spot diagram versus the number of traced rays per field in the pupil averaged over the surface definitions in logarithmic scale for the two mirror design

A.2 Results of the systematic study averaged over the different sampling schemes

This is an averaging over the different distributions to find if the Zernike Polynomials gives better results that Qtype freeform polynomials, as the Extended polynomials are clearly the best surface definition in our study. As the samplings do not exactly use the same number of rays, the values shown is the number of rays drawn before the removal of the rays outside of the pupil for the cartesian sampling, and before the addition of the central ray for the Gauss-Radau and Gauss-Lobatto quadratures.

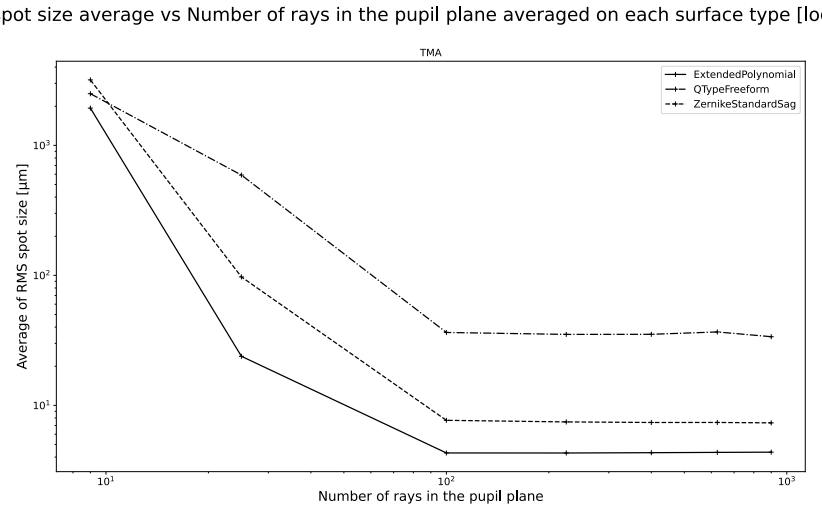

FIGURE A.4: RMS spot diagram versus the number of traced rays per field in the pupil averaged over the different sampling schemes in logarithmic scale for the TMA design

A.3 Proof of the existence of a recurrence relation

This section details the proof of existence of a recurrence relation for the evaluation of orthogonal polynomials from section 2.4.3. Take a set of orthogonal polynomials P_n, the properties of such polynom is:

$$P_n = \sum_{i=0}^{n} k_{n,i} x^i \tag{A.1}$$

With $k_{n,i}$ being the coefficients of the monomial x^i for the polynom of order n P_n.

$$< P_n, P_m >= 0 \text{ for } n \neq m \tag{A.2}$$

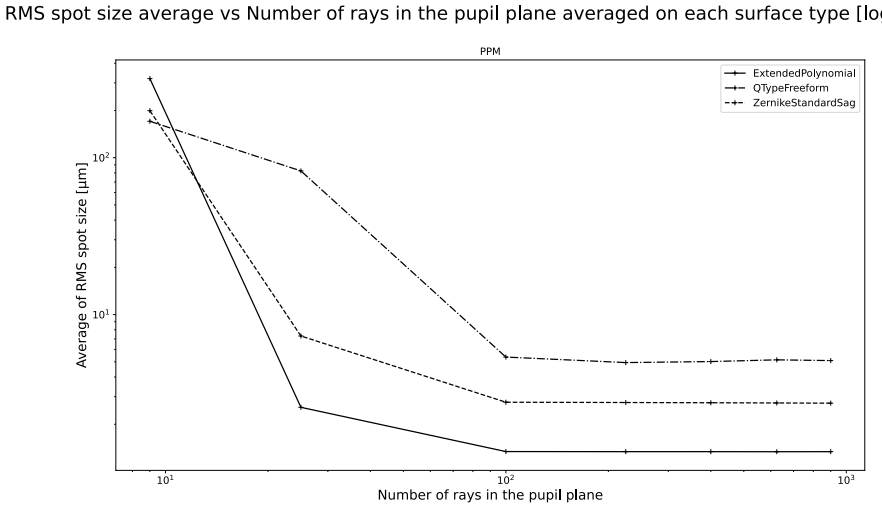

FIGURE A.5: RMS spot diagram versus the number of traced rays per field in the pupil averaged over the different sampling schemes in logarithmic scale for the Pamplemousse design

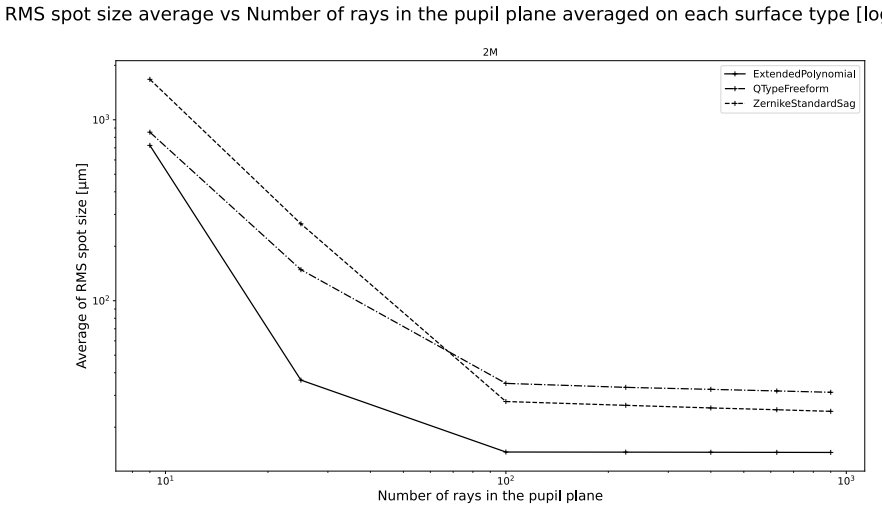

FIGURE A.6: RMS spot diagram versus the number of traced rays per field in the pupil averaged over the different sampling schemes in logarithmic scale for the two mirror design

If we look at the polynomial xP_n:

$$xP_n(x) = \sum_{i=0}^{n+1} \alpha_i x^i = \sum_{i}^{n+1} \beta_i P_i(x) \tag{A.3}$$

$$< xP_n, P_i >=< P_n, xP_i >=< \sum_{i}^{n+1} \beta_i P_i(x), xP_i >= 0 \text{ if } i < n-1 \tag{A.4}$$

It then proceeds that:

$$xP_n(x) = a_n P_{n+1}(x) + b_n P_n(x) + c_n P_{n-1}(x) \text{ for } n > 0 \tag{A.5}$$

$$xP_0(x) = a_0 P_1(x) + b_0 P_0(x) \text{ for } n = 0 \tag{A.6}$$

it comes that:

$$a_n = \frac{k_{n,n}}{k_{n+1,n+1}} \tag{A.7}$$

With $h_i =< P_i, P_i >> 0$.

Let's prove that $a_n c_{n+1} > 0$

$$< xP_n, P_{n+1} >=< a_n P_{n+1} + b_n P_n + C_n P_{n-1}, P_{n+1} >= a_n h_{n+1} \tag{A.8}$$

$$< xP_{n+1}, P_n >=< a_{n+1} P_{n+2} + b_{n+1} P_{n+1} + c_{n+1} P_n, P_n >= c_{n+1} h_n \tag{A.9}$$

It follows, from the first equality of equation A.4 that:

$$a_n c_{n+1} = a_n^2 \frac{h_{n+1}}{h_n} > 0 \tag{A.10}$$

The reciprocal is true, see proof in Chihara's book [164].

Appendix B

Alternative planar symmetric designs

In this Appendix are listed the data to implement all the designs presented in the manuscript, presented in a Zemax OpticStudio formatting. All data is rounded to four significant digits.

B.1 Designs of Chapter 2

B.1.1 Lens data of the two mirror design for the systematical study

TABLE B.1: sequential description of the 2M design (OpticStudio Formatting). CB = Coordinate Break. IMA = Image

Line	Surf. Type	curvature radius (mm)	Thick. (mm)	Material	Tilt X (deg)
OBJ	Standard	INF	INF	-	-
1(STOP)	Standard	INF	0	-	-
2	CB	-	0	-	20
3 M1	Standard	-2726	0	MIRROR	-
4	CB	-	-112.8	-	20
5	CB	-	0	-	10
6 M2	Standard	299.8	0	MIRROR	-
7	CB	-	132.9	-	10
IMA	Standard	INF	-	-	-

B.1.2 Lens data of the TMA design for the systematical study

TABLE B.2: sequential description of the TMA design (OpticStudio Formatting)

Line	Surf. Type	curvature radius (mm)	Thick. (mm)	Material	Tilt X (deg)
OBJ	Standard	INF	INF	-	-
1	CB	-	0	-	-30.37
2 M1	Standard	-576.6	0	MIRROR	-
3	CB	-	99.20	-	-30.37
4	CB	-	0	-	40.08
5 M2(STOP)	Standard	-260.89	0	MIRROR	-
6	CB	-	82.23	-	40.08
7	CB	-	0	-	-18.63
8 M3	Standard	-140.9	0	MIRROR	-
9	CB	-	0	-	-18.63
IMA	Standard	INF	-	-	-

B.1.3 Lens data of the pamplemousse design for the systematical study

TABLE B.3: sequential description of the PPM design (OpticStudio Formatting)

Line	Surf. Type	curvature radius (mm)	Thick. (mm)	Material	Tilt X (deg)
OBJ	Standard	INF	INF	-	-
1	CB	-	0	-	-20
2 M1	Standard	51.19	0	MIRROR	-
3	CB	-	-17.65	-	-20
4	CB	-	0	-	20
5 M2	Standard	-1953	0	MIRROR	-
6	CB	-	20.62	-	20
7	CB	-	0	-	10
8 M3(STOP)	Standard	-34.66	0	MIRROR	-
9	CB	-	0	-	10
IMA	Standard	INF	-	-	-

B.2 Designs of Chapter 3

B.2.1 Lens data of the Urban Heat Island TMA

Lens Data of the TMA designed for urban heat island (UHI) study of section 3.3.2.

TABLE B.4: Freeform mirrors shape description of the TMA for the UHI study. All data has been rounded to the 4th significant digit

Parameter	**M1**	**M2**	**M3**
surface radius (mm)	52.32	28.83	67.06
base sphere curvature radius (mm)	-1.660E+3	-2.047E+2	-1.885E+2
Normalization radius (mm)	33.3	33.3	33.3
k	-7.393	4.650	2.714E-1
X0Y2	-9.339E-2	-4.267E-2	6.469E-3
X2Y1	9.749E-2	2.376E-1	6.331E-2
XOY3	-1.452E-2	-3.062E-1	1.017E-2
X4Y0	3.824E-3	2.661E-2	1.961E-3
X2Y2	2.629E-3	5.630E-3	-2.837E-3
X0Y4	2.103E-3	-1.350E-2	3.631E-4
X4Y1	4.766E-4	1.020E-2	1.985E-3
X2Y3	-5.010E-4	-2.209E-2	3.034E-3
X0Y5	-1.790E-4	-3.208E-2	6.808E-4

TABLE B.5: Sequential positioning of surfaces (OpticStudio Formatting) of the TMA for the UHI study. Surface 2 is the global coordinate reference. All data has been rounded to the 4th significant digit

Line	**Surface Type**	**Thickness (mm)**	**Material**	**Tilt X (deg)**
OBJ	Standard	Infinity	-	-
1	Coordinate Break	-	-	-20
2	Standard	0	-	-
3	Coordinate Break	-	-	20
4	Standard	99.9	-	-
5	Coordinate Break	-	-	-32.06
6 M1	Extended Polynomial	-	MIRROR	-
7	Coordinate Break	-134.4	-	-32.06
8	Coordinate Break	-	-	32.66
9 M2(STOP)	Extended Polynomial	-	MIRROR	-
10	Coordinate Break	116.4	-	32.66
11	Coordinate Break	-	-	-13.99
12 M3	Extended Polynomial	-	MIRROR	-
13	Coordinate Break	-155.6	-	-13.99
14	Coordinate Break	-	-	1.016
IMA	Standard	-	-	-

B.2.2 Lens data of the TMA prototype

Lens Data of the TMA prototype of section 3.3.3.

TABLE B.6: Freeform mirrors shape description of the TMA prototype. All data has been rounded to the 4th significant digit

Parameter	**M1**	**M2**	**M3**
surface radius (mm)	46.5	25.24	51
base sphere curvature radius (mm)	-6.851E+2	-1.460E+2	-1.470E+2
Normalization radius (mm)	33.3	33.3	33.3
k	-6.897E-1	2.454	3.332E-1
X0Y2	-1.743E-1	-3.293E-1	-5.459E-2
X2Y1	1.344E-1	4.182E-1	1.335E-1
XOY3	3.458E-2	-1.409E-1	6.353E-2
X4Y0	9.056E-3	7.058E-2	8.941E-3
X2Y2	1.214E-2	2.503E-2	-2.969E-3
X0Y4	1.991E-3	-9.754E-3	-3.550E-3
X4Y1	4.0949E-5	1.516E-2	6.742E-3
X2Y3	-4.545E-4	-2.905E-3	1.257E-2
X0Y5	-2.140E-4	-2.890E-2	4.967E-3

TABLE B.7: Sequential positioning of surfaces (OpticStudio Formatting) of the TMA prototype. All data has been rounded to the 4th significant digit

Line	Surface Type	Thickness (mm)	Material	Tilt X (deg)
OBJ	Standard	Infinity	-	-
1	Standard	99.9	-	-
2	Coordinate Break	-	-	-30.37
3 M1	Zernike Polynomial	-	MIRROR	-
4	Coordinate Break	-99.20	-	-30.37
5	Coordinate Break	-	-	40.08
6 M2(STOP)	Zernike Polynomial	-	MIRROR	-
7	Coordinate Break	82.23	-	40.08
8	Coordinate Break	-	-	-18.63
9 M3	Zernike Polynomial	-	MIRROR	-
10	Coordinate Break	-119.6	-	-18.63
IMA	Standard	-	-	-

B.2.3 Lens data of the planar symmetric system from the non planar symmetric study

Lens data of the planar symmetric system from section 3.4.

TABLE B.8: Freeform mirrors shape description of the large FOV TMA. All data has been rounded to the 4th significant digit

Parameter	**M1**	**M2**	**M3**
surface radius (mm)	27.29	14.50	16.78
base sphere curvature radius (mm)	-2.397E+2	-1.192E+2	-2.899E+2
Normalization radius (mm)	35	12	15
Z1	-2.317E-3	-6.300E-4	-1.341E-3
Z3	4.854E-2	2.112E-2	1.864E-2
Z6	-6.082E-2	-3.073E-2	-7.449E-3
Z7	1.719E-2	7.436E-3	6.555E-3
Z9	-2.265E-3	-1.868E-3	-4.983E-3
Z11	1.042E-3	2.831E-4	5.997E-4
Z12	3.177E-4	3.884E-4	8.264E-5
Z14	9.289E-5	-4.372E-5	-2.050E-5
Z17	1.422E-5	-1.770E-5	-2.262E-5
Z19	-4.906E-6	-8.462E-6	9.682E-6
Z21	3.432E-6	2.840E-6	-3.889E-5
Z22	5.125E-6	1.164E-6	2.268E-8
Z24	-3.749E-7	-2.162E-6	-1.158E-6
Z26	-1.731E-6	-9.410E-7	-4.681E-6
Z28	-8.145E-8	-1.080E-8	3.515E-6
Z29	5.762E-7	-2.114E-7	-2.747E-6
Z31	8.806E-7	4.250E-7	3.250E-6
Z33	7.190E-7	4.876E-7	3.427E-6
Z35	1.416E-6	6.976E-7	7.981E-6

TABLE B.9: sequential positioning of surfaces (OpticStudio Formatting). All data has been rounded to the 4th significant digit

Line	Surface Type	Thickness (mm)	Material	Tilt X (deg)
OBJ	Standard	Infinity	-	-
1	Coordinate Break	-	-	0
2	Standard	0	-	-
3	Coordinate Break	-	-	0
4	Standard	99.9	-	-
5	Coordinate Break	-	-	-18.55
6 M1(STOP)	Zernike Polynomial	-	MIRROR	-
7	Coordinate Break	-73.77	-	-18.55
8	Coordinate Break	-	-	25.73
9 M2	Zernike Polynomial	-	MIRROR	-
10	Coordinate Break	67.56	-	25.73
11	Coordinate Break	-	-	-9.674
12 M3	Zernike Polynomial	-	MIRROR	-
13	Coordinate Break	-66.81	-	-9.674
14	Coordinate Break	-	-	0
IMA	Standard	-	-	-

B.2.4 Lens data of the non planar symmetric system from the non planar symmetric study

Lens data of the non planar symmetric system from section 3.4.

TABLE B.10: Freeform mirrors shape description of the large FOV TMA. All data has been rounded to the 4th significant digit

Parameter	**M1**	**M2**	**M3**
surface radius (mm)	29.93	16.62	24.12
base sphere curvature radius (mm)	-3.288E+2	-1.486E+2	-2.521E+2
Normalization radius (mm)	30	15	20
Z1	-5.459E-4	-7.640E-4	-5.805E-4
Z2	4.382E-3	5.731E-3	1.195E-3
Z3	1.241E-2	1.409E-2	6.641E-3
Z5	9.126E-3	2.491E-3	3.245E-3
Z6	-2.482E-2	-2.769E-2	-6.147E-3
Z7	4.385E-3	4.963E-3	2.341E-3
Z8	1.546E-3	2.007E-3	4.337E-4
Z9	2.773E-4	7.098E-4	2.255E-4
Z10	-1.338E-5	-4.055E-4	-6.659E-4
Z11	2.449E-4	3.443E-4	2.615E-4
Z12	3.536E-5	1.117E-4	9.990E-6
Z13	-2.801E-5	-6.267E-5	-8.732E-6
Z14	6.006E-6	2.662E-5	1.021E-5
Z15	-1.601E-6	7.852E-6	5.717E-6
Z16	-1.782E-6	-1.298E-5	6.596E-7
Z17	-2.252E-7	-1.176E-5	-8.144E-6
Z18	-2.452E-6	-1.178E-5	-5.989E-6
Z19	1.537E-6	5.159E-6	1.038E-5
Z20	-6.846E-7	-6.519E-6	-5.096E-7
Z21	5.454E-7	2.636E-6	-3.124E-6
Z22	6.854E-7	2.196E-6	1.642E-6
Z23	-8.068E-8	1.154E-7	1.996E-7
Z24	3.252E-8	-3.958E-7	-8.485E-7
Z25	4.895E-8	5.486E-7	2.263E-6
Z26	-2.420E-7	-3.899E-7	-7.037E-7
Z27	2.507E-7	1.436E-6	1.075E-6
Z28	-2.489E-7	-7.505E-7	-1.501E-6
Z29	8.445E-8	-9.426E-7	-2.707E-6
Z30	-1.828E-7	-1.763E-6	-3.498E-6
Z31	1.896E-7	9.584E-7	2.808E-6
Z32	-2.206E-7	-1.209E-6	-2.450E-6
Z33	1.136E-7	6.393E-7	3.095E-7
Z34	-1.582E-7	-9.529E-7	-3.030E-6
Z35	-1.1989E-7	-2.252E-7	-8.726E-8
Z36	-5.602E-8	-5.267E-7	-1.325E-6

TABLE B.11: sequential positioning of surfaces (OpticStudio Formatting). All data has been rounded to the 4th significant digit. Std stands for Standard, Thi. stands for Thickness, EP stands for Extended Polynomial and CB stands for Coordinate Break. Tilts are in degrees.

Line	**Surf. Type**	**Thi. (mm)**	**Material**	**Tilt X**	**Tilt Y**	**Tilt Z**
OBJ	Std	Infinity	-	-	-	-
1	CB	-	-	0	0	0
2	Std	0	-	-	-	-
3	CB	-	-	0	0	0
4	Std	99.9	-	-	-	-
5	CB	-	-	-14.59	3.161	0
6 M1(STOP)	EP	-	MIRROR	-	-	-
7	CB	-98.83	-	-14.59	3.161	0
8	CB	-	-	16.18	6.964E-1	0
9 M2	EP	-	MIRROR	-	-	-
10	CB	92.54	-	16.18	0.6964	0
11	CB	-	-	0	-8.912	0
12 M3	EP	-	MIRROR	-	-	-
13	CB	-98.46	-	0	-8.912	0
14	CB	-	-	0	0	3.451E-2
IMA	Std	-	-	-	-	-

B.3 Designs of Chapter 4

B.3.1 Lens data of the 8x6 degrees FOV pamplemousse design

Lens data of the 8x6 degrees FOV pamplemousse design from section 4.1.

TABLE B.12: Freeform mirrors shape description of the 8X6 degrees FOV pamplemousse design

Parameter	**M1**	**M2**	**M3**
surface radius (mm)	20.33	26.10	34.73
base sphere curvature radius (mm)	2.189E+2	4.533E+2	-1.871E+2
Normalization radius (mm)	21	27	35
X0Y2	-1.959E-1	-2.953E-1	4.331E-3
X2Y1	-4.159E-3	5.444E-2	-9.208E-2
XOY3	2.096E-1	3.572E-1	2.539E-1
X4Y0	1.348E-2	-1.401E-2	-1.681E-2
X2Y2	2.749E-2	-4.738E-2	-5.124E-2
X0Y4	5.151E-2	-4.262E-2	-1.851E-2
X4Y1	-3.553E-3	1.418E-3	1.659E-3
X2Y3	3.551E-3	1.162E-2	1.701E-2
X0Y5	1.030E-2	1.334E-2	2.065E-2

TABLE B.13: sequential positioning of surfaces (OpticStudio Formatting) of the 8X6 degrees FOV pamplemousse design

Line	Surface Type	Thickness (mm)	Material	Tilt X (deg)
OBJ	Standard	Infinity	-	-
1	Standard	130	-	-
2	Coordinate Break	-	-	15.74
3 M1	Extended Polynomial	-	MIRROR	-
4	Coordinate Break	-81.42	-	15.74
5	Coordinate Break	-	-	18.96
6 M2(STOP)	Extended Polynomial	-	MIRROR	-
7	Coordinate Break	75.67	-	18.96
8	Coordinate Break	-	-	14.39
9 M3	Extended Polynomial	-	MIRROR	-
10	Coordinate Break	-105.7	-	14.39
IMA	Standard	-	-	-

B.3.2 Lens data of the 24x18 degrees FOV pamplemousse design

Lens data of the 24x18 degrees FOV pamplemousse design from section 4.1.

TABLE B.14: Freeform mirrors shape description

Parameter	**M1**	**M2**	**M3**
surface radius (mm)	16.81	16.58	22.59
base sphere curvature radius (mm)	9.599E+1	-9.895E+2	-9.101E+1
Normalization radius (mm)	20	20	25
X0Y2	-1.417	-2.172	-5.415E-1
X2Y1	-4.458E-2	4.29E-1	2.400E-2
XOY3	2.519E-1	1.170	9.897E-2
X4Y0	1.836E-2	-9.711E-2	-1.655E-2
X2Y2	-4.88E-2	-4.719E-1	-6.772E-2
X0Y4	2.588E-2	-6.169E-1	-5.092E-2
X4Y1	-5.280E-2	4.885E-2	3.020E-3
X2Y3	4.347E-2	2.967E-1	1.351E-2
X0Y5	3.284E-2	4.086E-1	1.025E-2
X6Y0	3.735E-3	-1.230E-2	-2.025E-3
X4Y2	1.567E-4	-1.013E-1	-8.558E-3
X2Y4	7.291E-3	-3.273E-1	-1.231E-2
X0Y6	2.459E-3	-3.382E-1	-5.585E-3
X6Y1	1.098E-1	2.258E-2	1.399E-3
X4Y3	-5.723E-2	6.383E-2	2.102E-3
X2Y5	-5.733E-2	1.941E-1	3.209E-3
X0Y7	-3.055E-2	1.519E-1	1.302E-3

TABLE B.15: sequential positioning of surfaces for the large FOV pamplemousse (OpticStudio Formatting)

Line	**Surface Type**	**Thickness (mm)**	**Material**	**Tilt X (deg)**
OBJ	Standard	Infinity	-	-
1	Standard	80	-	-
2	Coordinate Break	-	-	15.36
3 M1	Extended Polynomial	-	MIRROR	-
4	Coordinate Break	-57.41	-	15.46
5	Coordinate Break	-	-	17.68
6 M2(STOP)	Extended Polynomial	-	MIRROR	-
7	Coordinate Break	59.44	-	17.68
8	Coordinate Break	-	-	8.716
9 M3	Extended Polynomial	-	MIRROR	-
10	Coordinate Break	-66.76	-	8.716
11	Coordinate Break	-	-	21.95
IMA	Standard	-	-	-

B.3.3 Lens data of the αZ prototype

Lens data of the αZ prototype

TABLE B.16: Freeform mirrors shape description of the αZ design

Parameter	**M1**	**M2**	**M3**
surface radius (mm)	15.5	16	21.16
base sphere curvature radius (mm)	3.236E+2	-5.0114E+1	-6.988E+1
Normalization radius (mm)	15.5	14	20
X0Y2	4.685E-1	1.236	2.668E-1
X2Y1	-1.499E-1	-3.874E-1	1.583E-2
XOY3	-4.225E-1	-4.210E-1	-2.668E-2
X4Y0	5.404E-3	-1.366E-1	-6.578E-3
X2Y2	-5.182E-2	-2.594E-1	-4.953E-3
X0Y4	-1.075E-1	-1.833E-1	8.594E-3
X4Y1	-1.773E-2	-1.117E-1	1.613E-3
X2Y3	-5.004E-2	-2.303E-1	1.593E-3
X0Y5	-8.044E-2	-1.282E-1	-1.455E-3
X6Y0	1.135E-2	-1.174E-2	-6.730E-4
X4Y2	2.293E-2	-1.258E-1	-1.936E-3
X2Y4	5.524E-3	-1.949E-1	-1.774E-3
X0Y6	1.773E-2	-6.819E-2	3.937E-4
X6Y1	2.592E-2	7.896E-3	1.552E-4
X4Y3	3.803E-2	-6.132E-2	3.838E-4
X2Y5	5.646E-3	-7.476E-2	7.517E-4
X0Y7	4.796E-2	-1.855E-2	-9.983E-6

TABLE B.17: sequential positioning of surfaces for the αZ design (OpticStudio Formatting)

Line	**Surface Type**	**Thickness (mm)**	**Material**	**Tilt X (deg)**
OBJ	Standard	Infinity	-	-
1	Standard	60	-	-
2	Coordinate Break	-	-	24.79
3 M1	Extended Polynomial	-	MIRROR	-
4	Coordinate Break	-24.46	-	24.79
5	Coordinate Break	-	-	33.76
6 M2	Extended Polynomial	-	MIRROR	-
7	Coordinate Break	54.34	-	33.76
8	Coordinate Break	-	-	-13.41
9 M3(STOP)	Extended Polynomial	-	MIRROR	-
10	Coordinate Break	-65.29	-	-13.41
IMA	Standard	-	-	-

Appendix C

Alternative planar symmetric designs

C.1 Study of a TMA for a larger field of view

The first system has been generated in 2019, the update of the design for prototyping has been made in 2020. Following the fact that faster microbolometers did not appear in the meantime, a study with a lower focal length and larger field of view, using a GSD of 100m, has been performed to reduce the motion blur. As a new SXGA (1280 x 1024 pixels) microbolometer with $12\mu m$ pixel pitch has also been disclosed by Lynred, a study using this array has been performed. The specifications have been modified as follow in equations C.1 and C.2:

$$f = \frac{mean\,altitude * pixel\,size}{GSD} \approx 70mm \tag{C.1}$$

The half field of view (half FOV) along each direction when using a SXGA detector is:

$$\begin{aligned} half\,FOV &= tan^{-1}(\frac{half\,image\,size}{f}) \\ half\,FOV\,X &\approx 6,25^\circ \\ half\,FOV\,Y &\approx 5^\circ \end{aligned} \tag{C.2}$$

To be more compliant with cubesats standards, we chose an allocated volume of 100 x 200 x 300mm^3, which is a 6U volume. To account for the mirrors substrate, mechanical design and detector electronics, we will allow a 100x150x250mm^3 volume for the optical design itself. Table C.1 and figure C.1 summarize the specifications of the optical payload.

This design has been optimized using XY polynomials but have been converted to zernike polynomials. The main reason for this conversion is that most people are familiar with this basis and could easily use this data to compare their systems to ours. Moreover, the results of the systematic study from Chapter 2 were not fully known at the time and previous studies (as the article from Muslimov et al. [133] and manuscrit of Brömel [97]) led us to believe that using Zernike polynomial would be a better choice than XY polynomials. The conclusion of chapter 2 tend to show that this choice

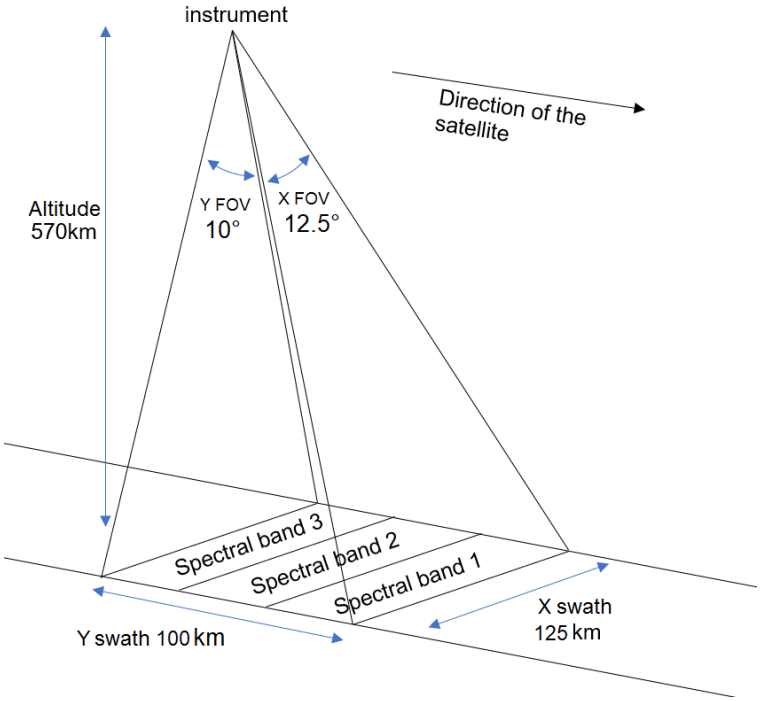

FIGURE C.1: Summary of specifications and illustration of the field division for the multispectral imaging

TABLE C.1: Summary of specifications

specification	value
effective focal length	70mm
half FOV X	6,25°
half FOV Y	5°
F#	1.5
pixel size	12μm
number of pixels	1280 X * 1024 Y
max X dimension	100mm
max Y dimension	250mm
max Z dimension	150mm

finally did not have any significant impact on the final design. The pupil has been moved from the secondary mirror to the third mirror, as the increase of the FOV had a significant impact on the size of this mirror, the most compact solution was to use the third mirror as the exit pupil and the stop. This choice results from an empirical study.

The design specifications are given in tables C.2 and C.3. The layout is shown in figure C.2. Finally, the nominal RMS spot radius over the field of view is given in figure C.3. The system has been optimized up to the seventh radial order.

TABLE C.2: Freeform mirrors shape description of the large FOV TMA. All data has been rounded to the 4th significant digit

Parameter	**M1**	**M2**	**M3**
surface radius (mm)	56.00	41.00	48.11
base sphere curvature radius (mm)	1.285E+4	-2.459E+2	-1.824E+2
Normalization radius (mm)	33.3	33.3	33.3
k	-1.366E+4	-1.337	1.677E-1
Z1	-1.065E-3	2.731E-2	1.376E-4
Z3	-3.870E-2	-1.588E-1	2.464E-4
Z6	7.187E-3	-1.207E-1	-2.823E-2
Z7	-1.380E-2	-5.911E-2	9.316E-5
Z9	1.474E-2	3.492E-2	4.689E-3
Z11	4.815E-4	-1.262E-2	-6.385E-5
Z12	-4.722E-4	1.561E-3	-2.627E-4
Z14	4.064E-4	-1.346E-3	2.912E-4
Z17	-5.957E-5	-1.662E-3	3.961E-6
Z19	2.375E-6	5.881E-4	3.191E-5
Z21	-2.223E-5	2.474E-4	-1.884E-5
Z22	4.461E-6	-3.436E-4	-1.948E-6
Z24	-5.842E-6	1.170E-4	-1.728E-6
Z26	6.744E-6	-1.816E-5	3.064E-6
Z28	6.619E-7	-2.436E-5	-1.749E-6
Z29	2.635E-6	-3.103E-5	4.344E-7
Z31	2.513E-6	2.911E-5	3.235E-7
Z33	5.454E-6	3.367E-5	-6.185E-8
Z35	1.752E-6	1.731E-5	3.209E-7

The departures from the best spheres for each mirror are pictured on figure C.4 and the surface slopes are given in figure C.5.

Surfaces that are shown here have a few millimeters sag and orthoradial slopes are only a few degrees. Those values are in the range of diamond turning machines capabilities [50]. The main drawback of having large

TABLE C.3: sequential positioning of surfaces (OpticStudio Formatting) for the large FOV TMA. All data has been rounded to the 4th significant digit

Line	Surface Type	Thickness (mm)	Material	Tilt X (deg)
OBJ	Standard	Infinity	-	-
1	Standard	99.9	-	-
2	Coordinate Break	-	-	-21.45
3 M1	Zernike Polynomial	-	MIRROR	-
4	Coordinate Break	-90.02	-	-21.45
5	Coordinate Break	-	-	33.73
6 M2(STOP)	Zernike Polynomial	-	MIRROR	-
7	Coordinate Break	96.22	-	33.73
8	Coordinate Break	-	-	-13.20
9 M3	Zernike Polynomial	-	MIRROR	-
10	Coordinate Break	-75.85	-	-13.20
IMA	Standard	-	-	-

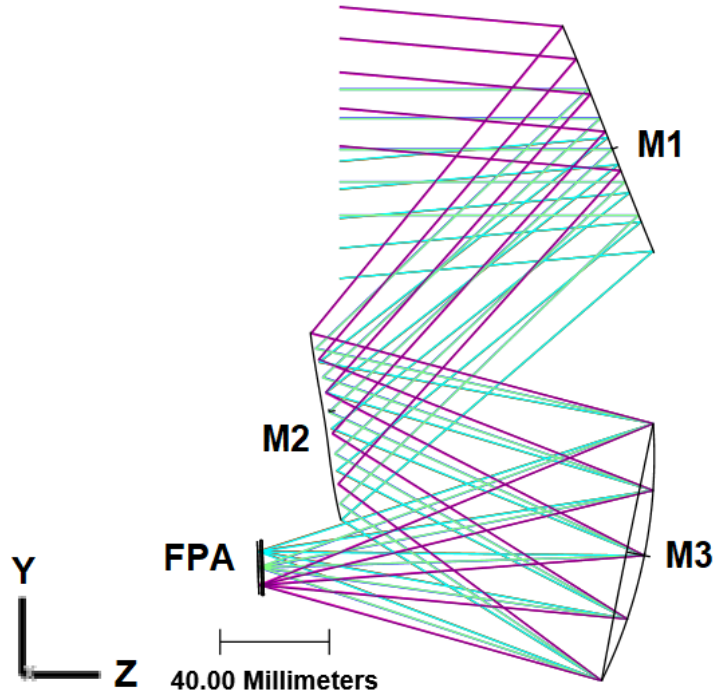

FIGURE C.2: Layout of the large FOV TMA design resulting of the optimization

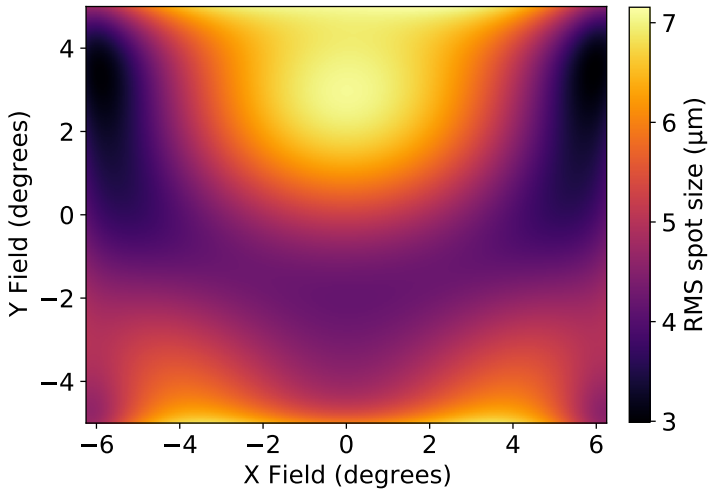

FIGURE C.3: RMS spot radius in the focal plane of the large FOV TMA mirror design over a 12.5x10 degrees field of view

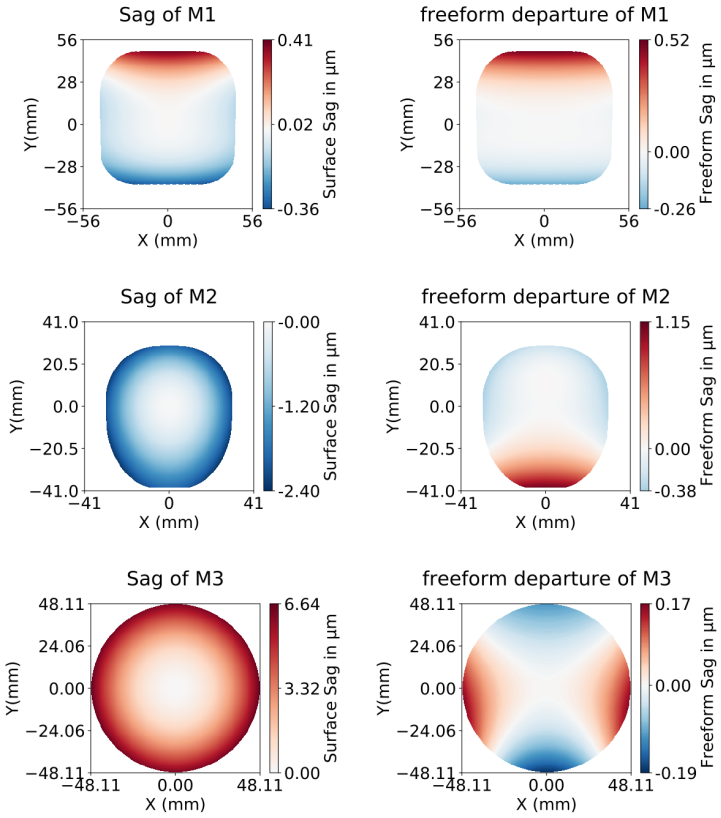

FIGURE C.4: Sag of the mirrors and departure from the best fit sphere for each mirror.

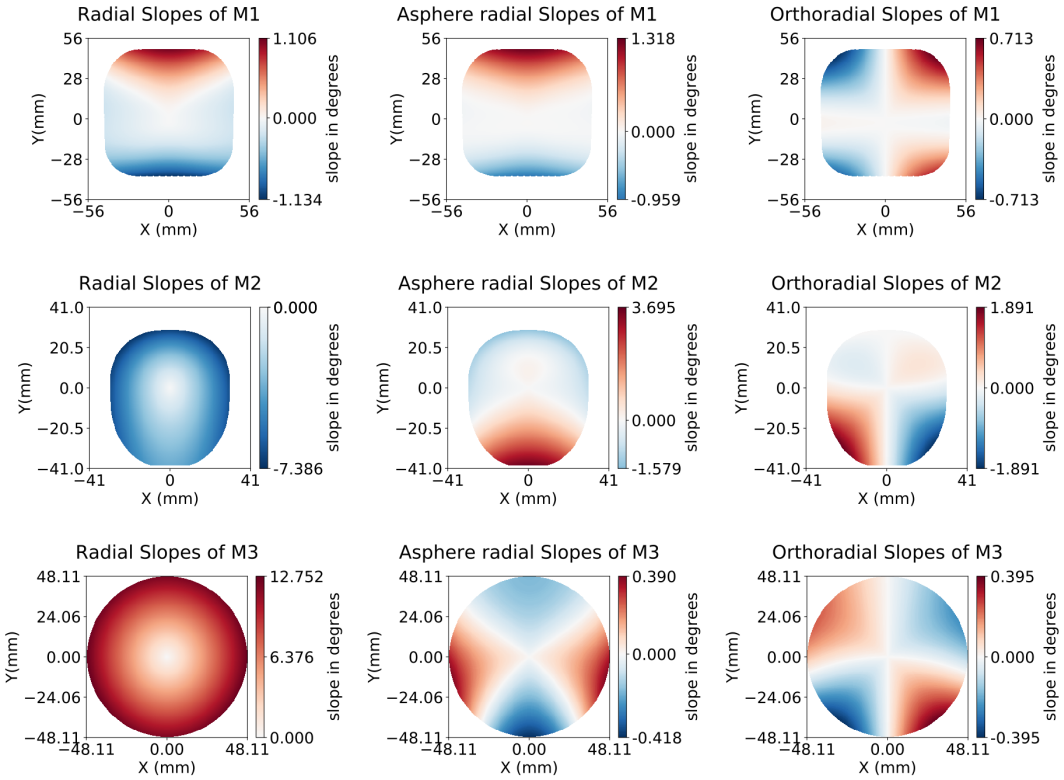

FIGURE C.5: local slopes of the three mirrors

FOV is that the freeform departure on the M2 is very high and this could complicate metrology measurements and manufacturing of this specific mirror, leading to additional manufacturing costs. Constraining the departure of this surface, via methods such as the one presented by Takaki et al. [60], could lead to a cheaper solution with only a slight degradation of the optical quality.

To ensure that the system is manufacturable, manufacturability of each surface is not sufficient. In this work, we performed a tolerance analysis of the system. The tolerances are given in Table C.4 and the compensators are the focus and the tip/tilt of the third mirror.

TABLE C.4: Summary of tolerances

parameter	**value**
Position of the mirrors	100 μm (X,Y,Z)
Tilt of the mirrors	1 mrad
Tilt of the focal plane	0.1 degree

A Monte Carlo approach has been used to analyse the toleranced performance of this system. A total of one thousand systems have been generated, each tolerance parameter being generated using a normal distribution. The results, given in Table C.5, show that alignment tolerances

should not impact the result provided that the third mirror is aligned in tip and tilt.

TABLE C.5: Tolerancing results

Nominal RMS spot radius (field averaged)	5,15 μm
Mean RMS spot radius	6,00 μm
standard deviation	0,52 μm
M3 tilt X standard deviation	0,028 degrees
M3 tilt Y standard deviation	0,019 degrees
focus standard deviation	30 μm

A straylight analysis such as the one from section 3.3.2 can be performed. Figure C.6 show that the specular straylight can still be avoided. Red rays are issued from the detector. All red rays leaving the system are from the useful field of view. The blue rays are the rays reaching directly the M3 from the entrance aperture and cannot reach the area close to the detector.

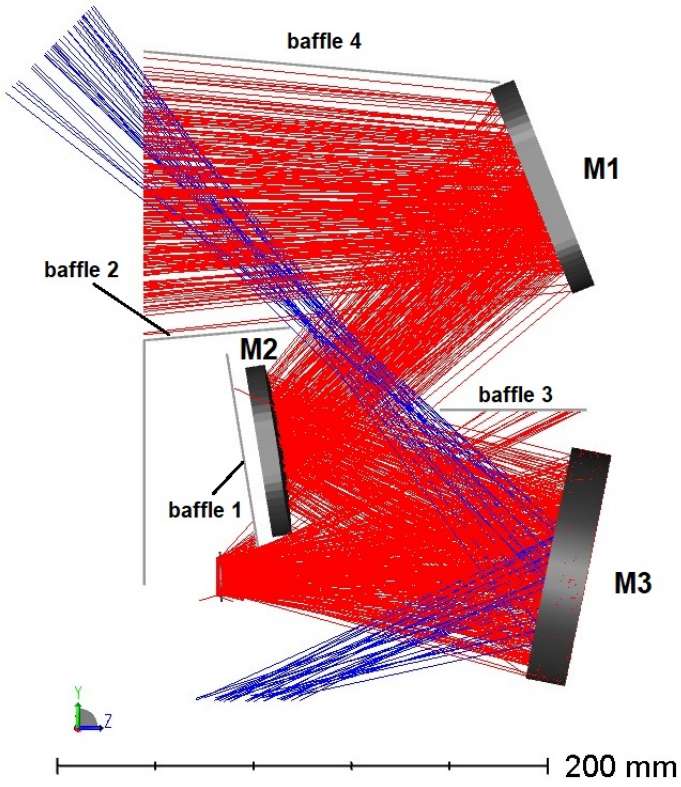

FIGURE C.6: Straylight analysis summary of the large FOV TMA optical system

Appendix D

Alternative planar symmetric designs

D.1 Alternative planar symmetric design with M1 and M3 close to each other

The planar symmetric design has an unconventional layout, with a large space between the M1 and M3. Event though this layout does not increase the overall cubic extent of the design, it is possible to doubt that this solution has a better optical quality than one with the M3 closer to the M1. To ensure that this is not a suboptimal local minimum found by our optimizer, we also optimized another design with a constraint to reduce the distance between M1 and M3, while keeping the effective focal length. The layout of the result is show in Figure D.1.

Table D.2 gives the sequential positioning of the surfaces, and table D.1 give the shapes of the mirrors.

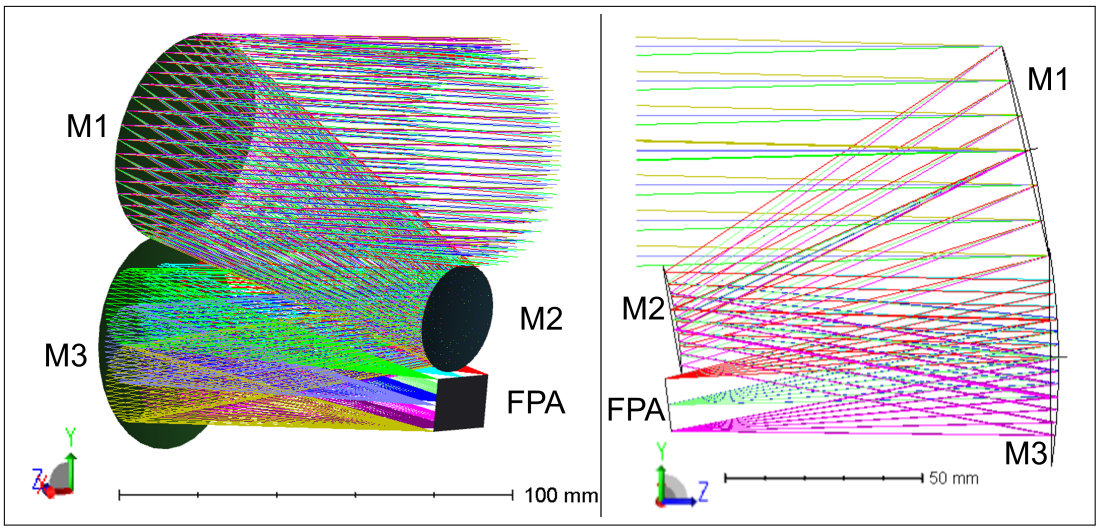

FIGURE D.1: Left: 3D Layout of the alternative planar symmetric design. Right: projection of the design in the YZ plane.

The Figure D.2 shows the RMS spot size of this design. This figure shows that this design has larger RMS spot radius than the design selected, explaining our choice to keep the design used in the main text.

TABLE D.1: Freeform mirrors shape description of the system. All data has been rounded to the 4th significant digit

Parameter	**M1**	**M2**	**M3**
surface radius (mm)	27.15	13.95	27.51
base sphere curvature radius (mm)	-3.033E+2	-9.908E+1	-1.848E+2
Normalization radius (mm)	35	12	15
Z1	-1.215E-3	-4.900E-4	-6.059E-5
Z3	1.859E-2	9.216E-3	2.466E-3
Z5	-2.097E-2	-1.175E-2	-1.798E-3
Z7	6.557E-3	3.237E-3	8.826E-4
Z9	-1.967E-4	-4.256E-4	-2.766E-4
Z11	5.443E-4	2.202E-4	2.638E-5
Z12	6.899E-5	5.285E-5	5.738E-6
Z14	4.906E-6	1.829E-6	9.262E-6
Z17	-1.114E-5	-1.645E-5	3.865E-6
Z19	1.544E-5	1.866E-5	-3.370E-6
Z21	-7.817E-6	-1.258E-5	1.074E-6
Z22	8.956E-7	8.580E-7	-6.066E-7
Z24	1.260E-7	-1.156E-6	6.616E-7
Z26	-2.698E-6	-2.015E-6	-1.281E-6
Z28	4.824E-6	4.6291E-6	1.644E-6
Z29	-1.415E-6	-3.127E-6	-1.339E-6
Z31	2.821E-6	3.211E-6	1.388E-6
Z33	-1.838E-6	-2.076E-6	-1.172E-6
Z35	3.0646E-6	3.559E-6	1.370E-6

TABLE D.2: sequential positioning of surfaces (OpticStudio Formatting). All data has been rounded to the 4th significant digit

Line	Surface Type	Thickness (mm)	Material	Tilt X (deg)
OBJ	Standard	Infinity	-	-
1	Coordinate Break	-	-	0
2	Standard	0	-	-
3	Coordinate Break	-	-	0
4	Standard	99.9	-	-
5	Coordinate Break	-	-	-12.73
6 M1(STOP)	Extended Polynomial	-	MIRROR	-
7	Coordinate Break	-99.52	-	-12.73
8	Coordinate Break	-	-	15.56
9 M2	Extended Polynomial	-	MIRROR	-
10	Coordinate Break	97.53	-	15.56
11	Coordinate Break	-	-	-6.299
12 M3	Extended Polynomial	-	MIRROR	-
13	Coordinate Break	-99.77	-	-6.299
14	Coordinate Break	-	-	0
IMA	Standard	-	-	-

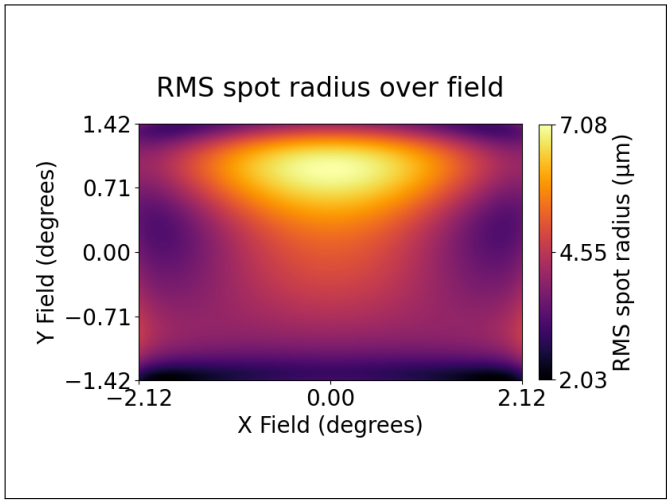

FIGURE D.2: RMS spot radius of the image for the FOV of the planar symmetric design of this appendix. Max RMS spot radius: 7,08μm. Mean RMS spot radius: 4.43μm. Airy spot radius 3.66μm at 0.6μm.

D.2 Alternative planar symmetric design with tilted FOV

As mentioned in the main text, it has been brought to our attention that the planar symmetric design can be improved if the constraint of having the parabasal ray normal to the YZ plane is removed. This section presents such a recalculation of this design, which will be called the tilted FOV planar symmetric design.

Table D.4 gives the sequential positioning of the surfaces, and table D.3 give the shapes of the mirrors.

TABLE D.3: Freeform mirrors shape description of the system. All data has been rounded to the 4th significant digit

Parameter	**M1**	**M2**	**M3**
surface radius (mm)	29.83	15.39	22.33
base sphere curvature radius (mm)	-2.711E+2	-1.148E+2	-2.239E+2
Normalization radius (mm)	30	20	15
X0Y2	1.502E-1	2.453E-1	7.163E-3
X2Y1	5.981E-2	1.902E-1	9.508E-3
XOY3	5.905E-2	1.929E-1	1.645E-2
X4Y0	5.799E-3	3.502E-2	2.513E-3
X2Y2	9.513E-3	4.193E-2	3.653E-3
X0Y4	4.004E-3	9.158E-3	1.570E-3
X4Y1	-2.337E-4	-2.804E-3	1.450E-4
X2Y3	-4.182E-4	-3.160E-3	4.941E-4
X0Y5	-2.417E-4	-1.827E-3	-9.480E-4
X6Y0	3.578E-5	-2.297E-4	-4.192E-5
X4Y2	1.688E-4	2.708E-3	1.382E-4
X2Y4	1.307E-4	2.160E-3	5.274E-6
X0Y6	3.401E-5	2.315E-4	4.762E-5
X6Y1	1.573E-4	-6.302E-4	-1.511E-5
X4Y3	4.709E-4	-2.794E-3	-1.283E-4
X2Y5	4.384E-4	-4.677E-3	-2.498E-4
X0Y7	1.657E-4	9.334E-4	4.928E-4

Figure D.3 presents the layout of the system, figure D.4 presents the RMS spot radius of the system, figure D.5 gives the distorsion and focal length of the system.

The optical quality, distorsion and focal length are comparable between this design and the non planar symmetric design. However, this design needs the removal of a constraint of the initial design. Moreover, it introduces

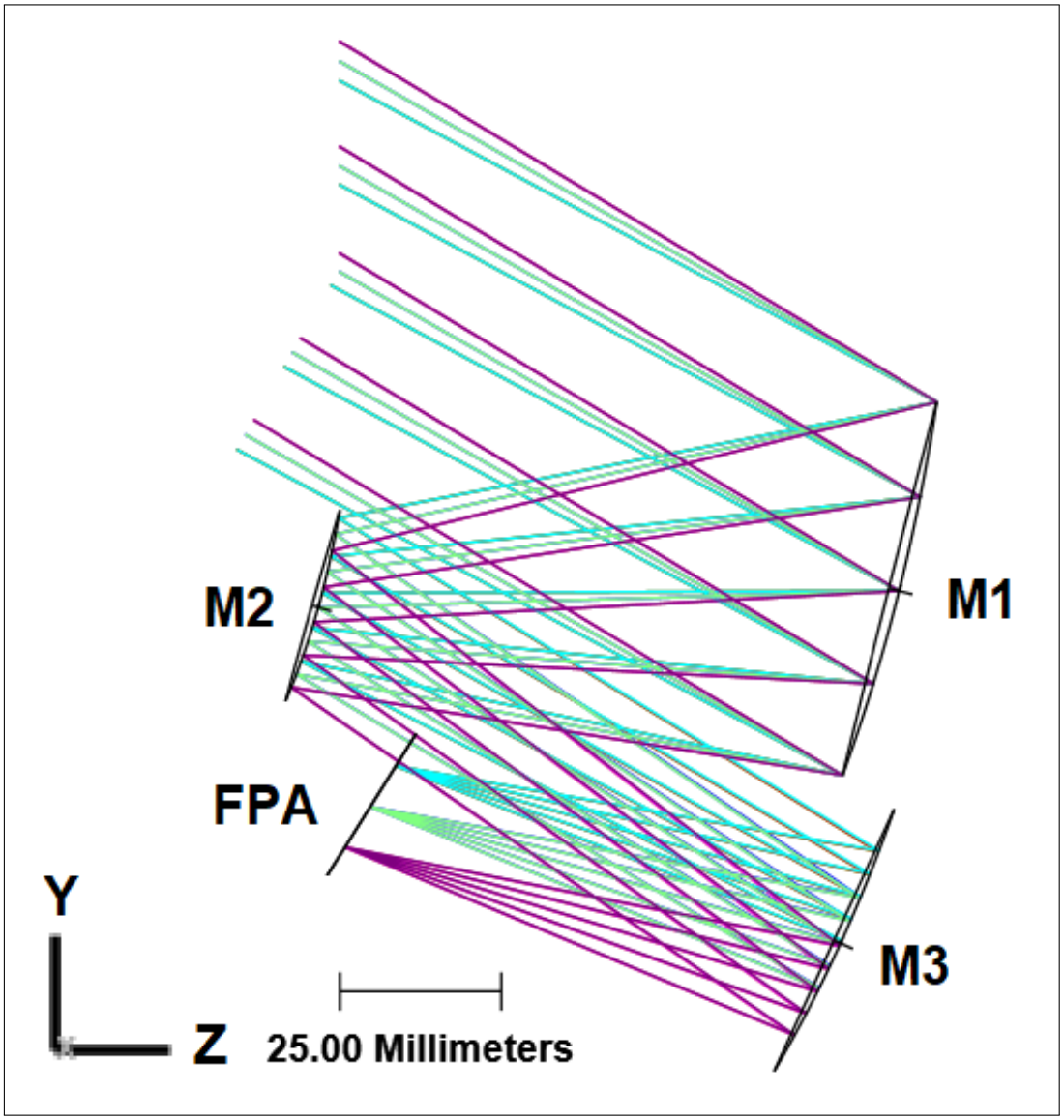

FIGURE D.3: Layout of the tilted FOV planar symmetric design.

TABLE D.4: sequential positioning of surfaces (OpticStudio Formatting). All data has been rounded to the 4th significant digit

Line	**Surface Type**	**Thickness (mm)**	**Material**	**Tilt X (deg)**
OBJ	Standard	Infinity	-	-
1	Coordinate Break	-	-	-29.71
2	Standard	0	-	-
3	Coordinate Break	-	-	29.71
4	Standard	99.9	-	-
5	Coordinate Break	-	-	-15.66
6 M1	Extended Polynomial	-	MIRROR	-
7	Coordinate Break	-134.4	-	-15.66
8	Coordinate Break	-	-	17.19
9 M2(STOP)	Extended Polynomial	-	MIRROR	-
10	Coordinate Break	116.4	-	17.19
11	Coordinate Break	-	-	-8.276
12 M3	Extended Polynomial	-	MIRROR	-
13	Coordinate Break	-155.6	-	-8.276
14	Coordinate Break	-	-	15.85
IMA	Standard	-	-	-

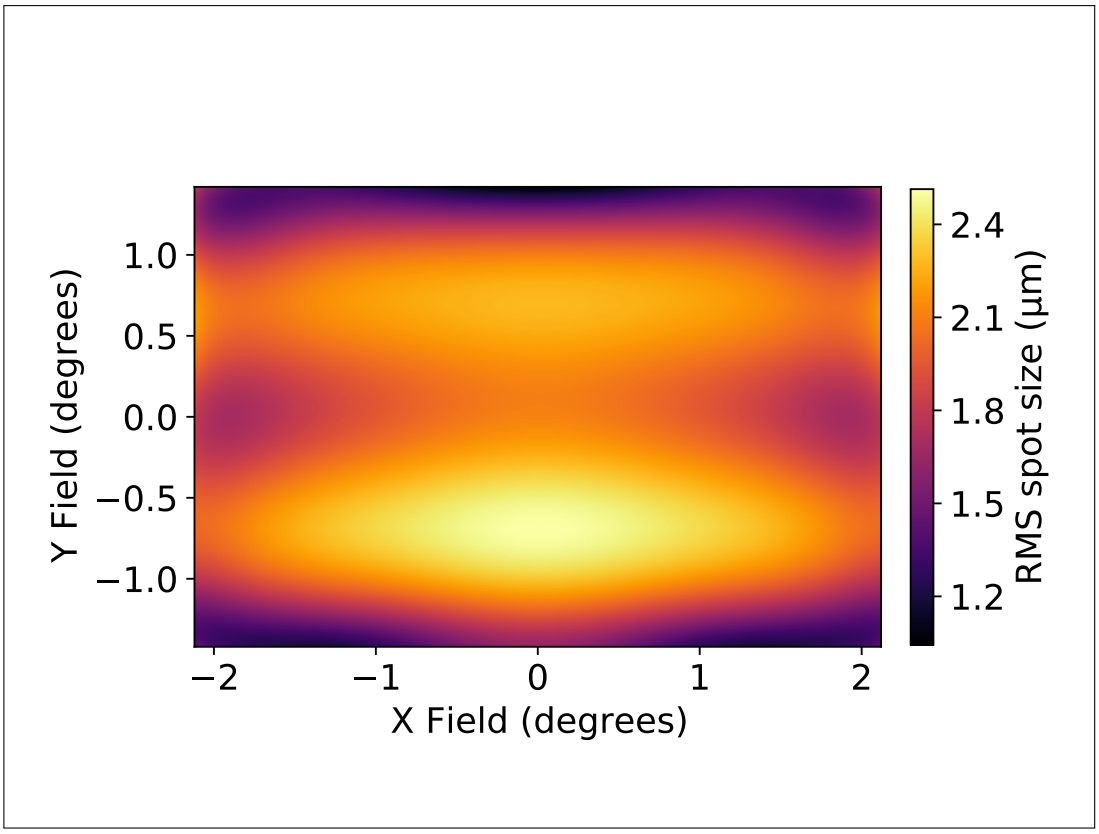

FIGURE D.4: Layout of the tilted FOV planar symmetric design.

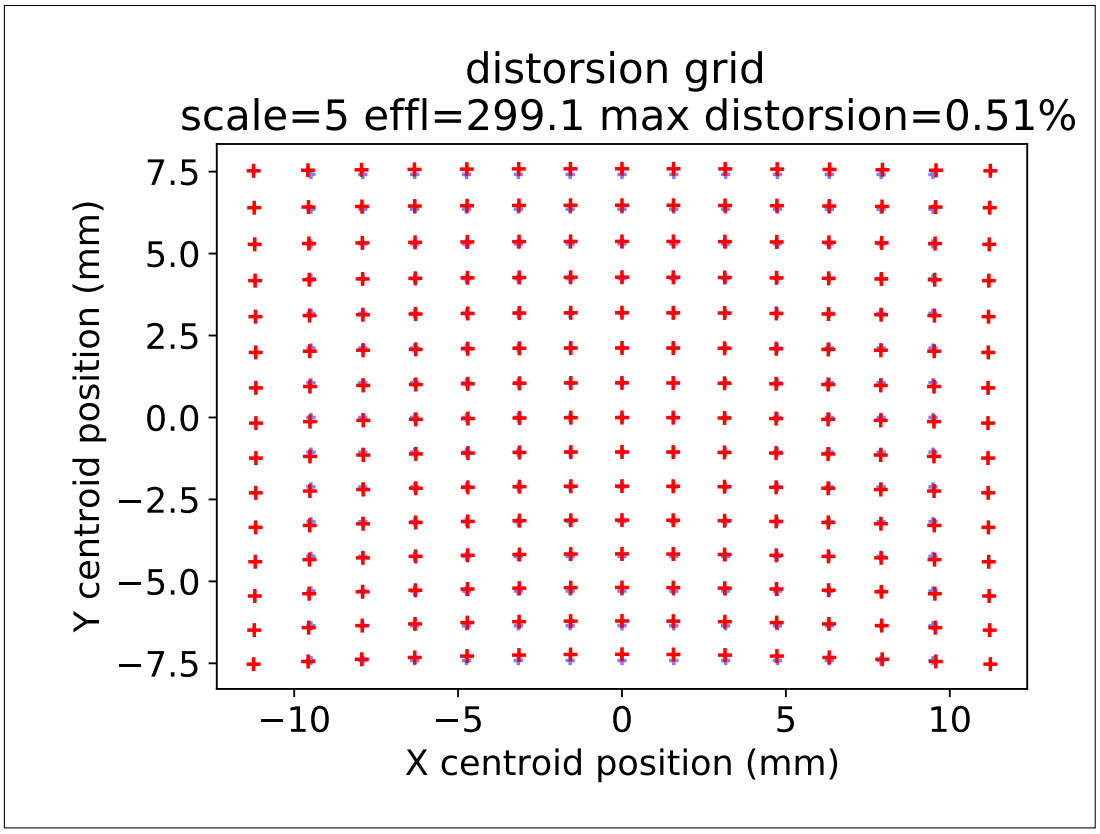

FIGURE D.5: Layout of the tilted FOV planar symmetric design.

a large tilt of the image plane, which could be problematic due to reflections on the detector window or the detector itself. A variation of this design in a non planar symmetric fashion is currently being studied at ONERA.

Bibliography

[1] H. W. Lee, "Improvements in lenses for photography and the like," en, pat. GB355452A, Aug. 1931 (cit. on p. 3).

[2] P. Angenieux, "Wide-angle photographic objective lens assembly," pat. US2649022A, Aug. 1953 (cit. on p. 3).

[3] H. Gross, F. Blechinger, and B. Achtner, "Photographic Lenses," in *Handbook of Optical Systems*, Section: 39 _eprint: https://onlinelibrary.wiley.com/doi/pdf/10.1002/9783527699247.ch4, John Wiley & Sons, Ltd, 2008, pp. 253–390, ISBN: 978-3-527-69924-7. DOI: https://doi.org/10.1002/9783527699247.ch4 (cit. on p. 3).

[4] T. Lepine, *Optical design lessons*, http://paristech.institutoptique.fr/site.php?id=562, Last accessed on 2021-09-08 (cit. on pp. 4, 123).

[5] E. Herman, A. Czajkowski, D. Stroschine, and S. Sparrold, "System design process for refractive simultaneous short and long wave infrared imaging," en, *Applied Optics*, vol. 52, no. 12, p. 2761, Apr. 2013. DOI: 10.1364/AO.52.002761 (cit. on p. 4).

[6] S. Sparrold, E. Herman, A. Czajkowski, and K. O'Shea, "Refractive lens design for simultaneous SWIR and LWIR imaging," B. F. Andresen, G. F. Fulop, and P. R. Norton, Eds., Orlando, Florida, United States, May 2011, p. 801 224. DOI: 10.1117/12.884043 (cit. on p. 4).

[7] A. M. Boyd, "Optical design of athermal, multispectral, radial gradient-index lenses," en, *Optical Engineering*, vol. 57, no. 08, p. 1, Aug. 2018. DOI: 10.1117/1.OE.57.8.085103 (cit. on p. 5).

[8] T. Stone and N. George, "Hybrid diffractive-refractive lenses and achromats," en, *Applied Optics*, vol. 27, no. 14, p. 2960, Jul. 1988. DOI: 10.1364/AO.27.002960 (cit. on p. 5).

[9] N. Davidson, A. A. Friesem, and E. Hasman, "Analytic design of hybrid diffractive–refractive achromats," en, *Applied Optics*, vol. 32, no. 25, p. 4770, Sep. 1993. DOI: 10.1364/AO.32.004770 (cit. on p. 5).

[10] D. Faklis and G. M. Morris, "Spectral properties of multiorder diffractive lenses," en, *Applied Optics*, vol. 34, no. 14, p. 2462, May 1995. DOI: 10.1364/AO.34.002462 (cit. on p. 5).

[11] Z. Wang, Y. Kim, and T. D. Milster, "High-harmonic diffractive lens color compensation," en, *Applied Optics*, vol. 60, no. 19, p. D73, Jul. 2021. DOI: 10.1364/AO.421032 (cit. on p. 5).

[12] M. Meem, A. Majumder, S. Banerji, *et al.*, "Imaging from the visible to the longwave infrared wavelengths via an inverse-designed flat lens," en, *Optics Express*, vol. 29, no. 13, p. 20 715, Jun. 2021. DOI: 10.1364/OE.423764 (cit. on p. 5).

[13] G. Druart, R. Allioux, P. Perrault, V. Lefranc, N. Cariou, and L. Rousset-Rouvière, "Study of infrared optical payloads to be integrated in a nanosat," en, in *Optical Design and Engineering VII*, L. Mazuray, R. Wartmann, and A. P. Wood, Eds., Frankfurt, Germany: SPIE, Jun. 2018, p. 18, ISBN: 978-1-5106-1917-3 978-1-5106-1918-0. DOI: 10.1117/12.2309789 (cit. on pp. 6, 54).

[14] H. Hopkins, *Wave Theory of Aberrations* (Monographs on the physics and chemistry of materials). Clarendon Press, 1950, ISBN: 978-0-598-88851-8 (cit. on p. 7).

[15] W. T. Welford, "Aberrations of the symmetrical optical system," *London: Academic Press*, 1974 (cit. on p. 7).

[16] W. T. Welford, *Aberrations of optical systems* (The Adam Hilger series on optics and optoelectronics). Bristol, Eng. ; Philadelphia: A. Hilger, 1989, ISBN: 978-0-85274-564-9 (cit. on p. 7).

[17] V. N. Mahajan, *Optical imaging and aberrations: Ray geometrical optics*. SPIE press, 1998, vol. 45 (cit. on p. 7).

[18] M. Born, E. Wolf, A. B. Bhatia, *et al.*, *Principles of Optics: Electromagnetic Theory of Propagation, Interference and Diffraction of Light*, 7th ed. Cambridge University Press, Oct. 1999, ISBN: 978-0-521-64222-4 978-0-521-78449-8 978-1-139-64418-1. DOI: 10.1017/CBO9781139644181 (cit. on pp. 7, 20).

[19] R. W. Gray, C. Dunn, K. P. Thompson, and J. P. Rolland, "An analytic expression for the field dependence of Zernike polynomials in rotationally symmetric optical systems," *Opt. Express*, vol. 20, no. 15, pp. 16 436–16 449, Jul. 2012, Publisher: OSA. DOI: 10.1364/OE.20.016436 (cit. on p. 7).

[20] J. Sasián, *Introduction to aberrations in optical imaging systems*. Cambridge University Press, 2013 (cit. on p. 7).

[21] J. Sasián, "Theory of sixth-order wave aberrations: Errata," en, *Applied Optics*, vol. 49, no. 33, p. 6502, Nov. 2010. DOI: 10.1364/AO.49.006502 (cit. on p. 7).

[22] J. Sasián, "Theory of sixth-order wave aberrations," en, *Applied Optics*, vol. 49, no. 16, p. D69, Jun. 2010. DOI: 10.1364/AO.49.000D69 (cit. on p. 7).

[23] R. V. Shack and K. Thompson, "Influence Of Alignment Errors Of A Telescope System On Its Aberration Field," R. N. Shagam and W. C. Sweatt, Eds., San Diego, Dec. 1980, pp. 146–153. DOI: 10.1117/12.959464 (cit. on p. 7).

[24] K. P. Thompson, "Aberration fields in tilted and decentered optical systems," en, Ph.D. dissertation, 1980 (cit. on p. 7).

[25] J. M. Rodgers and K. P. Thompson, *Benefits of freeform mirror surfaces in optical design*, English, 2004 (cit. on p. 7).

[26] K. Thompson, "Description of the third-order optical aberrations of near-circular pupil optical systems without symmetry," en, *Journal of the Optical Society of America A*, vol. 22, no. 7, p. 1389, Jul. 2005. DOI: 10.1364/JOSAA.22.001389 (cit. on p. 7).

[27] K. P. Thompson, T. Schmid, and J. P. Rolland, "The misalignment induced aberrations of TMA telescopes," en, *Optics Express*, vol. 16, no. 25, p. 20 345, Dec. 2008. DOI: 10.1364/OE.16.020345 (cit. on pp. 7, 78).

[28] K. P. Thompson, K. Fuerschbach, T. Schmid, and J. P. Rolland, "Using nodal aberration theory to understand the aberrations of multiple unobscured three mirror anastigmatic (TMA) telescopes," en, in *Optical System Alignment, Tolerancing, and Verification III*, R. N. Youngworth, Ed., San Diego, CA: SPIE, Aug. 2009, 74330B. DOI: 10.1117/12.826749 (cit. on p. 7).

[29] T. Schmid, K. P. Thompson, and J. P. Rolland, "Misalignment-induced nodal aberration fields in two-mirror astronomical telescopes," en, *Applied Optics*, vol. 49, no. 16, p. D131, Jun. 2010. DOI: 10.1364/AO.49.00D131 (cit. on p. 7).

[30] H. Shi, H. Jiang, X. Zhang, C. Wang, and T. Liu, "Analysis of nodal aberration properties in off-axis freeform system design," en, *Applied Optics*, vol. 55, no. 24, p. 6782, Aug. 2016. DOI: 10.1364/AO.55.006782 (cit. on p. 7).

[31] Y. Zhong and H. Gross, "Vectorial aberrations of biconic surfaces," en, *Journal of the Optical Society of America A*, vol. 35, no. 8, p. 1385, Aug. 2018. DOI: 10.1364/JOSAA.35.001385 (cit. on p. 7).

[32] J. Ouaknine, S. Gode, B. Napierala, *et al.*, "MTG Flexible Combined Imager optical design and performances," en, J. J. Butler, X. J. Xiong, and X. Gu, Eds., San Diego, California, United States, Sep. 2013, 88661A. DOI: 10.1117/12.2023078 (cit. on p. 7).

[33] A. Bauer, E. M. Schiesser, and J. P. Rolland, "Starting geometry creation and design method for freeform optics," en, *Nature Communications*, vol. 9, no. 1, p. 1756, Dec. 2018. DOI: 10.1038/s41467-018-04186-9 (cit. on pp. 7, 32, 35, 91, 95, 99).

[34] J. C. Papa, J. M. Howard, and J. P. Rolland, "Three-mirror freeform imagers," in *Optical Design and Engineering VII*, L. Mazuray, R. Wartmann, and A. P. Wood, Eds., Frankfurt, Germany: SPIE, Jun. 2018, p. 43, ISBN: 978-1-5106-1917-3 978-1-5106-1918-0. DOI: 10.1117/12.2314403 (cit. on pp. 7, 91).

[35] J.-B. Volatier, L. Duveau, and G. Druart, "An exploration of the freeform two-mirror off-axis solution space," *Journal of Physics: Photonics*, Nov. 2019. DOI: 10.1088/2515-7647/ab5c0d (cit. on pp. 7, 33, 41, 54).

[36] I. Trumper, A. Q. Anderson, J. M. Howard, G. West, and D. W. Kim, "Design form classification of two-mirror unobstructed freeform telescopes," *Optical Engineering*, vol. 59, no. 02, p. 1, Feb. 2020. DOI: 10.1117/1.OE.59.2.025105 (cit. on p. 7).

[37] L. G. Cook, "Three mirror anastigmatic optical system," pat. US4265510A, May 1981 (cit. on p. 8).

[38] J. P. Rolland, M. A. Davies, T. J. Suleski, *et al.*, "Freeform optics for imaging," en, *Optica*, vol. 8, no. 2, p. 161, Feb. 2021. DOI: 10.1364/OPTICA.413762 (cit. on pp. 9, 12).

[39] K. P. Thompson and J. P. Rolland, "Freeform Optical Surfaces: A Revolution in Imaging Optical Design," en, *Optics and Photonics News*, vol. 23, no. 6, p. 30, Jun. 2012. DOI: 10.1364/OPN.23.6.000030 (cit. on p. 9).

[40] information@eso.org, *M1 Mirror | ELT | ESO*, en, https://elt.eso.org/mirror/M1/, Last accessed on 2021-11-30 (cit. on p. 10).

[41] W. T. Plummer, "Free-form optical components in some early commercial products," en, R. E. Fischer, Ed., San Diego, CA, Aug. 2005, pp. 586 509–586509–7. DOI: 10.1117/12.623875 (cit. on p. 10).

[42] R. Geyl, F. Houbre, Y. Cornil, T. Lepine, and Y. Sortais, "Optiques freeforms : Défis et perspectives," *Photoniques*, no. 106, pp. 17–21, Jan. 2021. DOI: 10.1051/photon/202110617 (cit. on p. 10).

[43] J. Reimers, A. Bauer, K. P. Thompson, and J. P. Rolland, "Freeform spectrometer enabling increased compactness," en, *Light: Science & Applications*, vol. 6, no. 7, e17026–e17026, Jul. 2017. DOI: 10.1038/lsa.2017.26 (cit. on p. 10).

[44] M. P. Chrisp, "Convex diffraction grating imaging spectrometer," pat. US5880834A, Mar. 1999 (cit. on p. 10).

[45] R. Geyl, E. Ruch, R. Bourgois, R. Mercier-Ythier, H. Leplan, and F. Riguet, "Freeform optics design, fabrication and testing technologies for Space applications," in *International Conference on Space Optics—ICSO 2018*, vol. 11180, International Society for Optics and Photonics, 2019, 111800P (cit. on p. 10).

[46] E. M. Schiesser, A. Bauer, and J. P. Rolland, "Effect of freeform surfaces on the volume and performance of unobscured three mirror imagers in comparison with off-axis rotationally symmetric polynomials," en, *Optics Express*, vol. 27, no. 15, p. 21 750, Jul. 2019. DOI: 10.1364/OE.27.021750 (cit. on pp. 10, 80).

[47] S. Wills, "Freeform Optics: Notes from the Revolution," en, *Optics and Photonics News*, vol. 28, no. 7, p. 34, Jul. 2017. DOI: 10.1364/OPN.28.7.000034 (cit. on p. 11).

[48] N. Claytor, D. M. Combs, O. M. Lechuga, J. J. Mader, and J. Udayasankaran, "An overview of freeform optics production," in *Proceedings of the SPIE*, vol. 5494, Citeseer, 2004 (cit. on p. 11).

[49] P. van Grol, F. Bociort, and M. van Turnhout, "Finding order in the design landscape of simple optical systems," P. Z. Mouroulis, R. B. Johnson, and V. N. Mahajan, Eds., San Diego, CA, Aug. 2009, p. 742 808. DOI: 10.1117/12.825495 (cit. on p. 11).

[50] F. Fang, X. Zhang, A. Weckenmann, G. Zhang, and C. Evans, "Manufacturing and measurement of freeform optics," en, *CIRP Annals*, vol. 62, no. 2, pp. 823–846, 2013. DOI: 10.1016/j.cirp.2013.05.003 (cit. on pp. 12, 107, 136, 171).

[51] S. Zhang, S. To, S. Wang, and Z. Zhu, "A review of surface roughness generation in ultra-precision machining," en, *International Journal of Machine Tools and Manufacture*, vol. 91, pp. 76–95, Apr. 2015. DOI: 10.1016/j.ijmachtools.2015.02.001 (cit. on p. 12).

[52] R. A. Jones, "Optimization of computer controlled polishing," en, *Applied Optics*, vol. 16, no. 1, p. 218, Jan. 1977. DOI: 10.1364/AO.16.000218 (cit. on p. 12).

[53] X. Tonnellier, P. Comley, X. Q. Peng, and P. Shore, "Robot based sub-aperture polishing for the rapid production of metre-scale optics," 2013 (cit. on p. 12).

[54] D. C. Harris, "History of magnetorheological finishing," R. W. Tustison, Ed., Orlando, Florida, United States, May 2011, 80160N. DOI: 10.1117/12.882557 (cit. on p. 12).

[55] D. Schaefer, "Basics of ion beam figuring and challenges for real optics treatment," in *Fifth European Seminar on Precision Optics Manufacturing*, C. Schopf and R. Rascher, Eds., Teisnach, Germany: SPIE, Aug. 2018, p. 9, ISBN: 978-1-5106-2270-8 978-1-5106-2271-5. DOI: 10.1117/12.2318572 (cit. on p. 12).

[56] D. Gurganus, S. Novak, A. Symmons, and M. Davies, "Process evaluation and optimization for freeform precision glass molding," in *Optical Manufacturing and Testing XIII*, R. Rascher and D. W. Kim, Eds., Online Only, United States: SPIE, Aug. 2020, p. 31, ISBN: 978-1-5106-3780-1 978-1-5106-3781-8. DOI: 10.1117/12.2568958 (cit. on p. 13).

[57] Y. E. Tohme, J. A. Lowe, Moore, and A. Winchester, "Machining of Freeform Optical Surfaces by Slow Slide Servo Method," 2003 (cit. on p. 13).

[58] J. Bryan, "System and method for forming a non-rotationally symmetric portion of a workpiece," en, pat. US20040003689A1, Jan. 2004 (cit. on pp. 13, 65).

[59] G. E. Davis, J. W. Roblee, and A. R. Hedges, "Comparison of freeform manufacturing techniques in the production of monolithic lens arrays," en, in *Optical Manufacturing and Testing VIII*, J. H. Burge, O. W. Fähnle, and R. Williamson, Eds., San Diego, CA: SPIE, Aug. 2009, p. 742 605. DOI: 10.1117/12.824451 (cit. on pp. 13, 65).

[60] N. Takaki, A. Bauer, and J. P. Rolland, "On-the-fly surface manufacturability constraints for freeform optical design enabled by orthogonal polynomials," en, *Optics Express*, vol. 27, no. 5, p. 6129, Mar. 2019. DOI: 10.1364/OE.27.006129 (cit. on pp. 13, 63, 87, 174).

[61] G. W. Forbes, "Characterizing the shape of freeform optics," en, *Optics Express*, vol. 20, no. 3, p. 2483, Jan. 2012. DOI: 10.1364/OE.20.002483 (cit. on pp. 13, 21, 51).

[62] K. Garrard, T. Bruegge, J. Hoffman, T. Dow, and A. Sohn, "Design tools for freeform optics," en, P. Z. Mouroulis, W. J. Smith, and R. B. Johnson, Eds., San Diego, California, USA, Aug. 2005, 58740A. DOI: 10.1117/12.617680 (cit. on p. 13).

[63] A. J. MacGovern and J. C. Wyant, "Computer Generated Holograms for Testing Optical Elements," en, *Applied Optics*, vol. 10, no. 3, p. 619, Mar. 1971. DOI: 10.1364/AO.10.000619 (cit. on p. 13).

[64] S. Scheiding, M. Beier, U.-D. Zeitner, S. Risse, and A. Gebhardt, "Freeform mirror fabrication and metrology using a high performance test CGH and advanced alignment features," G. von Freymann, W. V. Schoenfeld, and R. C. Rumpf, Eds., San Francisco, California, USA, Mar. 2013, 86130J. DOI: 10.1117/12.2001690 (cit. on p. 13).

[65] B. Toulon, "La mesure d'amplitudes complexes par interférométrie à décalage multi-latéral," PhD Thesis, 2009 (cit. on p. 13).

[66] E. Savio, L. De Chiffre, and R. Schmitt, "Metrology of freeform shaped parts," en, *CIRP Annals*, vol. 56, no. 2, pp. 810–835, 2007. DOI: 10.1016/j.cirp.2007.10.008 (cit. on p. 13).

[67] I. Trumper, B. T. Jannuzi, and D. W. Kim, "Emerging technology for astronomical optics metrology," en, *Optics and Lasers in Engineering*, vol. 104, pp. 22–31, May 2018. DOI: 10.1016/j.optlaseng.2017.09.009 (cit. on p. 14).

[68] C. Supranowitz, J.-P. Lormeau, C. Maloney, P. Murphy, and P. Dumas, "Freeform metrology using subaperture stitching interferometry," en, J. Kovacicinova, Ed., Liberec, Czech Republic, Nov. 2016, p. 101510D. DOI: 10.1117/12.2257279 (cit. on p. 14).

[69] G. Häusler, C. Faber, E. Olesch, and S. Ettl, "Deflectometry vs. interferometry," en, P. H. Lehmann, W. Osten, and A. Albertazzi, Eds., Munich, Germany, May 2013, p. 87881C. DOI: 10.1117/12.2020578 (cit. on p. 14).

[70] D. Perard and J. Beyerer, "Three-dimensional measurement of specular free-form surfaces with a structured-lighting reflection technique," K. G. Harding and D. J. Svetkoff, Eds., Pittsburgh, PA, Dec. 1997, pp. 74–80. DOI: 10.1117/12.294443 (cit. on p. 14).

[71] T. Houllier, N. Rousselet, Y. Surrel, and T. Lépine, "Advanced optical freeform substrates fabricated by ceramic 3D printing and controlled by deflectometry," en, in *Optical Fabrication, Testing, and Metrology VI*, S. Schröder and R. Geyl, Eds., Frankfurt, Germany: SPIE, Jun. 2018, p. 24, ISBN: 978-1-5106-1921-0 978-1-5106-1922-7. DOI: 10.1117/12.2312649 (cit. on pp. 14, 15, 57).

[72] M. Brunelle, J. Yuan, K. Medicus, and J. DeGroote Nelson, "Importance of fiducials on freeform optics," J. L. Bentley and S. Stoebenau, Eds., Rochester, New York, United States, Oct. 2015, p. 963 318. DOI: 10.1117/12.2195350 (cit. on p. 14).

[73] J. Zhu, W. Hou, X. Zhang, and G. Jin, "Design of a low F-number freeform off-axis three-mirror system with rectangular field-of-view," en, *Journal of Optics*, vol. 17, no. 1, p. 015 605, Jan. 2015. DOI: 10.1088/2040-8978/17/1/015605 (cit. on pp. 14, 32, 57, 77).

[74] *CubeSat Information*, en-US, https://www.cubesat.org/cubesatinfo, Last accessed on 2022-01-12 (cit. on p. 14).

[75] A. Zuccaro Marchi, L. Maresi, and M. Taccola, "Technologies and designs for small optical missions," in *International Conference on Space Optics — ICSO 2018*, N. Karafolas, Z. Sodnik, and B. Cugny, Eds., Chania, Greece: SPIE, Jul. 2019, p. 70, ISBN: 978-1-5106-3077-2 978-1-5106-3078-9. DOI: 10.1117/12.2535990 (cit. on p. 14).

[76] M. Esposito and A. Zuccaro Marchi, "In-orbit demonstration of the first hyperspectral imager for nanosatellites," en, in *International Conference on Space Optics — ICSO 2018*, N. Karafolas, Z. Sodnik, and B. Cugny, Eds., Chania, Greece: SPIE, Jul. 2019, p. 71, ISBN: 978-1-5106-3077-2 978-1-5106-3078-9. DOI: 10.1117/12.2535991 (cit. on p. 14).

[77] A. Poghosyan and A. Golkar, "CubeSat evolution: Analyzing CubeSat capabilities for conducting science missions," en, *Progress in Aerospace Sciences*, vol. 88, pp. 59–83, Jan. 2017. DOI: 10.1016/j.paerosci.2016.11.002 (cit. on pp. 14, 54).

[78] M. Beier, J. Hartung, T. Peschel, *et al.*, "Development, fabrication, and testing of an anamorphic imaging snap-together freeform telescope," en, *Applied Optics*, vol. 54, no. 12, p. 3530, Apr. 2015. DOI: 10.1364/AO.54.003530 (cit. on p. 15).

[79] C. M. Dubbeldam, R. Content, J. R. Allington-Smith, S. Pokrovski, and D. J. Robertson, "Integral field unit for the Gemini near-infrared spectrograph," M. Iye and A. F. M. Moorwood, Eds., Munich, Germany, Aug. 2000, p. 1181. DOI: 10.1117/12.395437 (cit. on p. 15).

[80] R. Content, J. R. Allington-Smith, D. J. Robertson, *et al.*, "ESA NGST integral field and multiobject spectrograph slicer system," J. B. Breckinridge and P. Jakobsen, Eds., Munich, Germany, Jul. 2000, pp. 851–860. DOI: 10.1117/12.394052 (cit. on p. 15).

[81] F. Henault, R. Bacon, C. Bonneville, *et al.*, "MUSE: A second-generation integral-field spectrograph for the VLT," M. Iye and A. F. M. Moorwood, Eds., Waikoloa, Hawai'i, United States, Mar. 2003, p. 1096. DOI: 10.1117/12.462334 (cit. on p. 15).

[82] D. R. Lobb, R. G. Talbot, D. J. Robertson, *et al.*, "The integral field unit for the James Webb space telescope's near-infrared spectrograph," in *International Conference on Space Optics — ICSO 2010*, N. Kadowaki, Ed., Rhodes Island, Greece: SPIE, Nov. 2017, p. 85, ISBN: 978-1-5106-1619-6 978-1-5106-1620-2. DOI: 10.1117/12.2309221 (cit. on p. 15).

[83] W. Jahn, M. Ferrari, and E. Hugot, "Innovative focal plane design for large space telescope using freeform mirrors," en, *Optica*, vol. 4, no. 10, p. 1188, Oct. 2017. DOI: 10.1364/OPTICA.4.001188 (cit. on p. 15).

[84] Y. Xie, X. Mao, J. Li, *et al.*, "Optical design and fabrication of an all-aluminum unobscured two-mirror freeform imaging telescope," en, *Applied Optics*, vol. 59, no. 3, p. 833, Jan. 2020. DOI: 10.1364/AO.379324 (cit. on p. 15).

[85] T. Nakano and Y. Tamagawa, "Configuration of an off-axis three-mirror system focused on compactness and brightness," en, *Applied Optics*, vol. 44, no. 5, p. 776, Feb. 2005. DOI: 10.1364/AO.44.000776 (cit. on pp. 15, 93).

[86] K. Fuerschbach, J. P. Rolland, and K. P. Thompson, "A new family of optical systems employing phi-polynomial surfaces," en, *Optics Express*, vol. 19, no. 22, p. 21 919, Oct. 2011. DOI: 10.1364/OE.19.021919 (cit. on pp. 15, 93).

[87] K. Fuerschbach, G. E. Davis, and K. P. Thompson, "Pamplemousse: The optical design, fabrication, and assembly of a three-mirror freeform imaging telescope," en, M. Figueiro, S. Lerner, J. Muschaweck, and J. Rogers, Eds., Kohala Coast, Hawaii, United States, Dec. 2014, p. 92930L. DOI: 10.1117/12.2074479 (cit. on pp. 15, 32, 93, 94).

[88] R. Steinkopf, L. Dick, T. Kopf, A. Gebhardt, S. Risse, and R. Eberhardt, "Data handling and representation of freeform surfaces," A. Duparré and R. Geyl, Eds., Marseille, France, Sep. 2011, p. 81690X. DOI: 10.1117/12.896848 (cit. on pp. 17, 20).

[89] H. Gross, A. Brömel, M. Beier, *et al.*, "Overview on surface representations for freeform surfaces," en, in *SPIE Optical Systems Design*, L. Mazuray, R. Wartmann, and A. P. Wood, Eds., Jena, Germany, Sep. 2015, 96260U. DOI: 10.1117/12.2191255 (cit. on pp. 17, 20).

[90] J. Ye, L. Chen, X. Li, Q. Yuan, and Z. Gao, "Review of optical freeform surface representation technique and its application," en, *Optical Engineering*, vol. 56, no. 11, p. 1, Nov. 2017. DOI: 10.1117/1.OE.56.11.110901 (cit. on pp. 17, 20).

[91] T. Houllier, "Freeform imaging optical systems, Optical design and deflectometry for surface metrology," en, Ph.D. dissertation, 2021 (cit. on pp. 17, 20, 22).

[92] O. Cakmakci, B. Moore, H. Foroosh, and J. P. Rolland, "Optimal local shape description for rotationally non-symmetric optical surface design and analysis," en, *Optics Express*, vol. 16, no. 3, p. 1583, 2008. DOI: 10.1364/OE.16.001583 (cit. on p. 18).

[93] O. Cakmakci, S. Vo, H. Foroosh, and J. Rolland, "Application of radial basis functions to shape description in a dual-element off-axis magnifier," en, *Optics Letters*, vol. 33, no. 11, p. 1237, Jun. 2008. DOI: 10.1364/OL.33.001237 (cit. on p. 18).

[94] I. Kaya and J. P. Rolland, "Hybrid Radial Basis Function and Local phi-Polynomial Surfaces," en, in *Renewable Energy and the Environment: Postdeadline Papers*, Tucson, Arizona: OSA, 2013, FW2B.4, ISBN: 978-1-55752-990-9. DOI: 10.1364/FREEFORM.2013.FW2B.4 (cit. on p. 18).

[95] J. Ni, T. Yang, Y. Liu, D. Cheng, and Y. Wang, "Description and tolerance analysis of freeform surface figure error using specific-probability-distributed Gaussian radial basis functions," en, *Optics Express*, vol. 27, no. 22, p. 31 820, Oct. 2019. DOI: 10.1364/OE.27.031820 (cit. on p. 18).

[96] J. Ni, T. Yang, D. Cheng, and Y. Wang, "Design of freeform nonsymmetric three-mirror systems using Gaussian radial basis functions freeform surfaces," in *2019 International Conference on Optical Instruments and Technology: Optical Systems and Modern Optoelectronic Instruments*, T. Nomura, J. Liu, B. Jia, X. Yao, and Y. Wang, Eds., Beijing, China: SPIE, Mar. 2020, p. 13, ISBN: 978-1-5106-3646-0 978-1-5106-3647-7. DOI: 10.1117/12.2540906 (cit. on p. 18).

[97] A. Brömel, "Development and evaluation of freeform surface descriptions," en, Ph.D. dissertation, Friedrich-Schiller-Universität Jena, 2018. DOI: 10.22032/DBT.38072 (cit. on pp. 19, 40, 49, 169).

[98] V. N. Mahajan and G.-m. Dai, "Orthonormal polynomials for hexagonal pupils," en, *Optics Letters*, vol. 31, no. 16, p. 2462, Aug. 2006. DOI: 10.1364/OL.31.002462 (cit. on p. 19).

[99] V. N. Mahajan and G.-m. Dai, "Orthonormal polynomials in wavefront analysis: Analytical solution," *JOSA A*, vol. 24, no. 9, pp. 2994–3016, 2007, Publisher: Optical Society of America. DOI: https://doi.org/10.1364/JOSAA.24.002994 (cit. on p. 19).

[100] G.-m. Dai and V. N. Mahajan, "Nonrecursive determination of orthonormal polynomials with matrix formulation," en, *Optics Letters*, vol. 32, no. 1, p. 74, Jan. 2007, II7. DOI: 10.1364/OL.32.000074 (cit. on p. 19).

[101] G.-m. Dai and V. N. Mahajan, "Orthonormal polynomials in wavefront analysis: Error analysis," *Appl. Opt.*, vol. 47, no. 19, pp. 3433–3445, Jul. 2008, Publisher: OSA. DOI: 10.1364/AO.47.003433 (cit. on p. 19).

[102] R. J. Noll, "Zernike polynomials and atmospheric turbulence*," en, *Journal of the Optical Society of America*, vol. 66, no. 3, p. 207, Mar. 1976. DOI: 10.1364/JOSA.66.000207 (cit. on p. 20).

[103] G. W. Forbes, "Shape specification for axially symmetric optical surfaces," en, *Optics Express*, vol. 15, no. 8, p. 5218, 2007. DOI: 10.1364/OE.15.005218 (cit. on p. 21).

[104] G. W. Forbes, "Robust and fast computation for the polynomials of optics," en, *Optics Express*, vol. 18, no. 13, p. 13 851, Jun. 2010. DOI: 10.1364/OE.18.013851 (cit. on pp. 21, 51).

[105] G. Forbes, "Better Ways to Specify Aspheric Shapes Can Facilitate Design, Fabrication and Testing Alike," en, in *International Optical Design Conference and Optical Fabrication and Testing*, Jackson Hole, WY: OSA, 2010, JMA1, ISBN: 978-1-55752-893-3. DOI: 10.1364/IODC.2010.JMA1 (cit. on p. 21).

[106] K. P. Thompson, F. Fournier, J. P. Rolland, and G. W. Forbes, "The Forbes Polynomial: A More Predictable Surface For Fabricators," en, in *International Optical Design Conference and Optical Fabrication and Testing*, Jackson Hole, WY: OSA, 2010, OTuA6, ISBN: 978-1-55752-893-3. DOI: 10.1364/OFT.2010.OTuA6 (cit. on p. 21).

[107] R. Bridson, "Fast Poisson disk sampling in arbitrary dimensions," en, in *ACM SIGGRAPH 2007 sketches on - SIGGRAPH '07*, San Diego, California: ACM Press, 2007, 22–es, ISBN: 978-1-4503-4726-6. DOI: 10.1145/1278780.1278807 (cit. on p. 28).

[108] P. Zun, *Poisson disc sampling*, https://github.com/diregoblin/poisson_disc_sampling, Last accessed on 2021-11-05, Aug. 2021 (cit. on p. 28).

[109] G. W. Forbes, J. Ruoff, A. Flesch, and N. Kerwien, "Ray selection for optimization of rotationally symmetric systems," en, *Advanced Optical Technologies*, vol. 5, no. 3, Jan. 2016. DOI: 10.1515/aot-2016-0019 (cit. on p. 29).

[110] G. W. Forbes, "Optical system assessment for design: Numerical ray tracing in the Gaussian pupil," en, *Journal of the Optical Society of America A*, vol. 5, no. 11, p. 1943, Nov. 1988. DOI: 10.1364/JOSAA.5.001943 (cit. on p. 29).

[111] Y. Zhong and H. Gross, "Initial system design method for non-rotationally symmetric systems based on Gaussian brackets and Nodal aberration theory," en, *Optics Express*, vol. 25, no. 9, p. 10 016, May 2017. DOI: 10.1364/OE.25.010016 (cit. on pp. 33, 34).

[112] J.-B. Volatier, Á. Menduiña-Fernández, and M. Erhard, "Generalization of differential ray tracing by automatic differentiation of computational graphs," en, *Journal of the Optical Society of America A*, vol. 34, no. 7, p. 1146, Jul. 2017. DOI: 10.1364/JOSAA.34.001146 (cit. on p. 33).

[113] J.-B. Volatier and G. Druart, "Differential method for freeform optics applied to two-mirror off-axis telescope design," en, *Optics Letters*, vol. 44, no. 5, p. 1174, Mar. 2019. DOI: 10.1364/OL.44.001174 (cit. on p. 33).

[114] P. Benı´tez, "Simultaneous multiple surface optical design method in three dimensions," en, *Optical Engineering*, vol. 43, no. 7, p. 1489, Jul. 2004. DOI: 10.1117/1.1752918 (cit. on pp. 33, 147).

[115] J. C. Miñano, P. Benítez, W. Lin, J. Infante, F. Muñoz, and A. Santamaría, "An application of the SMS method for imaging designs," en, *Optics Express*, vol. 17, no. 26, p. 24 036, Dec. 2009. DOI: 10.1364/OE.17.024036 (cit. on p. 33).

[116] F. Corrente, P. Benítez, W. Lin, J. C. Miñano, and F. Muñoz, "SMS design and aberrations theory," en, L. Mazuray, R. Wartmann, A. P. Wood, *et al.*, Eds., Barcelona, Spain, Dec. 2012, p. 855 010. DOI: 10.1117/12.981163 (cit. on p. 33).

[117] L. Wang, "Advances in the Simultaneous Multiple Surface optical design method for imaging and non-imaging applications," PhD Thesis, Doctoral thesis, Universidad Politécnica de Madrid, 2012 (cit. on p. 33).

[118] Z. Hou, M. Nikolic, P. Benitez, and F. Bociort, "SMS2D designs as starting points for lens optimization," en, *Optics Express*, vol. 26, no. 25, p. 32 463, Dec. 2018. DOI: 10.1364/OE.26.032463 (cit. on p. 33).

[119] M. Nikolić, "SMS for imaging systems using free-forms," PhD Thesis, Universidad Politécnica de Madrid, 2017. DOI: 10.20868/UPM.thesis.46748 (cit. on p. 33).

[120] R. Mohedano, P. Benítez, M. Nikolic, *et al.*, "Notes on the design of free-form optics," en, in *AI and Optical Data Sciences*, K.-i. Kitayama and B. Jalali, Eds., San Francisco, United States: SPIE, Feb. 2020, p. 3, ISBN: 978-1-5106-3361-2 978-1-5106-3362-9. DOI: 10.1117/12.2547832 (cit. on p. 33).

[121] T. Yang, D. Cheng, and Y. Wang, "Direct generation of starting points for freeform off-axis three-mirror imaging system design using neural network based deep-learning," en, *Optics Express*, vol. 27, no. 12, p. 17 228, Jun. 2019. DOI: 10.1364/OE.27.017228 (cit. on p. 33).

[122] M. v. Turnhout, "A systematic analysis of the optical Merit function landscape: Towards improved optimization methods in optical design.," English, ISBN: 9789078314110 OCLC: 840411749, Ph.D. dissertation, [s.n.], S.l., 2009 (cit. on p. 34).

[123] Y. Nie, D. R. Shafer, H. Ottevaere, H. Thienpont, and F. Duerr, "Automated freeform imaging system design with generalized ray tracing and simultaneous multi-surface analytic calculation," en, *Optics Express*, vol. 29, no. 11, p. 17 227, May 2021. DOI: 10.1364/OE.426207 (cit. on p. 34).

[124] S. Yamazaki, K. Inoguchi, Y. Saito, H. Morishima, and N. Taniguchi, "Thin wide-field-of-view HMD with free-form-surface prism and applications," J. O. Merritt, M. T. Bolas, and S. S. Fisher, Eds., San Jose, CA, May 1999, pp. 453–462. DOI: 10.1117/12.349411 (cit. on p. 34).

[125] H Morishima, T Akiyama, N Nanba, and T Tanaka, "The design of off-axial optical system consisting of aspherical mirrors without rotational symmetry," in *20th Optical Symposium, Extended Abstracts*, vol. 21, 1995, pp. 53–56 (cit. on p. 34).

[126] H. Hoshi, N. Taniguchi, H. Morishima, T. Akiyama, S. Yamazaki, and A. Okuyama, "Off-axial HMD optical system consisting of aspherical surfaces without rotational symmetry," en, M. T. Bolas, S. S. Fisher, and J. O. Merritt, Eds., San Jose, CA, Apr. 1996, pp. 234–242. DOI: 10.1117/12.237443 (cit. on p. 34).

[127] K. Takahashi, *Image display apparatus comprising an internally reflecting ocular optical system*, US Patent 5,699,194, Dec. 1997 (cit. on p. 34).

[128] A. Okuyama and S. Yamazaki, *Optical system, and image observing apparatus and image pickup apparatus using it*, US Patent 5,706,136, Jan. 1998 (cit. on p. 34).

[129] D.-w. Cheng, Y.-t. Wang, J. Chang, Y. Liu, and K. Xu, "Design of a lightweight and wide field-of-view HMD system with free-form-surface prism," *Infrared and Laser Engineering*, vol. 36, no. 3, p. 309, 2007, Publisher: EDITORIAL BOARD OF JOURNAL OF INFRARED AND LASER ENGINEERING (cit. on p. 34).

[130] D. Reshidko and J. Sasian, "Method for the design of nonaxially symmetric optical systems using free-form surfaces," *Optical Engineering*, vol. 57, no. 10, p. 1, May 2018. DOI: 10.1117/1.OE.57.10.101704 (cit. on pp. 34, 40).

[131] D. Reshidko and J. Sasian, "Method for the design of nonaxially symmetric optical systems using free-form surfaces (Erratum)," *Optical Engineering*, vol. 60, no. 11, pp. 1 –5, 2021, Publisher: SPIE. DOI: 10.1117/1.OE.60.11.119801 (cit. on pp. 34, 40).

[132] N. Takaki, A. Bauer, and J. P. Rolland, "Degeneracy in freeform surfaces described with orthogonal polynomials," en, *Applied Optics*, vol. 57, no. 35, p. 10 348, Dec. 2018. DOI: 10.1364/AO.57.010348 (cit. on p. 35).

[133] E. Muslimov, E. Hugot, W. Jahn, *et al.*, "Combining freeform optics and curved detectors for wide field imaging: A polynomial approach over squared aperture," en, *Optics Express*, vol. 25, no. 13, p. 14 598, Jun. 2017. DOI: 10.1364/OE.25.014598 (cit. on pp. 40, 49, 169).

[134] I. Kaya, K. P. Thompson, and J. P. Rolland, "Edge clustered fitting grids for phi-polynomial characterization of freeform optical surfaces," en, *Optics Express*, vol. 19, no. 27, p. 26 962, Dec. 2011. DOI: 10.1364/OE.19.026962 (cit. on p. 40).

[135] I. Kaya, K. P. Thompson, and J. P. Rolland, "Comparative assessment of freeform polynomials as optical surface descriptions," en, *Optics Express*, vol. 20, no. 20, p. 22 683, Sep. 2012. DOI: 10.1364/OE.20.022683 (cit. on p. 40).

[136] T. Houllier and T. Lépine, "Comparing optimization algorithms for conventional and freeform optical design," en, *Optics Express*, vol. 27, no. 13, p. 18 940, Jun. 2019. DOI: 10.1364/OE.27.018940 (cit. on pp. 49, 52).

[137] N. J. Higham, *Accuracy and stability of numerical algorithms*, 2nd ed. Philadelphia: Society for Industrial and Applied Mathematics, 2002, ISBN: 978-0-89871-521-7 (cit. on p. 50).

[138] G. W. Forbes, "Robust, efficient computational methods for axially symmetric optical aspheres," en, *Optics Express*, vol. 18, no. 19, p. 19 700, Sep. 2010. DOI: 10.1364/OE.18.019700 (cit. on p. 51).

[139] T. B. Andersen, "Efficient and robust recurrence relations for the Zernike circle polynomials and their derivatives in Cartesian coordinates," en, *Optics Express*, vol. 26, no. 15, p. 18 878, Jul. 2018. DOI: 10.1364/OE.26.018878 (cit. on p. 51).

[140] A. C. R. Newbery, "Error analysis for polynomial evaluation," en, *Mathematics of Computation*, vol. 28, no. 127, pp. 789–793, 1974. DOI: 10.1090/S0025-5718-1974-0373227-8 (cit. on p. 51).

[141] J. Oliver, "Rounding error propagation in polynomial evaluation schemes," en, *Journal of Computational and Applied Mathematics*, vol. 5, no. 2, pp. 85–97, Jun. 1979. DOI: 10.1016/0771-050X(79)90002-0 (cit. on p. 51).

[142] C. Mesztenyi and C. Witzgall, "Stable evaluation of polynomials," en, *Journal of Research of the National Bureau of Standards Section B Mathematics and Mathematical Physics*, vol. 71B, no. 1, p. 11, Jan. 1967. DOI: 10.6028/jres.071B.003 (cit. on p. 51).

[143] J. B. Scarborough, *Numerical mathematical analysis*. Johns Hopkins Press Baltimore, 1966, vol. 493 (cit. on p. 51).

[144] M. Santamouris, "Regulating the damaged thermostat of the cities—Status, impacts and mitigation challenges," en, *Energy and Buildings*, vol. 91, pp. 43–56, Mar. 2015. DOI: 10.1016/j.enbuild.2015.01.027 (cit. on p. 53).

[145] K. De Ridder, B. Maiheu, D. Lauwaet, *et al.*, "Urban Heat Island Intensification during Hot Spells—The Case of Paris during the Summer of 2003," en, *Urban Science*, vol. 1, no. 1, p. 3, Nov. 2016. DOI: 10.3390/urbansci1010003 (cit. on p. 53).

[146] M. L. Imhoff, P. Zhang, R. E. Wolfe, and L. Bounoua, "Remote sensing of the urban heat island effect across biomes in the continental USA," en, *Remote Sensing of Environment*, vol. 114, no. 3, pp. 504–513, Mar. 2010. DOI: 10.1016/j.rse.2009.10.008 (cit. on p. 53).

[147] A. Mohajerani, J. Bakaric, and T. Jeffrey-Bailey, "The urban heat island effect, its causes, and mitigation, with reference to the thermal properties of asphalt concrete," en, *Journal of Environmental Management*, vol. 197, pp. 522–538, Jul. 2017. DOI: 10.1016/j.jenvman.2017.03.095 (cit. on p. 53).

[148] J.-P. Lagouarde, B. Bhattacharya, P. Crebassol, *et al.*, "The Indian-French Trishna Mission: Earth Observation in the Thermal Infrared with High Spatio-Temporal Resolution," in *IGARSS 2018 - 2018 IEEE International Geoscience and Remote Sensing Symposium*, Valencia: IEEE, Jul. 2018, pp. 4078–4081, ISBN: 978-1-5386-7150-4. DOI: 10.1109/IGARSS.2018.8518720 (cit. on p. 53).

[149] Omkar, D. M. S. S. KULKARNI, and Ashokavanjare, "Hyperspectral Signal Processing to Identify Land Cover Pattern," Tech. Rep., 2014, doi:10.13140/RG.2.1.3397.2968 (cit. on p. 55).

[150] L. Duveau, G. Druart, T. Lépine, E. Hugot, and X. Briottet, "Design strategies of three mirror telescopes with freeform surfaces," Jan. 2020 (cit. on p. 57).

[151] L. Duveau, T. Lépine, E. Hugot, X. Briottet, and G. Druart, "Design strategies of an unobscured three mirror telescope with freeform surfaces for infrared nanosatellite imagery," en, in *International Conference on Space Optics — ICSO 2020*, Z. Sodnik, B. Cugny, and N. Karafolas, Eds., Online Only, France: SPIE, Jun. 2021, p. 11, ISBN: 978-1-5106-4548-6 978-1-5106-4549-3. DOI: 10.1117/12.2599153 (cit. on p. 57).

[152] D. L. Morstad and D. L. Helder, "Use of Pseudo-Invariant Sites for Long-Term Sensor Calibration," in *IGARSS 2008 - 2008 IEEE International Geoscience and Remote Sensing Symposium*, Boston, MA, USA: IEEE, 2008, pp. I–253–I–256, ISBN: 978-1-4244-2807-6. DOI: 10.1109/IGARSS.2008.4778841 (cit. on p. 62).

[153] S. Lacherade, B. Fougnie, P. Henry, and P. Gamet, "Cross Calibration Over Desert Sites: Description, Methodology, and Operational Implementation," *IEEE Transactions on Geoscience and Remote Sensing*, vol. 51, no. 3, pp. 1098–1113, Mar. 2013. DOI: 10.1109/TGRS.2012.2227061 (cit. on p. 62).

[154] J. McCorkel, B. Cairns, and A. Wasilewski, "Imager-to-radiometer in-flight cross calibration: RSP radiometric comparison with airborne and satellite sensors," en, *Atmospheric Measurement Techniques*, vol. 9, no. 3, pp. 955–962, Mar. 2016. DOI: 10.5194/amt-9-955-2016 (cit. on p. 62).

[155] M. M. Farhad, M. Kaewmanee, L. Leigh, and D. Helder, "Radiometric Cross Calibration and Validation Using 4 Angle BRDF Model between Landsat 8 and Sentinel 2A," en, *Remote Sensing*, vol. 12, no. 5, p. 806, Mar. 2020. DOI: 10.3390/rs12050806 (cit. on p. 62).

[156] L. Clermont and L. Aballea, "Stray light control and analysis for an off-axis three-mirror anastigmat telescope," *Optical Engineering*, vol. 60, no. 05, May 2021. DOI: 10.1117/1.OE.60.5.055106 (cit. on p. 62).

[157] J. Kumler, "Designing and specifying aspheres for manufacturability," P. Z. Mouroulis, W. J. Smith, and R. B. Johnson, Eds., San Diego, California, USA, Aug. 2005, p. 58740C. DOI: 10.1117/12.615197 (cit. on p. 65).

[158] K. Fuerschbach, G. E. Davis, K. P. Thompson, and J. P. Rolland, "Assembly of a freeform off-axis optical system employing three \varphi-polynomial Zernike mirrors," en, *Optics Letters*, vol. 39, no. 10, p. 2896, May 2014. DOI: 10.1364/OL.39.002896 (cit. on pp. 72, 90, 93, 125).

[159] Q. Meng, W. Wang, H. Ma, and J. Dong, "Easy-aligned off-axis three-mirror system with wide field of view using freeform surface based on integration of primary and tertiary mirror," en, *Applied Optics*, vol. 53, no. 14, p. 3028, May 2014. DOI: 10.1364/AO.53.003028 (cit. on p. 77).

[160] Q. Meng, H. Wang, W. Liang, Z. Yan, and B. Wang, "Design of off-axis three-mirror systems with ultrawide field of view based on an expansion process of surface freeform and field of view," en, *Applied Optics*, vol. 58, no. 3, p. 609, Jan. 2019. DOI: 10.1364/AO.58.000609 (cit. on p. 91).

[161] Naguyi, *Smallest enclosing circle*, https://www.nayuki.io/page/smallest-enclosing-circle, Last accessed on 2021-09-03 (cit. on p. 95).

[162] I. RIBET, M. CAES, S. DERELLE, S. BERNHARDT, and J. JAECK, "Detecteurs matriciels pour l infrarouge," *Techniques de l'ingenieur Composants optoelectroniques*, vol. base documentaire : TIB451DUO. No. ref. article : e4060, 2021 (cit. on pp. 115, 130, 133).

[163] B. Woollatt, *Reverse Lens Technique for Macro Photography*, https://photographylife.com/reverse-lens-technique-for-macro-photography, Last accessed on 2021-09-03, Feb. 2019 (cit. on p. 117).

[164] T. S. Chihara, *An introduction to orthogonal polynomials* (Dover books on mathematics), Dover ed. Mineola, N.Y: Dover Publications, 2011, OCLC: ocn630478036, ISBN: 978-0-486-47929-3 (cit. on p. 153).